The Impact of Submesoscale Flows on Mesoscale Agulhas Dynamics

Dissertation

zur Erlangung des Doktorgrades

der Mathematisch-Naturwissenschaftlichen Fakultät

der Christian-Albrechts-Universität zu Kiel

vorgelegt von

René Schubert

Kiel, 2020

Main Supervisor and 1st Reviewer	Prof. Dr. Arne Biastoch GEOMAR Helmholtz Centre for Ocean Research Kiel RD1, Ocean Dynamics and Christian-Albrechts University Kiel
2nd Reviewer	Prof. Dr. Peter Brandt GEOMAR Helmholtz Centre for Ocean Research Kiel RD1, Physical Oceanography and Christian-Albrechts University Kiel
Additional Supervisor in the Framework of the Integrated School of Ocean Sciences	Prof. Dr. Richard J. Greatbatch GEOMAR Helmholtz Centre for Ocean Research Kiel RD1, Ocean Dynamics and Christian-Albrechts University Kiel
Additional Supervisor in the Framework of the Integrated School of Ocean Sciences	Prof. Dr. Burkard Baschek Helmholtz Centre Geesthacht Head of the Institute of Coastal Research
Date of Submission	February 6th, 2020
Date of Oral Examination	March 27th, 2020
Approved for Publication	
Signature of the Dean	_____ Prof. Dr. Frank Kempken

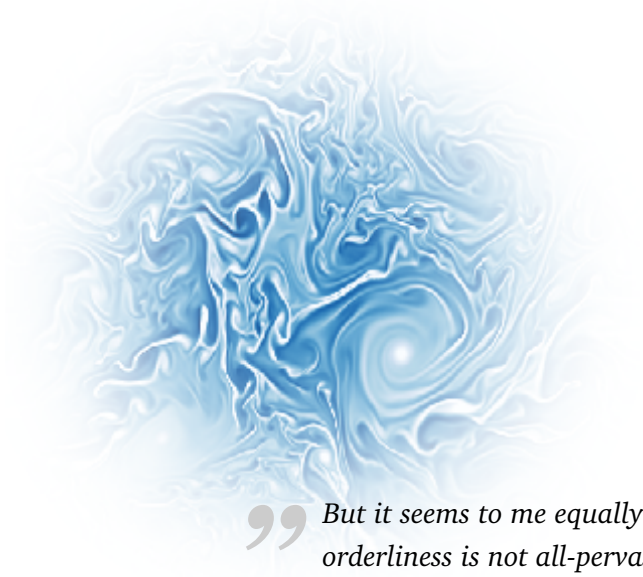

But it seems to me equally obvious that the orderliness is not all-pervasive. There are streaks of order to be found among the chaos, and the nature of scientific method is to seek these out and to stick to them when found and to reject or neglect the chaos. It is obvious that we have succeeded in finding some order in nature, but this fact in itself does not prove anything farther.

— **Arthur David Ritchie**
in Ritchie (1923)

Abstract

Mesoscale eddies are central to the oceanic circulation and the global climate. Of particular importance, in this respect, are mesoscale eddies in the Agulhas region south of Africa, as they govern the inflow of warm and salty Indian Ocean waters into the Atlantic Ocean. In this dissertation, it is shown that these eddies are strengthened by submesoscale flows. This highlights the importance of including submesoscale effects for a realistic representation of the mesoscale dynamics in ocean models. First, a general circulation ocean model for the Agulhas region is improved with respect to the simulation of submesoscale dynamics by increasing the vertical and horizontal resolution and reducing the model diffusion and dissipation. Second, a model validation based on horizontal-wavenumber spectra computed from high-resolution satellite sea-surface temperature and sea-surface height measurements is performed. It demonstrates that the simulated submesoscale and mesoscale circulation in the Cape Basin are extraordinary well represented in this model. A comparison to two parallel model experiments, of which the first only resolves the largest and the second no submesoscale flows, reveals that the mesoscale spectral density of sea-surface height increases the more submesoscales are resolved. The results of an eddy detection algorithm show that this can be attributed to a strengthening of the mesoscale eddies. Third, a coarse-graining approach for the transfer of kinetic energy between spatial scales is applied to the model outputs. The results indicate that the mesoscale eddies are strengthened in spring or early summer by the absorption of submesoscale eddies resulting from baroclinic mixed-layer instability in winter. Fourth, this analysis complemented with the computation of the transfer of kinetic energy between temporal scales reveals that submesoscale eddies emerging from barotropic instabilities at the northern boundary of the Agulhas Current are important for the strength of shear-edge eddies and further of lee cyclones that propagate into the Cape Basin. The model comparison shows that the combination of both strengthening effects contributes to an increase of the surface mesoscale kinetic energy in the Cape Basin by 28 %, if submesoscale processes are resolved.

Zusammenfassung

Mesoskalische Wirbel sind von zentraler Bedeutung für die Ozeanzirkulation und das globale Klima. Von besonderer Bedeutung sind dabei mesoskalische Wirbel in der Agulhas Region südlich von Afrika, da diese den Einstrom warmer und salziger Wassermassen aus dem Indischen Ozean in den Atlantik bestimmen. In dieser Dissertation wird gezeigt, dass diese Wirbel von submesoskalischen Strömungen verstärkt werden. Dies verdeutlicht, dass submesoskalische Effekte für eine realistische Repräsentation von mesoskalischen Wirbeln in Ozeanmodellen enthalten sein müssen. Zuerst wird ein Modell der generellen Ozeanzirkluation in der Agulhas Region im Hinblick auf die Simulation submesoskalischer Dynamik verbessert, indem die vertikale und horizontale Auflösung erhöht und die Diffusion und Dissipation im Modell verringert wird. Anschließend wird eine Modellvalidierung durchgeführt, bei der horizontale Wellenzahlspektren aus hochauflösenden Satellitendaten der Meeresoberflächentemperatur und der Meeresspiegelhöhe berechnet werden. Diese zeigt, dass die simulierte submesoskalische als auch mesoskalische Zirkulation im Cape Basin außerordentlich gut in diesem Modell repräsentiert sind. Der Vergleich mit zwei parallelen Modellexperimenten, von denen das Erste nur die größten und das Zweite gar keine submesoskalischen Strömungen auflöst, zeigt, dass die mesoskalische spektrale Dichte der Meeresspiegelhöhe mit besserer Auflösung der Submesoskala zunimmt. Die Ergebnisse eines Wirbelerfassungs-Algorithmus zeigen, dass dies auf eine Verstärkung der mesoskalischen Wirbel zurückzuführen ist. Danach wird ein Filteransatz für den Transfer kinetischer Energie zwischen räumlichen Skalen auf die Modellergebnisse angewandt. Die Ergebnisse deuten darauf hin, dass die mesoskalischen Wirbel verstärkt werden, in dem sie im Frühling oder frühen Sommer submesoskalische Wirbel absorbieren, die durch barokline Deckschichtinstabilitäten im Winter entstehen. Abschließend zeigt diese Analyse, ergänzt durch die Berechnung des Transfers kinetischer Energie zwischen zeitlichen Skalen, dass submesoskalische Wirbel, die bei barotropen Instabilitäten am Nordrand des Agulhasstroms entstehen, wichtig für die Stärke von Shear-Edge Wirbeln und weiter für Lee-Zyklonen sind, die in das Cape Basin driften. Der Modellvergleich zeigt, dass die Kombination beider verstärkender Effekte dazu beiträgt, dass die mesoskalische kinetische Energie an der Oberfläche im Cape Basin um 28 % erhöht ist, wenn submesoskalische Prozesse aufgelöst werden.

Contents

1 Introduction Part I: The Agulhas Current System

> *What we know is a point to what we do not know.*
>
> — **Ralph Waldo Emerson**
> in Emerson and Cameron (1940)

The ocean is crucial for stabilizing the Earth's climate as its global overturning circulation is associated with a net heat transport from the tropics towards the polar regions (e.g. Hsiung, 1985). The global overturning circulation is mainly driven by the large-scale atmospheric winds and to a lesser extent by thermohaline driving factors (Ferrari and Wunsch, 2009). It basically consists of anticyclonic subtropical and cyclonic subpolar gyres, zonal current systems along the equator and around Antarctica, as well as deep return flows (Fig. 1.1). In particular the western boundary currents of the subtropical gyres, such as the Agulhas Current, the Gulf Stream and the Kuroshio, contribute an important part to the warm, poleward, near-surface branch of the global overturning circulation.

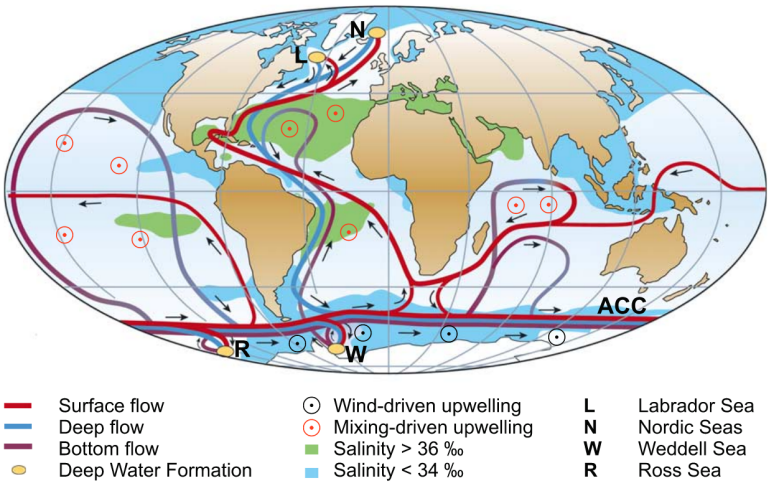

Fig. 1.1: *A simplified sketch of the global overturning circulation. The figure is taken from Kuhlbrodt et al. (2007) who published a modified version of the figure by Rahmstorf (2002). "ACC" marks the location of the Antarctic Circumpolar Current (ACC).*

The Agulhas current system (Fig. 1.2) south of Africa connects the subtropical gyres of both the South Atlantic and the South Indian Ocean to one supergyre (Speich et al., 2007). The inflow of warm and salty Indian Ocean waters, the **Agulhas leakage**, is of importance for the stratification in the South Atlantic (De Ruijter et al., 1999), the sea-surface temperature (SST) variability in the tropical Atlantic (Lübbecke et al., 2015) as well as the Atlantic Meridional Overturning Circulation (Weijer et al., 2002; Biastoch et al., 2008b). Partly due to the contribution of Agulhas leakage, the South Atlantic is the only basin with a net equatorward transport of heat (Talley, 2003). Further it is found to correlate with the Atlantic multi-decadal oscillation with a lag of 15 years (Biastoch et al., 2015) which is in agreement with estimated transit times of particles from the Agulhas region into the North Atlantic (Rühs et al., 2013).

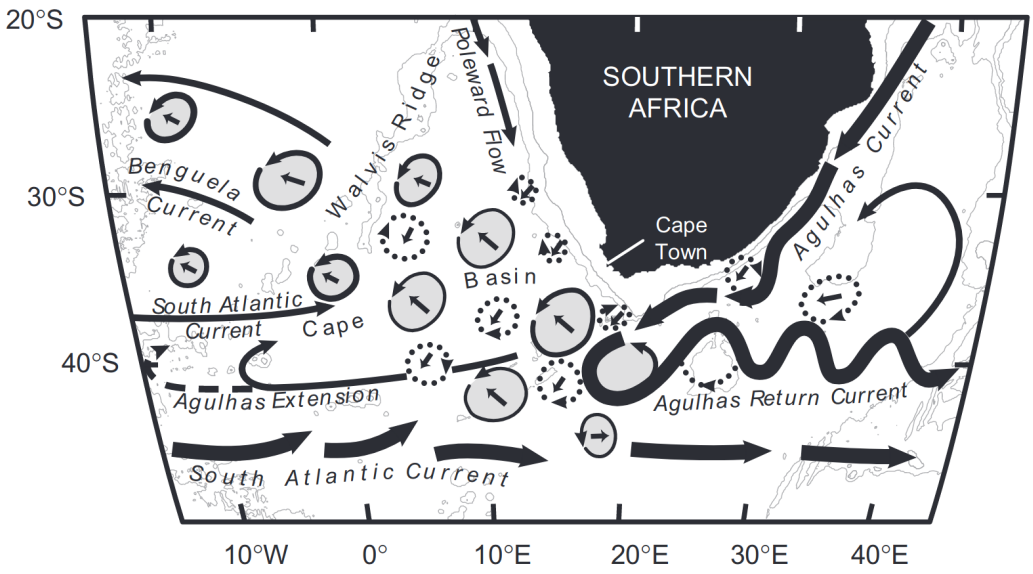

Fig. 1.2: *A sketch of the Agulhas current system taken from Richardson (2007).*

The **Agulhas Current** (AC), the western boundary current of the South Indian subtropical gyre, flows southwestward along the continental slope of the African continent. The presence of the warm AC waters influences the regional atmospheric circulation (Reason, 2001) and further the regional rainfall over South Africa (Nkwinkwa Njouodo et al., 2018; Jury et al., 1993). Besides for the weather and climate, the Agulhas current system is of regional importance for the fishery (e.g. Barlow et al., 2010) and the seafaring (e.g. Lavrenov, 1998). Estimates of the transport rate of the AC range between 72 Sv (1 Sv = 10^6 m^3/s) and 86 Sv through a section extending 300 km offshore (Beal et al., 2015). With this transport and time-mean surface velocities of up to 1.8 m/s (Beal et al., 2015), the AC is the

strongest western boundary current of the Southern Hemisphere and one of the strongest currents of the world ocean. Waters of the AC originate mainly from the Southwest Indian Ocean subgyre, as well as from Mozambique Eddies and eddies that detach from the East Madagascar Current (Lutjeharms, 2007). Regarding the far-field forcing, changes of the AC transport and temperature have been connected to the Indonesian Throughflow (Le Bars et al., 2013) and the El Niño–Southern Oscillation (Putrasahan et al., 2016).

South of Africa, the AC separates from the continental slope and retroflects towards the east, where it continues along the subtropical convergence zone as the **Agulhas Return Current** (ARC, Lutjeharms and Ansorge, 2001). The counterpart to the ARC along the Atlantic subtropical convergence zone is the South Atlantic Current (SAC), which is part of the subtropical gyre of the South Atlantic. The South Indian and the South Atlantic subtropical gyres are connected through the turbulent Agulhas leakage that merges with a part of the SAC and forms the **Benguela Current** (e.g. Gordon, 1986).

The Agulhas leakage can be mainly attributed to anticyclonic **Agulhas rings** that intermittently detach from the retroflection (Lutjeharms, 2007). Further, but small, contributions are provided by **Agulhas filaments** that develop at the northern wall of the AC and by a direct leakage (Lutjeharms, 2007). Agulhas rings are among the most energetic and largest eddies of the world ocean with an available potential energy of up to 71 PJ (Goni et al., 1997) and diameters of up to 500 km (Arhan et al., 2003). They mix most of their water mass properties into the surrounding **Cape Basin** and decay exponentially after their shedding (Boebel et al., 2003; Van Aken et al., 2003; De Ruijter et al., 1999). Advected by the Benguela Current, as well as driven by the β-effect, they propagate northwestward into the South Atlantic (De Ruijter et al., 1999). In the central South Atlantic, they propagate zonally across the basin and reach the western boundary with about 10 % of their intial sea-surface height (SSH) amplitude (Byrne et al., 1995).

The amount of Agulhas leakage computed from observations is usually estimated as the average transport of individual Agulhas rings multiplied with the average number of six rings per year detected by satellite altimetry (De Ruijter et al., 1999). Estimating the Agulhas leakage of single rings from hydrographic observations is however a challenging task, as the water-masses of shedded Agulhas rings strongly change due to the strong heat and freshwater fluxes at the sea-surface (De Ruijter et al., 1999). The respective estimates consequently have a wide range from about 0.5 Sv to 1.5 Sv per ring yielding an Agulhas ring leakage between 3 Sv and 9 Sv (Richardson, 2007). Based on drifter and float data, Richardson (2007) estimated

for the upper 1000 m a larger value of 10.4 Sv to 12.8 Sv for the Agulhas ring leakage and at least 15 Sv for the total Agulhas leakage (including filaments and direct leakage).

On the large scales, the Agulhas leakage is controlled by the strength and position of the southern hemisphere winds (Durgadoo, 2013; Biastoch et al., 2009b). Agulhas leakage is found to increase with the poleward strengthening of the westerlies (Biastoch et al., 2009b; Biastoch and Böning, 2013) that has been observed in the last decades and predicted to continue under global warming (Swart and Fyfe, 2012). Regionally, the Agulhas leakage is controlled by the complex scale-interactions within the Agulhas region which further is influenced by the regional bathymetry (Biastoch et al., 2008c; Lutjeharms, 2007). See Figure 1.3 for an overview over the bathymetry and associated features in the Agulhas region.

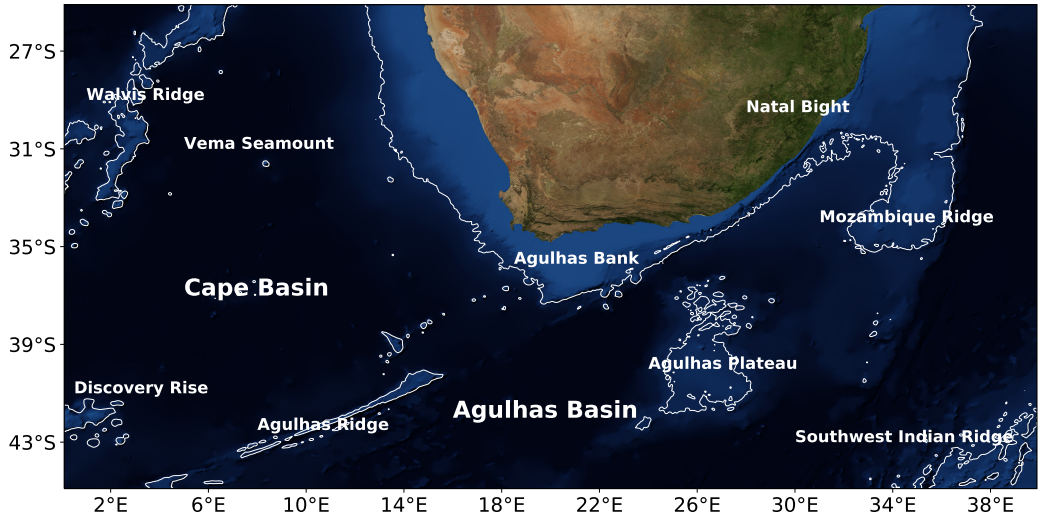

Fig. 1.3: *Bathymetric features of the Agulhas Region. The background picture is used throughout the thesis and taken from Stöckli et al. (2005). The 3000 m depth contour of the ETOPO1 bathymetry (www.earthmodels.org/data-and-tools/topography/etopo) is shown in white.*

The shallow continental slope around the **Natal Bight** enables the AC to become unstable at around $30°S$, when it is triggered by eddies of both Mozambique Channel and East Madagascar Current origin (Schouten et al., 2002; Lutjeharms, 2007). Large downstream-propagating meanders, the **Natal Pulses**, develop and are responsible for the majority of the AC's variability (Lutjeharms and Roberts, 1988). At the eastern **Agulhas Bank**, the associated upwelling drives a strong biological productivity which is important for the fishery of South Africa (Barlow et al., 2010). Further downstream, Natal Pulses are observed to trigger the shedding of Agulhas rings (Schouten et al., 2002; van Leeuwen et al., 2000). Natal Pulses are associated

with cyclones on their landward side that have diameters of 100 to 200 km (Lutjeharms and Roberts, 1988; Gründlingh, 1979; Lutjeharms et al., 2003a). South of the **Agulhas bank**, it is observed that these cyclones are occasionally shed southwestward, propagate through the retroflected AC and initialize the shedding of an Agulhas ring (Lutjeharms et al., 2003a). Large Natal Pulses can lead to a separation of the AC at around $28°E$, resulting in a flow directly along the eastern slope of the **Agulhas Plateau** (Lutjeharms and Van Ballegooyen, 1988b). In the case of such an "early retroflection", the Agulhas leakage is suppressed. In the usual case of no early retroflection, the Agulhas Plateau is important for the Agulhas ring shedding as the ARC attaches to its western flank and supports the occlusion of the retroflected loop. Further, the Agulhas plateau determines the location of the westernmost time-mean meander of the ARC (Fig. 1.2).

Between $30.5°S$ and $34.0°S$, the AC follows a very steep continental slope that suppresses mesoscale instabilities of the current (De Ruijter et al., 1999; Gründlingh, 1983). South of $34°S$, the flatter slope along the Agulhas Bank allows for intense instabilities that are associated with the formation of **plumes**, **shear-edge eddies**, meanders and submesoscale vortices (Lutjeharms et al., 1989, 2003a,b; Krug et al., 2017; Tedesco et al., 2019). The plumes move onto the Agulhas Bank and can drift into the South Atlantic as Agulhas filaments (Lutjeharms and Cooper, 1996). Shear-instability driven submesoscale vortices with a diameter of 10–20 km were measured at the northern boundary of the AC with seagliders (Lutjeharms et al., 2003a) and RAFOS floats (Krug et al., 2017). Those are to my knowledge the only studies using submesoscale-resolving in situ measurements in the Agulhas region. Shear-edge eddies as well as meanders travel downstream growing to scales of 50 - 100 km (Lutjeharms et al., 1989). The shear-edge eddies are trapped between the AC and the Agulhas bank and collect the cyclonic vorticity of other passing features (Lutjeharms et al., 2003b). The matured shear-edge eddies are either shed southwestward into the open ocean or leak their vorticity into a mesoscale **lee cyclone** west of the Agulhas bank (Penven et al., 2001; Boebel et al., 2003; Lutjeharms et al., 2003a). The lee cyclone occasionally detaches (Penven et al., 2001) and propagates southwestward into the ocean (Boebel et al., 2003). The southwestward shedding of **Agulhas cyclones** (lee, shear-edge, and Natal Pulse cyclones) contributes to the strong heat transport from the the Agulhas region into the Southern Ocean (Gille, 2003). Additional eddies originate from the southern Benguela upwelling system and travel westward into the Cape Basin (Lutjeharms and Stockton, 1987; Rubio et al., 2009).

The Cape Basin is one of the regions with the most energetic mesoscale eddy dynamics of the world ocean (Xu et al., 2014). Observed trajectories of anticyclones

and cyclones as presented by Boebel et al. (2003) are shown in Figure 1.4. Agulhas rings and Agulhas cyclones, as well as other eddies strongly interact within the Cape Basin, in particular in its eastern part which is, because of this, also referred to as the **Cape Cauldron** (Boebel et al., 2003).

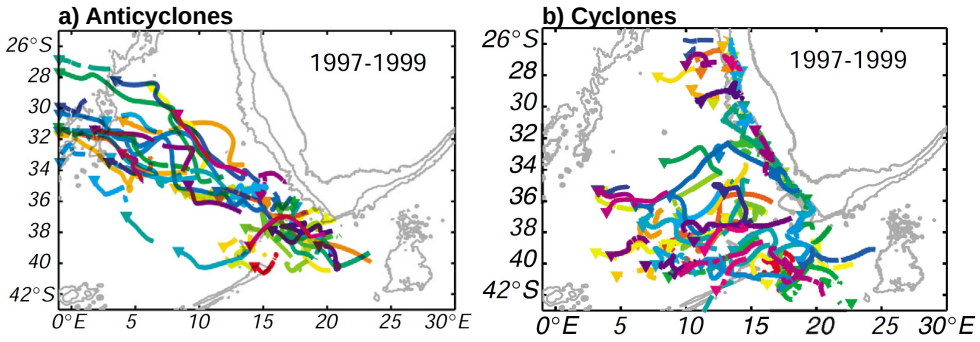

Fig. 1.4: *Trajectories of anticyclones (a) and cyclones (b) computed from MODAS-2D SSH in 1997 - 1999. The plots are taken from Boebel et al. (2003).*

The eddy-eddy interactions in the Cape Basin are associated with the development of strong fronts between the eddies that undergo submesoscale instabilities which drive a strong exchange of Agulhas rings with their surrounding (Richardson, 2007; Capuano et al., 2018a; Sinha et al., 2019). Submesoscale dynamics are thus expected to play an essential role in setting the properties of the water that reaches the South Atlantic and thus the Agulhas leakage (Capuano et al., 2018a; Boebel et al., 2003).

It remains unclear, which impact the submesoscale flows have on the mesoscale eddies in the Agulhas region and further on the Agulhas leakage. Moreover, it is not known, which role submesoscale dynamics at the northern boundary of the AC play in the formation of Agulhas cyclones that are important for the eddy-eddy interactions in the Cape Basin. These open issues are addressed in this dissertation.

2

Introduction Part II: Submesoscale Dynamics in the Surface Mixed-Layer

> *It truly takes a village.*
>
> — **James C. McWilliams**
> in McWilliams (2016).

The movement of the ocean can be described as a superposition of oceanic flows associated with different temporal and spatial scales ranging from the very quick movements of single water particles to the global overturning circulation. The global overturning circulation (Fig. 1.1) is usually referred to as the **large-scale** or planetary circulation. Large-scale flows, in particular large-scale currents such as the Gulf Stream, the Kuroshio and the Agulhas Current undergo baroclinic and barotropic instabilities that lead to the shedding of eddies with diameters of $\mathcal{O}(100\text{ km})$. These and other features of similar size are referred to as the **mesoscale**. **Submesoscale** dynamics span a wide range of scales that are smaller and shorter than those of the mesoscales but larger and longer than those of the isotropic **microscales**. A common dynamical definition of submesoscale flows bases on the non-dimensional Rossby and gradient Richardson numbers.

Rossby Number The Rossby number, Ro, describes to which extent the flow is in geostrophic balance and is defined to be the ratio of the magnitudes of horizontal momentum advection and Coriolis term: $Ro = \frac{|\mathbf{u}^h \nabla \mathbf{u}^h|}{|f \times \mathbf{u}^h|}$ (Gill, 1982). Here, $\mathbf{u}^h = (u, v)$ is the horizontal velocity vector, with the zonal component u and the meridional component v and $f = 2\Omega sin(2\pi \frac{\theta}{360^\circ})$ is the Coriolis parameter with the latitude θ and the angular speed of the Earth $\Omega = \frac{2\pi}{86400}\ s^{-1}$. An alternative definition of Ro bases on the vorticity equation and is given by $Ro = \frac{|\zeta|}{|f|}$, where $\zeta = v_x - u_y$ is the vertical component of the relative vorticity[1] and f the planetary vorticity (similar to the Coriolis parameter) (Thomas et al., 2008).

[1] Partial derivatives are written as $\frac{\partial a}{\partial b} = a_b$ throughout the dissertation.

Gradient Richardson Number The gradient Richardson number, Ri, is defined as the ratio of stratification and vertical shear $Ri = \frac{N^2}{|\mathbf{u}_z^h|^2}$ (Cushman-Roisin and Beckers, 2009), where $N = \sqrt{b_z}$ is the Brunt-Väisälä frequency with the buoyancy $b = -\frac{g}{\rho_0}\rho$, where ρ is the potential density, $\rho_0 = 1024$ kg/m^3 the reference density and $g = 9.81$ m/s^2 the gravitational acceleration. If the Richardson number is larger than 0.25 a stratified shear flow is stable (Cushman-Roisin and Beckers, 2009). For hydrostatic geostrophy, the thermal wind relation gives $Ri = \frac{(fN)^2}{|\nabla_h b|^2}$ which directly relates vertical and horizontal buyancy gradients.

Mesoscale dynamics are mainly two-dimensional (2D) and dominated by the influence of Earth's rotation ($Ro \ll 1$) and the effect of the stratification ($Ri \gg 1$). Microscale turbulence is associated with three-dimensional (3D) isotropic flows for which the rotation of the Earth as well as the stratification is not important ($Ro \gg 1$, $Ri \ll 1$). Submesoscale dynamics are not dominated but influenced by Earth's rotation and stratification and are defined to be associated with $Ro \approx \mathcal{O}(1)$ and larger, and $Ri \approx \mathcal{O}(1)$ (Thomas et al., 2008; McWilliams, 2016).

Submesoscale dynamics can be generated almost everywhere in the ocean (McWilliams, 2016). Most of the submesoscale related research has however focused on the upper ocean as most of the submesoscale resolving observations are available near and in particular at the sea-surface. Moreover, in ocean models, submesoscale flows are found to be much more energetic in the upper ocean than in the interior (e.g. Klein et al., 2011). This indicates that their potential for impacts on the larger scale flows is also larger in the upper ocean than in the interior. For these reasons, this dissertation focuses on the upper ocean submesoscale dynamics.

A characteristic feature of the upper ocean is the presence of the homogenized **surface mixed-layer** (ML) (e.g. de Boyer Montégut et al., 2004). In the ML, the temperature, the salinity, and consequently the density is vertically almost uniform as a consequence of strong turbulent mixing. A major control on this turbulence is the atmospheric forcing at the sea-surface (Mahadevan et al., 2010). Surface cooling, evaporation and momentum input by the wind increase the near-surface turbulence which reduces the stratification. In contrast, surface heating and precipitation increase the stratification. Regional differences in the forcing as well as meso- and large-scale dynamics lead to horizontal density gradients in the ML (Boccaletti et al., 2007). As a consequence of these horizontal density gradients, submesoscale frontal circulations and instabilities develop. These submesoscale processes are of essential importance for the stratification of the upper ocean and thus for the heat and salt budgets of the ML (Boccaletti et al., 2007; Fox-Kemper et al., 2008).

As the surface forcing in the midlatitudes is associated with a strong seasonal cycle, also the mixed-layer depth (MLD) and consequently the submesoscale activity are associated with a seasonal cycle (Brannigan et al., 2015). Smaller wind-stress in summer leads to a shallower ML, while larger wind-stress in winter leads to a deeper ML. The larger the MLD, the more available potential energy is stored in submesoscale fronts and the more energetic are flows resulting from frontal instabilities (see section 2.2). Therefore, the winter is sometimes referred to as the "submesoscale season" as then the submesoscales are most energetic.

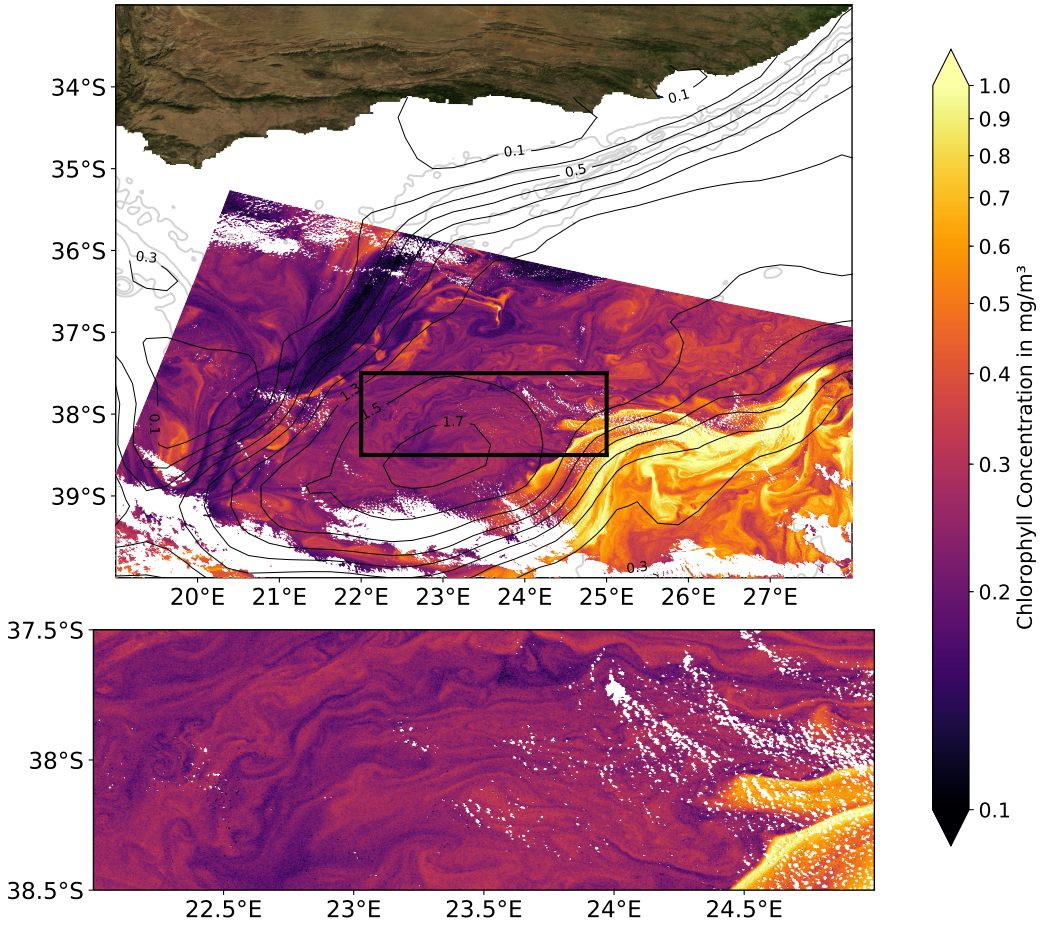

Fig. 2.1: *A Medium Resolution Imaging Spectrometer (MERIS, NASA Goddard Space Flight Center, 2012) satellite image of the surface chlorophyll concentration with extraordinary good quality taken on Dec 30th 2005 south of Africa. The image has a horizontal resolution of ≈300 m and visualizes the area-covering occurrence of submesoscale flows. The lower panel shows a zoom into the region marked in the upper panel. Data gaps in the chlorophyll concentration are due to cloud-cover. Black contours in the upper panel show the SSH in m on the same day from the L4 Copernicus Marine and Environment Monitoring Service satellite altimetry product (http://www.marine.copernicus.eu). The SSH contours mark the location of the Agulhas Current and its retroflection. Gray contours show the 200 m, 1000 m, 2000 m and 3000 m isobaths from the ETOPO1 bathymetry (www.earthmodels.org/data-and-tools/topography/etopo).*

Vertical velocities associated with near-surface submesoscale flows are usually one magnitude larger than those of the mesoscales (Thomas et al., 2008) and thus submesoscale flows dominate the vertical transport in the upper ocean (e.g. Klein et al., 2008). This has important implications for the transport of nutrients (for example nitrate, phosphate, iron, and silicate) into the sunlit ocean which feeds phytoplankton growth that is the fundament of life in the ocean (Lévy et al., 2001; Mahadevan, 2016). Because of this, the surface chlorophyll concentration often visualizes the presence of submesoscale flows. Figure 2.1 shows a respective ≈300 m horizontal resolution image taken with a Medium Resolution Imaging Spectrometer (MERIS, NASA Goddard Space Flight Center, 2012) from satellite in the region of the Agulhas retroflection. The picture reveals the area-covering occurrence of submesoscale flows. Further, the submesoscale vertical transport is of importance for the air-sea gas exchange of dissolved gasses such as carbon dioxide (Thomas et al., 2008). Moreover, submesoscale vertical velocities enhance the subduction of organic matter and thus the carbon export (Thomas et al., 2008).

Submesoscale ML flows strongly interact with the mesoscale interior below (Thomas, 2005; Badin et al., 2011; Klein et al., 2011; Ramachandran et al., 2014). Both regimes are connected through the vertical velocity field (Klein et al., 2011). Through mass conservation, near-surface frontogenesis related divergent motions drive thereby an interior mesoscale vortex stretching (Lapeyre et al., 2006; Klein et al., 2011). Consistently, the mesoscale component of the root-mean-square vertical velocity is found to be twice as high in a submesoscale resolving ($(1/80)^\circ$ horizontal resolution) simulation of the Kerguelen region by Rosso et al. (2014) compared to a $(1/20)^\circ$ simulation.

Submesoscale dynamics are thought to play a large role for the oceans general circulation as they provide a pathway from the geostrophically balanced flows to dissipation (Capet et al., 2008b; Molemaker et al., 2010; Thomas and Taylor, 2010; D'Asaro et al., 2011; Thomas et al., 2013) but are also associated with an upscale transfer of kinetic energy (Capet et al., 2008b; Klein et al., 2011; Soh and Kim, 2018). This upscale transfer has not yet been attributed to a particular process. Lévy et al. (2010) even found a strengthening of the subtropical gyre circulation if submesoscale flows are permitted in an idealized model simulation. Consistently, Hurlburt and Hogan (2000) as well as Chassignet and Xu (2017) showed an improvement in the pathway, penetration and variability of the simulated Gulf Stream with increased resolution of submesoscale flows. At the small-scale end submesoscale flows interact with the Langmuir turbulence (Hamlington et al., 2014) and are found to be a major control on the height of surface-waves (Ardhuin et al., 2017).

2.1 Typical Spatial and Temporal Scales

Typical horizontal scales of submesoscale flows range from values of the turbulent boundary layer thickness ($\mathcal{O}(10\ m)$ or $\mathcal{O}(100\ m)$) to the first baroclinic deformation radius ($\mathcal{O}(10\ km)$) (McWilliams, 2016). At smaller scales, the flow is close to isotropic and at larger scales, the flow is close to geostrophy. This dissertation focuses on the submesoscale dynamics that are resolvable by a model grid with $\approx 1.5\ km$ grid spacing. Thus, the focus lies on the larger-scale portion of submesoscale flows that are still associated with a large geostrophically balanced component. A typical length scale for partly geostrophically-balanced submesoscale flows in the surface mixed-layer is derived by Thomas et al. (2008):

The Mixed-Layer Rossby Radius of Deformation While the Rossby radius of deformation, a typical length scale for the mesoscale eddies and large-scale boundary currents, is defined as the length scale, where the effect of the relative vorticity balances the one of internal vortex stretching (Chelton et al., 1998; Gill, 1982), the mixed-layer Rossby radius of deformation is defined as the length scale R_{ML}, where the relative vorticity balances the planetary vorticity - and thus, where $Ro = 1$. Scaling gives $Ro \approx U/|f|L = 1$ and further $R_{ML} \equiv L = U/|f|$. Here L is the horizontal length scale and U is the horizontal velocity scale that can be replaced by the mixed-layer thermal wind balance $U \approx \nabla_h(b)D/|f|$, where D is the mixed-layer depth, resulting in $R_{ML} = \nabla_h(b)D/f^2$. Horizontal and vertical buoyancy gradients are related at an adjusted front by $N^2 = \nabla_h(b)^2/f^2$ (Tandon and Garrett, 1994) leading to

$$R_{ML} = N_{ML}D/|f|, \tag{2.1}$$

where N_{ML} is the average Brunt-Väisälä frequency in the mixed-layer. Consequently, R_{ML} (and thus the typical length scale of submesoscale flows) depends on horizontal or vertical buoyancy gradients, mixed-layer depth and latitude. Typical values ($N_{ML} = 10^{-3}\ 1/s$, $D = 50\ m$ and $|f| = 0.5 \times 10^{-4}\ 1/s$) give $R_{ML} = 1\ km$ (Thomas et al., 2008). The form of the so-derived R_{ML} is close to the first baroclinic Rossby radius of deformation $R_r = N_H H/\pi|f|$ (Chelton et al., 1998), where H is the total water depth and N_H the Brunt-Väisälä frequency averaged over the whole water column.

Typical vertical scales of submesoscale flows are 10 m to 1 km (McWilliams, 2016). Scaling of the gradient Richardson number for the mixed-layer gives $Ri \approx N_{ML}^2 D^2/U^2$. Combined with the scaling for the Rossby number ($Ro \approx U/|f|L$) and $Ro \approx Ri \approx 1$ leads to that the aspect ratio of vertical and horizontal length scales, H/L, scales with $|f|/N$ which is typically very small (Thomas et al., 2008). Consequently, as the hydrostatic balance is accurate to $\mathcal{O}(Ro^2 H/L)$, the hydrostatic approximation is valid to describe most of the submesoscale processes (Thomas et al., 2008).

Typical time scales are hours to days (McWilliams, 2016). An exception are long-lived submesoscale coherent vortices that can exist for years (McWilliams, 2016). A common proxy for a typical time-scale T of submesoscale dynamics is the inverse of the growth rate of baroclinic mixed-layer instabilities (see 2.2.2) $T \approx 1/\omega_{growth} = \sqrt{Ri}/f$ (Thomas et al., 2008). $Ri = 1$ and $f = 10^{-4}$ s^{-1} give a typical time scale of $T \approx 2.8$ h for the midlatitudes.

2.2 Submesoscale Dynamical Processes in the Surface Mixed-Layer

2.2.1 Frontogenesis

Oceanic fronts are regions of sharp horizontal density gradients that develop as a consequence of a confluent background flow (Hoskins, 1982). In particular the strain between advected mesoscale eddies is a major driver of the intensification of fronts (frontogenesis) in the open ocean (McWilliams, 2016). Frontogenesis is usually investigated with the frontogenetic tendency.

Frontogenetic Tendency The frontogenetic tendency is defined as $\frac{d}{dt}(\nabla_h \rho)^2 = \mathbf{Q} \cdot \nabla_h \rho$ (e.g. Giordani and Caniaux, 2001). The vector $\mathbf{Q}$ can be split into a thermodynamic and a dynamic part. The contribution of the straining by the horizontal flow field to the increase in horizontal density gradient is given by $\mathbf{Q}^s = -(u_x \rho_x + v_x \rho_y, u_y \rho_x + v_y \rho_y)$ (Giordani and Caniaux, 2001) leading to a respective frontogenetic tendency

$$FT = \mathbf{Q}^s \cdot \nabla_h \rho = -[u_x \rho_x^2 + (v_x + u_y)\rho_x \rho_y + v_y \rho_y^2].$$

Positive values indicate frontogenetic and negative frontolytic regions.

Splitting $\mathbf{Q}^s$ into a geostrophic and an ageostrophic component shows that the geostrophic contribution to frontogenesis is constant over depth but relatively small, while the ageostrophic contribution is surface-intensified, strong and strengthens the front at the heavier side and weakens it on the light side (Capet et al., 2008b). Moreover, ageostrophic frontogenesis acts faster than geostrophic frontogenesis (Klein et al., 2008).

The oceanic mixed-layer is a region that is particularly conducive to frontogenesis due to the presence of the sea-surface (Thomas et al., 2008). Submesoscale fronts in the mixed-layer are associated with surface intensified horizontal density gradients that are sharp enough for the along front flow to break the geostrophic balance. An ageostrophic secondary circulation develops in the cross-front plane with upwelling and surface divergence on the lighter side and downwelling and surface convergence on the denser side (McWilliams, 2016). The secondary circulation tilts the sloped isopycnals towards the horizontal (restratifies the mixed-layer) restoring geostrophic balance and accelerating the geostrophic flow (Capet et al., 2008b).

Vertical velocities of the ageostrophic circulation are of $\mathcal{O}$(100 m/day) which is typically one magnitude larger than those of the mesoscales (Thomas et al., 2008). They are of large importance for the vertical transport in the upper ocean and the exchange of the mixed-layer and the interior which has important implications for the concentration of nutrients and dissolved gasses (Thomas et al., 2008). For the ocean dynamics, the vertical velocitites are of importance as they induce further anticyclonic (cyclonic) near-surface relative vorticity by vortex stretching on the lighter (denser) side (McWilliams, 2016). Cyclonic vorticities and downward velocities are thereby much stronger than anticyclonic vorticities and upward velocities (McWilliams, 2016).

2.2.2 Unforced Instabilities

A sheared flow in the mixed-layer with $Ri \approx Ro \approx \mathcal{O}(1)$ that is in thermal wind balance with a constant horizontal density gradient is associated with two modes of baroclinic instability (Molemaker et al., 2005; Thomas et al., 2008). The first mode is mostly geostrophically balanced and well captured with the hydrostatic approximation (Stone, 1966). This mode is usually referred to as the **mixed-layer baroclinic instability** (MLI). The second mode is ageostrophic with a large non-hydrostatic component and is referred to as the **anticyclonic ageostrophic instability**. While the ageostrophic mode is relevant for the forward kinetic energy cascade (Molemaker et al., 2005), in this dissertation indication is found that the geostrophic mode is important for the inverse kinetic energy cascade (see chapter 7.8). The anticyclonic ageostrophic instability will not be considered further as it is not resolved by the model experiments that are executed for this dissertation.

Similar to the mesoscale baroclinic instability, the MLI tilts time-mean isopycnals towards the horizontal (restratification) and is associated with an energy transfer from available potential energy of the time-mean density field (MPE) to mean kinetic energy of the time-varying circulation, (EKE, "Eddy Kinetic Energy"). A measure for the respective energy transfer into the EKE is the Vertical Buoyancy Flux (VBF) $VBF = \overline{w'b'}$ (Storch et al., 2012; McWilliams, 2016), where w is the vertical velocity component. The overbar denotes the time-mean and the dashes deviations from that time-mean. As MLI and associated features develop within periods not longer than a few weeks (e.g. Boccaletti et al., 2007; Fox-Kemper et al., 2008), a reference and averaging period of about a month is a useful choice. In ocean models, the restratification by MLI can be parameterized in terms of an overturning streamfunction tilting the isopycnals towards the horizontal (Fox-Kemper et al., 2008).

Situations preceding MLIs and the respective mechanisms are described by Boccaletti et al. (2007). A typical example is a storm event that homogenizes the upper ocean in the vertical and leaves a deep mixed-layer with horizontal density gradients. Initially a gravitational overturning starts to tilt the almost vertical isopycnals (Tandon and Garrett, 1995). Under the influence of Earth's rotation, the flow adjusts geostrophically which leads to a sheared flow in thermal wind balance with $Ri \approx Ro \approx \mathcal{O}(1)$ that undergoes MLI. The MLI then drives the bulk of the restratification within a few days (Thomas and Ferrari, 2008; Boccaletti et al., 2007). This highlights its importance for the mixed-layer heat and salt budgets and further for the SST. Frontogenesis driven by mesoscale straining is a further mechanism that can establish the conditions for MLI. Very strong straining can however also suppress the MLI (e.g. Bishop, 1993).

A typical length-scale of MLI is the wavelength of the fastest growing mode of the Eady (1949) baroclinic instability problem extended by ageostrophic perturbations (Stone, 1970):

$$\lambda_s = \frac{2\pi u_0}{|f|}\sqrt{\frac{1+Ri}{5/2}}, \tag{2.2}$$

where $u_0 = |\nabla_h b|D/|f|$ is the thermal wind in the ML. With $Ri \approx 1$, λ_s is very similar to the mixed-layer Rossby radius of deformation R_{ML} (see section 2.1). Typical values for the midlatitudes ($u_0 = 0.05$ m/s, $f = 7.29 \times 10^{-5}$ s^{-1}, $Ri = 1$) give $\lambda_s = 3.9$ km (Fox-Kemper et al., 2008) consistent with respective observations (e.g. Hosegood et al., 2006). After the MLI reaches finite amplitude, the perturbations grow to scales of about 10 - 50 km due to a nonlinear upscale kinetic energy flux (Fox-Kemper et al., 2008). It remains unclear, which impact these features have on the mesoscale dynamics. In chapter 7 of this dissertation indication is presented that these features are absorbed by the mesoscale eddies driving a submesoscale inverse kinetic energy cascade.

Besides the MLI, submesoscale frontal jets can undergo **barotropic instability** similar to the mesoscale barotropic instability (Gula et al., 2014). Mean kinetic energy of the time-mean circulation (MKE) is thereby transferred to the EKE. A measure of the respective energy transfer is the Horizontal Reynolds Stress (HRS) term $HRS = -\rho_0[\overline{u'u'}\overline{u}_x + \overline{u'v'}(\overline{u}_y + \overline{v}_x) + \overline{v'v'}\overline{v}_y]$. Similar to the MLI, the submesoscale barotropic instability can be suppressed by strong mesoscale straining (Moore and Saffman, 1975; Dritschel et al., 1991).

2.2.3 Forced Instabilities

Submesoscale ML processes are strongly linked to the atmospheric forcing. As described above, horizontal differences in the atmospheric forcing drive horizontal density gradients in the ML that are associated with submesoscale dynamics. Further, also a uniform cooling of mesoscale eddies is found to be associated with the development of MLIs (Legg et al., 1998; Legg and McWilliams, 2001). Moreover, in the presence of a front, the wind can either have a stratifying or a restratifying effect on the ML depending on the angle between wind direction and the orientation of the front (Fig. 2.2). In the case of a down-front wind, which is defined as a wind blowing in the direction of the frontal jet (and thus with denser waters to the right on the Southern Hemisphere), the induced Ekman transport reduces or even overcomes the MLI induced restratification (Mahadevan et al., 2010). Up-front winds accelerate the MLI inherent restratification. Note that the maximum cross-front Ekman transports are found to occur for wind directions that slightly deviate from the direction of the frontal jet, as the front does not extend vertically over the whole Ekman layer (Capet et al., 2008b).

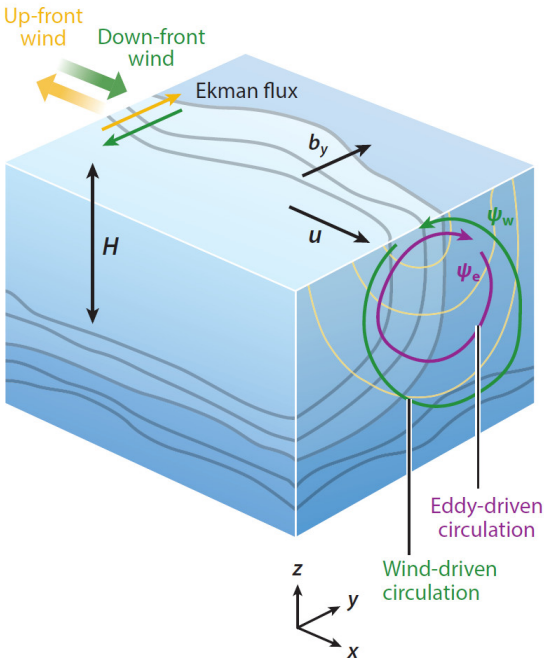

Fig. 2.2: *The effect of surface wind-forcing on a Northern Hemisphere front. A down-front wind (green) leads to wind-induced overturning circulation Ψ_w (green) that counteracts the mixed-layer instability induced eddy overturning circulation Ψ_e (violet). The graphic is taken from Mahadevan (2016).*

2.2.4 Secondary Instabilities

If the Ekman transport induced by a down-front wind transports denser water over lighter, convective mixing occurs (see Fig. 2.2) that can lead to positive Ertel potential vorticity $PV = (f\hat{k} + \nabla \times \mathbf{u}) \cdot \nabla b$ in the ML (Thomas et al., 2008). Here, $\hat{k}$ is the vertical unit vector and $\mathbf{u} = (u, v, w)$ is the 3D velocity vector. Due to the weak stratification, the mixed-layers PV is very small compared to the pycnocline below (Capet et al., 2008b). Usually, the PV has thereby the same sign as the planetary vorticity, which is negative on the Southern hemisphere. If the wind causes the PV to become positive, secondary instabilities develop (Hoskins, 1974).

The different secondary instabilities are symmetric, centrifugal, and gravitational instabilities, named after the respective cause leading to positive PV. Here the definitions of Haine and Marshall (1998) and Thomas et al. (2013) are summarized. The PV can be decomposed into a baroclinic component

$$PV_{bc} = (u_z - w_x)b_y + (w_y - v_z)b_x$$

and a vertical component

$$PV_v = (f + \zeta)b_z$$

(Thomas et al., 2013). **Symmetric instabilities** occur, if PV_v is negative and PV_{bc} is positive and larger than the magnitude of PV_v. For geostrophic flows with $w_x << u_z$ and $w_y << v_z$, the thermal wind relation gives $PV_{bc}^g = -\frac{1}{f}|\nabla_h b|^2$ which is positive on the Southern Hemisphere. For this case, instabilities occur when PV_v is also positive or when PV_v is negative but its magnitude is smaller than PV_{bc}^g. Instabilities in barotropic geostrophic flows with $PV_{bc}^g = 0$ occur only when PV_v is positive. Then, for stable stratification ($b_z > 0$), **centrifugal instabilities** occur when the flow is associated with large anticyclonic vorticity ($\zeta > 0$, $Ro > 1$). For unstable stratification ($b_z < 0$), **gravitational instabilities** occur[2].

In the case of symmetric instability, the instability extracts kinetic energy from the jet and induces a restratifying vertical circulation that opposes the wind-induced effect (Fig. 2.2) (D'Asaro et al., 2011). The symmetric unstable front is equilibrated by the formation of subsequent Kelvin-Helmholtz instabilities that transfer kinetic energy to the dissipative microscales (Taylor and Ferrari, 2009). The development of submesoscale fronts that undergo forced symmetric instabilities and subsequent secondary instabilities is thus thought to provide a possible route to dissipation for

[2]The PV_v can however get negative, if the flow is associated with strong anticyclonic vorticity ($Ro > 1$).

the ocean (Thomas and Taylor, 2010; Thomas et al., 2013).

The secondary instabilities are the reason for the cyclone-anticyclone asymmetry observed in the upper ocean (Roullet and Klein, 2010; Buckingham et al., 2016). The near-surface distribution of ζ/f is skewed towards cyclonic movements as secondary instabilities occur when anticyclonic flows exceed a critical Ro. In the non-winter seasons, anticyclonic flows with $Ro > 1$ become centrifugally unstable. Thus, flows with larger anticyclonic Ro occur only rarely. In winter, Ri can be as small that anticyclonic flows become symmetrically unstable before they reach $Ro = 1$ (Fig. 2.3). The anticyclonic flow then gets symmetrically unstable already at $Ro > |-1 + 1/Ri|$ (Buckingham et al., 2016).

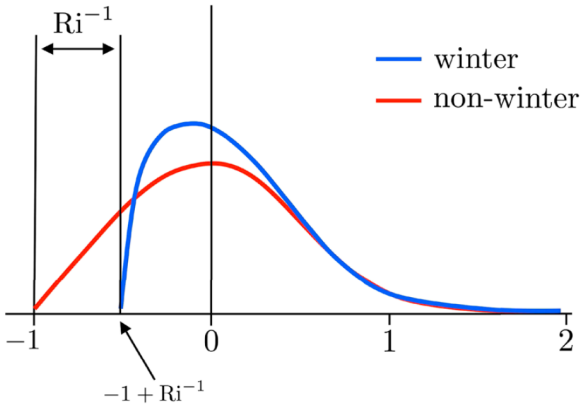

Fig. 2.3: *An illustration demonstrating the seasonal cycle of the skewed distribution (y-axis) of upper ocean normalized relative vorticity ζ/f (x-axis) taken from Buckingham et al. (2016). Ri is the gradient Richardson number.*

2.3 Submesoscale and Mesoscale Theories and Their Predictions for the Slope of Horizontal Wavenumber Spectra

Mesoscale dynamics are well described by **quasigeostrophic** (QG) theory (e.g. Gill, 1982). The QG equations are derived by scaling the primitive equations using the assumptions $Ro \ll 1$ and $Ri \gg 1$. As submesoscale flows are associated with $Ro \approx Ri \approx \mathcal{O}(1)$, the QG theory is obviously not able to capture the characteristics of the full submesoscale spectrum properly. However, as a fraction of submesoscale flows is partially QG balanced, the QG theory is nevertheless used to interpret a part of the observed and simulated submesoscale flows in terms of their dynamics.

QG flows can be decomposed into a component due to interior-PV and surface-buoyancy anomalies (Lapeyre and Klein, 2006). There are two theories associated with the extremes that one of both components is neglectable. **Surface quasi-geostrophic** dynamics (SQG, Blumen, 1978; Held et al., 1995) assume uniform interior PV and **interior quasigeostrophic** dynamics (IQG, Charney, 1971) uniform surface PV. If both PV components are non-uniform, which is usually the case in the real ocean, the surface and the interior regime strongly interact (Lapeyre and Klein, 2006).

Under the assumption that turbulence is mainly forced at scales of the Rossby radius of deformation through baroclinic instability and mainly dissipated at the very small scales, an inertial range exists in between where the energy and enstrophy are nonlinearly transferred across spatial scales. For isotropic and horizontally homogeneous turbulence, characteristic slopes of the horizontal wavenumber spectra of kinetic and potential energy can be derived for this inertial range (Callies and Ferrari, 2013). While the IQG theory predicts a k^{-3} slope for the horizontal spectra of kinetic and potential energy, the SQG theory predicts $k^{-5/3}$ spectral slopes[3] (Callies and Ferrari, 2013). Moreover, in the inertial range, the spectra of kinetic energy and (passive) tracer variance are related in a way that steeper kinetic energy spectra lead to flatter tracer variance spectra (Vallis, 2006). In other words, IQG dynamics lead to a strong filamentation of a tracer, while the energetic small-scale dynamics

[3]The SQG prediction of the $k^{-5/3}$ spectral slope is only valid for the surface. Below the surface, the spectrum is found to follow the SQG prediction for scales larger than a transition scale and the IQG prediction for smaller scales (Callies and Ferrari, 2013). The transition scale shifts to larger scales with increasing depth. Moreover, the predicted spectral slopes from SQG theory depend on the assumptions for the stratification (Callies and Ferrari, 2013).

in SQG turbulence reduce the tracer variance strongly at the small scales trough mixing (Callies and Ferrari, 2013). Regions of steeper kinetic energy spectra are thus expected to be associated with flatter SST spectra.

Strong baroclinic currents such as the Gulf Stream are associated with a deep reversal of the PV gradient and are dominated by the interior PV (Callies and Ferrari, 2013). The deep PV reversal leads to deep baroclinic instability that is the major driver of IQG turbulence. Consistently, in the region of the Gulf Stream, the kinetic energy spectrum is found to be associated with a k^{-3} slope (Lapeyre and Klein, 2006). Further, also the SSH spectrum of the Gulf Stream region is found to be associated with slopes close to k^{-5} (Xu and Fu, 2012) which is the geostrophically corresponding slope to a k^{-3} kinetic energy spectral slope. Similar SSH spectral slopes are found for the regions of the Kuroshio, the ACC and the Agulhas region (Xu and Fu, 2012). It is expected that, at least at the larger mesoscales, the region of the AC, its retroflection, and the ARC, as well as the Agulhas ring path are dominated by the interior PV component and thus IQG dynamics.

For a very different dynamical regime, the Californian upwelling system, a transition is found from k^{-3} to k^{-2} kinetic energy slopes, when the horizontal resolution is increased from 12.0 to 1.5 km and thus more and more submesoscale flows are resolved in a respective series of model experiments (Capet et al., 2008a). The flatter slopes suggest in the QG framework that the dynamics are closer to SQG the more submesoscale flows are resolved. Further, the dynamics are closer to the altimetric observations that show a SSH spectral slope close to $k^{-11/3}$ offshore of the US coast (Xu and Fu, 2012) which geostrophically corresponds to the SQG prediction of $k^{-5/3}$. SQG turbulence is however a result of purely geostrophic frontogenesis (Callies and Ferrari, 2013). Ageostrophic frontogenesis is not captured by SQG theory. It evolves much faster than in SQG theory and is associated with strong near-surface divergence and $Ro > 1$ (Capet et al., 2008a; Klein et al., 2008). The respective dynamics thus need more complex theories than SQG to capture the nonlinear interactions with the high Rossby number flows (Klein et al., 2008).

If the advection by the ageostrophic flows is added to the SQG equations, a theoretical k^{-2} slope for kinetic and potential energy is predicted (Boyd, 1992; Capet et al., 2008a). The results of Capet et al. (2008a) agree with this prediction. Boyd (1992) point out that fronts directly after their breaking are associated with a kinetic energy spectral slope close to $k^{-8/3}$ and thus most accurately predicted by **semi-geostrophic** theory (SG, Hoskins, 1975; Andrews and Hoskins, 1978). Semi-geostrophic theory is accurate for relatively straight flows as for example frontal

flows (Thomas et al., 2008) and is valid if the flow evolves in a Lagrangian view on timescales much longer than an inertial period (Hoskins, 1975). For relatively curved flow as it is the case for submesoscale coherent vortices, the **balanced equations** (BE, e.g. Bolin, 1956) are the most accurate (Thomas et al., 2008). In the framework of BE theory, the velocity and density field can be derived by applying an invertibility principal to the horizontal stream function instead of the PV in the previous mentioned theories. A detailed comparison of SG, BE and other intermediate models, between QG and the primitive equations, is presented by McWilliams and Gent (1980).

It remains unclear, whether an intermediate model is suitable to describe all characteristics of submesoscale flows properly as unbalanced[4] flows such as internal gravity waves, tides, inertial oscillations and other ML flows with strong ageostrophic components significantly contribute to submesoscale turbulence (Callies and Ferrari, 2013). The interaction of internal gravity waves and QG balanced submesoscale flows is mainly thought to be weak, but is still poorly understood (McWilliams, 2016). For the internal-wave continuum at scales smaller than 10 km, a k^{-2} slope is predicted for the kinetic and potential energy spectra by Garrett and Munk (1972) and Callies and Ferrari (2013). Theories on how tides and inertial oscillations imprint into the kinetic energy spectrum are not yet found (Callies and Ferrari, 2013).

[4]Unbalanced flows are flows that are not in quasigeostrophic balance.

2.4 Remote Sensing of Submesoscale Dynamics

As submesoscale resolving in situ measurements are extremely rare in the Agulhas region (see section 1), submesoscale research mainly needs to rely on remote sensing data. The measured signal of modern **satellite altimetry**, with which the mesoscale dynamics are to a large extent measurable, exceeds the respective noise mainly at scales that are larger than the submesoscales (Dufau et al., 2016). The geostrophic component of near-surface submesoscale flows is thus not measurable with present-day satellite altimetry. In the Agulhas region, satellite altimetry is capable to measure oceanic scales down to about 50 km (Dufau et al., 2016). The rough sea-state in winter, when the submesoscale dynamics are most energetic, however shifts this scale to larger scales in winter-time. **Satellite-based radar measurements** of the surface velocity field are available with a resolution of 4 - 8 km and are thus able to resolve the very large submesoscales (Rouault et al., 2010). **Shore-based high-frequency radar measurements** provide, when available, submesoscale permitting oceanic surface current products with resolutions down to 1.5 km but are however limited to the coastal ocean (e.g. Soh and Kim, 2018). High-resolution shore-based radar measurements of the Agulhas region are unfortunately not available for the scientific community, as far as I know. The same is true for **airborne** remote sensing of submesoscales (see e.g. Marmorino et al. (2018) for a short review). **Satellite SST** is available for cloud-free regions with a resolution of about 1 km from for example Moderate Resolution Imaging Spectroradiometer (MODIS, Minnett et al., 2002). Although the submesoscale flows imprint into the SST field as well a into the **reflectance** (e.g. colour) of the ocean surface (that is measurable with an even higher resolution from space), it is hard to directly link the associated structures to the underlying flows.

3 Introduction Part III: The Horizontal Diffusion and Dissipation

> *If this is some kind of practical joke, it's not funny, and I know funny. I'm a clownfish.*
>
> **— Marlin, the father of Nemo,**
> in Stanton and Unkrich (2003)

The major method used for this dissertation is the execution and analysis of numerical ocean general circulation model experiments. Simulations are performed that aim at simulating the submesoscale to large-scale dynamics in the Agulhas region as realistically as possible. In those simulations, the submesoscales occur just above the small-scale end of the resolved physical processes. At these scales, the model diffusion and dissipation are key to the successful simulation of the oceanic flows.

In the ocean modeling community, the term **model diffusion** is used for the reduction of tracer variance and **model dissipation** for the reduction of kinetic energy at the grid-scale. Both terms describe the combined effect of explicit (sec. 3.1) and numerical (sec. 3.3) diffusion and dissipation. While the **explicit diffusion and dissipation** are terms in the model equations, the **numerical diffusion and dissipation** occur due to diffusive model errors that depend on the discretization of the model equations. The importance of both physical and numerical aspects leads the choice of the model diffusion and dissipation settings to be a major issue in ocean modelling. In this chapter, theoretical approaches for the decision on the explicit horizontal diffusion and dissipation are summarized. The vertical model diffusion and dissipation are not addressed in this dissertation.

3.1 Explicit Diffusion and Dissipation

The horizontal tracer diffusion can be parameterized with Fick's second law (Fick, 1855)

$$\phi_t = \kappa \nabla^2 \phi, \tag{3.1}$$

where κ is the Laplacian (harmonic) diffusivity and ϕ is a tracer concentration (for example salinity or temperature). For the horizontal momentum diffusion, also a Laplacian operator is physically the most justifiable choice (Hecht et al., 2008)

$$\mathbf{u}_t^h = \nu \nabla^2 \mathbf{u}^h, \tag{3.2}$$

where ν is the Laplacian viscosity. Both parameterizations can be explicitely added to the equation of the respective tracer and the momentum equations. The associated diffusion and dissipation are then referred to as "explicit diffusion" and "explicit dissipation". When applied to the model solution at the grid-scale, both parameterizations do also affect the larger-scale solution, however the smallest scales more than the larger ones. One can enhance the selection of mainly the smallest scales for diffusion and dissipation by using a bi-Laplacian (biharmonic) operator for the parameterization. For example

$$\mathbf{u}_t^h = -\nu_b \nabla^4 \mathbf{u}^h, \tag{3.3}$$

for the dissipation, where ν_b the bi-Laplacian viscosity. Note that the bi-Laplacian operator is not physically motivated and used for solely practical reasons.

The horizontal scales at which the diffusion and dissipation mostly act, depend on the grid-spacing. If the grid-spacing can resolve mesoscale eddies, Laplacian dissipation is the best choice (Madec et al., 2016). For models that do not fully resolve the mesoscales, a bi-Laplacian operator is more useful. The bi-Laplacian operator than dissipates kinetic energy from scales mainly below the mesoscales and resolved mesoscales are maintained. For intermediate resolutions, also a combination of Laplacian and bi-Laplacian dissipation is possible. Semtner and Mintz (1977) derived a relation between Laplacian and bi-Laplacian viscosities assuming that the damping time-scales for a given wavelength λ are the same for both operators: $\nu_b = -0.25\nu\lambda^2$. For the grid wave ($\lambda = 2d$, where d is the horizontal grid-spacing), this gives $\nu_b = -\nu d^2$. This relation can alternatively be derived by equating (3.2) and (3.3), and scaling with respect to the grid-spacing

$$\nu \nabla^2 \mathbf{u} = -\nu_b \nabla^4 \mathbf{u} \Rightarrow \nu \frac{U}{d^2} = -\nu_b \frac{U}{d^4} \iff \nu_b = -\nu d^2. \tag{3.4}$$

A lower bound for the viscosity is provided by the Munk boundary layer criterion:

The Munk Boundary Layer Criterion In the region of western boundary currents, horizontal friction is a leading-order term and therefore creates a frictional boundary layer (Munk, 1950). For the case of a no-slip boundary condition, a viscous boundary layer has to be resolved at the side walls to suppress the excitation of a computational mode (Bryan et al., 1975). The width of the Munk layer was derived by Munk (1950) to be

$$L_m = \frac{\pi}{\sqrt{3}} \sqrt[3]{\frac{\nu}{\beta}}, \tag{3.5}$$

where $\beta = f_\theta = \frac{2\Omega}{R} cos(2\pi \frac{\theta}{360^\circ})$ with the Earth's radius $R = 6371\ km$. The Munk layer has to be resolved by at least one grid point to suppress computational instability (Bryan et al., 1975). Additionally, Griffies et al. (2000) pointed out, that two grid points in the Munk layer are needed to minimize the level of spurious diapycnal mixing associated with tracer advection for the model MOM. The Munk boundary layer criterion thus states

$$L_m \geq n \cdot max(d(i,j)) = n d_{max}, \tag{3.6}$$

where n is the number of grid points within the Munk layer. β increases from zero at the poles towards the equator to $\beta(\theta = 0^\circ) = \frac{2\Omega}{R} = 2.28e11\ ms^{-1}$. For regional or nested configurations the latitude closest to the equator is crucial for the constant coefficient $\beta_{max} = \beta(min(|\theta|))$. Equations (3.5) and (3.6) thus give

$$\nu_{min} = \beta_{max} (n d_{max} \frac{\sqrt{3}}{\pi})^3, \tag{3.7}$$

or for a bilaplacian viscosity with (3.4):

$$\nu_{b,min} = -\beta_{max} (n \frac{\sqrt{3}}{\pi})^3 d_{max}^5. \tag{3.8}$$

3.2 Suppressing Numerical Dispersive Modes

Numerical models are associated with model errors that can be split into diffusive and dispersive errors (e.g. Soufflet et al., 2016). Dispersive errors lead to unphysical numerical instabilities that have to be suppressed by the model diffusion and dissipation. The development of dispersive modes and their suppression is commonly illustrated with the simplest case of solving the steady-state balance of advection and diffusion (Burger's equation) that is spatially discretized with a centered difference scheme and uses constant coefficients (Griffies, 2004). Based on the Reynolds number ($Re = Ud/\nu$) respectively a Péclet number ($Pe = Ud/\kappa$), the solution can be split into a physical correct part with $Re < 2$ ($Pe < 2$) and a numerical dispersive part for $Re >= 2$ ($Pe >= 2$) that needs to be suppressed. These criteria are referred to as the **Reynolds and Péclet number criteria** and demand, in simple words, that the advection should not dominate the diffusion at the grid scale. The criteria identify a minimum for both, the diffusivity and the viscosity, depending on the maximum velocity scale and the maximum grid-spacing for a given domain:

$$\kappa_{min} = \nu_{min} = 0.5 U_{max} d_{max}. \tag{3.9}$$

With (3.4), (3.9) gives the respective lower bound for the bi-Laplacian viscosity

$$\nu_{b,min} = -0.5 U_{max} d_{max}^3. \tag{3.10}$$

It is questionable to which extent these lower bounds from simplified theory are transferable to the full set of equations. NEMO (Nucleus for European Modelling of the Ocean; Madec et al., 2016), the model used in this dissertation, uses a leapfrog scheme for momentum advection (Madec et al., 2016). Thus, at least, the momentum advection is discretized in space with a centered difference as used for the theoretical lower bounds above.

3.3 Numerical Diffusion and Dissipation

In contrast to the dispersive errors, the effect of diffusive errors on the model solution is rather similar to a physical diffusion or dissipation. Thus, it can be used as a (partial) substitute for the explicit diffusion and dissipation. Diffusion (Dissipation) as a consequence of diffusive errors is called numerical diffusion (dissipation). The combination of explicit and numerical diffusion (dissipation) needs to suppress numerical dispersive modes. The amount of numerical diffusion (dissipation) in NEMO mostly depends on the choice of the advection scheme for tracers and the discretization of the vorticity term in the momentum balance and is non-trivial to quantify. This undermines the usefulness of the theoretical lower bounds for the explicit viscosities and diffusivites and makes the choice of the explicit diffusion and dissipation a challenging task.

In NEMO, the Coriolis and momentum advection terms of the momentum equation are discretized with a leapfrog scheme. For the vorticity term, one can choose between different schemes that are either vector invariant or flux form schemes. Standardly, the vector-invariant energy enstrophy conserving scheme (EEN, Arakawa and Hsu, 1990) is used. It conserves both the potential enstrophy of horizontally non-divergent flow and the horizontal kinetic energy and has noise reducing and current-topography interaction improving properties (Barnier et al., 2006; Madec et al., 2016). The scheme is however associated with the excitation of symmetric instability of the computational kind (Ducousso et al., 2017) and needs to be Hollingsworth corrected (Hollingsworth et al., 1983). For the discretization of the tracer-advection, standardly the total variance dissipation scheme (TVD, Zalesak, 1979) is used.

An alternative, that is used for this dissertation, is the third-order upstream biased scheme (UBS, Farrow and Stevens, 1995; Madec et al., 2016; Webb et al., 1998) that is available for both the discretization of the vorticity term and the tracer-advection. It is diffusive and dissipative enough so that no additional explicit diffusion and dissipation are needed. Noteworthy is also the second order centered scheme (CEN2, Madec et al., 2016) which is also available for both tracer and vorticity and is not associated with numerical diffusion and dissipation at all. The presented theoretical lower bounds from Munk and Reynolds/Péclet criteria should be most useful for such a scheme.

3.4 Downscaling Diffusivities and Viscosities

Under the assumption of constant U_{max}, the Reynolds and Péclet number criteria show a linear scaling of the viscosity and diffusivity with respect to the grid-spacing for the Laplacian formulations and a cubic scaling for the bi-Laplacian (see eq. 3.9 and 3.10). Another approach for scaling is to assume a constant diffusion term

$$-\nu_{b,l}\nabla^4\mathbf{u} = -\nu_{b,h}\nabla^4\mathbf{u} \Rightarrow -\nu_{b,l}\frac{U}{d_l^4} = -\nu_{b,h}\frac{U}{d_h^4}, \tag{3.11}$$

where the index l marks low and the index h high resolution. Assuming constant U, this leads to a scaling with the grid spacing to the power 4 for the bi-Laplacian viscosity.

In the ocean dynamics research unit at GEOMAR, the latest successful nested runs used mainly a quadratic downscaling for the biharmonic viscosity and linear for the harmonic diffusivity when TVD advection scheme for tracers and the Hollingsworth-corrected EEN scheme for the vorticity formulation have been used (Schwarzkopf et al., 2019). The quadratic scaling bases purely on experience. Simulations that applied the quadratic scaling for the biharmonic viscosity respectively the linear scaling for the harmonic diffusivity ran numerically stable.

4 Aims, Structure, Approaches and Publications

> *We have to remember that what we observe is not nature herself, but nature exposed to our method of questioning.*
>
> — **Werner Heisenberg**
> in Heisenberg and Bond (1959)

4.1 Aims

As pointed out above, not much is known about the impact of submesoscale flows on mesoscale dynamics in general and even less about the specific importance of submesoscale flows in the core Agulhas region. Also the impact of submesoscale flows on the Agulhas leakage, which is of particular interest for the research on the global climate, is not known. These gaps of knowledge cannot be closed on the basis of the current available observations as area-covering observations do not exist for most parts of the spectrum of submesoscale flows (see section 2.4). Instead, a numerical model approach is used in this dissertation to make progress.

As oceanic flows at submeso- to large-scales are regionally very different, it is aimed to simulate the oceanic flows in the Agulhas region as realistic as possible from the submesoscales to the large-scales. This aim comes along with the requirement that the model solution is validatable against area-covering observations at all scales. In the Agulhas region, the observations with the highest resolution that enable such a validation are satellite-derived SSTs with a horizontal resolution of about 1 km. Thus, this dissertation focuses on the impact of submesoscale flows larger than 1 km including frontogenesis, forced and unforced baroclinic and barotropic mixed-layer instabilities. As such a grid-spacing potentially resolves only the large-scale portion of the spectrum of secondary instabilities and internal waves, these, as well as non-hydrostatic processes such as Langmuir turbulence and anticyclonic ageostrophic instabilities are not considered further in this dissertation.

If the impact of the resolved submesoscales on specific larger scales shall be investigated, these larger scales also need to be resolved by the model with a sufficiently large domain size and integration period. With a given grid-spacing, a large scale limit to the investigatable scales is set by the availability of mainly computational power but also data storage capacity. Varying the grid-spacing within the model domain gives rise to further degrees of freedom. A common approach is the use of grid-refinements for a specific region embedded in a coarser resolution global grid. The INALT family of ocean model configurations (Schwarzkopf et al., 2019), developed in Prof. Dr. Arne Biastoch's working group, provides a broad range of such ocean model configurations with grid-refinements for the Agulhas region. Different resolutions and different sizes of the refined domain were used to address a broad range of scientific questions with the current resources at the respective time. Previous INALT studies focused mainly on the impact of mesoscale Agulhas dynamics on the climate (Biastoch et al., 2008b,c; Rühs et al., 2013; Biastoch et al., 2015; Lübbecke et al., 2015; Rühs et al., 2018) as well as on the large-scale Agulhas current system (Biastoch et al., 2009a,b; Biastoch and Böning, 2013; Durgadoo et al., 2013) and hence the large-scales and longer periods.

For this dissertation, the required compromise is shifted to higher resolution, smaller domain size and smaller integration period. Schwarzkopf et al. (2019) suggested such a compromise by introducing INALT60, a model configuration with two grid refinements for the Agulhas region down to a submesoscale-permitting[5] $(1/60)^\circ$ (≈ 1.5 km) grid spacing. This compromise is adopted for this dissertation to address the following questions:

1. How can the simulated Agulhas dynamics be validated against observations for all scales ranging from the large-scales down to the submesoscales?

2. What are the numerical choices to simulate the submesoscale flows as realistic as possible with INALT60?

3. **How and how much do the near-surface submesoscales impact the mesoscale eddies in the Agulhas region?**

The third question is the main question addressed in this dissertation. As it will be pointed out at the end of the next chapter, the INALT60 simulation is very expensive in terms of computational power and data storage. For this dissertation, a main integration of INALT60 with a length of 8 model years was affordable. This integration period is long enough to answer this main question. However, it is too

[5] Thomas et al. (2008) defined horizontal grid-spacings smaller than 1 km "submesoscale-resolving". The ≈ 1.5 km-grid of INALT60 is thus named "submesoscale-permitting" in this dissertation.

short to investigate the submesoscale effect on the Agulhas leakage properly, as the respective statistics need a longer period to be robust. Some results are nevertheless shown at the very end of this dissertation and discussed in the framework of this dissertation.

4.2 Structure, Approaches and Publications

Chapter 5
The Model Configurations and Their Further Development
Chapter 6
Study I: Submesoscale Impacts on Mesoscale Agulhas Dynamics

First, in chapter 5 and chapter 6, the first two questions of this dissertation are answered (sec. 4). A series of ocean model experiments with increasing capability in resolving submesoscale dynamics is developed, compared and validated. The model configuration development focuses thereby on the vertical and horizontal resolution, as well as the diffusion and dissipation settings. In chapter 6, the comparison of horizontal wavenumber spectra of SST from satellite observations and from the simulations is presented as a new way to validate simulated submesoscales. The simulated mesoscales are validated and compared using horizontal wavenumber spectra from along-track SSH data, as well as SSH variability and eddy statistics from gridded SSH products. Chapter 6 mainly addresses the question, whether and how much the simulated mesoscale dynamics in the Cape Basin change with increasing resolution of submesoscales and whether this change is directed towards a more realistic representation of the mesoscale eddies.

On the basis of chapter 5, I contributed the section 3.1.1 "Towards resolving the submesoscale - an outlook" to

Schwarzkopf, F. U., Biastoch, A., Böning, C. W., Chanut, J., Durgadoo, J. V., Getzlaff, K., Harlaß, J., Rieck, J. K., Roth, C., Scheinert, M. M., & ***Schubert, R.*** *(2019). The INALT family - a set of high-resolution nests for the Agulhas Current system within global NEMO ocean/sea-ice configurations. Geoscientific Model Development, 12(7), 3329-3355. https://doi.org/10.5194/gmd-12-3329-2019*

Chapter 6 has been published as

Schubert, R.*, Schwarzkopf, F.U., Baschek, B., & Biastoch, A. (2019). Submesoscale impacts on mesoscale Agulhas dynamics. Journal of Advances in Modeling Earth Systems, 11. https://doi.org/10.1029/2019MS001724*

Chapter 7

Study II: Strengthening of Agulhas Mesoscales by the Submesoscale Inverse Kinetic Energy Cascade

Second, in chapter 7, the kinetic energy cascade is investigated in a submesoscale-permitting simulation and a parallel experiment without submesoscale flows. The classical spectral approach, as well as for the first time (as far as I know) a coarse-graining approach for the computation of the kinetic energy flux across spatial scales is applied to a submesoscale-permitting model output. The kinetic energy cascade is presented as a function of space and time to mainly answer the questions how and when the open-ocean submesoscale flows impact the mesoscale eddies in the Agulhas region.

Chapter 7 has been submitted to the Journal of Physical Oceanography in December 2019 and is currently under review as

***Schubert, R.**, Gula, J., Greatbatch, R. J., Baschek, B., & Biastoch, A. (2020). Strengthening of Agulhas Mesoscales by the Submesoscale Inverse Kinetic Energy Cascade. Journal of Physical Oceanography*

Chapter 8

Study III: The Role of Submesoscale Dynamics in the Formation of Mesoscale Eddies at the Agulhas Bank

Third, in chapter 8, the question is addressed, how the submesoscale flows impact the formation of mesoscale eddies, in particular cyclones, at the northern boundary of the AC. For this study, the parallel model experiments are compared again. The results for the kinetic energy transfer across spatial scales are complemented by computations of the energy transfer across temporal scales. Moreover, periods with and without Natal Pulses are analyzed separately.

Chapter 9

Synthesis and Outlook

A synthesis of the results, as well as an outlook are provided in chapter 9. At the end of this final chapter, some results on the effect of the submesoscales on the Agulhas leakage are shown and discussed in the context of the results of this dissertation.

5 The Model Configurations and Their Further Development

> *With great processing power comes great responsibility.*
>
> — **Hackerman**
> in Hackerman's Hacking Tutorials
> How To Hack Time

Simulating the Agulhas region at eddy-resolving model resolutions and its impact on the global climate has been a focus of Prof. Dr. Arne Biastoch and his working group at GEOMAR for more than 10 years (Biastoch et al., 2008b,c, 2009a,b; Durgadoo et al., 2013; Schwarzkopf et al., 2019). For most of the simulations, the primitive equations (e.g. Gill, 1982) were solved with the ocean model **NEMO** (Nucleus for European Modelling of the Ocean; Madec et al., 2016) using global model configurations that were developed within the DRAKKAR community (Barnier et al., 2007). To NEMO, the Louvain-La-Neuve sea-ice model version 2 with a viscous-plastic rheology (LIM2-VP, Fichefet and Maqueda, 1997) is coupled. To resolve the mesoscales within the Agulhas and adjacent regions, regional grid-refinements (**nests**) are embedded into the global coarse-resolution grid (**host**). For the nesting, the Adaptive Grid Refinement in FORTRAN (**AGRIF**; Debreu et al., 2008) is used. AGRIF enables an active two-way exchange of the model solution between the nest and the respective host. The two-way nesting provides a good representation of the mesoscale interactions through the boundary of the high-resolution domain(s).

5.1 The INALT Family

The first INALT configuration, **INALT01**, has been introduced by Durgadoo et al. (2013) as a further development of its predecessor **AG01** (Biastoch et al., 2008b,c, 2009a,b). The name "INALT" was chosen by Durgadoo (2013) based on "inaliti" meaning "needle" in isiXhosa, which further means "Agulhas" in portuguese. The latest nested configurations for the Agulhas region are introduced by Schwarzkopf

et al. (2019) as a consistent hierarchy of ocean model configuratuions, the INALT model family. First, **INALT10**, a further developed version of INALT01, has been published by Schwarzkopf et al. (2019). Both, INALT01 and INALT10, consist of a $(1/2)^\circ$ host with a $(1/10)^\circ$ nest extending over the whole South Atlantic, as well as the western part of the South Indian Ocean. The grid-spacings and the extend of the nest(s) are shown for these configurations as well as for the following in Figure 5.1. The global $(1/2)^\circ$ configuration without the nest is referred to as **ORCA05** (Biastoch et al., 2008a). For the global grid, as well as the nest grid, the model solution is computed on a rectangular grid with size $i \times j$, where i is mainly directed zonally and j meridionally. The global grid is associated with two North-poles over Siberia and Canada to avoid a singularity at the geographical North-pole. The grid is curvilinear in the region north of $20^\circ N$, leading to deviations of directed variables such as horizontal velocity components u and v (normal to the grid cell boundaries) from the zonal and the meridional direction. All nests of the INALT family are located south of $20^\circ N$ and thus i and j grids are aligned in zonal and meridional direction in the nests.

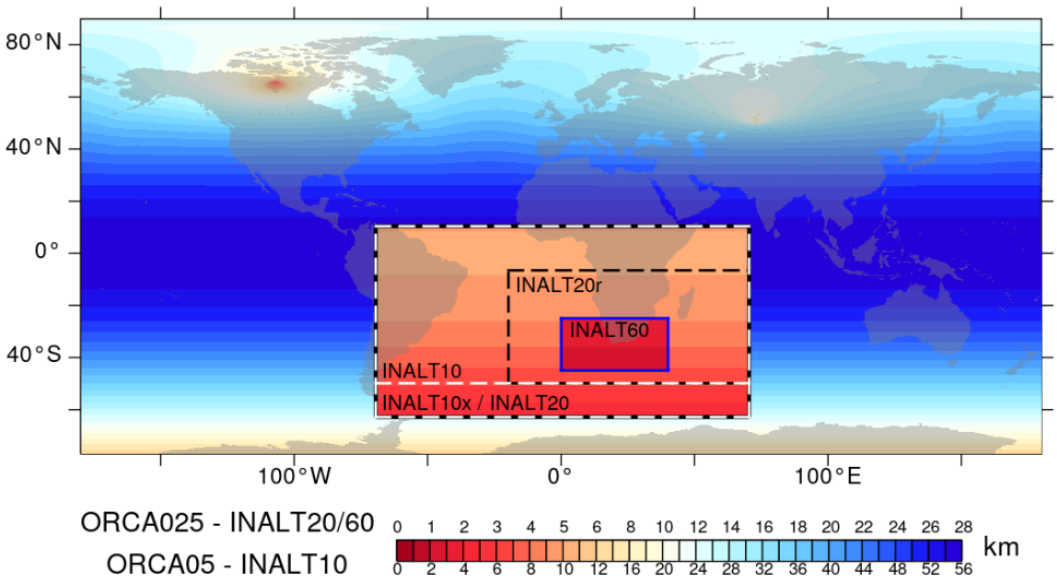

Fig. 5.1: *Grid sizes in the INALT family: shown is the zonal grid length (in km) for the global ORCA025 grid with the embedded INALT20 (outer black box), INALT20r (inner black box) and INALT60 (blue box) grids (upper scale), as well as for ORCA05 with the embedded INALT10x (white dashed box, same as INALT20) and INALT10 with its southern boundary shifted north (lower scale). The figure and the caption are taken from Schwarzkopf et al. (2019).*

INALT10x is a version of INALT10 with a grid refinement that extends further south and covers the region of the Antarctic Circumpolar Current (ACC). **INALT20**, is associated with the same nested region as INALT10x but doubled horizontal resolu-

tion using a $(1/4)^\circ$ global host and a $(1/20)^\circ$ nest. The global $(1/4)^\circ$ configuration without the nest is called **ORCA025** and has been developed by Barnier et al. (2006). Finally, **INALT60** consists of a $(1/4)^\circ$ global host, a first $(1/20)^\circ$ nest with reduced extend compared to INALT20 and a secondary $(1/60)^\circ$ nest for the core Agulhas region. It has 1442×1021 grid points in the host grid, 1804×1024 in the first nest and 2404×1483 in the second nest. The configuration without the secondary nest is referred to as **INALT20r**. INALT60, INALT20r, and INALT10 do not use the ice model LIM2-VP in the nest, as no ice enters the nested domain (Schwarzkopf et al., 2019).

INALT60 provides sufficiently large resolution and domain size to answer the questioning of this dissertation. A horizontal resolution of ≈ 1.5 km is able to potentially resolve a larger portion of the submesoscale spectrum (McWilliams, 2016; Chassignet and Xu, 2017) and the resolved features are validatable with current satellite SST swath measurements (section 2.4 and chapter 6). Further, the size of the submesoscale-permitting $(1/60)^\circ$ nest of INALT60 is large enough to simulate mesoscale dynamics in the core Agulhas region. An integration period of 8 years is affordable and ensures a robust mesoscale eddy statistic. A comparison of INALT60 experiments and parallel INALT20r experiments enables the investigation of the influence of the horizontal resolution in general as well as of the impact on the mesoscales when submesoscale flows are resolved to a different degree in the simulations. For this dissertation, first the original configurations of INALT20r and INALT60 are optimized with respect to the simulation of submesoscale flows.

Members of the INALT family as introduced by Schwarzkopf et al. (2019) share many similarities. In the following, those which are important for the subsequent model development are listed. The INALT configurations use a vertical grid with 46 z-levels with a grid spacing of minimum 6 m at the surface and maximum 250 m in the deep ocean. For the explicit iso-neutral diffusion (horizontal dissipation), a Laplacian (bi-Laplacian) operator is used. The standard ORCA025 diffusivity (viscosity) of 300 m^2/s ($-1.5e11\ \mathrm{m}^4/\mathrm{s}$), which is shown to be associated with a successful simulation of the global ocean (e.g. Barnier et al., 2007), is linearly (quadratically) scaled down with respect to the grid spacing to 60 m^2/s ($-6.0e9\ \mathrm{m}^4/\mathrm{s}$) for the $(1/20)^\circ$ nest and to 20 m^2/s ($-6.7e8\ \mathrm{m}^4/\mathrm{s}$) for the $(1/60)^\circ$ nest. Further numerical diffusion and dissipation are contributed by the use of the Total Variance Dissipation (TVD) scheme for the discretization of the tracer advection and the Energy Enstrophy Conserving (EEN) scheme for the vorticity term. The ocean is forced by the atmosphere using COREv2 (Large and Yeager, 2009) data and bulk formulae. The COREv2 forcing is associated with a spatial resolution of 2° and a variable-dependent temporal resolution. Wind speed, atmospheric temperature and humidity were prescribed

6-hourly, short- and longwave radiation daily and precipitation monthly. The model output has been written as 5-day or daily means.

Further configuration settings of INALT60 and INALT20r, that are for the upper ocean dynamics of particular importance but are not addressed further in this dissertation, are listed in the following. A linearized and filtered free surface formulation (Roullet and Madec, 2000) is used for the SSH. The surface ocean velocities are considered in the computation of the wind-stress ("relative winds"). The EOS-80 equation of state has been used (Fofonoff and Millard Jr, 1983). At the lateral boundaries, a free-slip condition is used in the host grid and a no-slip in the nest grids. Vertical eddy diffusivities and viscositites are computed with a turbulent kinetic energy closure model (Blanke and Delecluse, 1993) parameterizing the vertical mixing. Vertical diffusivities and viscosities are enhanced by a factor of 10 when static instabilities occur. For the direction of lateral mixing in the mixed-layer, the iso-neutral slope used for the lateral mixing below the mixed layer is interpolated linearly to a zero slope at the surface. Tides are not explicitely simulated. Only their effect on the bottom turbulent kinetic energy is taken into account within the parameterization of the bottom-friction (Madec et al., 2016). Further configuration settings are listed in detail in section 2.2 of Schwarzkopf et al. (2019).

5.2 Pre-existing INALT20r and INALT60 Experiments

The first INALT20r and INALT60 experiments were designed and executed by Dr. Franziska U. Schwarzkopf. They were integrated with the above listed settings and are described in detail by Schwarzkopf et al. (2019). Essential for this dissertation, is the experiment INALT20r.L46-KFS013[6]. This experiment is a spin-up initialized at the beginning of 1980 from rest with hydrographic data from Steele et al. (2001). The simulation has been integrated until the end of 2009 under COREv2 forcing. The model data at the last time-step (in the modelling community called "restart") provides the initial conditions for all INALT20r and INALT60 experiments that were executed for the main chapters 6, 7 and 8 of this dissertation (see section 5.4).

The first successful INALT60 experiment, INALT60.L46-KFS004, was initialized similarly in 1980 and was integrated until the end of 1986. Based on the restart of INALT60.L46-KFS004, a second integration (INALT60.L46-KFS005) was set up from 1985 to the end of 1989 using the Hollingsworth corrected EEN scheme for the discretization of the vorticity term (Hollingsworth et al., 1983). The correction removes spurious numerical instabilities, the original EEN scheme was associated with (Bell et al., 2017; Ducousso et al., 2017). Whenever the EEN scheme is used in this dissertation, the Hollingsworth corrected version is used. Moreover, the model year 1989 was repeated with a corrected runoff (INALT60-KFS006), which also has been used for all experiments performed for this dissertation. The experiments are listed in table 5.1.

Tab. 5.1: *Integration periods, the experiment were the restart was taken from, applied corrections, forcing and number of vertical levels for the pre-existing INALT60 experiments executed by Dr. Franziska Schwarzkopf (KFS), as well as for two first sensitivity experiments performed for this dissertation (KRS).*

Experiment	Restart from	Period	Hollingsworth Corr.	Runoff Corr.	Forcing	Vertical Levels
KFS004	rest	1980 - 1986	no	no	COREv2	46
KFS005	KFS004	1985 - 1989	yes	no	COREv2	46
KFS006	KFS005	1989	yes	yes	COREv2	46
KRS0002	KFS005	1989	yes	yes	JRA55-do	46
KRS0005	KFS005	1987 - APR 1989	yes	yes	JRA55-do	120

[6]The abbreviation connects the configuration (INALT20r), the vertical axis (46 vertical levels), the location of the working group (K = Kiel), the executor of the experiment (FS = Dr. Franziska U. Schwarzkopf) and the experiment number (13).

5.3 Optimizing the Simulation of Submesoscales with INALT60

Whether the submesoscale flows that are resolvable by a $(1/60)^\circ$ horizontal resolution grid are indeed resolved, depends on many other factors. The model forcing, the vertical resolution as well as the model diffusion and dissipation settings are important apart from the horizontal resolution. Optimizing the model solution with respect to the simulation of submesoscale flows therefore is a challenging task, as each factor can suppress the simulation of submesoscale flows in the mixed-layer (a too coarse resolution of the forcing, too coarse vertical resolution as well as too strong model dissipation and diffusion). Further, the high computational costs (see the end of this chapter) limit the number and lengths of sensitivity experiments.

As one of the first sensitivity experiments, executed for this dissertation, the model year 1989 was repeated using the new JRA55-do v1.1 atmospheric forcing (Tsujino et al., 2018) instead of COREv2 (INALT60.L46-KRS0002, see tab. 5.1). The JRA55-do forcing is associated with higher temporal (3 h) and spatial resolution ($(1/2)^\circ$) compared to COREv2 ($>$ 6 h, 2°) which is promising with respect to the simulation of the submesoscales. The sensitivity experiment showed however only minor improvements with respect to the simulated submesoscale flows (not shown here).

As a second step, the vertical resolution has been increased from 46 levels (6 - 250 m vertical grid-spacing) to 120 vertical levels (1 - 100 m vertical grid-spacing) (see section 6.4.2 for details on the vertical grid-spacing). A parallel INALT60 experiment was initialized at the beginning of 1987 with a INALT60.L46-KFS005 restart using 120 vertical levels. The experiment was integrated under JRA55-do forcing until the mid of 1989 (INALT60.L120-KRS0005, see tab. 5.1). The year 1987 was chosen for the initialization instead of 1989, as a secondary spin-up was expected when the vertical resolution is changed. Additionally, based on a suggestion by Prof. Dr. Julien le Sommer, who contributed to the development of NATL60[7], Upstream Biased Schemes (UBS) for tracer advection and the vorticity term instead of TVD and EEN were used in INALT60.L120-KRS0005. The use of UBS schemes should improve the simulation of the submesoscales. However, due to a misunderstanding, the explicit diffusion and dissipation were not reduced. This is usually done as the UBS schemes are numerically diffusive enough and do not mandatorily need additional explicit diffusion. As a consequence, the resulting simulation did again not show

[7] NATL60 is a regional $(1/60)^\circ$ horizontal resolution NEMO configuration simulating the North Atlantic.

the expected improvements in the simulation of the submesoscale flows (also not shown here).

Subsequently, six 25-day sensitivity experiments were initialized with the same restart of INALT60.L120-KRS0005 in spring at model day Nov 2nd 1988, where the previously used diffusivity and viscosities in the second nest are gradually reduced to zero as listed in Table 5.2. Note that all experiments use the same standard diffusion and dissipation settings in the base model and the first nest (TVD/EEN plus biharmonic dissipation and harmonic diffusion). In the nest region, the choice for the host has only a very small influence, as AGRIF overwrites the model solution in the host.

Tab. 5.2: *Diffusivities (κ) as well as Laplacian (ν) and bi-Laplacian (ν_b) viscosities used for the sensitivity experiments for Figure 5.2*

Experiment	κ [m²/s]	ν [m²/s]	ν_b [m^4/s]
HIGH DIFF - HIGH VISC	10	0	-6.7e8
HIGH DIFF - MEDIUM VISC	10	10	-3.3e7
HIGH DIFF - LOW VISC	10	1	-3.3e6
LOW DIFF - LOW VISC	2	1	-3.3e6
NO DIFF - LOW VISC	0	1	-3.3e6
NO DIFF - NO VISC	0	0	0

The effect of the reduction in explicit diffusion and dissipation is very quickly visible. In Figure 5.2, snapshots of surface normalized relative vorticity (ζ/f) and SST are shown for the region of the subtropical front south of the Agulhas ring path. The snapshots are taken on Nov 24th 1988 (12 PM), 22.5 days after the initialization.

As expected, the diffusivity is critical mainly for the SST and the viscosities mainly for the vorticity (Fig. 5.2). Reducing the explicit dissipation by switching to a combination of Laplacian and bi-Laplacian viscosities with an effective bi-Laplacian viscosity[8] of -5.6e7 m^4/s leads to stronger vorticities but almost no change in the SST field (Fig. 5.2a and 5.2b). Reducing the effective bi-Laplacian viscosity further to 10 % of the previous values increases the vorticity strikingly and many submesoscale mixed-layer eddies form (Fig. 5.2c). The SST field nevertheless is still almost not distinguishable from the one of the previous experiments.

[8]For the effective bi-Laplacian viscosity, equation 3.4 and an average grid-spacing of $d = 1500$ m is used to transform the value of the Laplacian viscosity into a bi-Laplacian one. The effective bi-Laplacian viscosity is then derived as the sum of this value and the one of the original bi-Laplacian viscosity.

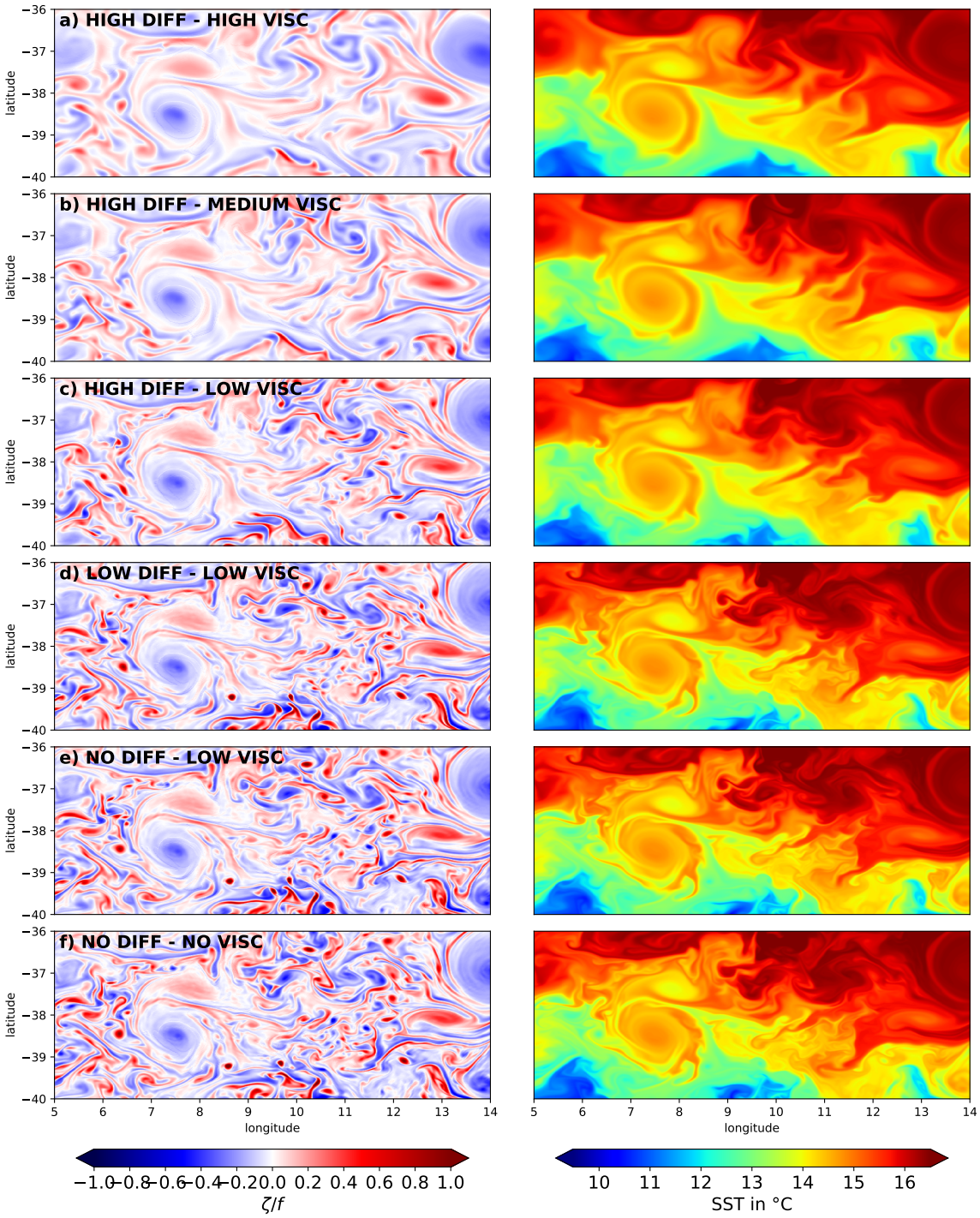

Fig. 5.2: *Snapshots of surface normalized relative vorticity (left) and SST (right) for the region of the subtropical front south of the Agulhas ring path in INALT60. Each snapshot is taken on model day Nov 24th 1988 (12 PM), 22.5 days after the initialization from the same restart under different diffusivities and viscosities that are listed in Table 5.2. All sensitivity experiments use UBS schemes.*

If additionally the diffusivity is reduced to 20 %, the SST shows much more small-scale structures (Fig. 5.2d). This has also an effect on the vorticity field. Small scale structures are associated with larger Ro and tend to be more circular and less elongated. Removing the diffusivity (Fig. 5.2e) and finally also the viscosities (Fig. 5.2f) is not associated with a visible change, as the previous values were already very small.

Finally, the question is addressed, whether similar submesoscale flows can be simulated with the standard TVD/EEN setting and explicit diffusivities and viscosities that are tuned to a minimum. Let us consider first the theoretical lower bounds for the biharmonic viscosity (for details see section 3). The Munk and Reynolds criteria as well as results of a downscaling from the ORCA025 standard value ($\nu_b = -1.5e11$ $m^4 s^{-1}$) are shown in Figure 5.3 as a function of the grid-spacing. The Reynolds criteria is associated for all grid-spacings with the largest values and the one-grid-cell Munk criterion with the lowest.

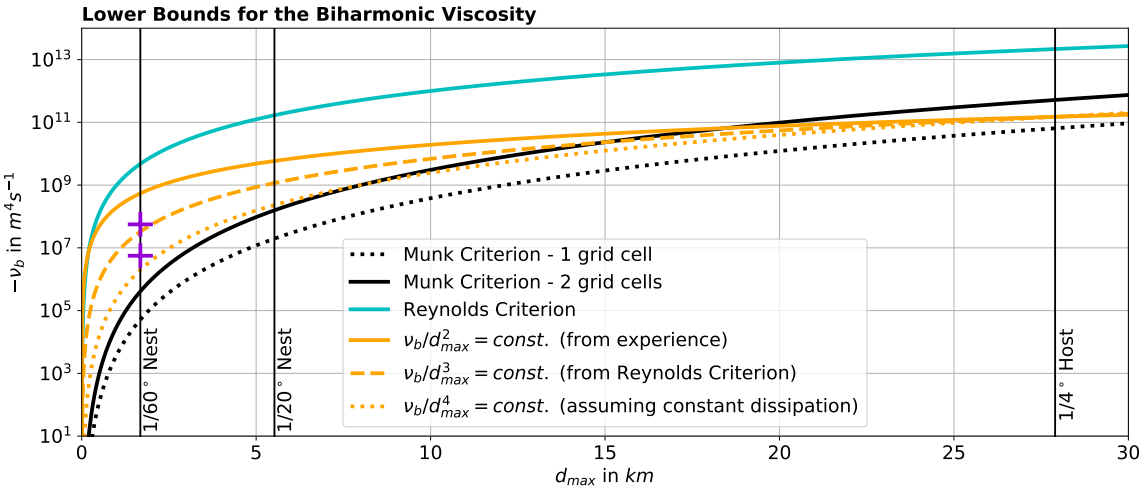

Fig. 5.3: *Lower bounds for the bi-Laplacian viscosity in dependence on the maximum grid spacing of a model. The Munk boundary layer criterion (using $\beta_{max} = \beta(\theta = 0°)$) is shown in black; the Reynolds criterion (using $U_{max} = 2\ ms^{-1}$) in cyan. Scalings to the power two, three and four from the ORCA025 standard value ($-1.5e11\ m^4 s^{-1}$) are shown in orange. Black vertical lines show the maximum grid spacing of INALT60 in the host grid and both nests. Violet crosses mark the effective biharmonic viscosity of the two sensitivity experiments "TVD/EEN - some EXPL" and "TVD/EEN - more EXPL" (see Tab. 5.3).*

Note that ORCA025 is running stable although its standard bi-Laplacian viscosity is much smaller than the Reynolds criterion as well as the 2-grid-cell Munk criterion. This implicates that the numerical dissipation provided by the discretization schemes are large enough to prevent the simulation from beeing numerically unstable. As the standard value was shown to be associated with a promising simulation of the global

ocean, theory can be used to downscale this value for higher resolution nests. At larger grid-spacings the two-grid-cell Munk criterion is associated with larger values than the scaling laws from the standard ORCA025 value. At smaller grid-spacings the opposite is the case and for both INALT60 nests, $1/20°$ and $1/60°$, all scaling laws predict a larger lower bound than the two-grid-cell Munk criterion.

Theory suggests that the quadratic scaling of the viscosity (that is used for the original INALT60 configuration) is rather conservative and that the viscosity could be further reduced (see section 3.4). Further sensitivity experiments, similar to those presented in Figure 5.2, are executed to investigate whether a more realistic simulation of the submesoscales can be achieved by using TVD/EEN when explicit diffusivity and viscosities are reduced to the minimum required to prevent the simulation from developing spurious dispersive modes. The experiments are again initialized with the same restart from INALT60.L120-KRS0005 on Nov 2nd 1988. At this initial time, the simulation is associated with a rich eddy field in the Agulhas ring path and submesoscale fronts in between (Fig. 5.4).

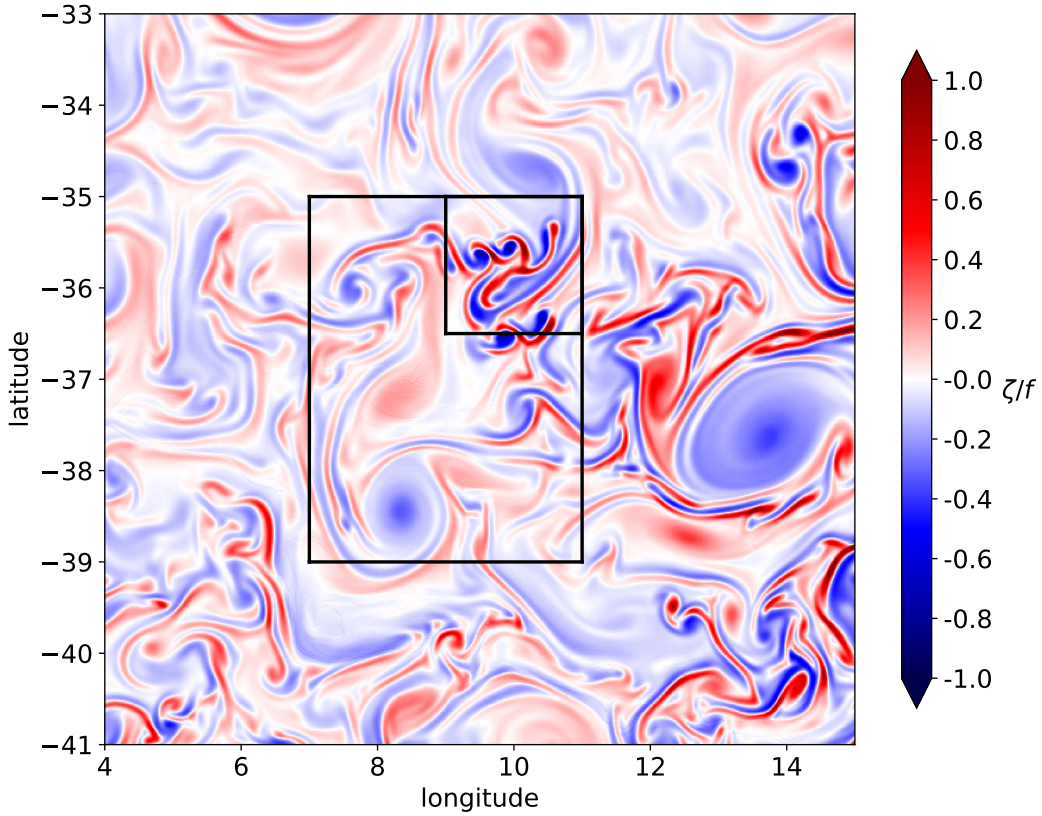

Fig. 5.4: *A snapshot of surface normalized relative vorticity on model day Nov 4th 1988 in the Agulhas ring path of INALT60.L120-KRS0005. The previous restart field, on Nov 2nd 1988 has been used for the sensitivity experiments on the diffusion and dissipation settings. The black boxes mark the regions for the zooms in Figure 5.5*

Four parallel five-day sensitivity experiments with the diffusion and dissipation settings listed in Table 5.3 are executed. First, the explicit diffusion and dissipation are turned off ("TVD/EEN - no EXPL"). For the second and the third experiment, a combination of Laplacian and bi-Laplacian viscosities is used as INALT60 is expected to resolve most of the mesoscale dynamics. The effective bi-lapacian viscosities are similar to the ones used before (-5.6e6 m^4s^{-1} for "TVD/EEN - some EXPL" and -5.6e7 m^4s^{-1} for "TVD/EEN - more EXPL"). The value for "TVD/EEN some EXPL" lies between the values that a downscaling to the power 3 and 4 suggests and the values for "TVD/EEN - more EXPL" is slightly larger than the one derived from cubic downscaling (see the violet crosses in Fig. 5.3). Finally, the three experiments are compared to one with UBS schemes without explicit diffusion and dissipation ("UBS/UBS - no EXPL").

Tab. 5.3: *Diffusion and dissipation settings used in the $(1/60)^\circ$ nest of INALT60 for the sensitivity experiments for Figure 5.5 and the one Schwarzkopf et al. (2019) used. Diffusivities (κ) as well as Laplacian (ν) and bi-Laplacian (ν_b) viscositie are listed.*

Experiment	Tracer Advection Scheme	Vorticity Scheme	κ $[m^2s^{-1}]$	ν $[m^2s^{-1}]$	ν_b $[m^4s^{-1}]$
TVD/EEN - no EXPL	TVD	EEN	0	0	0
TVD/EEN - some EXPL	TVD	EEN	2	1	-3.3e6
TVD/EEN - more EXPL	TVD	EEN	10	10	-3.3e7
UBS/UBS - no EXPL	UBS	UBS	0	0	0
Schwarzkopf et al. (2019)	TVD	EEN	10	0	-6.7e8

Numerical instabilities develop rapidly and are best observed in snapshots of the surface normalized relative vorticity which highlights the small-scale dynamics. In Figure 5.5, snapshots on model day Nov 4$^{\text{th}}$ 1988 (12 PM) - 2.5 days after the initialization from the same restart - are shown for the four experiments. As expected, dispersive modes develop with TVD/EEN when no explicit diffusion is used (Fig. 5.5a). In particular, regions of larger Rossby numbers ($Ro = |\zeta/f|$), which are mainly submesoscale fronts, are associated with the excitation of numerical dispersive modes. If some explicit diffusion and dissipation is added, less and weaker dispersive modes occur (Fig. 5.5b). If more explicit diffusion and dissipation is used, most of the dispersive modes are suppressed (Fig. 5.5c). However, the Rossby numbers, in particular at the fronts, are strongly reduced. This is best seen for the front between the two eddies along $37.7^\circ S$. The increasing diffusion and dissipation more and more damp the submesoscale flows.

The very strong fronts in the Northeastern part of the investigated domain are still associated with the excitation of some weak dispersive modes. This result

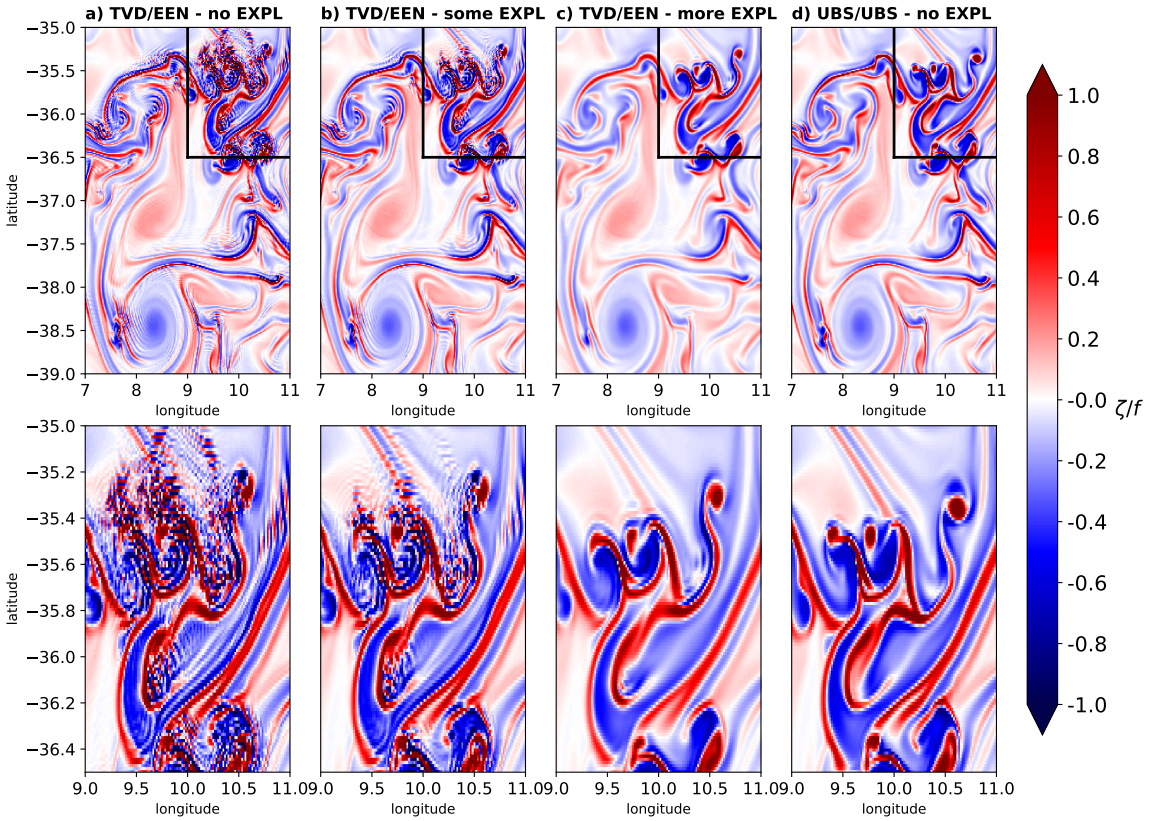

Fig. 5.5: *Snapshots of the surface normalized relative vorticity from four sensitivity experiments with reduced diffusion and dissipation in the Agulhas ring path (See table 5.3 for details on the diffusion and dissipation settings). All experiments were intialized on model day Nov 2nd 1988 from the same restart of the strongly diffusive and dissipative simulation INALT60.L120-KRS0005. The snapshots show the surface field 2.5 days later. The bottom panels show a zoom into the region of the marked boxes in the top panels.*

emphasizes one disadvantage of constant diffusivities and viscosities: they have to be large enough to suppress numerical instabilities at the strongest gradients and shears. Simultaneously, they also decrease the gradients and shears in regions where no numerical instabilities would have occurred. For example, well resolved intermediately steep fronts are unnecessarily damped to ensure that the steepest fronts do not lead to numerical dispersive modes. The flow-awareness of the dissipation necessary to avoid this behavior could be provided by Smagorinsky-type viscosities that vary over space and time depending on the local deformation rate (Smagorinsky, 1993). This approach is not followed here. Instead, the flow-awareness of the very diffusive UBS schemes is used. The snapshot for the UBS/UBS experiment without explicit diffusion and dissipation does not show numerical dispersive modes at all (Fig. 5.5d). Even more important, the steep fronts are maintained with this setting. Thus, the UBS scheme is better suitable for the

simulation of small-scale flows in INALT60 than TVD/EEN with diffusivities and viscosities that are tuned to a minimum.

The question remains, whether the submesoscale flows that are simulated by INALT60.L120 with UBS schemes without explicit diffusion and dissipation could be too energetic. If this is the case, some explicit diffusion and dissipation can be added again. Theoretical approaches for the choice of the explicit diffusion and dissipation are however not useful, as the amount of numerical diffusion and dissipation is not known. Thus, to make the choice of the explicit diffusion and dissipation it is mandatory to compare the simulated small-scale flows to area-covering submesoscale resolving observations in order to examine whether the simulated submesoscales are realistic. This is done in the next Chapter 6 by comparing horizontal wavenumber spectra of SST derived from INALT60 to those from high-resolution (≈ 1 km) satellite swath data.

5.4 Designing a Series of Non-Submesoscale Resolving to Submesoscale-Permitting Model Experiments

Based on the experience of the model configuration development presented in this chapter, a series of non-submesoscale resolving to submesoscale-permitting model experiments is designed (see table 5.4). The results, presented in this thesis, base to the largest extent on the analysis of the following four experiments. First, a non-submesoscale resolving INALT20r.L46 simulation is performed using TVD/EEN and the standard explicit diffusion (INALT20r.L46-KRS001). Second, the experiment is repeated with 120 vertical levels to investigate, whether the simulated Agulhas dynamics change, if the vertical resolution is increased (INALT20r.L120-KRS006). Third, the INALT20r.L120 experiment is repeated using UBS schemes without explicit diffusion (INALT20r.L120-KRS007). This experiment is expected to resolve more submesoscale flows than the previous ones. Finally, a parallel INALT60.L120 simulation is performed also using UBS schemes without explicit diffusion and dissipation (INALT60.L120-KRS0020). The names that are used in the following for the experiments, are listed in table 5.4.

Tab. 5.4: *Highest horizontal resolution, number of vertical levels, diffusion and dissipation settings (TVD/EEN is using the standard explicit diffusion and dissipation, UBS/UBS none) and the name used for the experiment. Note that INALT20r.L120.HighDiff is called in chapters 7 and 8 simply "INALT20r".*

Experiment	Highest Hor. Res.	Vertical Levels	Diff./Diss. Settings	Name
INALT20r.L46-KRS001	$(1/20)^\circ$	46	TVD/EEN	INALT20r.L46.HighDiff
INALT20r.L120-KRS006	$(1/20)^\circ$	120	TVD/EEN	INALT20r.L120.HighDiff
INALT20r.L120-KRS007	$(1/20)^\circ$	120	UBS/UBS	INALT20r.L120.LowDiff
INALT60.L120-KRS0020	$(1/60)^\circ$	120	UBS/UBS	INALT60

All four experiments are initialized with an INALT20r.L46-KFS013 restart at the end of the model year 2009 and are integrated under JRA55-do v1.3 forcing (Tsujino et al., 2018) for 8 years until the end of 2017. This integration period has the advantage that high-resolution satellite data are available for a model validation at all simulated spatial scales (chapter 6).

The increase in vertical and horizontal resolution, as well as the change of the diffusion and dissipation settings are associated with an increase in computational costs. The computational costs are further increased as the model output frequency is partially increased to resolve the simulated submesoscales with the model output.

For INALT60, additional to the daily mean data for the whole water column, 4-hour mean data and a model snapshot each fifth day are written to the output for the upper 250 m of the water column. The same is done for the surface layer in the INALT20r experiments.

While INALT20r.L46.HighDiff needs about 22,500 CPUh/year[9] on 104 nodes with 24 CPUs each, increasing the number of vertical levels to 120 leads to an almost linear increase of the computational costs to about 60,500 CPUh/year. Switching to UBS schemes without explicit diffusion and dissipation is associated with a further increase to about 70,500 kCPUh/year as the time-step needs to be reduced from 1200 s in the host and 200 s in the nest to 900 s in the host and 150 s in the nest for a stable simulation. INALT60 is associated with massive computational costs of about 390,000 kCPUh/year on 158 nodes with 24 CPUs each. Due to queue times and many unantizipated interruptions and technical issues, the 8-year integration of INALT60 needed 3.5 months in real-time to be finalized. The high-resolution model output in both time and space needs 53 TB data storage, 6.6 TB per model year. The computational power, the data storage, as well as the time that the integration need in real-time limited the affordable integration period of INALT60 for this dissertation to 8 years.

[9] The unit CPUh/year means the amount of CPUs that were used times the number of hours the computation took per model year.

6 Study I: Submesoscale Impacts on Mesoscale Agulhas Dynamics

> *Poyekhali! (Off we go!)*
>
> — **Yuri A. Gagarin**
> at the Vostok 1 lift off on Apr 12 1961

In this chapter, model experiments with increasing capability in resolving submesoscale dynamics in the Agulhas region are compared to each other and validated against satellite and insitu observations. It is demonstrated that the simulated Agulhas eddies, and in particular strong cyclones, are stronger and thus closer to the observations, the more submesoscale flows are resolved by the model. INALT60 is shown to simulate realistic oceanic flows in the Agulhas ring path on all captured horizontal scales in a very good agreement with the observations. This chapter has been published on July 29th 2019 in the Journal of Advances in Modeling Earth Systems (JAMES):

Schubert, R., Schwarzkopf, F.U., Baschek, B., & Biastoch, A. (2019). Submesoscale impacts on mesoscale Agulhas dynamics. Journal of Advances in Modeling Earth Systems, 11. https://doi.org/10.1029/2019MS001724

6.1 Key Points

- Submesoscale-permitting ocean models can be validated with wavenumber spectra from satellite observations
- Simulated mesoscale Agulhas eddies strengthen with the increasing resolution of submesoscale dynamics
- Simulated mesoscale dynamics in the Agulhas ring path converge to observations in a $(1/60)^\circ$ ocean model

6.2 Abstract

Mesoscale dynamics of the Agulhas Current system determine the exchange between the Indian and Atlantic oceans, thereby influencing the global overturning circulation. Using a series of ocean model experiments compared to observations, we show that the representation of mesoscale eddies in the Agulhas ring path improves with increasing resolution of submesoscale flows. Simulated submesoscale dynamics are validated with time-mean horizontal-wavenumber spectra from satellite sea surface temperature measurements and mesoscale dynamics with spectra from sea surface height. While the Agulhas ring path in a nonsubmesoscale-resolving $(1/20)^\circ$ configuration is associated with too less power spectral densities on all scales and too steep spectral slopes, the representation of the mesoscale dynamics improves when the diffusion and the dissipation of the model are reduced and some small-scale features are resolved. Realistic power spectral densities over all scales are achieved when additionally the horizontal resolution is increased to $(1/60)^\circ$ and a larger portion of the submesoscale spectrum is resolved. Results of an eddy detection algorithm applied to the model outputs as well as to a gridded sea surface height satellite product show that in particular strong cyclones are much better represented when submesoscale flows are resolved by the model. The validation of the submesoscale dynamics with sea surface temperature spectra provides guidance for the choice of advection schemes and explicit diffusion and dissipation as well as for further subgrid-scale parameterizations. For the Agulhas ring path, the use of upstream biased advection schemes without explicit diffusion and dissipation is found to be associated with realistically simulated submesoscales.

6.3 Introduction

In the greater Agulhas region, the subtropical supergyre (Speich et al., 2007) strongly exchanges water masses between the Atlantic and the Indian Ocean. This has important implications for the global thermohaline circulation and in particular the Atlantic meridional overturning circulation (Beal et al., 2011; Biastoch et al., 2008b; Speich et al., 2007; Weijer et al., 2002). The turbulent upper ocean inflow of Indian Ocean waters into the Atlantic, the "Agulhas leakage," strongly controls the South Atlantic heat and salt budgets and thus its stratification (De Ruijter et al., 1999; Weijer et al., 2002). A part of this water reaches the South Atlantic western boundary and is transported into the equatorial current system where it is an important driver of decadal sea surface temperature (SST) variability (Lübbecke et al., 2015; Rühs et al., 2018). In respect to the far-field influence, the Atlantic multidecadal oscillation is found to correlate with the strength of the Agulhas leakage with a lag of 15 years (Biastoch et al., 2015). This is consistent with the transit times from the Agulhas region into the North Atlantic derived by Rühs et al. (2013).

The Agulhas Current (AC) is the western boundary current of the subtropical gyre in the South Indian Ocean. It flows along the continental slope, separates from the Agulhas Bank south of Africa, retroflects to the east, and forms the Agulhas Return Current (ARC; Lutjeharms and Ansorge, 2001). With a transport rate of 70 Sv (1 Sv = 10^6 m^3/s) and a core velocity of more than 2 m/s measured at the Agulhas Current Time-series (ACT) section (Beal et al., 2011), the AC is the strongest western boundary current of the Southern Hemisphere. At the retroflection, large rings are shed that are referred to as Agulhas rings. With observed diameters of more than 500 km (Arhan et al., 2003) and available potential energy of up to 71 PJ (Goni et al., 1997), Agulhas rings are among the largest and most energetic ocean eddies. After their shedding, they decay quickly to less than half of their initial size, mixing the bulk of their water mass properties into the surrounding Cape Basin (Boebel et al., 2003; De Ruijter et al., 1999). The Agulhas rings propagate northwestward into the South Atlantic partly due to the β effect and partly due to the advection by the Benguela drift (De Ruijter et al., 1999). They transport mass, momentum, heat, and salt from the Indian into the Atlantic Ocean and are the dominant contribution to the Agulhas leakage (Lutjeharms, 2007). Agulhas rings are observed to extend from the surface to depths of about 2,000 m (Casanova-Masjoan et al., 2017; McDonagh et al., 1999). Close to their shedding region, they were even found to reach to the bottom (Van Aken et al., 2003) where they might contribute to the observed frequent occurrence of benthic storms (Cronin et al., 2013) interacting with the deep

flow transporting North Atlantic Deep Water into the retroflection region (Arhan et al., 2003). These deep waters are found to be mainly transported by the deep ARC into the Indian Ocean (Arhan et al., 2003). Only a smaller portion of about 2–6 Sv contributes to the Agulhas Undercurrent (AUC) flowing northeastward below the AC (Arhan et al., 2003; Beal and Bryden, 1997; Biastoch et al., 2009a; van Aken et al., 2004)

The Agulhas leakage is controlled on the large-scale by the southern boundary of the Indo-Atlantic subtropical supergyre - the subtropical front - that is determined by the location of the atmospheric subtropical convergence zone (Biastoch et al., 2009b; Durgadoo et al., 2013). Regionally, the Agulhas leakage is highly turbulent and a result of the complex and energetic mesoscale and submesoscale dynamics and their interaction with the large-scale dynamics in the Agulhas region (Biastoch et al., 2008c; Lutjeharms, 2007). Around $30°S$, close to the Natal Bight, shallow slopes allow for mesoscale instabilities of the AC leading to the development of downstream propagating large meanders that are referred to as Natal Pulses (Lutjeharms and Roberts, 1988). Natal Pulses impact the separation point, the retroflection, and the Agulhas ring shedding (Lutjeharms et al., 2003a; Schouten et al., 2002; van Leeuwen et al., 2000). Furthermore, they are associated with cyclonic eddies with spatial scales of 100–200 km on their landward side (Gründlingh, 1979; Lutjeharms et al., 2003a). Large Natal Pulses are thought to result in early retroflections, where the AC separates already around $28°E$ and flows directly along the eastern flank of the Agulhas Plateau (Lutjeharms and Van Ballegooyen, 1988a). Between $30.5°S$ and $34.0°S$, the very steep continental slope suppresses instabilities, while the slope south of $34°S$ is flatter (de Ruijter et al., 1999; Gründlingh, 1983).

The region south of $34°S$ is a key region for the AC system where small-scale dynamics can have a large impact on the Agulhas leakage and thus on the global ocean. At the northern boundary of the AC, shear-edge instabilities lead to the formation of meanders, shear-edge eddies, filaments, plumes, and submesoscale vorticies (Krug et al., 2017; Lutjeharms et al., 1989, 2003a,b). The warm and salty plumes advected from the northern flank of the AC move either onto the Agulhas Bank or drift northwestward into the South Atlantic Ocean as “Agulhas filaments” (Lutjeharms and Cooper, 1996). The filaments transport only 0.1 Sv (Lutjeharms, 2007) but provide about 13 % of the total inter-ocean salt flux (Lutjeharms and Cooper, 1996) and thus are a minor but important contribution to the leakage of salt from the Indian Ocean. Meanders and shear-edge eddies grow in size to scales of 50–100 km traveling downstream (Lutjeharms et al., 1989). Shear edge and Natal Pulse related cyclones are observed to be either shed southwestward into

the open ocean or to feed their vorticity into a lee eddy on the western side of the Agulhas Bank (Boebel et al., 2003; Lutjeharms et al., 2003a; Penven et al., 2001). Lutjeharms et al. (2003b) further found indication in a model that the shear-edge eddies and other passing cyclonic features are trapped between the eastern side of the Agulhas Bank and the AC, providing a prereservoir of cyclonic vorticity that irregularly leaks into the lee eddy. The lee eddy is observed to occasionally detach from the shelf (Penven et al., 2001) and to travel southwestward (Boebel et al., 2003). In conclusion, the formation of Agulhas cyclones (shedded shear-edge and Natal Pulse-related cyclones as well as detached lee eddies) and filaments is strongly linked to small-scale activity. Agulhas cyclones interact with anticyclonic Agulhas rings (Boebel et al., 2003) and sometimes even trigger their shedding (Lutjeharms et al., 2003a). This indicates also a dependence of anticyclonic Agulhas rings and their shedding on small-scale flows. Further cyclones and anticyclones are found to form under strong interaction with smaller-scale flows in the frontal zone of the southern Benguela upwelling system and travel westward where they interact with the Agulhas rings (Lutjeharms and Stockton, 1987; Rubio et al., 2009).

Recent high-resolution model studies found that submesoscale dynamics play an essential role in the mixing of Agulhas ring waters into the Cape Basin and thus in setting the properties of the water masses that are exported into the Atlantic (Capuano et al., 2018a; Sinha et al., 2019). On the basis of a high-resolution regional model ($(1/108)^\circ$) for a very limited domain, Capuano et al. (2018a) found that submesoscale dynamics in the Cape Basin drive a strong exchange of both upper and intermediate waters of Atlantic and Indian Ocean origin. They conclude that the simulation of a realistic Indo-Atlantic exchange requires the resolution of a large portion of the submesoscale spectrum. Supporting these findings, Lagrangian analysis applied by Sinha et al. (2019) to a global $(1/48)^\circ$ model showed substantial leakage of water through the boundaries of the mesoscale eddies in the Agulhas region driven by high-frequency submesoscale flows.

In this study, we investigate the impact of submesoscale flows on the dynamics of mesoscale eddies in the Agulhas region via model comparison. We use a nested modeling approach to achieve a submesoscale-permitting horizontal resolution: the implementation of two-way interacting grid refinements ("nests") for the greater Agulhas region into global ocean general circulation models with coarser resolution ("hosts") (Biastoch et al., 2018; Holton et al., 2017; Schwarzkopf et al., 2019). Several of such configurations have been developed within the INALT family (Schwarzkopf et al., 2019) with horizontal grid refinements of down to $(1/10)^\circ$ and $(1/20)^\circ$ (i.a., INALT20r), as well as a double-nested configuration with $(1/60)^\circ$

horizontal resolution (INALT60). In this study, we compare a nonsubmesoscale-permitting INALT20r simulation to parallel experiments where we gradually increase the vertical resolution, decrease the diffusion and the dissipation of the model, and increase the horizontal resolution to resolve more and more small-scale and submesoscale flows. The model development is lead by a systematic model validation down to the smallest resolved scales and results in a further developed submesoscale-permitting INALT60 that is shown to be in very good agreement with the observations. Commonly, ocean general circulation models are validated by comparing the simulated sea surface height (SSH) anomaly to those of gridded products derived from along-track satellite altimetry as well as by comparing simulated and observed vertical sections through the large-scale currents, such as the ACT vertical section through the Agulhas (Under) Current (Beal et al., 2015). This common validation covers only the simulated large-scale circulation and integrated eddy activity. For a scale-dependent validation of the simulated mesoscale dynamics, we additionally compare the time-mean horizontal-wavenumber spectra of SSH from the model simulations with those from JASON-2 along-track measurements as well as of the SSH spectral slope from the simulations with predictions by quasi-geostrophic theory.

Submesoscale flows are associated with Rossby numbers of order 1 (Thomas et al., 2008). The Rossby number is a measure of the influence of Earth's rotation on the flow defined as $Ro = |\zeta/f|$. Here $\zeta = \partial v/\partial x - \partial u/\partial y$ is the vertical component of the relative vorticity (u and v are the flow components in zonal [x] and meridional [y] direction) and $f = 2\Omega \sin \varphi$ is the planetary vorticity with the Earth's rotation rate $\Omega = 7.2921 \times 10^{-5}$ rad/s and the latitude φ. The Rossby number as well as the normalized relative vorticity ζ/f can thus be used to quantify and compare the occurrence of submesoscale currents in the model experiments. The validation against observations is, however, a challenging task. In situ observations with a focus on submesoscale dynamics have only been carried out in limited regions of the Agulhas region. Submesoscale eddies with diameters of 10–20 km were observed at the inshore front of the AC with RAFOS floats (Lutjeharms et al., 2003a) and with seagliders (Krug et al., 2017). They were attributed to shear instabilities of the AC jet (Krug et al., 2017). The signal of present-day satellite altimetry exceeds the associated noise at scales larger than about 50 km in the greater Agulhas region (Dufau et al., 2016). Dufau et al. (2016) further point out that in winter time, when the submesoscale dynamics are most active (Callies et al., 2015), the rough sea state shifts this signal-equals-noise scale to even larger scales. Present-day altimetry is thus not able to resolve submesoscale dynamics. Very high resolution (order of tens of meters) satellite observations of reflectance and derivable products such as

chlorophyll concentration are hard to interpret in terms of the underlying ocean dynamics and are not comparable to models without biogeochemical components. One of the few remaining possibilities today for an area-covering validation of submesoscale mixed-layer dynamics with satellite products is the analysis of its imprint into the SST field. For this study, we apply spatial spectral analysis to Moderate Resolution Imaging Spectroradiometer (MODIS) data with a horizontal resolution of about 1 km and compare the time-mean spectra to those from the models. The spectral approach applied to both SST and SSH provides a scale-dependent model validation and comparison from the largest simulated scales down to the smallest submesoscales resolvable with a $(1/60)^\circ$ model. Moreover, the validation with SST spectra can justify or guide the choice of explicit diffusion and dissipation, advection schemes as well as the development of new subgrid-scale parameterizations.

The paper is structured in the following ways: In section 6.4, the model configurations and experiments are described in detail and evaluated with respect to the simulation of submesoscale flows with Rossby numbers of order 1. Subsequently, the simulated ocean dynamics are compared and validated against observations: the submesoscale dynamics with horizontal-wavenumber SST spectra from swath data in section 6.5, the large-scale circulation and the integrated eddy activity with a gridded SSH product and a vertical section of in situ observations in section 6.6, and the mesoscale dynamics with horizontal-wavenumber SSH spectra from along-track data as well as with an eddy detection algorithm applied to a gridded SSH product in section 6.7. A conclusion and discussion of the results is provided in section 6.8.

6.4 Model Configurations and the Simulation of Submesoscale Dynamics

The hydrostatic and Boussinesq-approximated primitive equations are solved with the Nucleus for European Modelling of the Ocean Version 3.6 (Madec et al., 2014). The Nucleus for European Modelling of the Ocean model configurations used for this study are part of the INALT family (Schwarzkopf et al., 2019). In this section, we give an overview of the used model configurations. For more details, we refer to Schwarzkopf et al. (2019). The INALT configurations are global ocean general circulation models with horizontal grid refinements for the greater Agulhas region and adjacent ocean basins. The global ocean is simulated building on the configuration ORCA025 (Barnier et al., 2006) and consists of an ocean general circulation model coupled to the viscous-plastic sea ice model Louvain-la-Nueve Ice Model Version 2 (Fichefet and Maqueda, 1997). For the discretization, a time step of 20 min and an Arakawa C-grid (Arakawa and Lamb, 1977) are used. Horizontally, the host grid has an eddy-permitting resolution of $(1/4)^\circ$ distributed on a tripolar grid with poles located at the South Pole and over Siberia and Canada to avoid singularities at the geographical North Pole. Vertically, 46 and 120 z levels were used with a partial cell at the bottom (25-m minimum vertical extent) to improve the influence of bathymetry on the dynamics of the ocean (Barnier et al., 2006). The vertical distribution of the z levels is shown in Figure 6.4, and the data set used for the ORCA025 bathymetry is described in Barnier et al. (2006). ORCA025 uses free-slip lateral momentum boundary condition for the component parallel to the boundary and no-normal flow condition.

For tracer advection, the total variance dissipation (TVD) scheme (Zalesak, 1979) has been used and for momentum advection, the vector invariant (VI) form with energy- and enstrophy-conserving scheme (Arakawa and Hsu, 1990) for the vorticity term. As the original energy- and enstrophy-conserving scheme has been shown to be associated with symmetric instabilities of the computational kind (Ducousso et al., 2017), a Hollingsworth-corrected version was used (Hollingsworth et al., 1983). The numerical diffusion and dissipation associated with both advection schemes are assisted by explicit horizontal diffusion and dissipation terms in the primitive equations. For tracers, an isoneutral Laplacian scheme with a nominal horizontal eddy diffusivity of 300 m^2/s was used. For momentum, a horizontal bilaplacian scheme with a nominal horizontal eddy viscosity of $-1.5 \times 10^{11}\ m^4/s$ was applied. Vertical diffusion and dissipation are represented with a 1.5-level turbulent kinetic energy scheme (Blanke and Delecluse, 1993). The downward flux of horizontal

momentum at the bottom is parameterized as $C_D \mathbf{u}_{h,btm} \sqrt{u_{btm}^2 + v_{btm}^2 + \epsilon}$ with the bottom drag coefficient $C_D = 0.001$, the horizontal velocity vector in the bottom grid cell $\mathbf{u}_{h,btm} = (u_{btm}, v_{btm})$, and $\epsilon = 0.0025$ m²/s accounting for unresolved currents due to tides, internal wave breaking, and others. A diffusive scheme with a horizontal mixing coefficient of 1,000 m²/s is used for the parameterization of the effect of the bottom boundary layer dynamics on tracers.

For the configuration INALT20r, a horizontal grid refinement of five and a temporal refinement of 3 with respect to the host grid is applied, resulting in a horizontal resolution of $(1/20)^\circ$ (≈ 4.5 km) and a nest time step of 400 s for the greater Agulhas region ($6^\circ S - 50^\circ S$, $20^\circ W - 70^\circ E$, see Fig. 6.1). The nesting is done with the two-way nesting scheme Adaptive Grid Refinement in FORTRAN (Debreu et al., 2008) enabling an active interaction between both grids and a two-way exchange of signals through the boundary of the nest. In contrast to the global host grid, a no-slip boundary condition is used for the horizontal momentum within the nest. The no-slip condition is the more physical one as the velocities vanish at the resting seafloor. The free-slip condition was nevertheless used for the coarse-resolution host grid as else the simulated boundary current transports are too weak. For the high-resolution nest of a comparable $(1/20)^\circ$ configuration, Schwarzkopf et al. (2019) found only minor changes of the AC and AUC transports when the sidewall boundary condition is switched from free to no slip. Thus, for this study, the no-slip lateral boundary is used for the nests. Eddy diffusivity is linearly scaled down from the host grid values to 60 m²/s, and viscosity is quadratically scaled down to -6×10^9 m^4/s. The bathymetry for the nest is generated via interpolation from the ETOPO1 bathymetry (www.earthmodels.org/data-and-tool/topography/etopo). The initial conditions, for the experiments of this study, are taken from a 30-year spin-up of INALT20r that was initialized with climatological temperature and salinity fields from Steele et al. (2001). It was spun up from 1980 to 2009 under atmospheric forcing and bulk formulas developed for the Coordinated Ocean-Ice Reference Experiments 2 (Griffies et al., 2009; Large and Yeager, 2009). The forcing variables are prescribed with a 2° spatial resolution. Atmospheric temperature, wind speed, and humidity are prescribed 6-hourly, radiation daily, and precipitation monthly. A vertical axis with 46 z levels (L46) and a resolution of 6 m near the surface to 250 m in the deep ocean has been used for this integration (Figure 6.4). All of the following four experiments start on 1 January 2010 from the spin-up fields and are integrated under JRA55-do(v1.3) forcing (Tsujino et al., 2018) from 2010 to 2017. JRA55-do provides surface forcing in a temporal and horizontal resolution of 3 hr and 0.5°. Since a large part of the spectrum of submesoscale flows evolve at time scales shorter than a day (McWilliams, 2016), its representation in the simulation is expected to improve

with a better resolved daily cycle in the forcing. The fast evolution of submesoscale dynamics is also accompanied by the need for high-frequency model output, which is written as 4-hr means for the surface grid cells. For the horizontal-wavenumber spectra, an additional sea surface snapshot is written every 5 day at noon (UTC) into the model output.

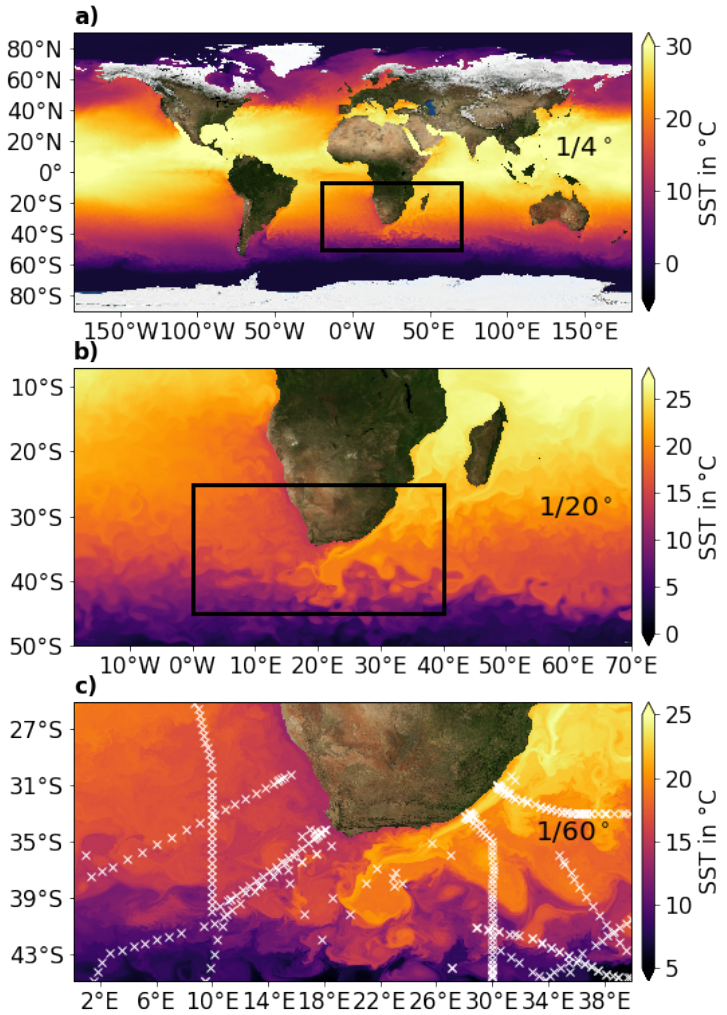

Fig. 6.1: *The nesting setup of INALT60: A global* $(1/4)°$ *horizontal resolution host grid [a]) with a* $(1/20)°$ *nest [b]) and a secondary* $(1/60)°$ *nest [c]). INALT20r is the same configuration without the secondary nest. Shading shows the sea surface temperature (SST) in degrees Celsius simulated with INALT60 on model date 11 August 2015, 12 p.m. (UTC). For the host grid and the first nest, the centered 5-day mean is shown and for the secondary nest the model snapshot. The black boxes show the location of the nests. White crosses in the lower panel show the location of the World Ocean Circulation Experiment CTD measurements that are used by Stewart et al. (2017) to derive the requirements for the vertical grid spacing as shown in Figure 6.4. All land backgrounds that are shown in this paper are taken from Blue Marble Next Generation (Stöckli et al., 2005).*

6.4.1 The Non-Submesoscale-Resolving $(1/20)^\circ$ Experiment (INALT20r.L46.HighDiff)

The first experiment is performed with the described configuration with 46 vertical levels and is called INALT20r.L46.HighDiff to highlight the horizontal and vertical resolution as well as the diffusion and dissipation setup. This reference experiment is strongly eddying but permits almost no submesoscale flows. $Ro > 1$ are found to occur only barely in INALT20r.L46.HighDiff (Figure 6.2a); on average in only 0.17 % of the domain area (Figure 6.2b). A snapshot of the surface Rossby number on the model day 4 September 2012 shows that even in the Southern Hemisphere winter, when the submesoscales should be most active (Callies et al., 2015), the surface flow is mainly associated with low Rossby numbers and small-scale features are almost absent from the simulation (Figure 6.3a). There are no submesoscale flows simulated in the Agulhas ring path. Only some smaller-scale currents are found in the retroflection and occasionally east of the AC. The time series of $Ro > 1$ shows only a very weak seasonal cycle (Figure 6.2b).

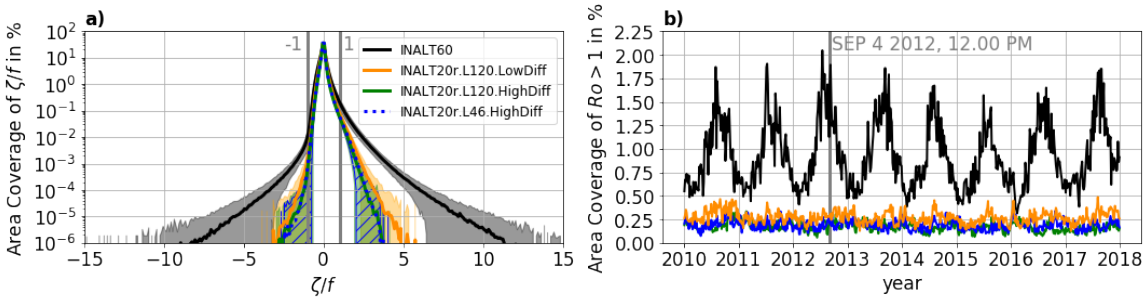

Fig. 6.2: *(a) The area coverage of the surface relative vorticity ζ normalized by the planetary vorticity f in percent for the period 2012 - 2017 for the core Agulhas region shown in Figure 6.1c. Filled areas show the range of ± 1 standard deviation σ. The analysis is based on model snapshots. (b) The time series of the area coverage of Rossby numbers $Ro = |\zeta/f| > 1$ in the same region shown for each model with the same color as in (a).*

6.4.2 Increasing the Vertical Resolution (INALT20r.L120.HighDiff)

Increasing horizontal resolution provides the potential for resolving smaller-scale currents. To achieve this, it is necessary that the vertical resolution resolves at least the vertical structure of the horizontal flows (Stewart et al., 2017). Under the assumption that baroclinic modal basis functions represent the vertical structure of the horizontal flows, requirements for the vertical resolution to resolve each mode can be derived from CTD measurements by demanding that the model grid at the

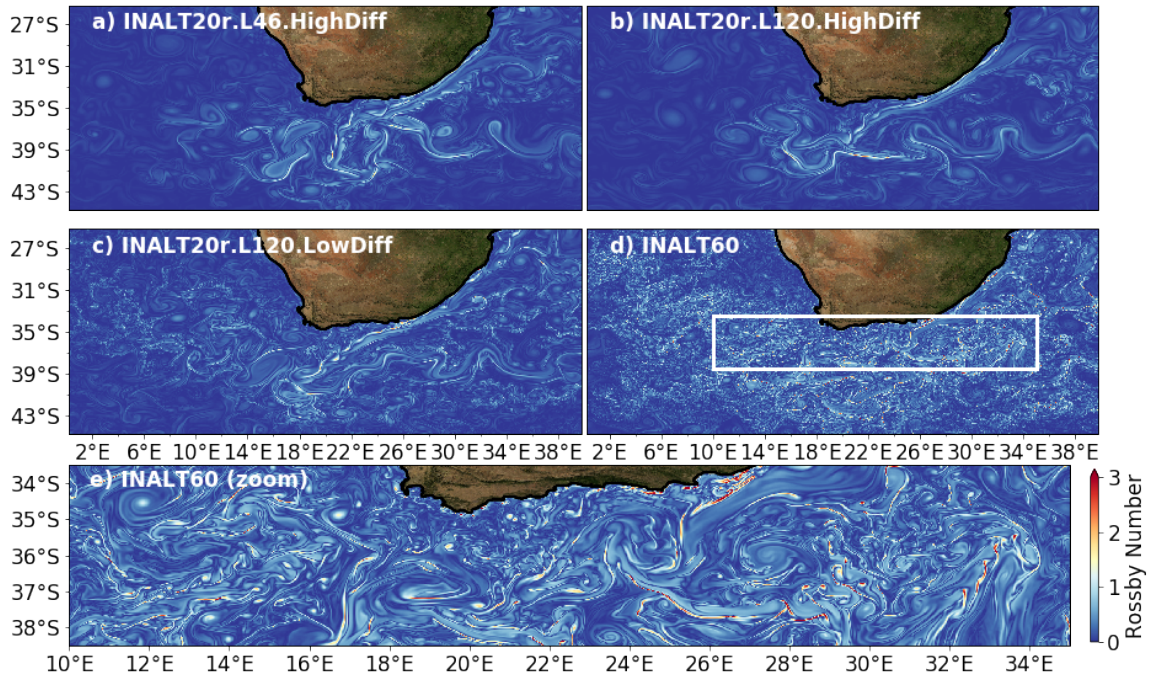

Fig. 6.3: *Snapshots of the surface Rossby number on model date 4 September 2012 12.00 p.m. (UTC) for (a) INALT20r.L46.HighDiff, (b) INALT20r.L120.HighDiff, (c) INALT20r.L120.LowDiff, (d) INALT60, and (e) a zoom from INALT60 for the region marked in (d).*

location of the measurement has to be associated in the vertical with at least three cells between each pair of modal function zero crossings as well as between the surface (bottom) and the nearest zero crossing (Stewart et al., 2017). The respective requirements for each mode derived by Stewart et al. (2017) from World Ocean Circulation Experiment observations are shown in Figure 6.4 for the measurement within the core Agulhas region (Figure 6.1c). If the vertical grid spacing at a specific depth is smaller than the requirements, the respective mode is resolved by the vertical grid. Only the first baroclinic mode is resolved with L46 (Figure 6.4). With reference to the requirements derived by Stewart et al. (2017), we construct a new vertical grid spacing with 120 vertical levels (L120) that resolves the third baroclinic mode almost everywhere.

Near the surface and in the deep ocean, the vertical grid spacing is chosen independently from the baroclinic mode approach. A further requirement for the vertical grid spacing is that it shall permit the processes in the mixed-layer even in summer when the mixed-layer depth is occasionally less than 20 m in the Agulhas region (de Boyer Montégut et al., 2004). Thus, we placed 10 vertical levels in the upper 20 m with a minimum grid spacing of 1 m at the surface. Capuano et al. (2018b) argue that a uniform vertical grid spacing of about 50 m - in particular at interme-

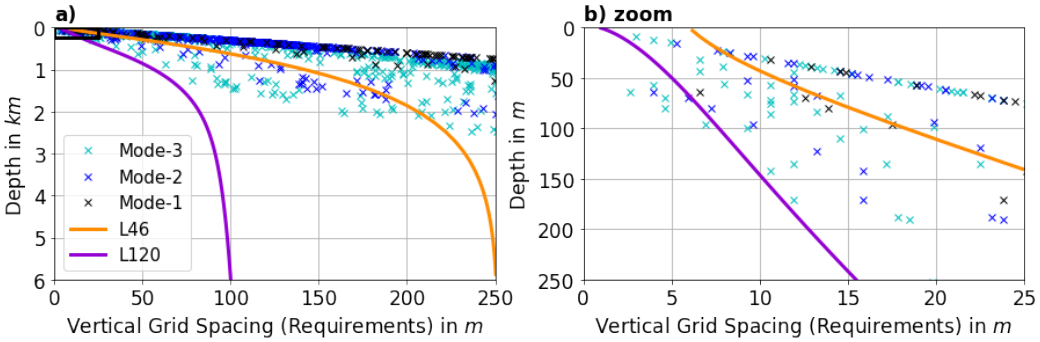

Fig. 6.4: *The vertical grid spacing as a function of depth for the 46 vertical levels (L46) and the 120 vertical levels (L120). Crosses show the requirements on the vertical grid spacing to resolve the first, second, and third baroclinic mode as derived by Stewart et al. (2017) from CTD measurements at the locations shown in Figure 6.1c. The right panel shows a zoom into the near-surface box marked in the left panel.*

diate depths - is needed for the realistic simulation of the exchange of Indian and Atlantic Ocean intermediate waters. As a compromise with respect to computational costs and the near-surface focus of this study, we gradually increase the vertical grid spacing to a maximum of 100 m in the deep ocean. The L120 experiment is named INALT20r.L120.HighDiff. $Ro > 1$ is found to occur as rarely as with L46 (Figure 6.2a and 6.2b) and small-scale features show up again only occasionally in the respective winter time snapshot of near-surface Ro (Figure 6.3b). As also the results of almost all other analyses, we present in this paper, are similar for L46 and L120, the results for INALT20r.L46.HighDiff are not discussed explicitly but are shown in the figures throughout the paper. The similar results do not imply that the increase in vertical resolution is not important for the simulation of small-scale flows. We hypothesize that a too high model diffusion and dissipation inhibit the simulation of small-scale flows and thus masks the effect of an increase in vertical resolution.

6.4.3 Reducing the Diffusion and the Dissipation of the Model (INALT20r.L120.LowDiff)

The diffusion and the dissipation of the model are further constraints for the simulation of the small-scale flows that are potentially resolved by the given horizontal and vertical grid spacing. The model diffusion (dissipation) is the combined effect of numerical and explicit diffusion (dissipation) in the primitive equations. The diffusion (dissipation) removes tracer variance (kinetic energy) mainly from the smaller scales. The numerical diffusion (dissipation) depends on the choice of the advection schemes for tracer (momentum). For the combination TVD/VI, the numer-

ical contribution has to be assisted by additional explicit diffusion and dissipation to avoid the excitation of spurious numerical modes. In the configurations above, the explicit horizontal diffusion (dissipation) is realized as an Laplacian (Bilaplacian) operator, applied to the model solution multiplied by a constant diffusion (dissipation) coefficient. The coefficients have to be large enough to prevent numerical instabilities everywhere in the model domain. Short sensitivity experiments with INALT60 showed that the small scales are still strongly damped with TVD/VI when the coefficients are tuned to a minimum value protecting the simulation from numerical instability (not shown). By contrast, a sensitivity test with a flux-form third-order upstream biased scheme (UBS; Farrow and Stevens, 1995; Madec et al., 2014; Webb et al., 1998) for both tracer and momentum without explicit diffusion and without explicit dissipation showed no exertation of numerical modes and a conservation of the small-scale energy down to scales of about 10 km. UBS schemes do not require additional explicit diffusion and dissipation to keep the simulation numerically stable. We perform an experiment where we switch in the nest from TVD/VI with explicit diffusion and dissipation to UBS without explicit diffusion and dissipation. On the host grid we keep the TVD/VI setup as described above. We refer to the experiment as INALT20r.L120.LowDiff. The model time steps had to be decreased to 15 min in the host grid and to 150 s in the nest to run the simulation.

In the winter time snapshot of near-surface Ro, small eddies, sharp fronts, and other smaller-scale currents occur more often compared to the previous configurations - especially in regions where mesoscale activity is strongest (Figure 6.3c). Small-scale activity is now also found in the Agulhas ring path, mainly between the rings, as well as south of the ARC. $Ro > 1$ still occurs on average in only 0.27 % of the domain area (Figures 6.2a and 6.2b) and shows up only occasionally in the winter time snapshot (Figure 6.3c), indicating that most of these smaller-scale flows are close to geostrophic balance. The time series of the area coverage of $Ro > 1$ shows, although weak, the typical seasonal cycle of submesoscale activity (Figure 6.2b).

6.4.4 Increasing the Horizontal Resolution (INALT60)

Within INALT20r, a secondary nest with a horizontal resolution of $(1/60)^\circ$ (≈ 1.5 km) is implemented covering the core Agulhas region ($0^\circ E - 40^\circ E$, $25^\circ S - 45^\circ S$, see Figure 6.1), together constituing the configuration INALT60. The INALT60 experiment presented by Schwarzkopf et al. (2019) was a first sensitivity study with respect to the horizontal resolution simulating the 1980s. Here, we build on their work and

use a further developed INALT60 with L120, UBS advection schemes, JRA55-do forcing, and an integration period from 2010 to 2017. The submesoscale-permitting INALT60 simulation is the main experiment for this study and performed as the fourth parallel simulation. Again, two-way nesting is provided by Adaptive Grid Refinement in FORTRAN and the bathymetry is interpolated from ETOPO1 which has also a resolution of $(1/60)^\circ$. From INALT60, we write both 4-hr means and 5-day snapshots for the upper 250 m of the secondary nest. In INALT60, small-scale motions are simulated all over the greater Agulhas region (Figure 6.2f). Strongest small-scale activity is again found, where the mesoscale eddy activity is strongest. The distribution of ζ/f shows the typical skewness toward cyclonic motions at higher Ro (Rudnick, 2001). $Ro > 1$ occur much more often than in the $(1/20)^\circ$ configurations (on average 0.93 % of the area) and show a very pronounced seasonal cycle (Figure 6.2b). Although Rossby numbers of up to 15 occur in the simulation, most of the smaller-scale flows have $Ro < 3$ (Figure 6.3e) and thus still have a large geostrophically balanced component. The success in simulating submesoscale dynamics is attributed to the combination of higher vertical and horizontal resolution and the reduction of the diffusion and dissipation. The previously described $(1/20)^\circ$ experiments and several short sensitivity experiments showed a strongly reduced ability to simulate submesoscale flows if only one or two of these parameters are changed.

For all experiments, the 3-D averaged kinetic energy density (here not shown) within the region of the secondary nest reaches a new stable level after a 2-year secondary spin-up. Thus, we mainly analyze the model period from 2012 to 2017 in this study.

6.5 Validating Submesoscale Dynamics with SST Spectra

In this section, we validate the simulated submesoscale dynamics by comparing its time-mean horizontal-wavenumber SST spectrum and its characteristics to those derived from MODIS (Minnett et al., 2002) swath measurements provided by National Aeronautics and Space Administration Aqua (NASA Goddard Space Flight Center, 2016a) and Terra (NASA Goddard Space Flight Center, 2016b) satellites. MODIS bulk SST is estimated from skin SST in the 11 μm thermal infrared band. It is available twice a day with a horizontal resolution of about 1 km. The MODIS data are classified to be either "best," "good," "questionable," "bad," or "not processed." The latter two categories mainly represent the presence of clouds and are excluded from the analysis. A swath with extraordinary good quality taken on 30 October 2017 of the northeastern Agulhas ring path is partly shown in Figure 6.5a and compared to an INALT60 snapshot (Figure 6.5b). Submesoscale features such as fronts, filaments, and small-scale eddies can be seen in both the model solution and the observations. Submesoscale cold-core eddies are found in both data sets, for example, around $15.0°E$, $35.8°S$ (marked by the arrows in Figures 6.5a and 6.5b). The respective absolute value of the SST gradient $|\nabla_h SST|$ (Figure 6.5c and 6.5d) is a measure of the horizontal-wavenumber SST power spectral density (PSD). It is of comparable strength in the simulation and the observations. The MODIS swath, however, shows features of even smaller scales than in INALT60. A week earlier on 22 October 2017, a swath with very large cloud-free areas was taken. The SST gradients are shown in Figure 6.5e and compared to INALT60 (Figure 6.5f). The model SST gradients are too strong in the retroflection region as well as along the subtropical SST front. Time-mean SST from gridded (9-km horizontal resolution,) daytime and nighttime MODIS products (NASA Goddard Space Flight Center, 2015a,b,c,d) for the period 2012–2017 shows the location of the subtropical front around $\approx 39°S$ west of $14°E$ and $\approx 43°S$ east of $14°E$ (contours in Figure 6.6a). We expect that the model is associated with too large PSD in these regions.

To investigate the spatial distribution of the spectral characteristics, the Agulhas region is subdivided into subregions of $4° \times 4°$ (squares in Figure 6.6a and Figure 6.5). For both the model and the observations, the data of each subregion are treated separately. First, the noise of the MODIS data is reduced by applying a two-dimensional running mean with a box length of five data points to each swath within the subregion. Subsequently, for each subregion and each swath (model snapshot), the geographical coordinates are transformed into Cartesian coordinates using the

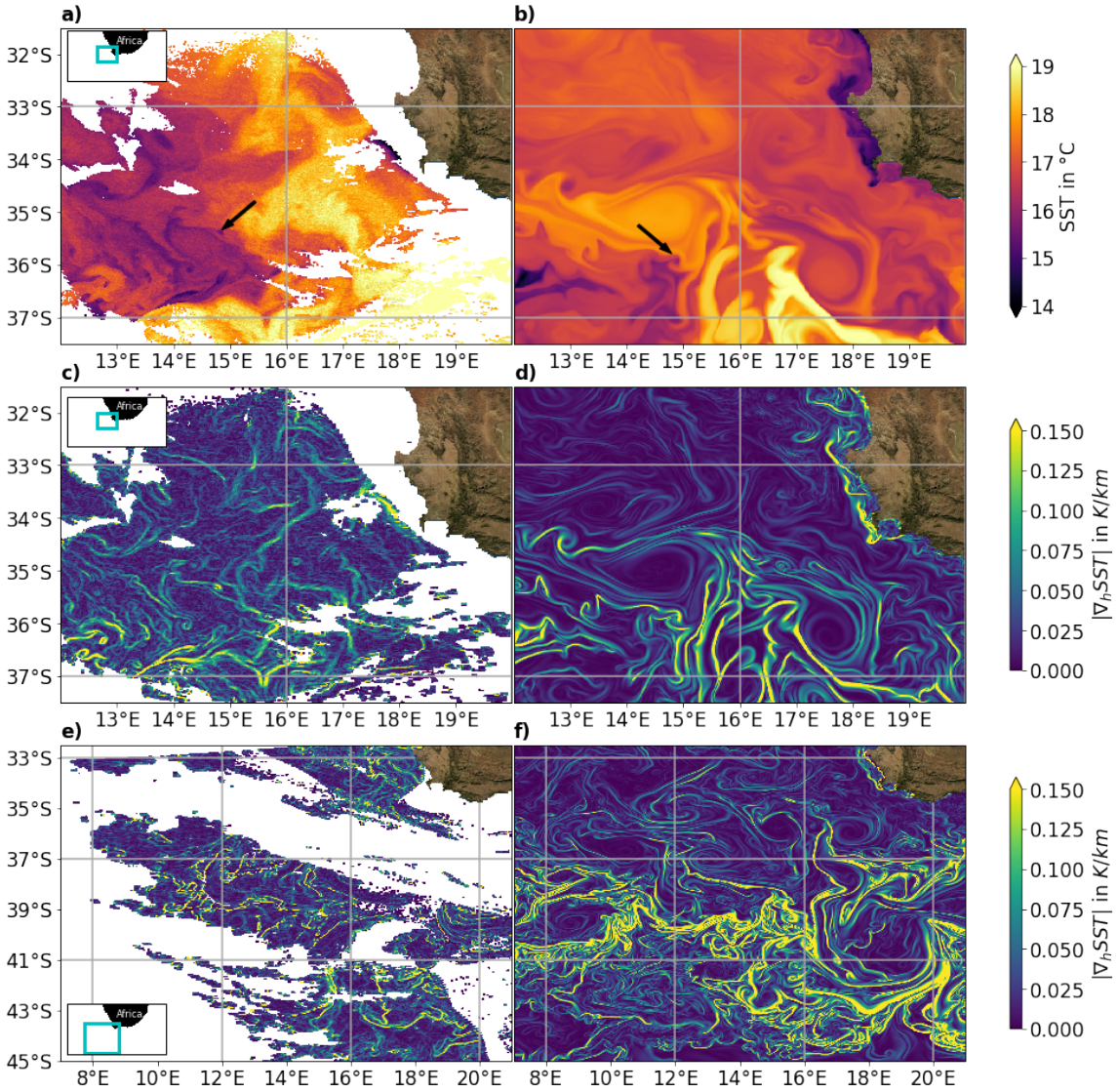

Fig. 6.5: *Sea surface temperature (SST) in degrees Celsius on 30 October 2017 from Moderate Resolution Imaging Spectroradiometer Terra (a) and INALT60 (b) and the respective absolute value of the SST gradient (c and d). White areas are associated with clouds. Arrows in (a) and (b) show the location of a submesoscale cold-core eddy. The absolute value of the SST gradient for a second swath with large cloud-free areas taken on 22 October 2017 is shown in (e) and compared to the one from the respective INALT60 snapshot (f). The location of each region is marked in the small maps on the left-hand side. Gray lines show the boundaries of the $4° \times 4°$ subregions used for the spectral analysis for Figure 6.6.*

European Petroleum Survey Group Geodesy numbers 4326 (World Geodetic System 1984) and 3395 (Cartesian). After that, the data are linearly interpolated onto a regular grid with 1-km grid spacing and scanned for cloud-free lines longer than 200 km in both quasi-zonal and quasi-meridional directions. The data are not used

for the spectral analysis in the respective subregion, if there are less than 100 of such lines in one swath (model snapshot) within the subregion (and thus if more than ≈ 90 % of the subregion is cloud covered). In particular south of $41°S$ only about 400 useful swaths are found for the period 2012–2017 for each subregion (Figure 6.6a). If there are more than 100 cloud-free lines longer than 200 km in the swath within the subregion, in both horizontal directions a one-dimensional horizontal-wavenumber spectrum is computed for each of these lines. For the computation of the each spectrum, mean and trend are subtracted and the data are multiplied by a Hanning window and an associated amplitude correcting factor of 2. To average spectra based on data lines with different length L, the data line is zero padded to a total length of 3,000 km before, which is not exceeded within the analysis. Afterward, the one-dimensional discrete Fourier transform is computed using the python numpy fast Fourier transform algorithm. The PSD is then computed as the squared absolute value of the first half of the Fourier transform normalized by the original length L. Values for wavelengths $\lambda > L/2$ are removed as they are strongly reduced by the Hanning window. For the model experiments, the spectral analysis is applied to snapshots every 5 days at noon (UTC). Similar to the observations, the spectral analysis is applied to quasi-zonal and quasi-meridional data lines on the regular Cartesian grid, the model output is interpolated on. The spatial-mean spectra within each subregion for both the models and the observations are averaged over the period 2012–2017. To avoid a potential temporal bias in the observations due to a seasonal cycle in cloud cover, monthly averages are calculated before the total time average. We refer to half the horizontal wavelength as the horizontal scale, as in the Fourier analysis the amplitude of quasi-elliptic features, such as eddies, imprint to a wavelength that is about twice as large as the horizontal extent of the features.

Maps of the mean spectral slope for the 20- to 50-km scale band show a comparable pattern for INALT60 and the observations (Figure 6.6, left): steeper slopes of about $k^{-2.5}$ are found for the AC, the retroflection, the upwelling region west of Africa, the ARC, and the area east of the AC and shallower slopes close to $k^{-2.1}$ in the Agulhas ring path. The slopes in the Agulhas ring path are found to be slightly shallower in the model than in the observations, while in the region of the southwest Indian Ocean subgyre slightly steeper slopes are found in the model. The largest differences are found in the southernmost part of the domain south of $41°S$, where the cloud cover is very large (Figure 6.7a). Maps of the mean PSD in the same scale band show again a similar pattern for INALT60 and the observations (Figure 6.6, right): large PSD in the upwelling region, the AC and ARC as well as the retroflection and south of the Agulhas ring path. However, the PSD is much larger in INALT60 in the region of the retroflection as well as along the subtropical front, while it is

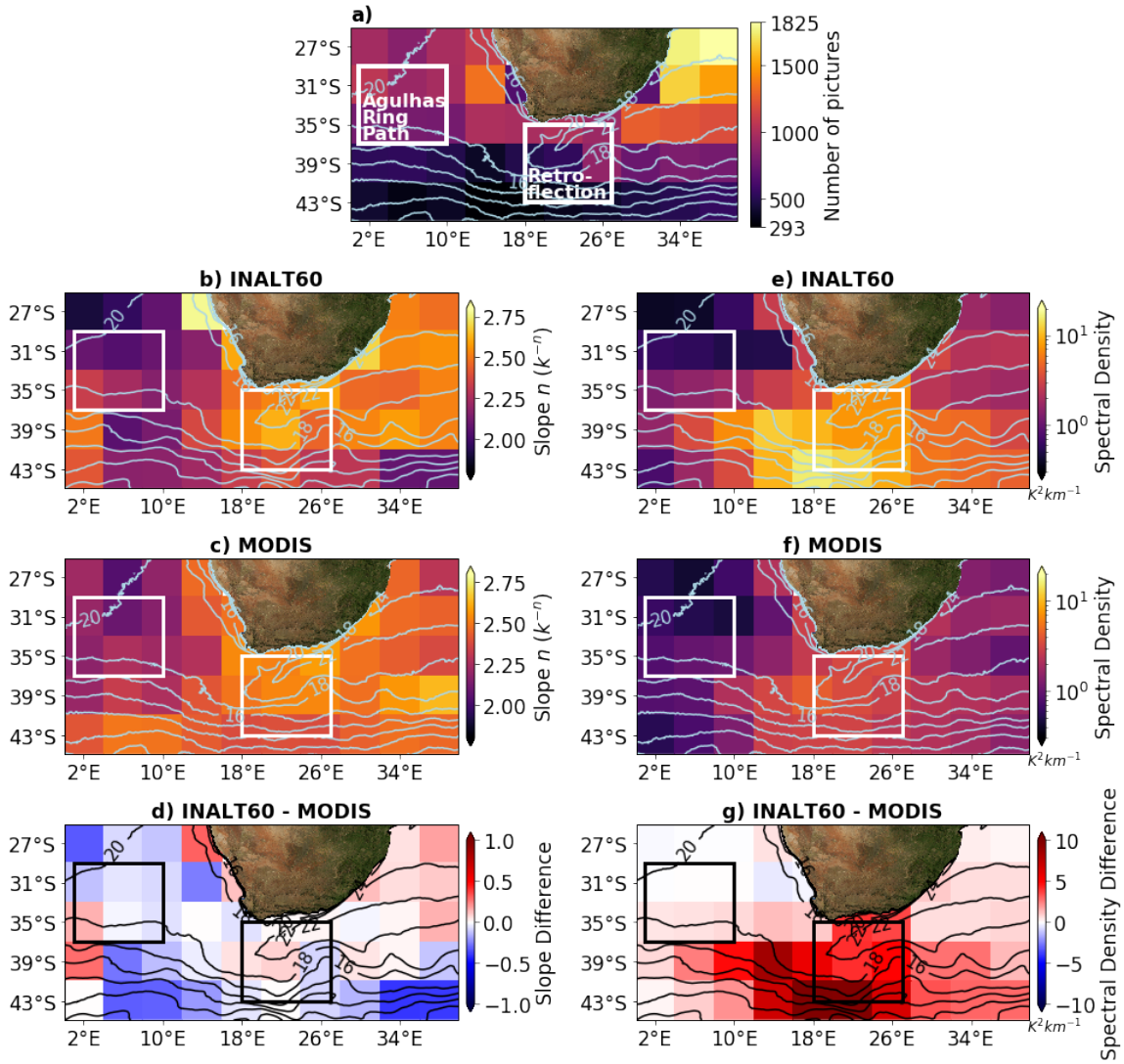

Fig. 6.6: *The number of MODIS pictures with more than 100 cloud-free, 1-km broad lines longer than 200 km that were used for the spectral analysis for $4° \times 4°$ subregions (a). Below the mean logarithmic SST spectral slope n (k^n, left, b–d) and mean SST power spectral density (e - g, right) for the 20- to 50-km scale band of the 2012–2017 time-mean SST spectra for each subregion in INALT60, MODIS, and their difference are shown. The boxes mark the subregions used for the spectra shown in Figure 6.7. Contours show the time-mean SST from INALT60, respectively, from the gridded 9-km daytime and nighttime MODIS products (NASA Goddard Space Flight Center, 2015a,b,c,d). MODIS = Moderate Resolution Imaging Spectroradiometer; SST = sea surface temperature.*

associated with the same amplitude in other regions such as the Agulhas ring path or the subgyre region (Figure 6.6, bottom right panel). This is consistent with the comparison of the SST gradient snapshots (Figures 6.5c–6.5f).

The Agulhas ring path is a region where the spectral characteristics of INALT60 are found to agree very well with the observations. Consistently, the time-mean spectrum of INALT60, derived for a $9° \times 8°$ region in the Agulhas ring path with the same procedure as described above for $4° \times 4°$ subregions, is almost identical to the one from MODIS (Figure 6.7a). Both spectra follow an almost straight line down to scales of 15 km with a slope of k^{-2}, where k is the wavenumber. At 8 km, the spectrum of INALT60 drops strongly due to the dominant effect of the diffusion and the dissipation of the model. Below these scale, the spectrum from MODIS is associated with more PSD than INALT60 consistent with that smaller features are covered by the observations. In INALT20r.L120.HighDiff almost no small-scale flows are simulated in the Agulhas ring path. Consistently, its spectrum is below 100 km associated with a too steep slope and thus too less PSD. When the diffusion and dissipation of the model are reduced (INALT20r.L120.LowDiff), the spectrum is found to be in good agreement with the observations down to 25 km. This scale can further be identified as the scale, where the SST spectra of the $(1/20)°$ simulations drop due to the dominant effect of the model diffusion and dissipation.

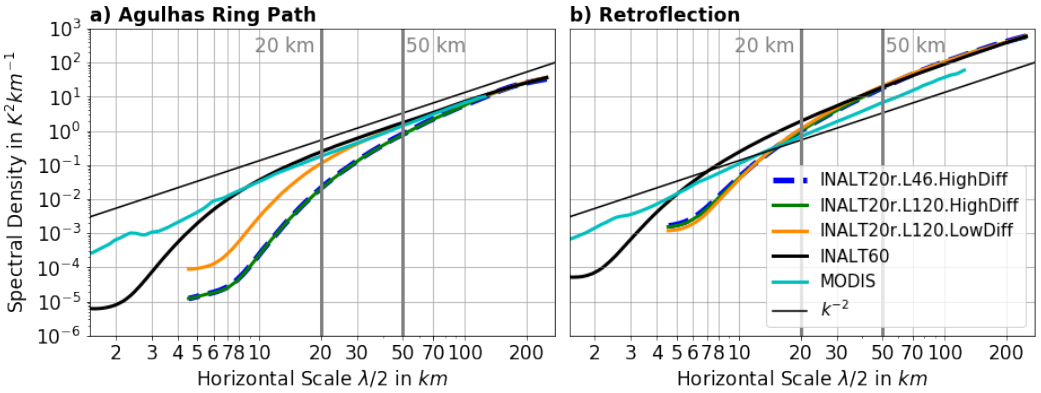

Fig. 6.7: *The 2012–2017 time-mean sea surface temperature spectra for the Agulhas ring path (a) and the retroflection (b). Both subregions are marked in Figure 6.6. The horizontal scale is identified as half the wavelength λ.*

The region of the retroflection is found to be a region of steeper spectral slopes ($\approx k^{-2.5}$) and larger PSD. While the slopes are similar for INALT60 and MODIS, in the model the PSD is too large. The time-mean spectrum of INALT60, derived for a $9° \times 8°$ domain in this region follows a straight line parallel to the one of MODIS down to 15 km (Figure 6.7b). In this region, all $(1/20)°$ experiments show a similar spectra that is in good agreement with the one of INALT60 down to 25 km. This is consistent with a presence of smaller-scale flows in the region of the retroflection in all experiments.

In conclusion, the validation indicates that submesoscale dynamics and their regional differences are well represented in INALT60. However, a lack of SST damping is found for the region of the retroflection and the subtropical front. For INALT60 and INALT20r, 8 and 25 km have been identified as the scales, where the effect of the model diffusion and dissipation gets dominant.

6.6 Differences in Large Scale Dynamics and Integrated Eddy Activity

For all four model experiments, the pattern of the simulated large-scale near-surface AC system compares well with observations. Simulated SSH anomalies, averaged from daily data for the period 2012–2017, show a very good agreement with the satellite-derived daily L4 product provided by the Copernicus Marine and Environment Monitoring Service CMEMS (Figure 6.8, left). Location and strength of the SSH gradient associated with the AC, its separation and the ARC compare well with the observations. Moreover, the meanders of the time-mean ARC are more or less at the observed locations and the Agulhas ring path, identifiable as a region of enhanced SSH anomaly, has the observed extent. While in INALT20r.L120.LowDiff and INALT60, the amplitude of the SSH anomalies in the Agulhas ring path is closer to the observations, the time-mean retroflection extends in both experiments too far south.

The temporal standard deviation of the SSH is a measure of the integrated geostrophic eddy activity. Its overall patterns are generally in good agreement with the observations, as expected from the good agreement of the time-mean SSH (Figure 6.8, middle). Deviations from the observations are found in the retroflection where the $(1/20)^\circ$ experiments show too much eddy activity, while the amplitude in INALT60 compares well. In the Agulhas ring path, the SSH variability of INALT60 is strongest and closest to the observations. Also very regional features, such as the observed small region of enhanced eddy activity south of the Agulhas Bank around $35^\circ S$, $24^\circ E$, that is driven by instabilities of the inshore front of the AC (Lutjeharms et al., 2003b), is captured very well in size and amplitude in INALT60. North of the ARC, all experiments slightly underestimate the observed SSH variability. The excess southward extent of the retroflection, in particular in INALT60, is consistently associated with more eddy activity compared to the observations. Due to the short integration period it is unclear whether this and other regional differences are systematic or only due to the strong nonlinearities in the AC system. Further, the along-track satellite measurements are interpolated both in space and time for the daily gridded product, which is thus only an approximation for the true daily means. Both arguments highlight the limitations of the validation of the eddy field with the standard deviation of gridded SSH and the need for a statistically more robust approach applied directly to along-track data (see section 6.7).

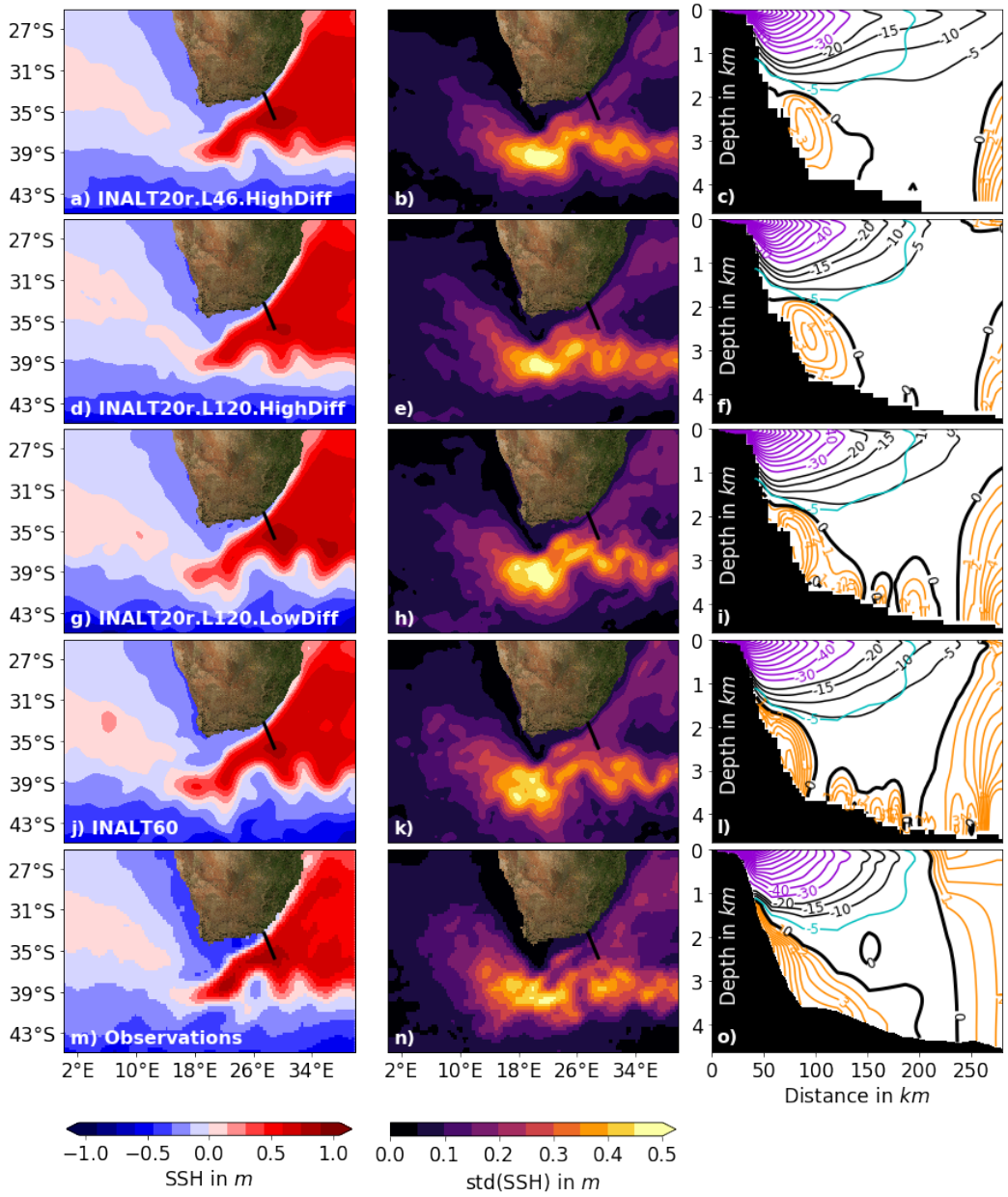

Fig. 6.8: *Time-mean (left column) and standard deviation (middle column) of daily sea surface height (SSH) for the period 2012–2017 from INALT20r.L46.HighDiff (a and b), INALT20r.L120.HighDiff (d and e), INALT20r.L120.LowDiff (g and h), INALT60 (j and k) and from the satellite-derived L4 CMEMS product (m and n). The black line shows the Agulhas Current Time-series section. The domain average has been subtracted for the left panels. Right: Mean velocity in centimeters per second at the Agulhas Current Time-series section for the time period from May 2010 to February 2013 from the simulations (c, f, i, and l) and from observations by Beal et al. (2015) (o). Orange contours show cross section "northeastward" velocities with a contour interval of 1 cm/s, black and violet contours mark "southwestward" velocities with a contour interval of 5 and 10 cm/s. The 5-cm/s isotach from the observations in the lower right panel is also shown in the plots for the models with a cyan line.*

The comparison of the time-mean cross-section velocity of the AC at the ACT section with observations by Beal et al. (2015) for the period from May 2010 to February 2013 shows for all experiments a very good agreement with respect to the strength and the vertical extent of the AC (Figure 6.8, right). The 30-cm/s isotach extends down to about 1,000 m, and the 5-cm/s isotach down to about 1,800 m. The horizontal extent of the AC is not comparable for such a short time period, as it strongly depends on the nonlinear recirculation from the ARC into the AC (Biastoch et al., 2018). The time-mean AC transports in the simulations have values between 70 and 84 Sv in the respective time period and compare well with the observed value of 78 Sv (Table 6.1). The AC transport is here defined as the "southwestward" barotropic cross-section transport integrated vertically and from the coast to the distance where the time-mean barotropic cross-section transport changes its sign (Beal et al., 2015). Due to the nonlinearities of the Agulhas system, the transports of the model experiments and the observations are not correlated in time (not shown). INALT20r.L120.LowDiff and INALT60 are associated with temporal standard deviations of the AC transport of about 25 Sv, which is higher than values of about 20 Sv for the high-diffusion/dissipation experiments but smaller than 31 Sv derived from the observations (Table 6.1). The AC transport in INALT60 is closest to the observations.

	Observed Period (May 2010 to February 2013)		Full Period (2010 - 2017)	
Data Source	AC	AUC	AC	AUC
INALT20r.L46.HighDiff	84 ± 19	3.5 ± 3.1	76 ± 23	4.0 ± 3.7
INALT20r.L120.HighDif	70 ± 20	3.6 ± 2.6	69 ± 24	4.4 ± 3.5
INALT20r.L120.LowDiff	70 ± 25	6.6 ± 5.5	71 ± 29	6.6 ± 5.4
INALT60.L120.LowDiff	73 ± 26	6.5 ± 5.2	67 ± 27	6.5 ± 5.8
Observations (Beal et al., 2015)	78 ± 31	7.0 ± 5.1	-	-

Tab. 6.1: *Time-mean transports in Sv of the Agulhas Current (AC) and Agulhas Under Current (AUC) at the ACT section (see Figure 6.8)*

For the representation of the AUC below the AC, a gradual improvement is found from INALT20r.L120.HighDiff to INALT60. Largest improvements are found when the diffusion and the dissipation are reduced while only a minor change is found when the horizontal resolution is increased. INALT20r.L120.HighDiff is associated with a weak time-mean AUC of less than 4 cm/s that is only found in the first 150 km from the coast (Figure 6.8c). With reduced diffusion and dissipation, near the bottom several AUC cores are found. Their extent from the coast of 200 km is in agreement with the observations. The simulated multicore structure does not have to be unrealistic, owing to the interpolation of the observations. The main core at the slope is associated with time-mean velocities of more than 5 cm/s, which are

below the observed 9 cm/s. The reduction of the diffusion and the dissipation is nevertheless associated with about a doubling of the AUC transport averaged over the observed period as well as its standard deviation from 3.6 ± 2.6 Sv to 6.6 ± 5.5 Sv which is close to the observed 7.0 ± 5.1 Sv (Table 6.1). The AUC transport is here defined as the "northeastward" cross-section transport below 2,000-m depth integrated vertically and from the coast to a distance of 200 km. In INALT60, both the horizontal extent and the maximum time-mean velocities of more than 8 cm/s (Figure 6.8i), as well as an AUC transport of 6.5 ± 5.2 Sv (Table 6.1) are very close to the observations.

6.7 Submesoscale Impacts on the Mesoscale Dynamics

6.7.1 SSH Spectra

In this section, we validate the time-mean horizontal-wavenumber spectra of SSH from the model experiments against those from Native GDR-D Jason-2 L3 along-track SSH anomalies from 2012–2015. The Ssalto/Duacs altimeter products were produced and distributed by CMEMS (`http://www.marine.copernicus.eu`). The SSH anomalies are available every 10 days with a resolution of about 5.1 km and are referenced to the mean SSH product CLS01 (Hernandez and Schaeffer, 2001). We excluded the data from 2016 and later from the analysis as the satellite orbit has been changed in October 2016. The location of the observed tracks is shown in Figure 6.10. To investigate the regional distribution of the spectral slope, we divide the Agulhas region into 4×13 subregions oriented at the crossings of the measurement tracks (Figure 6.10). The geographical coordinates of the data from observations and models are transformed into Cartesian coordinates, and the data are interpolated onto a regular 1-km spacing. One spectrum is computed for every measured track within each subregion. In the rare case of data gaps, for each segment longer 200 km a spectrum is computed and afterward all segment spectra are averaged. The time-mean spectrum for each subregion is derived by averaging the time-mean spectra of both diagonals. Averaging over all subregions gives one time-mean SSH anomaly spectrum for the Agulhas region (Figure 6.9a).

The spectrum from JASON-2 for the Agulhas region decreases toward smaller scales exponentially with a slope close to k^{-5}, where k is the wavenumber (Figure 6.9a). At scales of 90 km, the spectrum turns to almost white noise due to the instrument noise. Xu and Fu (2012) suggested to identify the instrument noise as the mean PSD of the 25- to 35-km wavelength band (12.5- to 17.5-km scale band) and to remove that from the whole spectrum. However, at the small scale end below 13 km, a drop in the spectrum is found—probably due to the interpolation technique—that would lead to a too low estimate of the mean noise. Thus, we remove the mean 15.0- to 37.5-km noise from the entire spectrum, where it is associated with almost white noise. The corrected spectrum drops with $\approx k^{-5}$ down to scales of 75 km and changes to a k^{-4} slope below. For the models, we interpolate the 5-day snapshots of SSH anomaly of the period 2012–2015 onto the mean track of the satellite data and proceed similarly as with the measured data. The SSH anomalies are referenced

to the 2012–2015 mean SSH. The mean track is identified as the linear regression through all measured data points on the respective diagonal in each subregion.

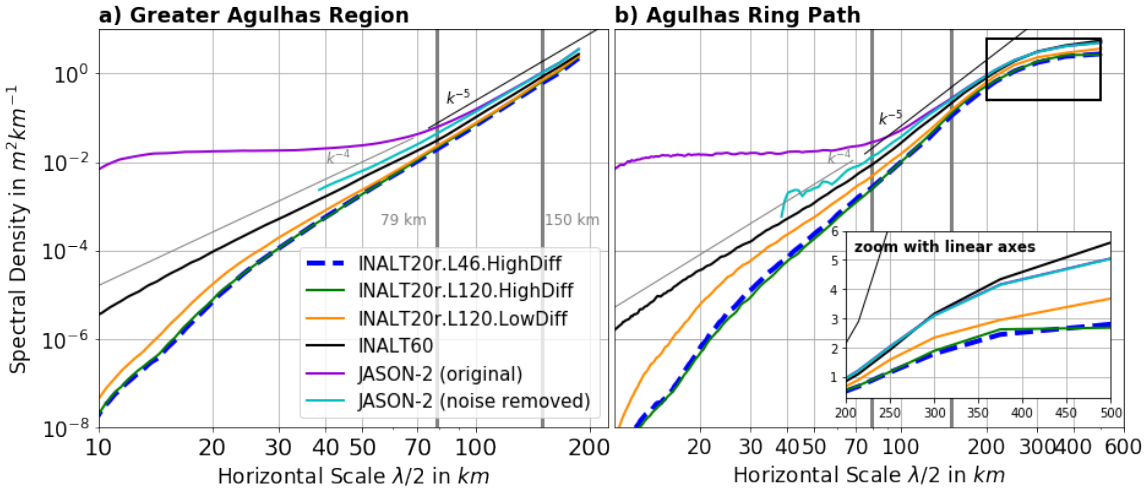

Fig. 6.9: *The 2012–2015 time-mean horizontal-wavenumber spectra derived from JASON-2 along-track sea surface height anomalies and the same tracks picked from the model output. The tracks are shown as gray lines in Figure 6.10. For the greater Agulhas region (a), the spectra were first averaged in time and for each subregion (rectangulars in Figure 6.10) before a spatial average over all subregions. The spectra for the model experiments have been computed from snapshots each fifth day and for the observations from the measured tracks each tenth day. For the observations, the original spectrum is shown, as well as the one where the mean noise of the 15.0- to 37.5-km scale band is removed from the whole spectrum. Thin straight lines show k^{-5} and k^{-4} slopes, where k is the wavenumber. Dark gray lines mark the 79- to 150-km scale band for the computation of the spectral slope for Figure 6.10. The horizontal scale is identified as half the wavelength λ. For the Agulhas ring path (b), all spectra for the measurement tracks that range over more than one subregion within the black box in Figure 6.10 are averaged. The y axis is the same as in (a). A zoom with linearly scaled axes is shown in the subwindow for the marked box.*

The SSH spectra of the high-diffusion/dissipation experiments show too less PSD on all scales and decrease with an almost constant slope down to scales of about 30 km (Figure reffig:paper1:sshspec1). At smaller scales, they drop due to the reduction of tracer variance (kinetic energy) by the model diffusion (dissipation). INALT20r.L120.LowDiff is associated with more PSD in the small-scale range consistent with more simulated small-scale features as demonstrated in sections 6.4 and 6.5. The spectrum from INALT60 shows very similar slopes compared to the observations above scales of 75 km (k^{-5}) as well as below (k^{-4}). The PSD is at all scales much higher than in INALT20r.L120.LowDiff and very close to the observations. The remaining small lack of PSD might be related to the absence of tidal induced motions in INALT60.

The map of the mean spectral slope of the 79- to 150-km scale band reveals for the observations that regions of large mesoscale activity such as the Agulhas ring path, the retroflection, and AC/ARC and adjacent regions are associated with steeper slopes close to k^{-5}. Open ocean regions such as southwest of the Agulhas ring path and north and south of the ARC east of $36°E$ show shallower slopes close to k^{-4} (Figure 6.10e). Away from the Agulhas ring path, all model configurations are overall in good agreement with the observations with respect to the spectral slope. For the open ocean k^{-4} slopes are found and for the retroflection, the ARC and adjacent regions k^{-5} slopes (Figure 6.10). In the Agulhas ring path, too steep slopes of around k^{-6} are found for the high-diffusion/dissipation configurations (Figure 6.10a and 6.10b). Reducing the diffusion and the dissipation leads to shallower spectral slopes in the Agulhas ring path that are closer to the observations but for some subregions still steeper than k^{-6}. In INALT60, the spectral slopes in the Agulhas ring path are found to be close to k^{-5} and compare very well with those from the observations.

To identify the impact of the submesoscale dynamics on the large mesoscales in the Agulhas ring path and to validate their simulation, we extend the length of the data lines and perform the computation of the spectra for a large region in the Agulhas ring path ($26.88 - 41.17°S$, $1.42 - 12.74°E$, Figure 6.10). Within this region, a spectrum is computed for each measured track that ranges over more than one of the small subregions identified before. The spectral analysis is performed analogous to the method described above. Subsequently, all spectra are averaged to one time-mean SSH spectrum for the Agulhas ring path and presented in Figure 6.9b. For scales smaller than 200 km, the results are similar to those of the whole Agulhas region. The shallowing of the spectral slope, when the diffusion and the dissipation of the model are reduced, is more pronounced in the Agulhas ring path consistent with the maps of the spectral slope. For scales larger than 200 km, the PSD for the high-diffusion/dissipation experiments is found to be almost only half of the observed. This indicates a too weak mesoscale eddy field. Reducing the diffusion and the dissipation of the model leads to a small improvement in PSD. If also the horizontal resolution is increased, the PSD shows very good agreement with the observations.

6.7.2 Agulhas Eddy Detection

In the Agulhas ring path, an increase of the mesoscale SSH spectral density, as shown in the previous section, can mainly be attributed to either an increase in the number of eddies or an increase in the strength of the eddies, or both. To specify this, the

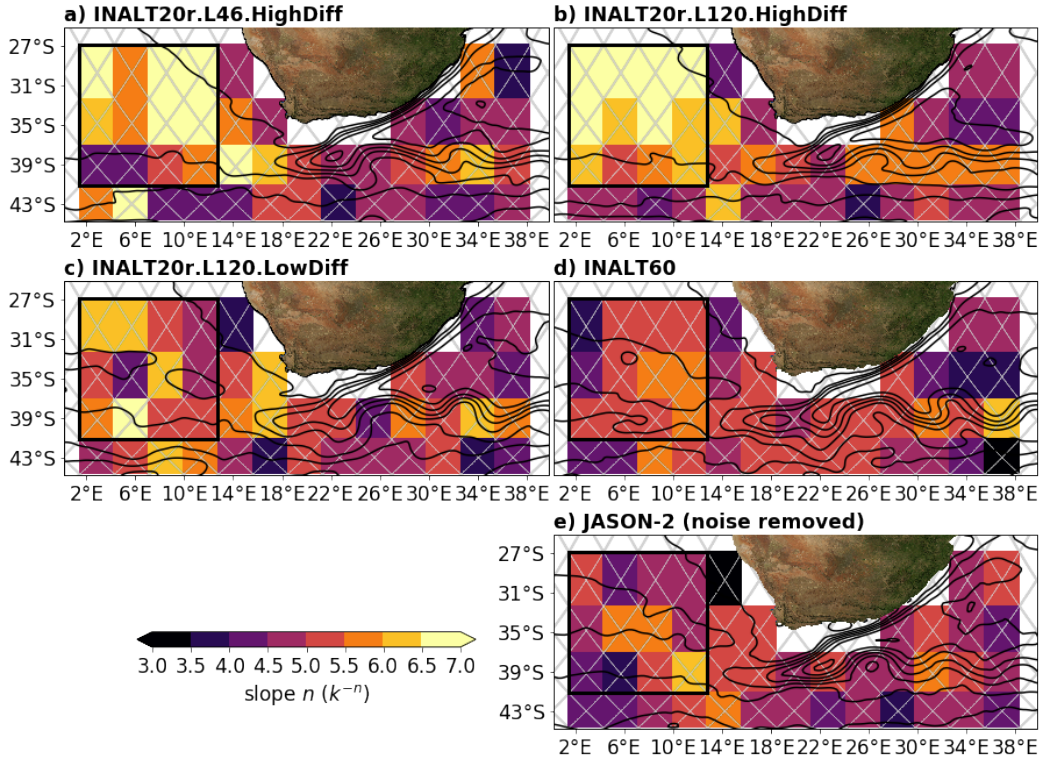

Fig. 6.10: *The mean spectral slope of the time-mean (2012–2015) spectrum for each subregion in the 79- to 150-km scale band for INALT20r.L46.HighDiff (a), INALT20r.L120.HighDiff (b), INALT20r.L120.LowDiff (c), INALT60 (d), and JASON-2 with removed noise (e). The slope n is shown with respect to k^n, where k is the wavenumber. Gray lines show the JASON-2 measurement tracks, and black contours the time-mean sea surface height reduced by the domain average with a contour interval of 0.2 m. The black box marks the region of the Agulhas ring path used for the computation of the sea surface height spectra (Figure 6.9b) and for the eddy detection (Figure 6.11).*

SSH-based automated eddy detection algorithm presented by Chelton et al. (2011) is applied to the daily CMEMS gridded L4 SSH product as well as to the daily model outputs interpolated onto the CMEMS grid for the same region in the Agulhas ring path (black box in Figure 6.10 and the period 2012–2017). The data sets are temporally detrended and the domain average is removed for each time step before the eddy detection. Anticyclones (cyclones) are detected as connected sets of minimum 8 to maximum 1,000 pixels with SSH anomalies above (below) a given threshold, a local maximum (minimum) with a maximum amplitude larger than 1 cm and a maximum distance of any pair of pixels of 700 km. The connected pixel set is thereby divided into interior and perimeter pixel, where the latter are associated with boundaries to the surrounding of the pixel set. The maximum amplitude A_{max} of an eddy is then computed as the SSH difference of the value of the local interior extrema and the mean value of the perimeter pixels. For each time step, the SSH fields are scanned

for connected pixel sets that fulfill the above-mentioned conditions for a threshold of 1 m (1 m) to 1 m (1 m) with an increment of 0.01 m for anticyclones (cyclones). If a connected region is identified to be an eddy, its interior pixels are removed from the further detection. The scale of an eddy is identified to be the diameter of a circle with the same area as the detected pixel set. A single eddy is detected at each daily mean model output time step as long as it remains in the investigated domain. In the subsequent analysis we do not investigate single eddies but analyze the eddy characteristics in a statistically average sense. We present histograms of the average number of eddies in dependence on their amplitude, scale, and direction of rotation for the Agulhas ring path region and the period 2012–2017. For a specific amplitude or scale range, the number of detected eddies with the respective properties is therefore summed up for all time steps and then divided by the total number of time steps.

The average eddy number does not increase substantially throughout the model experiments and is in good agreement with the observations. On average, about nine anticyclones as well as nine cyclones are detected in the domain for all experiments as well as for the observations. Only a small increase in average cyclone number from 8.4 to 9.2 is found when the diffusion and the dissipation of the model are reduced and a very small increase in anticyclone number from 8.7 to 9.1 when the horizontal resolution is increased. Both values are very close to those of the observations (9.3 and 9.2). Moreover, the distribution of the scale of all detected eddies is found to be very similar for all models and observations (Figure 6.11b and 6.11f).

Mesoscale eddies and in particular cyclones are found to strengthen when the diffusion and the dissipation are reduced and especially when the horizontal resolution is increased. Weak anticyclones (cyclones) with amplitudes between 1 and 7 cm occur on average more often in the INALT20r configurations (in sum ≈ 4.1 (≈ 5.5)) than in INALT60 (3.7 (3.8)) and the observations (3.3 (4.1)) (Figure 6.11a and 6.11d). The amount of medium amplitude anticyclones (cyclones) with amplitudes between 7 and 20 cm is too small in the high-diffusion/dissipation experiments (≈ 2.3 (≈ 2.6)), larger in INALT20r.L120.LowDiff (2.8 (3.6)), and similar in INALT60 (3.3 (4.5)) and the observations (3.7 (4.2)). The increase in medium amplitude eddy number is restricted to scales below about 300 km (not shown). Two strong amplitude anticylones with amplitudes larger than 20 cm are detected on average in all simulations and in the observations. The average distribution of their scale is very similar (Figure 6.11c). About one strong cyclone is detected on average in INATL60 and the observations with a similar scale distribution (Figure 6.11g). In contrast to the anticyclones, on almost all scales too less strong cyclones are detected on average

in INALT20r.L120.LowDiff (0.5) and in particular in the high-diffusion/dissipation experiments (≈ 0.3). Consistently, the maximum amplitude of all cyclones averaged over 10-km broad scale bands as a function of the scale shows the same results as we found for the SSH spectra (Figure 6.11e compared to Figure 6.9b, zoom).

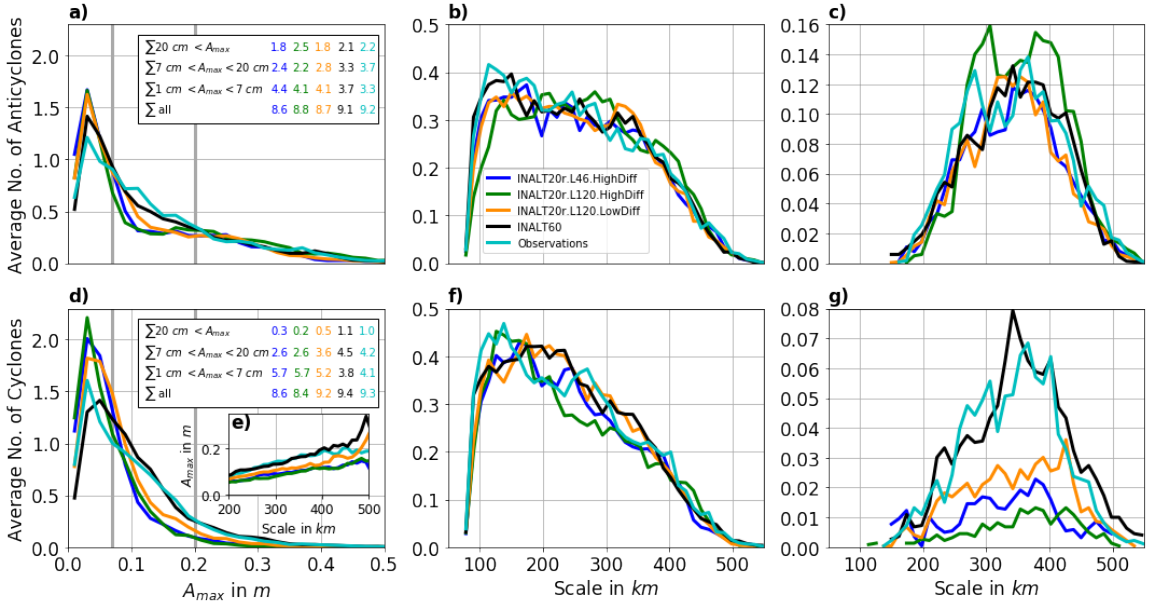

Fig. 6.11: *Histograms of the average number of anticyclones (a–c) and cyclones (d–f) in the Agulhas ring path region (black box in Figure 6.10) as a function of their maximum amplitude (a and d) and scale (b and f) for the period 2012–2017. The eddies were detected with the sea surface height (SSH)-based approach of Chelton et al. (2011) in a daily, $0.25°$ gridded, L4 SSH observational product from CMEMS and in the model outputs interpolated onto the observational grid. The histograms for the eddy scale are shown for all eddies (b and f) and for all eddies with $A_{max} > 20$ cm (c and g). The summed up average number of eddies for each range are shown in the tables with the same color as the respective graphs. For the cyclones additionally the average of the maximum amplitude of all cyclones within 10-km broad scale bands are shown as a function of the scale in (e) to compare with the SSH spectra shown in Figure 6.9b (zoom).*

6.8 Conclusion and Discussion

In this study, we compare a series of ocean model experiments to observations to show that the representation of mesoscale eddies in the Agulhas ring path improves with an increasing resolution of submesoscale flows. Commonly, ocean models are validated by comparing the time-mean and standard deviation of simulated SSH with gridded satellite altimeter products as well as vertical sections through important currents with respective measurements. Here, we extend the common validation of the mesoscale dynamics by comparing time-mean horizontal-wavenumber spectra of simulated SSH with those from JASON-2 along-track altimetry as well as the results of an SSH-based eddy detection algorithm applied to the model outputs as well as to a gridded SSH satellite product. The simulated small-scale mixed-layer dynamics are validated with SST horizontal-wavenumber spectra from the model experiments and MODIS swath measurements.

We start with the nonsubmesoscale-resolving reference configuration INALT20r.L46.HighDiff with $(1/20)^\circ$ horizontal resolution, 46 vertical levels, and relatively high model diffusion and model dissipation. The validation shows that, in the Agulhas ring path, the simulation is associated with too weak PSDs on all scales, too steep spectral slopes, and too weak mesoscale eddies. In particular, strong cyclones are not represented, while strong anticyclones are represented well. We hypothesize that the latter is due to a good representation of the Agulhas ring shedding in the simulation. Three parallel simulations are performed where we gradually increase the vertical resolution to 120 vertical levels (INALT20r.L120.HighDiff), decrease the diffusion and the dissipation of the model (INALT20r.L120.LowDiff), and increase the horizontal resolution to $(1/60)^\circ$ for the core Agulhas region (INALT60). An increase of only the vertical resolution does not lead to a substantial improvement in small-scale, mesoscale, and large-scale dynamics. An additional reduction of the diffusion and the dissipation of the model leads to an improvement of the AC variability as well as AUC variability and strength to a good agreement with the observations by Beal et al. (2015). In the Agulhas ring path, the reduced diffusion and dissipation lead to the simulation of some small-scale flows, larger PSD on all scales, shallower spectral slopes, and a better representation of cyclone strength and number. A small increase in cyclone number is found that might be attributable to the improved representation of the AC/AUC variability. Most of the mentioned results nevertheless show still a large gap to the observations. This gap is closed with the implementation of the secondary $(1/60)^\circ$ nest. In INALT60, much more and much stronger submesoscale flows occur all over the domain and the mesoscale

dynamics are well represented with respect to SSH variability, spectral slope, PSD, and eddy number and strength. It has to be clarified why substantial changes in SSH spectral slope are found only for the Agulhas ring path, while there is a good agreement with the observation throughout the model experiments away from the Agulhas ring path, consistent with similar temporal standard deviations of SSH. A limitation of the eddy detection method is the cutoff at the boundaries of the investigated region. The scale of detected eddies that continue outside the domain is underestimated. However, this affects models and observations equally so that it does not bias the comparison.

Comparing the time-mean SST horizontal-wavenumber spectra from the simulations and from MODIS satellite measurements is one of a few possible methods available today for a systematic validation of the mixed-layer dynamics and further for a justification of and guidance for the choice of advection schemes and explicit diffusion and dissipation. To our knowledge, this is the first study applying this approach. The 20- to 50-km mean spectral slope shows a similar spatial pattern for INALT60 and the observations with shallower slopes of about $k^{-2.1}$ in the Agulhas ring path and steeper slope of about $k^{-2.5}$ in the regions of the AC, the retroflection, the ARC, and the subgyre. Further, the PSD agrees very well for the Agulhas ring path and the subgyre region east of the AC. In the Agulhas ring path, the spectrum for INALT60 (INALT20r.L120.LowDiff) is in very good agreement with the observations down to 8 km (25 km). This justifies the use of upstream biased advection schemes without explicit diffusion and dissipation for this region. Below 8 km (25 km), the spectra drop due to the effect of the model diffusion and dissipation. The respective wavelengths are close to 10 times the grid spacing in accordance with the effective resolution identified by Soufflet et al. (2016). In regions of strong large-scale temperature gradients as for the region of the retroflection and along the subtropical front, INALT60 is associated with too large PSD for all comparable scales. The associated lack of SST damping across all scales might be attributable to nonrepresented atmosphere-ocean interaction in ocean-only models that are most important in regions of strong SST gradients. Comparing an example wintertime snapshot with large cloud-free areas with the respective INALT60 snapshot shows too strong temperature gradients in the model. This gives some evidence that the offset is not an artifact of the validation method.

A major limitation of the validation via infrared derived SST is the nonavailability of satellite data for cloudy regions. Largest offsets are found in regions with large cloud cover where the lowest amount of data is available. Systematic changes of the absolute SST for cloudy and cloud-free regions do not affect the spectral analysis.

However, a dependence of submesoscale turbulence on clouds as well as a bias in the orientation of the cloud-free lines to either zonal or meridional direction can lead to biases in the validation. A further bias can arise from uncertainties in the estimation of the bulk SST from the skin SST during the postprocessing of the MODIS products (Donlon et al., 2002; Kilpatrick et al., 2015; Schluessel et al., 1990) used here. A part of the uncertainties might be clarified by a spectral comparison to 4-km $\times$ 8-km resolution satellite-based radar-derived surface velocities (Rouault et al., 2010) or new high-resolution satellite altimeter products from the SWOT mission that will start in 2020 and are predicted to cover scales down to 10 km in the Agulhas region (Dufau et al., 2016).

In contrast to SSH, the model SST spectra show similar PSD at the larger scales (> 100 km). We attribute this to the fact that the SST variability is to some extent prescribed at the larger scales by the atmospheric forcing which is associated with a coarse horizontal resolution of $0.5°$ (≈ 50 km). The results are, however, not contrary to the ones for SSH as SST amplitudes are no measure of the geostrophic flow. The Agulhas region is associated with very strong surface heat fluxes that are in the retroflection directed toward the atmosphere throughout the year (Walker and Mey, 1988; Yu and Weller, 2007). These heat fluxes lead to a fast reduction in SST gradients, for example of recently shed Agulhas rings (Olson et al., 1992) compared to their surrounding.

Simulated mesoscale dynamics are validated and compared with time-mean SSH anomaly horizontal-wavenumber spectra against JASON-2 along-track measurements. The spectral SSH slopes can further be compared to theoretical predictions. The balanced component of the flow can be decomposed into components due to interior potential vorticity anomalies and surface density anomalies (Lapeyre and Klein, 2006). The two extrema, which one of both components is neglectable, predict spectral slopes of k^{-5} for interior-quasigeostrophic (IQG) dynamics (Charney, 1971) and $k^{-11/3}$ for surface-quasigeostrophic (SQG) dynamics (Blumen, 1978; Held et al., 1995), where k is the wavenumber. In SQG theory, advection by the ageostrophic flow is neglected. If included, it leads to a theoretical k^{-4} slope (Boyd, 1992; Xu and Fu, 2011). Semigeostrophic theory predicts a $k^{-8/3}$ slope for the kinetic energy spectrum (Andrews and Hoskins, 1978) that is close to the IQG prediction of k^{-3}. For the greater Agulhas region, the SSH spectral slope has been derived from satellite altimetry to be close to the SQG predicted value of $k^{-3.7}$ for the 100- to 300-km wavelength band (scales of 50-150 km) by Le Traon et al. (2008) and for the 70- to 250-km wavelength band (scales of 35-125 km) by Xu and Fu (2011). In the core Agulhas region (the region with $(1/60)°$ resolution in INALT60), Xu and Fu (2011)

found steeper slopes of k^{-4} consistent with SQG theory including ageostrophic advection. These estimates, however, did not remove the measurement noise from the spectra before the computation of the spectral slope. Xu and Fu (2012) showed that the spectral slope estimates for the Agulhas region are associated with values of k^{-4} - $k^{-4.5}$, when the mean white noise of the 25- to 35-km wavelength band is subtracted from the whole spectra before that. Regions of strong mesoscale activity are found to be associated with steeper spectral slopes than quieter regions (Chassignet and Xu, 2017; Dufau et al., 2016; Richman et al., 2012; Sasaki and Klein, 2012; Xu and Fu, 2012). In this study, we find slopes from JASON-2 along-track observations that are very close to SQG prediction including ageostrophic advection in regions of low mesoscale activity (southwest of the Agulhas ring path as well as north and south of the ARC east of $36°E$) and close to the IQG and semigeostrophic prediction in more energetic regions (everywhere else in the Agulhas region) for scales that are larger than about 75 km. A scale of 75 km corresponds to a wavelength of 150 km, which is close to the wavelength $2\pi R_d$ of the Rossby radius of deformation R_d that is about 25 km in the Agulhas region (Chelton et al., 1998). For smaller scales, just above the noise floor, shallower slopes are found that follow the SQG including ageostrophic advection prediction. Unbalanced motions might also contribute to the shallowing of the slope (Callies and Ferrari, 2013; Qiu et al., 2018). However, a separation of the SSH spectrum into a balanced and an unbalanced contribution, as applied by Qiu et al. (2018) to a global $(1/48)°$ horizontal resolution model, showed that balanced motions in the core Agulhas region dominate the SSH spectrum down to scales of 25 km or even smaller. Further research is needed to identify, which theoretical model is appropriate to describe the underlying dynamics. The good agreement of the spectral slope from the observations and INALT60 gives some confidence that the shallowing of the spectral slope at scales of about 75 km we found for the observations is not an artifact of the instrument noise. Our results thus suggest that the spectral slope changes within the scale band that Xu and Fu (2012) used for the computation of the slope. This can explain why they estimated shallower slopes than we find here. The steep slopes of k^{-5} are only identified when they are averaged over a scale band that is located above the wavelength of the Rossby radius.

Idealized gyre simulations with integration periods of 100 years by Lévy et al. (2010) showed that the simulated gyre circulation strengthened when the horizontal resolution is increased from $(1/9)°$ to $(1/54)°$. Assuming that their results are adaptable to the Indo-Atlantic supergyre, they indicate that there might be a submesoscale impact on the strength of the AC, and thus on the Agulhas ring shedding, that is not captured in our simulations. A much longer simulation, resolving the submesoscale dynamics for the full Indo-Atlantic supergyre, would be needed to address this.

In conclusion, the increasing resolution of submesoscale flows is found to be accompanied by a better representation of the mesoscale eddies in the simulated Agulhas ring path. The eddies are found to strengthen, the more submesoscale flows are resolved by the model. The model solution converges to the observations in our $(1/60)^\circ$ ocean simulation INALT60. Our results indicate that submesoscale dynamics drive a strong inverse kinetic energy cascade in the Agulhas ring path. This will be investigated in a follow-on study.

6.9 Acknowledgments

This study project received funding from the German Federal Ministry of Education and Research (BMBF) of the SPACES projects AGULHAS (Grant 03F0750A) and CASISAC (Grant 03F0796A). The Ssalto/Duacs altimeter products used for this study were produced and distributed by the Copernicus Marine and Environment Monitoring Service CMEMS (http://www.marine.copernicus.eu). We acknowledge the Ocean Biology Processing Group of the Ocean Ecology Laboratory of the NASA Goddard Space Flight Center for providing the MODIS sea surface temperature data. The authors thank Stewart et al. (2017) for sharing the data for the requirements on the vertical axis we used for Figure 6.4 and Beal et al. (2015) for the data of the Agulhas Current Timeseries section we used for Figure 6.8o and the last row of Table 6.1. All model simulations have been performed at the North-German Supercomputing Alliance (HLRN). The model output files used for this study exceed the capacities of a repository but can be made available upon request. We thank Shane Keating and two anonymous reviewers for the critical reading and their valuable comments.

6.10 Author Contributions

René Schubert and Prof. Dr. Arne Biastoch discussed and identified the overall research questions. René Schubert developed the specific strategy, executed the numerical model experiments, decided on the model output analysis techniques, performed all analysis, wrote the text of the manuscript and created all figures. Prof. Dr. Arne Biastoch, Prof. Dr. Burkard Baschek and Dr. Franziska U. Schwarzkopf contributed ideas to the analysis and reviewed the manuscript. Prof. Dr. Arne Biastoch further contributed ideas to the structure of the manuscript and helped to develop the analysis strategy. Dr. Franziska Schwarzkopf helped to execute the numerical model experiments.

7

Study II: Strengthening of Agulhas Mesoscales by the Submesoscale Inverse Kinetic Energy Cascade

> *Big whirls have little whirls that feed on their velocity, and little whirls have lesser whirls and so on to viscosity.*
>
> **— Lewis F. Richardson**

In this chapter, it is explicitely shown that submesoscale flows strengthen the mesoscales through an inverse kinetic energy cascade. Besides the classical spectral approach for the computation of the kinetic energy flux between different scales, for the first time (as far as I know) a coarse-graining approach is applied to a submesoscale-permitting ocean-general circulation model output. The associated advantage of an easy mapping of the cascade is used to demonstrate that the submesoscale inverse cascade is partially attributable to the mesoscale absorbtion of mixed-layer instability driven submesoscale features. As this process needs time, the strengthening is found to be delayed in time by a few months and contributes to the seasonal maximum of mesoscale kinetic energy in early summer. This chapter has been submitted for publication on December 12^{th} 2019 to the Journal of Physical Oceanography (JPO) and is currently under review:

Schubert, R., Gula, J., Greatbatch, R. J., Baschek, B., & Biastoch, A. (2020). Strengthening of Agulhas Mesoscales by the Submesoscale Inverse Kinetic Energy Cascade. Journal of Physical Oceanography.

7.1 Abstract

In this study, we investigate the kinetic energy cascade in a 1.5 km-resolution submesoscale-permitting simulation of the Agulhas region with a spectral and a coarse-graining approach. Largest submesoscale near-surface fluxes for both up- and downscale directions occur in winter-time in regions of strong mesoscale activity. In the Agulhas ring path, a winter-mean surface upscale cascade is found for scales larger than 13 km. Other parts of the Agulhas region show a change from up- to downscale fluxes at scales of 25 to 50 km. At smaller scales, downscale fluxes occur mainly in frontogenetic regions in the upper 30 m of the water column. In winter, in the ring path, largest sources of the upscale flux occur at scales around 15 km which is a typical scale of features that develop as a result of the mixed-layer baroclinic instability. A case study indicates that the developing mixed-layer eddies transfer their kinetic energy upscale and are absorbed by mesoscale eddies. Consistently, the maximum of the upscale flux shifts to larger scales in spring. Depending on the region, the kinetic energy reaches the mesoscales in spring or early summer aligned with the maximum of mesoscale kinetic energy. Our results thus indicate that submesoscale dynamics are important for the strength of mesoscale eddies and their seasonal cycle. In a non-submesoscale resolving experiment, the open-ocean upscale cascade in the Agulhas ring path is almost absent. This contributes to a reduction of surface kinetic energy at mesoscales larger than 100 km to about 80 % when submesoscale dynamics are not resolved by the model.

7.2 Introduction

The ocean moves on temporal and spatial scales ranging from the global thermohaline overturning circulation to the microscale turbulent motion of single fluid particles. The amount and scale-distribution of the associated kinetic energy is mainly controlled by the balance between atmospheric forcing and oceanic dissipation and the cross-scale energy fluxes (Ferrari and Wunsch, 2009). Atmospheric wind and buoyancy forcings mainly act on the large-scales. A part of this energy is dissipated to heat at molecular scales at the sea surface or transferred back to the atmosphere through intense atmosphere-ocean interactions (e.g. Ma et al., 2016). The rest of the energy input is dissipated in the ocean interior or at the coastlines and the sea floor. Key questions are how the energy is fluxed from the large scales to the dissipative scale (the "forward cascade") and how the scale distribution of kinetic energy and its temporal evolution are shaped. Large-scale ocean currents like the Gulf Stream, the Kuroshio or the Agulhas Current undergo mixed baroclinic-barotropic instabilities associated with the shedding of mesoscale eddies that act as a source of energy at the mesoscale (e.g. Cronin, 1996; Storch et al., 2012; Schubert et al., 2018). Satellite altimetry revealed that mesoscale dynamics subsequently transport kinetic energy towards larger scales (Scott and Wang, 2005). In combination with the large-scale energy sources of the ocean, this "inverse cascade" results in the larger mesoscale eddy field being the most energetic scale band of the ocean (Ferrari and Wunsch, 2009). A major question is, at which scales this inverse cascade changes to a forward cascade at its small-scale end. From altimetric data interpolated onto a regular grid by AVISO (Archiving, Validation and Interpretation of Satellite Oceanographic data, www.aviso.altimetry.fr), Scott and Wang (2005) found for the South Pacifc, and Scott and Arbic (2007) for the Kurushio extension, that the upscale kinetic energy flux changes to a downscale cascade around the wavelength of the Rossby radius of deformation. It is given by $\lambda_r = 2\pi R_r$, where R_r is the Rossby radius of deformation, and is about 170 km in the midlatitudes (Chelton et al., 1998). Tulloch et al. (2011) found similar results from satellite altimetry as well as from a coarse-resolution aqua-planet model. However, in ocean models with submesoscale permitting resolution ($\approx 1/30° \approx 4$ km at midlatitudes) the change from inverse to forward cascade occurred on smaller wavelengths of about 40 km (Arbic et al., 2013; Qiu et al., 2014). These studies showed that filtering the model results in space (Qiu et al., 2014), and both in space and time in a similar way as done in the AVISO postprocessing (Arbic et al., 2013), leads to spectral fluxes that are closer to those estimated from AVISO. This indicates that the scale fluxes from the altimetric measurements represent those of filtered mesoscale

dynamics, while the submesoscale kinetic energy cascade is not captured by the altimetric measurements. Consistent with the seasonal cycle of submesoscale activity (Callies et al., 2015), Qiu et al. (2014) found in their simulation a strong winter-time inverse cascade that extends down to scales of 35 km, while the summer-time inverse cascade is much weaker and changes to a forward cascade already at wavelengths of 100 km. The winter-time value is close to ≈ 30 km, as found by Klein et al. (2008) and Capet et al. (2008c) for submesoscale-permitting simulations with resolutions of 2 km and 1.5 km, although the investigated oceanic regimes were different. Capet et al. (2008c) found some evidence for convergence, as a similar wavelength was found for a 750 m horizontal resolution sensitivity experiment. In contrast to the ≈ 4 km horizontal-resolution experiments, a stronger forward cascade was found in the runs with a resolution of 2 km and higher. Capet et al. (2008c) showed that this forward cascade can be attributed to the ageostrophic (horizontal divergent) part of the flow and hypothesized that frontogenesis and submesoscale frontal instabilities are the responsible processes at work. Supporting these results, D'Asaro et al. (2011) observed enhanced dissipation of kinetic energy at an oceanic front in the Kuroshio, and attributed it to symmetric instability. Molemaker and McWilliams (2010) and Barkan et al. (2015) also found a vigorous forward cascade associated with frontal instabilities in idealized model experiments.

The representation of the mesoscale eddy field in ocean models depends on which part of the kinetic energy cascade is represented by either the resolution or the parameterization of the involved processes. Kjellsson and Zanna (2017) showed that the upscale kinetic energy flux as well as the spectral kinetic energy density increase for all horizontal scales when the horizontal resolution of their global ocean model is increased from 1° to $1/4^\circ$ to $1/12^\circ$. Furthermore, Schubert et al. (2019) found an increase in power spectral density of sea-surface height on all scales for the Agulhas ring path, if submesoscale currents are better resolved by a nested ocean model. They first reduced the diffusion and dissipation of a $1/20^\circ$ (≈ 4.5 km) model and subsequently increased the horizontal resolution to $1/60^\circ$ (≈ 1.5 km). A comparison to satellite altimetry data showed that the mesoscale model solution converged to observations at comparable scales in the $1/60^\circ$ horizontal resolution simulation, referred to as INALT60. This suggests that the inverse kinetic energy cascade is better resolved in INALT60.

The Agulhas region is associated with strong watermass exchanges between the Atlantic, Indian and Southern oceans. This exchange is of importance for the South Atlantic stratification (De Ruijter et al., 1999), the tropical Atlantic Ocean (Lübbecke et al., 2015) and the Atlantic Meridional Overturning Circulation (Weijer et al.,

2002; Biastoch et al., 2008b). The main feature of the Agulhas region is the Agulhas Current (AC) flowing poleward along the continental slope with a transport of about 77 Sv (1 Sv $= 10^6$ $\mathrm{m^3 s^{-1}}$) (Beal et al., 2015). South of Africa, the AC separates from the slope, retroflects to the east and continues as the Agulhas Return Current (ARC, Lutjeharms and Ansorge, 2001). In the retroflection, anticyclonic Agulhas rings are shed and propagate north-westward into the Atlantic. Although a part of their water masses are mixed with their surroundings (Boebel et al., 2003), in particular by submesoscale currents (Capuano et al., 2018a; Sinha et al., 2019), the Agulhas rings provide the largest portion of the "Agulhas leakage", which is the inflow of warm and salty Indian ocean waters into the Atlantic (Lutjeharms, 2007). Besides the anticyclonic Agulhas rings, south-westward propagating Agulhas cyclones are shed in the retroflection region (Lutjeharms et al., 2003a). Further westward propagating eddies develop at the front of the Benguela upwelling system west of Africa (Rubio et al., 2009). All these eddies strongly interact with the Agulhas rings in the Cape Basin (Boebel et al., 2003). Another hotspot of mesoscale eddy activity in the Agulhas region is the region east of the AC and north of the ARC, which we call the subgyre region. There, mesoscale eddies detach from the ARC and interact with those arriving from the South Indian Ocean as well as with features that detach from the AC (Lutjeharms, 2007). Horizontal wavenumber spectra of sea-surface temperature (SST), derived from MODIS satellite measurements and INALT60 show, with good agreement, that the spectral slopes are steeper in the subgyre region compared to the Agulhas ring path (Schubert et al., 2019). This indicates a systematic difference in the submesoscale dynamics for both regions.

In the present study, we build on Schubert et al. (2019) and investigate for the first time the submesoscale kinetic energy cascade in the Agulhas region on the basis of the submesoscale-permitting simulation INALT60 and a parallel non-submesoscale resolving $1/20^\circ$ simulation. A short overview of both experiments is presented in section 7.3. The simulated small-scale dynamics and the distribution of kinetic energy are investigated in section 7.4 with a focus on the comparison of the ring path and the subgyre region. The near-surface scale kinetic energy flux[10] is computed from both experiments with a classic spectral approach and a coarse-graining approach. Both approaches are described in section 7.5 and their results compared in section 7.6. Moreover, in section 7.6, the scale kinetic energy flux is presented as a function of time, region and depth. We identify the scales at which the flux changes its sign and at which sources and sinks occur. The main advantage of the coarse-graining

[10]The rate of transfer of kinetic energy through a specific horizontal scale from currents that are associated with smaller horizontal scales to currents that are associated with larger horizontal scales.

approach is an easy mapping of the scale kinetic energy flux. Although our study focusses on the Agulhas region, we contribute to a general understanding of the impact of submesoscale dynamics. In section 7.7, we explicitly show that downscale fluxes are mainly confined to frontogenetic regions in the model. Moreover, in section 7.8, we present indications that the submesoscale inverse cascade in eddy rich regions can be partially attributed to the mesoscale absorption of mixed-layer eddies. A discussion and a conclusion are presented in section 7.9.

7.3 The Model Experiments

In this study, we mainly analyze the output of the submesoscale-permitting numerical-model simulation "INALT60". Its configuration has been introduced by Schwarzkopf et al. (2019) and was further developed by Schubert et al. (2019). The model grid consists of a global host grid with a $1/4°$ horizontal resolution and 120-vertical-level, a first horizontal grid refinement ('nest') down to $1/20°$ (≈ 4.5 km) for the greater Agulhas region and a secondary nest down to $1/60°$ (≈ 1.5 km) for the core Agulhas region (Fig. 7.1).

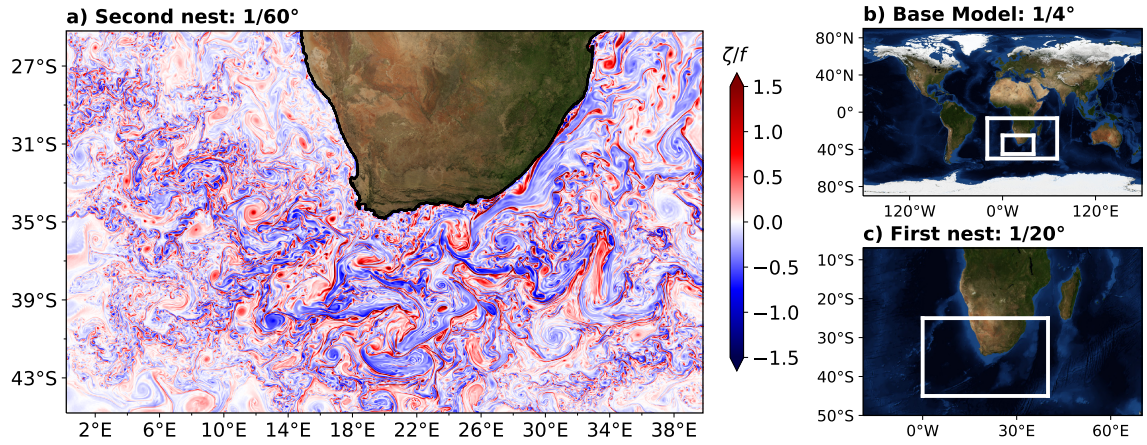

Fig. 7.1: *INALT60: A $1/4°$ horizontal resolution base model (b) with a first $1/20°$ nest (c) and a second $1/60°$ nest (a). In a) a snapshot of the simulated surface relative vorticity normalized by the planetary vorticity on model day Sep 9 2012 is shown. Land and bathymetry backgrounds are taken throughout the paper from Stöckli et al. (2005). White boxes in b) and c) show the location of the nests.*

The primitive equations are solved on an Arakawa C-grid (Arakawa and Lamb, 1977) with NEMOv3.6 (Nucleus for European Modelling of the Ocean, Madec et al., 2014). The nesting is done with an Adaptive Grid Refinement in FORTRAN (AGRIF, Debreu et al., 2008) allowing for a two-way exchange of the model solution between the host and the nest grids. For the host grid and the first nest, explicit dissipation with a bi-Laplacian operator and a constant viscosity is used. The viscosity is quadratically scaled down from the host-grid value of -1.5×10^{11} $\mathrm{m^4 s^{-1}}$ to -6×10^{9} $\mathrm{m^4 s^{-1}}$ for the first nest. For explicit tracer diffusion, a Laplacian operator with constant diffusivity is used in the host grid and the first nest. The diffusivity is linearly scaled down from the host-grid value of 300 $\mathrm{m^2 s^{-1}}$ to 60 $\mathrm{m^2 s^{-1}}$ for the first nest. For the discretization of the vorticity term, we use the vector invariant form with a Hollingsworth-corrected energy- and enstrophy-conserving scheme (Arakawa and Hsu, 1990; Hollingsworth et al., 1983; Bell et al., 2017; Ducousso et al., 2017). For tracer advection, we apply the total variance dissipation scheme (Zalesak, 1979).

In the second nest, no explicit diffusion/dissipation are used in combination with third-order upstream biased advection schemes (Webb et al., 1998; Farrow and Stevens, 1995; Madec et al., 2014) for both tracer and momentum. For the $1/60°$ domain, the model output is written as daily means for the whole water column and as 4h means for the upper 250 m. Moreover, for the upper 250 m, a model snapshot is written every fifth day at noon (UTC).

The results from INALT60 are compared to a parallel experiment without the secondary nest. This experiment resolves almost no submesoscale flows. Schubert et al. (2019) describe also this experiment in detail and refer to it as INALT20r.L120.HighDiff. The acronym stands for $1/20°$ horizontal resolution, 120 vertical levels and relatively high diffusion and dissipation settings. Here, we call it INALT20r for simplicity. The "r" emphasizes that the configuration is associated with a reduced nested domain compared to INALT20 (see Schwarzkopf et al. (2019) for details). Both experiments are integrated from 2010 to 2017. They are initialized from the same 30-year spinup of a similar INALT20r configuration that used only 46 vertical levels and CORE2 forcing (Large and Yeager, 2009; Griffies et al., 2009), while both experiments analyzed here use 120 vertical levels and JRA55-do forcing (v1.3, Tsujino et al., 2018). For more details on the simulations and configurations, we refer to Schubert et al. (2019) and Schwarzkopf et al. (2019).

7.4 Small-Scale Flows and Kinetic Energy Spectra in the Ring Path and the Subgyre

Regional differences in submesoscale dynamics are indicated by differences of the submesoscale slope of the horizontal-wavenumber spectrum derived from SST and kinetic energy. At 20 - 50 km, the spectral slope of the time-mean horizontal-wavenumber SST spectrum computed from INALT60 is relatively steeper in the region of the AC, ARC and the subgyre, compared to the Agulhas ring path (see Figures 6b and 6c in Schubert et al., 2019). Schubert et al. (2019) showed that this pattern is in good agreement with the one derived from MODIS satellite SST observations. Here, we compare the results to those of the kinetic energy spectrum.

Before the Fourier transformation of a horizontal field $F(x, y)$, where x and y are Cartesian coordinates in approximately zonal and meridional directions, the mean of F is subtracted and F is detrended in both horizontal directions. Here, we investigate square-shaped domains with N datapoints within the side length. As the domain is not periodic, nor infinitely large, F is multiplied by a 2D Hanning window and the associated amplitude correction factor of 1.5. The Fourier transform of F is defined as

$$\hat{F}(k,l) = \frac{1}{(2\pi)^2} \int_{-\infty}^{\infty} \int_{-\infty}^{\infty} F(x,y) e^{-i(kx+ly)} dx\, dy,$$

where k and l are the zonal and meridional wavenumber components. The cumulative power spectral density of horizontal velocities is derived as

$$E(K) = \frac{1}{N^4} \int_0^K \frac{1}{2} (\hat{u}^* \hat{u} + \hat{v}^* \hat{v}) dK,$$

where $K = \sqrt{k^2 + l^2}$ is the isotropic wavenumber. The complex conjugate is denoted by * and u and v are the quasi-zonal and quasi-meridional velocity components. The Fourier transforms $\hat{u}$ and $\hat{v}$ are normalized by the area N^2 before the computation of the power spectral density. The velocity components are quasi-zonal and quasi-meridional, as the model output on a geographical grid needs to be interpolated onto a regular Cartesian grid to apply the Fourier analysis. The power spectral density of horizontal velocities, in the following referred to as the kinetic energy spectrum, is then given by $2\pi \frac{dE}{dK}$. Similar to the time-mean SST spectrum in Schubert et al. (2019), the kinetic energy spectrum is computed first for each model snapshot every fifth day and subsequently averaged over all snapshots.

The 20 - 50 km spectral slope of the time-mean kinetic energy spectrum computed from INALT60 for 350 km $\times$ 350 km regions every 100 km in both horizontal directions (Fig. 7.2a) shows a similar pattern as the one for the SST (Fig. 6b and 6c in Schubert et al. (2019)). For the full 2012 - 2017 period, the subgyre, as well as the AC, ARC and the retroflection, are associated with slopes steeper than $K^{-2.5}$, while the Agulhas ring path and the rest of the domain are associated with slopes shallower than $K^{-2.0}$ (Fig. 7.2a). The comparison of the slope of the winter and summer kinetic energy spectra (Fig. 7.2b and 7.2c) shows that the pattern for the full period mainly is similar to the winter one. In summer-time, the largest part of the Agulhas region is associated with $\approx K^{-3.0}$ slopes (Fig. 7.2b).

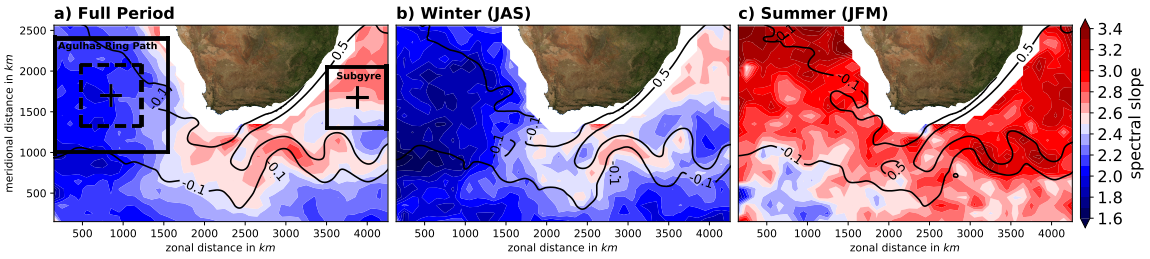

Fig. 7.2: *The mean slope of a) total, b) the winter (JAS) and c) the summer (JFM) mean kinetic energy spectrum from INALT60 for the period 2012 - 2017 in the scale band 20-75 km. The average slope n with respect to K^{-n} is shown. For the maps, every 100 km in both horizontal directions, a mean kinetic energy spectrum is computed for a 350 km $\times$ 350 km subregion. Solid lined boxes show the region for the computation of the kinetic energy spectra for Figure 7.4 and the spectral kinetic energy fluxes and flux divergences for Figures. The dashed lined boxes show the region for the Agulhas ring path that is compared to the subgyre region in Figure 7.3. Contours show the sea surface height in m averaged over the respective periods.*

In this study, we focus on the Agulhas ring path and the subgyre region and thus on regions that are associated with spatially different spectral slopes of submesoscale kinetic energy (Fig. 7.2) and with strong mesoscale eddy activity away from the mean current. Figure 7.3 shows characteristic snapshots of the normalized surface relative vorticity ζ/f for both regions. Here, $f = 2\Omega sin\varphi$ is the planetary vorticity with the Earth's rotation rate $\Omega = 7.2921 \times 10^{-5}$ rads^{-1} and the latitude φ. $\zeta = v_x - u_y$ is the vertical component of the relative vorticity at the surface. In winter, both regions are associated with a lot of submesoscale vortices and fronts (Fig. 7.3a and 7.3c). In summer, only a few small-scale vortices are present and the small-scale dynamics are dominated by fronts between the mesoscale eddies (Fig. 7.3b and 7.3d). Figure 7.3 indicates that submesoscale dynamics are more energetic in the subgyre. The winter-time subgyre is more crowded with submesoscale flows than the Agulhas ring path, where small-scale features occur mainly at the edge and

in between the mesoscale Agulhas eddies. Further, for both seasons, small-scale features in the subgyre have larger relative vorticity than in the ring path.

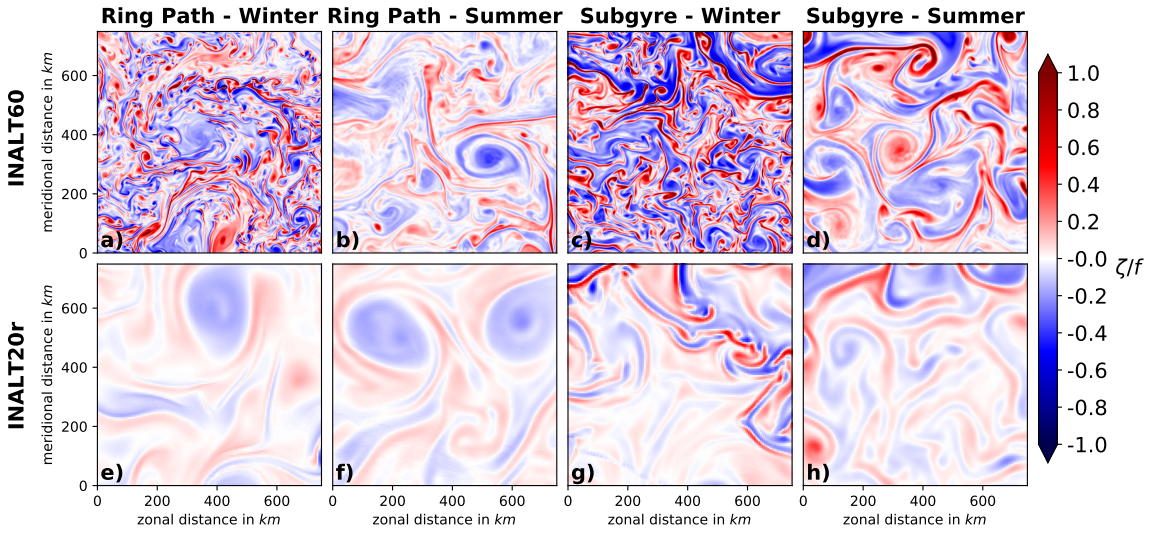

Fig. 7.3: *Characteristic snapshots of surface normalized relative vorticity ζ/f from INALT60 (top) and INALT20r (bottom) for the Agulhas ring path (left) and the subgyre region (right) for winter (Aug 5, 2012) and summer (Jan 18, 2012). The location of the regions is marked in Figure 7.2a.*

The near-surface kinetic energy spectra peak around 200 km for both regions and seasons (Fig. 7.4a and 7.4b). Consistent with the seasonal cycle of submesoscale activity, the winter-time spectra are associated with shallower spectral slopes ($\approx K^{-5/3}$) for both regions and thus more energetic smaller scales than in summer ($\approx K^{-3}$). The spectra diverge between both seasons at a scale of about 150 km in the subgyre and at 75 km in the ring path. In the 75 - 200 km band, the spectra of the subgyre is shallower than in the ring path. At even smaller scales, it is the opposite, with shallower spectra for the ring path, which is consistent with Figure 7.2b. Scales smaller than 100 km are more energetic in the subgyre than in the ring path (Fig. 7.4). This highlights a more vigorous submesoscale activity in the subgyre. Stronger submesoscales mix a tracer more efficiently leading to steeper spectral slopes of the horizontal tracer distribution (Callies and Ferrari, 2013). This can explain the pattern of the steeper SST spectral slope in the subgyre compared to the ring path observed by Schubert et al. (2019).

In INALT20r, the Agulhas ring path is associated with low-Rossby number ($Ro = |\zeta/f|$) flows in both seasons and thus almost no submesoscale flows (Fig. 7.3e, 7.3f and 7.3h). In the ring path, spectra in INALT20r are similar in both seasons with

less energy than in INALT60 at almost all scales and a steep slope (Fig. 7.4a). In the subgyre, some frontal dynamics with enhanced Ro are simulated in winter in INALT20r (Fig. 7.3g). The winter-time INALT20r spectrum is associated with more energy than in summer and, for both seasons, the spectra are closer to those of INALT60 for the very large mesoscales (> 200 km) (Fig. 7.4b). The effective resolution of both simulations can be identified as the scale where the horizontal-wavenumber spectra start to drop due to model diffusion and dissipation, which is about 8 km for INALT60 and about 25 km for INALT20r. Consistent with Soufflet et al. (2016), the respective wavelengths are about 10 times the gridspacing.

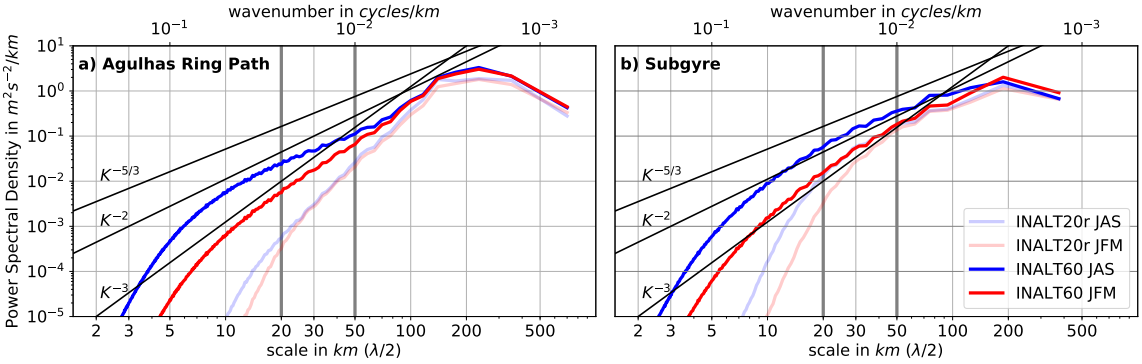

Fig. 7.4: *Winter (JAS, blue) and summer (JFM, red) mean kinetic energy spectrum for the period 2012 - 2017 for a) the Agulhas ring path and b) the subgyre region, marked with solid boxes in Figure 7.2a. For INALT60 the spectra are shown non-transparent and for INALT20r transparent. Straight black lines show spectral slopes of $K^{-5/3}$, K^{-2} and K^{-3}, where K is the isotropic wavenumber. Vertical light grey lines mark the 20 - 50 km band used for the computation of the spectral slope shown in Figure 7.2.*

7.5 The Computation of the Scale Kinetic Energy Flux

The scale kinetic energy flux $\Pi(L)$ is the rate of transfer of kinetic energy from currents with scales smaller than a specific horizontal scale L to currents with scales larger than L. The flux divergence $T(L) = \frac{\partial \Pi}{\partial L}$ yields sources and sinks of $\Pi(L)$. While we use the term "flux-divergence" throughout the paper, T is occasionally also referred to as the scale energy transfer as it is the source term in the budget of the power spectral kinetic energy density (e.g. Scott and Arbic, 2007). Here, we use two methods for the computation of Π: A spectral and a coarse-graining approach.

7.5.1 Spectral Approach

Energy is fluxed across scales by nonlinear interactions. The scale kinetic energy flux is usually derived using the integral of the Fourier transformed nonlinear advection term

$$\Pi_{sp}(K) = \rho_0 \int_K^\infty \hat{\mathbf{u}}_h^* \cdot (\mathbf{u}_h \widehat{\nabla_h \mathbf{u}_h}) dK,$$

where $\mathbf{u}_h = (u, v)$ is the horizontal velocity vector. Positive values of Π_{sp} indicate an upscale flux of kinetic energy. The spectral approach is associated with several limitations. First, one has to assume that turbulence is isotropic and homogeneous. Second, a value for the flux at the small-scale end has to be assumed. Here, we use the common assumption of zero flux at the smallest investigated scales. Third, the region, for which the energy flux is computed, is not well-defined due to the necessary windowing. Fourth, Π_{sp} is usually associated with noise leading to unreasonable high values of the flux-divergence (e.g. Scott and Wang, 2005).

7.5.2 Coarse-Graining Approach

In this study, we therefore focus on an alternative approach for the scale kinetic energy flux computations based on coarse-graining that is not associated with the above mentioned limitations of the spectral approach. The coarse-graining approach has been earlier applied to turbulence problems by Leonard (1975) and Germano (1992) and has been developed further by Eyink (2005). Aluie et al. (2018) applied the approach to a large-scale ocean general circulation model to investigate the scale energy flux between the oceanic mesoscale and large-scale circulation. Here, we study the energy cascade between the submesoscale and the mesoscale dynamics. In this section, we give a short overview of the derivation of scale energy flux based on

Germano (1992) and Aluie et al. (2018) and describe how we apply it to our model outputs.

A horizontal field $F(x, y)$ is low-pass filtered by applying a convolution $\overline{F}(x, y) = C * F(x, y)$ with a top-hat kernel

$$C(\mathbf{r}) = \begin{cases} 1/A & \text{if } |\mathbf{r}| < L/2, \\ 0 & \text{otherwise,} \end{cases} \tag{7.1}$$

where $A = \pi L^2/4$ is the circular normalization area of diameter L and $\mathbf{r}$ is the radial position vector. In other words, the low-pass filtered field is the result of a circular two-dimensional running-mean with diameter L that filters out all scales smaller than L from the original field $F(x, y)$. Applying the convolution to the rotating Boussinesq equations leads to the equations of motion for $\overline{\mathbf{u}}$, where $\mathbf{u} = (u, v, w)$ is the velocity vector with u, v, and the vertical component w. The form of the equations of motion does not change as the convolution is commutative with the spatial and temporal derivatives (Aluie et al., 2018). However, a new term arises from the nonlinear advection term:

$$\nabla \cdot \overline{\mathbf{u}\mathbf{u}} = \nabla \cdot \overline{\mathbf{u}}\,\overline{\mathbf{u}} + \nabla \cdot \overline{\tau}(\mathbf{u}, \mathbf{u}),$$

where $\overline{\tau}(\mathbf{u}, \mathbf{u}) = \overline{\mathbf{u}\mathbf{u}} - \overline{\mathbf{u}}\,\overline{\mathbf{u}}$ is the subfilter stress tensor. $\nabla \cdot \overline{\tau}(\mathbf{u}, \mathbf{u})$ is the force that the subfilter (small-scale) motions exert on the low-pass filtered (large-scale) flow. To derive the large-scale kinetic energy budget, the scalar product of the momentum equations with $\rho_0\overline{\mathbf{u}}$ is computed. The respective contribution of the subfilter stress can be split into

$$\rho_0\overline{\mathbf{u}} \cdot [\nabla \cdot \overline{\tau}(\mathbf{u}, \mathbf{u})] = \nabla \cdot (\rho_0\overline{\mathbf{u}} \cdot \overline{\tau}(\mathbf{u}, \mathbf{u})) - \rho_0\overline{S} : \overline{\tau}(\mathbf{u}, \mathbf{u}), \tag{7.2}$$

where the colon : is a tensor inner product. The first term on the right-hand side is the divergence of the transport of large-scale kinetic energy by small-scale currents. This term does not contribute to a flux of kinetic energy across scales. The second term is the scale kinetic energy flux $\Pi_{cg} = \rho_0\overline{S} : \overline{\tau}(\mathbf{u}, \mathbf{u})$, where $\overline{S} = (\nabla\overline{\mathbf{u}} + \nabla\overline{\mathbf{u}}^T)/2$ is the large-scale strain tensor. The separation into both contributions is associated with a gauge freedom. Here we followed the separation suggested by Aluie et al. (2018) which has the advantage of a Galilean invariant definition for the scale kinetic energy flux. Positive values of Π_{cg} are again associated with upscale kinetic

energy flux and negative with downscale. Neglecting the distribution of the vertical velocity component, the scale energy flux reduces to

$$\Pi_{cg}(\mathbf{x}) = \rho_0[(\overline{u^2} - \overline{u}^2)\overline{u}_x + (\overline{uv} - \overline{u}\,\overline{v})(\overline{u}_y + \overline{v}_x) + (\overline{v^2} - \overline{v}^2)\overline{v}_y].$$

Note that the form of the horizontal Π_{cg} is similar to the one of the barotropic instability term that transfers energy between the Reynolds-average based mean and eddy kinetic energy reservoirs integrated over closed domains (e.g. Harrison and Robinson, 1978).

The computation of Π_{cg} is much faster for regular grids and thus a constant convolution kernel C. The horizontal velocity components u and v are first interpolated onto the tracer grid points of the Arakawa C-grid. The respective geographical coordinates are transformed into Cartesian coordinates using the European Petroleum Survey Group Geodesy numbers 4326 (World Geodetic System 1984) and 3395 (Cartesian). Subsequently, both u and v are linearly interpolated onto a regular grid with 1 km grid-spacing before the horizontal convolution and the computations of Π_{cg} as well as Π_{sp} are performed. The computational cost of the convolution scales with L^2. Land cells are treated as cells with zero velocity, as suggested by Aluie et al. (2018). Π_{cg} is computed for the following length scales $L = 7, 10, 15, 20, 30, 45, 60, 100, 150, 200, 300$ km. We will show that the results are useful for a computation of the flux divergence $T_{cg} = \frac{\partial \Pi_{cg}}{\partial L}$. Positive values of T_{cg} show a source for the upscale flux and negative a sink.

The length scale L used for the coarse graining approach corresponds to half the wavelength λ used in the spectral approach. Elliptic features such as eddies will imprint in the spectrum at a wavelength which is about twice their diameter. The good agreement of the scale kinetic energy flux at the smaller scales computed with the spectral and the coarse-graining approach (Sec. 7.67.6.1) confirms this relation.

7.6 Scale Kinetic Energy Flux

7.6.1 Spectral versus Coarse-Graining Approach

For a comparison of the scale kinetic energy flux computed with both the spectral and the coarse-graining approach, the coarse-graining flux Π_{cg} is windowed in a similar way as the u and v data for the spectral flux. For that, a two-dimensional Hanning window of the same size and the associated correcting factor of 1.5 are multiplied to each horizontal field of Π_{cg}. Second, the windowed coarse-graining flux is spatially averaged. This method is a compromise with respect to computational power. For a very clean comparison, the coarse-graining method would need to be applied to the windowed u and v fields.

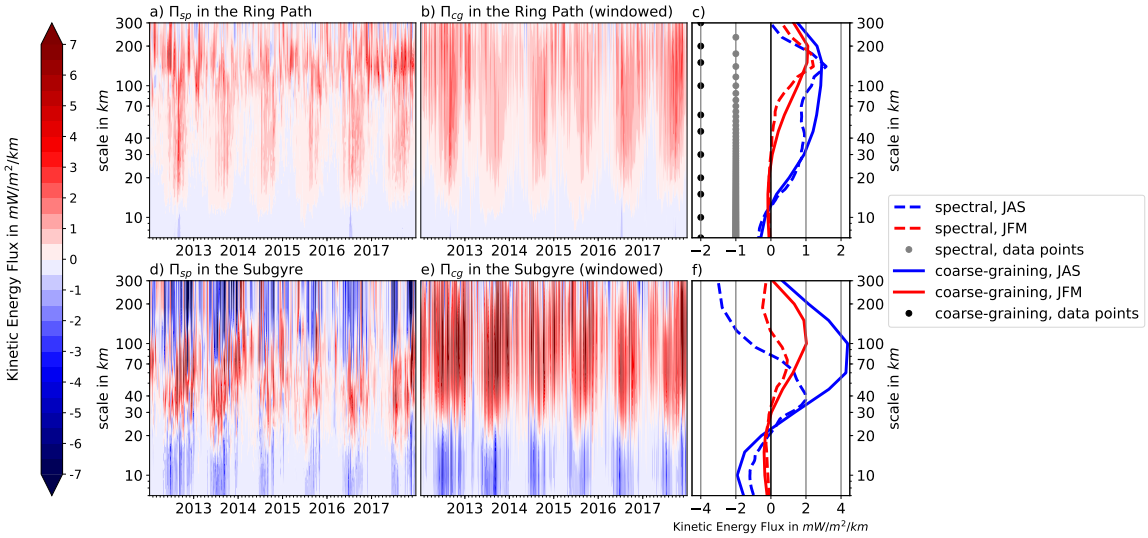

Fig. 7.5: *The surface scale kinetic energy flux as a function of time in the Agulhas ring path (a and b) and the subgyre (d and e) computed with the coarse-graining approach (a and d) and the spectral approach (b and e) for INALT60. The results are shown for model snap-shots every fifth day. The respective regions are marked with solid boxes in Fig. 7.2a. Note that for comparison, the coarse-graining flux is windowed similarly to the velocity components before the spectral flux computations and is subsequently averaged in space. In c) and f) the winter (blue, JAS) and summer (red, JFM) mean fluxes are shown for the coarse-graining (solid) and the spectral approach (dashed). Black and gray dots in c) mark for which scales the fluxes are computed. The scale is identified as half the wavelength for the spectral flux and as the diameter of the smoothing kernel G for the coarse-graining flux.*

For the Agulhas ring path, the surface scale kinetic energy fluxes computed with both approaches are very similar (Fig. 7.5a-c). The fluxes are towards larger scales (positive) for most of the investigated scales. The scale flux is larger in winter than in summer for almost all scales and for both up- and downscale directions (Fig.

7.5c). The surface inverse cascade changes to a forward cascade at scales around 13 km in winter and about 25 km in summer. The agreement between results from both approaches is particularly good at scales smaller than 30 km. This confirms that half the wavelength used in the spectral analysis represents the horizontal scale. At larger scales, the spectral flux is weaker and noisier than the coarse-graining flux.

In the subgyre, the coarse-graining scale fluxes are larger than in the Agulhas ring path for both up- and downscale directions (Fig. 7.5). Further, the change from winter-time inverse to forward cascade occurs at scales around ≈ 23 km, larger than in the ring path. The agreement with the spectral results is good for scales smaller than 30 km, but the spectral flux is associated with stronger downscale fluxes at larger scales (in particular larger than 100 km). We hypothesize that the assumption of homogeneous and isotropic turbulence, made for the spectral approach, is valid at the smallest scales but produces unrealistic results at larger scales. Indeed, results of the spectra and coarse-graining approch are closer in the ring path where the mesoscales are relatively isotropic (e.g. Wagner et al., 2019). The presence of the AC in the north-west corner of the subgyre box introduces some non-isotropy.

7.6.2 Delayed Strengthening of the Mesoscale

In the previous section, we showed that the upscale flux at scales smaller than ≈ 75 km is largest in winter-time in the ring path and the subgyre. This is consistent with the stronger submesoscale activity in winter and the associated higher kinetic energy at these scales (Fig. 7.4). For the mesoscale, around 200 km, the winter and summer energy spectra show almost no difference for the Agulhas ring path. For the subgyre, energy is stronger in summer. This indicates that the upscale fluxed kinetic energy is delayed in reaching the mesoscales. To investigate this, the monthly climatology of the scale kinetic energy flux is compared with the anomaly of the kinetic energy spectrum (Fig. 7.6). The annual mean is subtracted from the monthly climatology to highlight the seasonal cycle of kinetic energy. Note that for Figure 7.6 the coarse-graining flux is windowed before averaging in space to be comparable to the spectral results. Consistent with the previous results, the kinetic energy peaks for scales smaller than about 75 km in winter-time, between June and September. At the largest mesoscales, this peak is shifted to August to December in the ring path and even further to the summer (December to February) in the subgyre. The same is true for the maximum in upscale kinetic energy flux. In the ring path, the maximum upscale flux occurs in August at scales of 90 km and shifts to larger scales around 200 km in November. In the subgyre, the upscale flux peaks

in June at scales of 75 km and this maximum shifts to larger scales around 150 km in January. Our results indicate that the submesoscale-related upscale kinetic energy flux is an important driver of the seasonal cycle of mesoscale kinetic energy in both regions. In the subgyre, this relationship is more clear as the mesoscale kinetic energy climatology is less patchy than in the ring path.

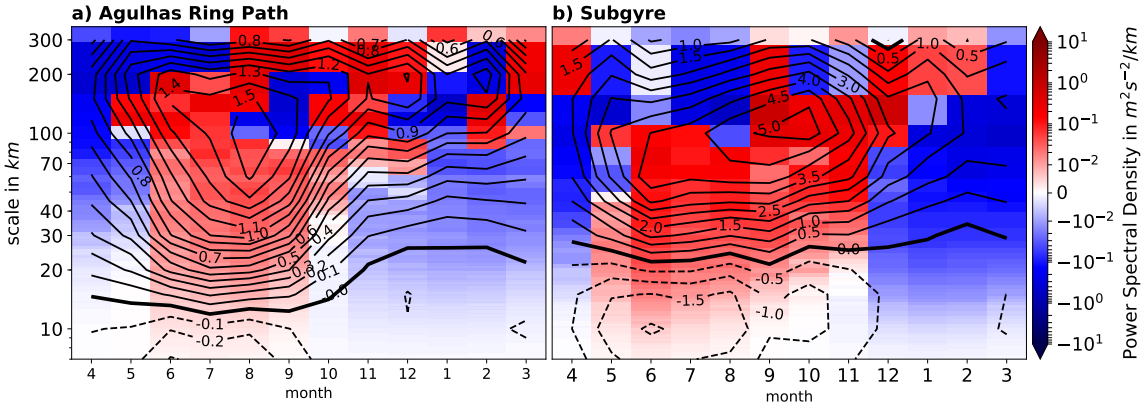

Fig. 7.6: *Monthly climatology of the surface kinetic energy spectrum referenced to the mean spectrum (in $\mathrm{m^2 s^{-2}/km}$, shading) and of the windowed and spatially averaged surface scale kinetic energy flux (in $\mathrm{mW/m^2/km}$, contours) for the period 2012 - 2017 in the Agulhas ring path (a) and the subgyre (b) in INALT60 (The regions are marked with solid boxes in Fig. 7.2a.). Note that the month axis starts with April to better visualize the upscale shift of the maximum in flux and power spectral density after the submesoscale season.*

7.6.3 Comparison to a Parallel Non-Submesoscale Resolving Simulation

The comparison of the coarse-graining scale kinetic energy flux in INALT60 with the one in the parallel non-submesoscale resolving simulation INALT20r shows the importance of the submesoscale dynamics for the surface kinetic energy cascade in the Agulhas ring path (Fig. 7.7a - 7.7c). In both winter and summer seasons about 7 times more kinetic energy is fluxed from the smaller scales to scales larger than 100 km in INALT60 (Fig. 7.7c). This missing amount of energy flux contributes to that the mean surface kinetic energy at scales larger than 100 km (computed from the velocity components that were smoothed with a 100 km diameter top-hat kernel) is reduced in the Agulhas ring path to 78 % in INALT20r compared to INALT60. This is consistent with the lack of mesoscale SSH power spectral density reported by Schubert et al. (2019). In INALT20r, the near-surface dynamics are associated with weak scale kinetic energy fluxes of changing sign that peak in the mesoscales around

200 km. Below scales of 50 km, the fluxes are almost zero due to the non-existing smaller-scale flows.

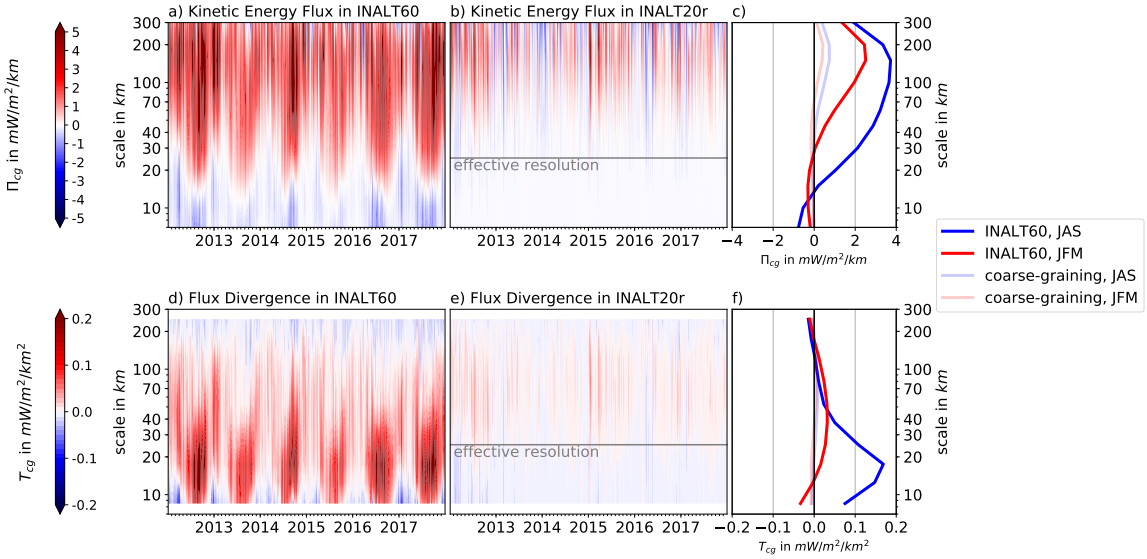

Fig. 7.7: *The surface scale kinetic energy flux (a - c) and its divergence with respect to the scale (d - e) in the Agulhas ring path computed with the coarse-graining approach (not windowed before spatial averaging) from INALT60 (a and d) and INALT20r (b and e). The region is marked with a solid box in Fig. 7.2a. In c) and f) the winter (blue, JAS) and summer (red, JFM) mean fluxes are shown for INALT60 (solid) and INALT20r (transparent)*

The divergence of the scale kinetic energy flux with respect to the scale gives the source of the flux at a particular scale (Fig. 7.7d-f). In INALT60, the largest sources for the inverse cascade are found in winter-time at scales around 15 to 20 km. The smallest investigated scales between 7 and 10 km are still associated with a source for the inverse cascade, while scales larger than 100 km are associated with a sink. In contrast, in summer, a sink is found for the smallest scales below 12 km. Larger scales are associated with a source extending to scales of up to 200 km. Compared to winter, these sources are weaker at scales below 50 km but stronger at larger scales. At 250 km scales, a sink for the inverse cascade is found throughout the year. This might be related to the role of the β-effect at these scales (see Rhines, 1975). Most of the sources for the inverse cascade are missing in INALT20r (Fig. 7.7e and 7.7f). Only the mesoscale dynamics around 100 km scales are associated with a source for the inverse cascade, but it is very weak.

7.6.4 The Scale Kinetic Energy Flux as a Function of Space

In this section, we investigate the scale kinetic energy flux as a function of depth and horizontal space in INALT60. First, the distribution of the scale kinetic energy flux in the upper 250 m is addressed. This is the depth range, where model snapshots were written in the output each fifth day and the full simulated spatial variability can be analyzed. Below 250 m, the fluxes computed for the full water column based on daily mean output are only very weak (not shown). We further restrict the analysis to two single model snapshots representative for the winter and summer season as the computational costs for the flux computations are very large. The spatial-mean scale kinetic energy flux and its partition into down- and upscale fluxes are shown for the ring path and the subgyre for both seasons in Figure 7.8.

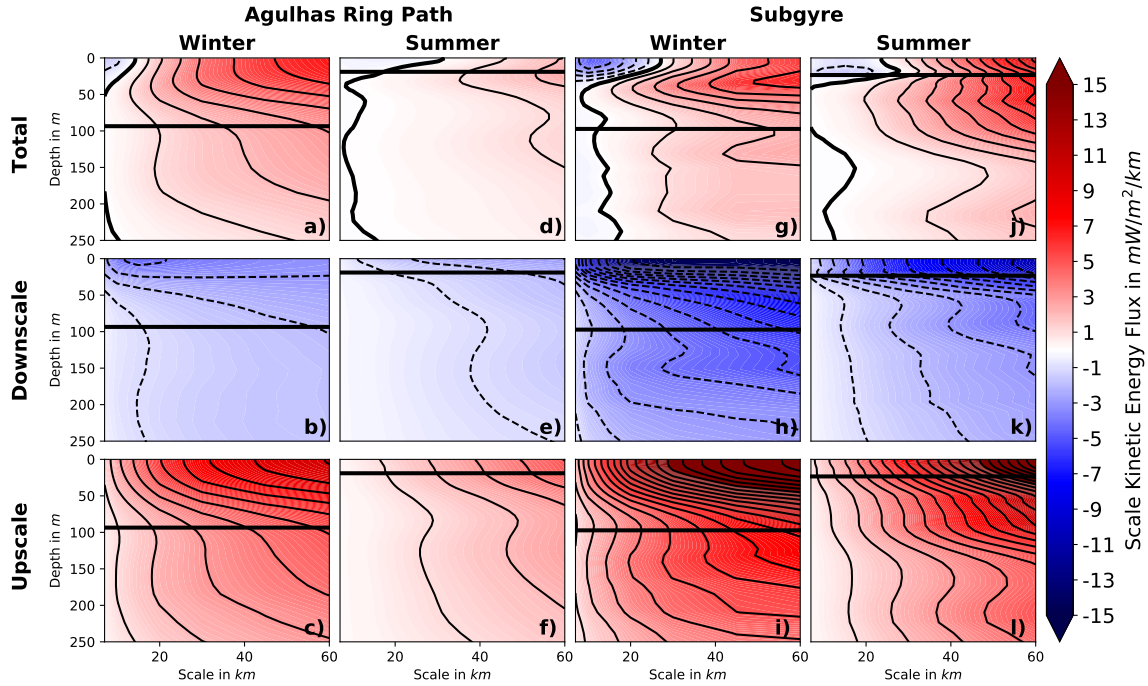

Fig. 7.8: *The spatial-mean scale kinetic energy flux (shading and contours with an interval of 1 $\mathrm{mW/m^2/km}$) computed with the coarse-graining approach from a winter (Sep 4 2012) and a summer (Jan 18 2012) model snapshot (top row) for the ring path (left) and the subgyre (right). Down- and upscale contributions to the total flux are shown in the middle and bottom row. They are computed by setting the positive respectively negative fluxes to zero before spatial averaging and give the total flux in the top row when added together. The regions for the computation are shown with solid boxes in Figure 7.2a. Black horizontal lines show the spatial mean mixed layer depth.*

Both the down- and the upscale kinetic energy fluxes are surface intensified (Fig. 7.8). In winter, the downscale flux is concentrated in the upper 30 m, while the upscale flux fills the entire mixed layer (about 100 m). In summer, when the

mixed-layer is thinner, both fluxes are concentrated in the mixed-layer and are much weaker than in winter. For both seasons, the amplitude of the fluxes mainly increases with the scale. An exception is the winter downscale flux in the Agulhas ring path that shows a near-surface maximum at scales around 15 km (Fig. 7.8b).

In the subgyre, the total fluxes change from up- to downscale at about 30 km near the surface, and at about 10 km below 50 m depth. In the ring path, the winter inverse cascade reaches, at the surface, even down to about 13 km, consistent with Figures 7.6 and 7.7. Below 50 m depth, the change of inverse to forward cascade occurs below 7 km, indicating that a small part of the inverse cascade is still not resolved by the simulation. In the winter subgyre, the large downscale fluxes near the surface (Fig. 7.8h) lead to the total flux showing a maximum upscale flux at about 40 m depth (Fig. 7.8g).

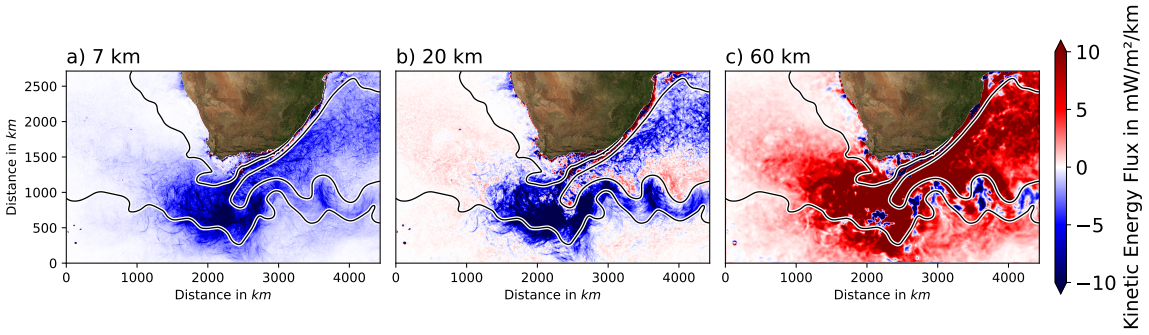

Fig. 7.9: *The 2012 - 2017 time-mean surface scale kinetic energy flux Π_{cg} computed from 4h-mean outputs of INALT60 for 7 km (a), 20 km (b) and 60 km (c) scales. Blue (Red) colours show downscale (upscale) fluxes. Selected contours of the respective average of sea-surface height highlight the location of the Agulhas Current system.*

The amplitude of the 2012-2017 time-mean total surface scale kinetic energy flux is largest in the region of the retroflection, strong in the subgyre and in the region of the ARC, weak in the Agulhas ring path and very weak in the open ocean at every scale (Fig. 7.9). An explanation for this spatial pattern might be that the fluxes are larger the stronger the submesoscale dynamics are and that the submesoscale dynamics are in turn stronger the stronger the mesoscale dynamics interact. At a scale of 60 km, the time-mean flux is upscale almost everywhere, while at a scale of 7 km it is downscale almost everywhere. The map of the flux at 20 km scales highlights that the change from up- to downscale occurs at different scales: In the retroflection, the subgyre and the ARC, the flux at a scale of 20 km is downscale, while in other regions, like the ring path, it is still upscale. The map of the scale where the winter-mean (JAS) surface scale kinetic energy flux changes from down to upscale shows that this change occurs in the Agulhas ring path at around 15 km,

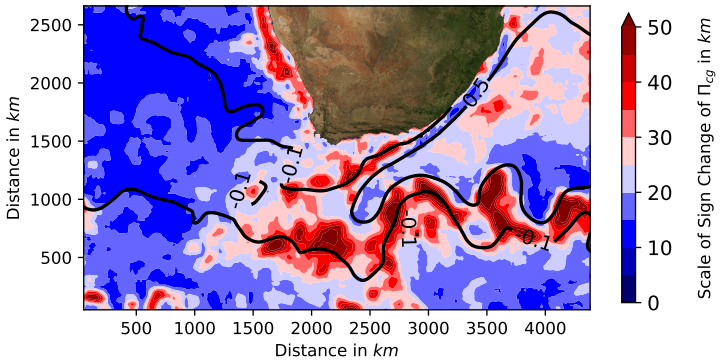

Fig. 7.10: *The scale where the 2012-2017 winter-mean (JAS) kinetic energy flux changes from down- to upscale computed from 4h mean INALT60 data. For the plot, the very patchy original field has been smoothed with a 100 km diameter top-hat kernel. Contours show the respective average of the sea-surface height in m.*

in the subgyre at around 25 km and in the retroflection and the ARC at even larger scales of 35 - 50 km (Fig. 7.10).

7.7 Downscale Fluxes Occur at Small Scales Mainly in Frontogenetic Regions

A winter-time snapshot of the simulated surface density ρ in the subgyre region of INALT60 shows the presence of sharp density fronts at the surface (Fig. 7.11a). Positive values of the frontal tendency,

$$FT = -[\rho_x^2 u_x + \rho_y^2 v_y + \rho_x \rho_y (u_y + v_x)],$$

here computed following Giordani and Caniaux (2001), mark frontogenetic regions. For the snapshot, most of the surface downscale fluxes at 7 km occur in frontogenetic regions with $FT > 0.1\ ((\mathrm{kg/m^3})/\mathrm{km})^2/\mathrm{day}$ (Fig. 7.11b). A vertical section through a front shows that the downscale flux occurs mainly at the frontogenetic flank of the frontal jet (Fig. 7.11bii-7.11biv). Below, the frontal secondary circulation is associated with upwelling as it is visible in an elevation of the mixed-layer depth (Fig. 7.11biv). The downscale flux occurs mainly in the upper 30 m, consistent with Figure 7.8h.

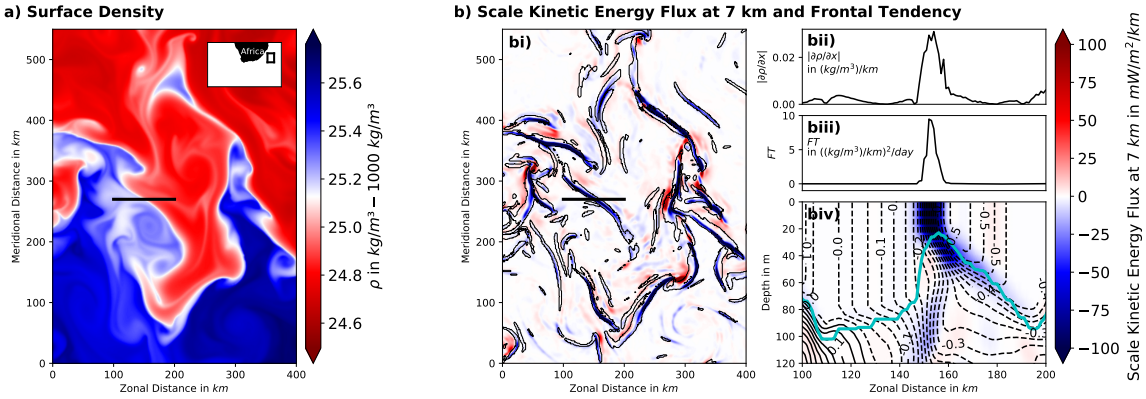

Fig. 7.11: *Downscale fluxes occur at small scales mainly in frontogenetic regions: An INALT60 snapshot (Sep 4 2012) of surface density (a) and the surface scale kinetic energy flux at 7 km computed with the coarse graining approach overlaid by the 0.1* $((\mathrm{kg/m^3})/\mathrm{km})^2/\mathrm{day}$ *frontogenetic tendency contour (bi) in the region shown in the small map in a). The zonal black line in a) and bi) shows the location for which in bii), the absolute value of the surface zonal density gradient, in biii) the surface frontal tendency and in biv) a vertical section of the scale flux at 7 km (shading) and the meridional velocity (contours with an interval of 0.025 m/s - dashed southward and solid northward) are shown. The cyan line in biv) marks the mixed layer depth.*

In the 5d snap-shot output for the $1/60°$ domain of INALT60 and the period 2012 - 2017, 61 % of the surface downscale flux at a scale of 7 km occur in frontogenetic regions with $FT > 0.1\ ((\mathrm{kg/m^3})/\mathrm{km})^2/\mathrm{day}$. The same percentage is derived to be

39 % in the ring path and 69 % in the subgyre. This indicates that frontogenesis and frontal processes such as frontal instabilities are major drivers of the forward cascade.

7.8 The Mesoscale Absorption of Mixed-Layer Eddies

The mixed-layer instability is a baroclinic instability that transfers potential energy of a mixed-layer front to kinetic energy of mixed-layer eddies and other developing features. Stone (1970) extended the baroclinic instability model of Eady (1949) by ageostrophic perturbations and derived the wavelength of its fastest growing mode to be

$$\lambda_s = \frac{2\pi u_0}{|f|}\sqrt{\frac{1+Ri}{5/2}}, \tag{7.3}$$

where u_0 is the magnitude of the thermal wind, f the Coriolis parameter and Ri the Richardson number. Typical values for the baroclinic instability of a mid-latitude mixed-layer front, $u_0 = 0.05$ ms-1, $f = 7.29 \times 10^{-5}$ s^{-1}, and $Ri = 1$, give $\lambda_s = 3.9$ km (Fox-Kemper et al., 2008). Fox-Kemper et al. (2008) showed with an idealized nonlinear model simulation that the linear theory captures the growth of the perturbations only in the first six days after initialization. After the instabilities reached finite amplitude, they observed a nonlinear transfer of kinetic energy to scales of about 10 - 50 km. It is a fact that most of these features are not present in summer-time (Fig. 7.3). Thus, they have to disappear within several months due to either dissipation or due to absorption by larger scale features. In this section, we find indications that the latter is the case. First, some evidence for that is presented with a characteristic case study on the process of mixed-layer instabilities and the subsequent mesoscale absorption of the associated submesoscale features by an Agulhas ring. Therefore we investigate the dynamics and the scale kinetic energy flux on the basis of a series of snapshots. On model day June 19 2012, the lighter waters of a warm-core, anticyclonic Agulhas ring are separated by a sharp density front from denser water east of the ring (Fig. 7.12a). South of the ring, submesoscale, high-Rossby-number features (Fig.7.12e) and positive vertical buoyancy fluxes $VBF = \rho_0 w' b'$ at 60 m depth (Fig. 7.12i) indicate the activity of mixed-layer instability in this part of the front. In the definition of the VBF, the dashes mark deviations from the respective monthly mean. Five days later, the whole front east of the ring is associated with strong positive VBF (Fig.7.12j) as well as mixed-layer instability driven submesoscale features with a scale of about 40 km (Fig. 7.12f). At this stage, the southern boundary of the ring is associated with large upscale kinetic energy fluxes into scales of 50 km as well as into 200 km and thus into the scale of the ring. Downscale fluxes northeast of the ring might be driven by a squeezing of the ring due to the northwestward advection of denser waters in this region (Fig. 7.12a and 7.12b).

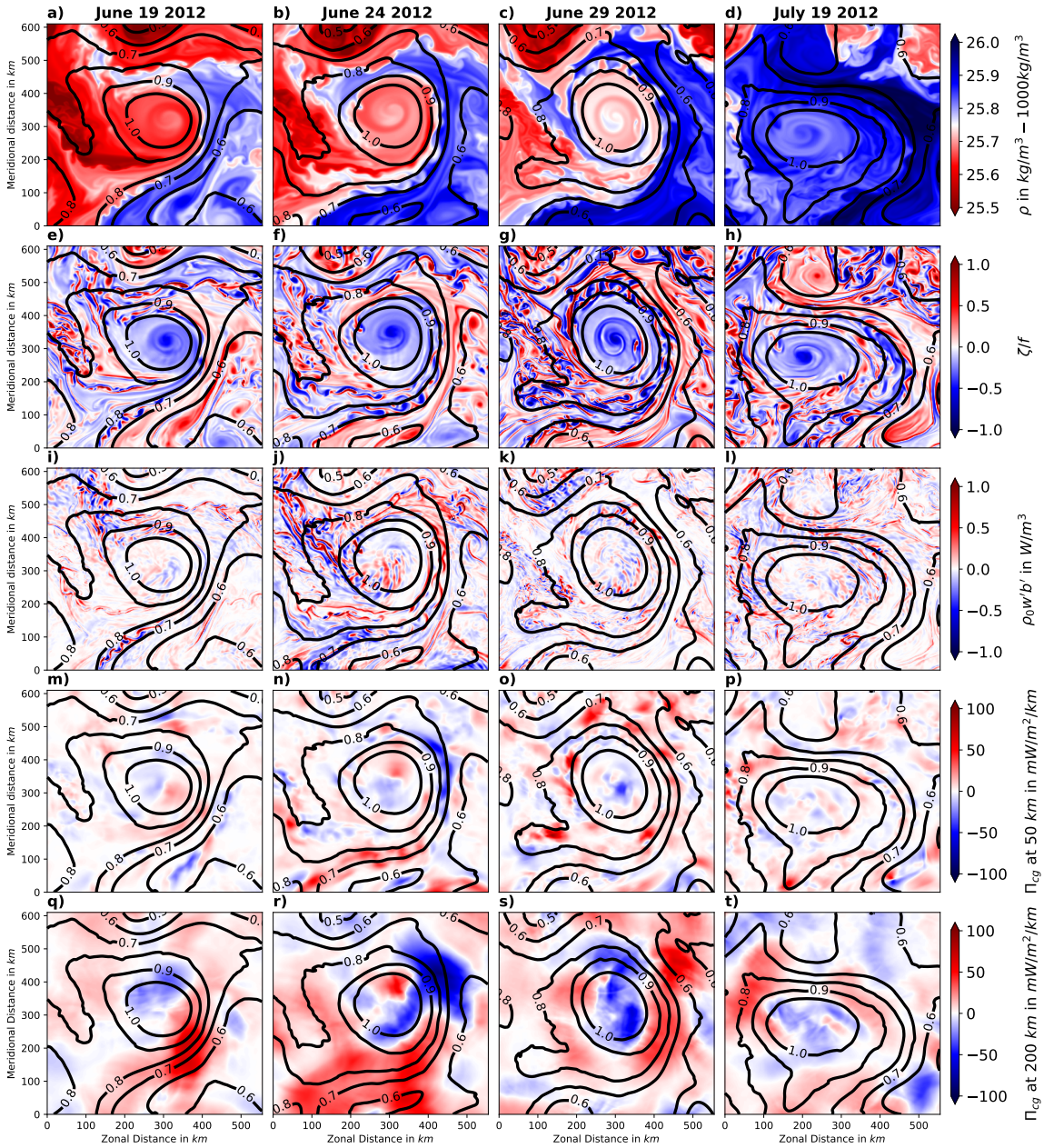

Fig. 7.12: *The absorption of mixed-layer instability generated features by an Agulhas ring in INALT60: Snapshots of surface density (a - d), surface normalized relative vorticity (e - h), Vertical buoyancy flux at 60 m depth (i - l), and of surface scale kinetic energy flux at 50 km (m - p) and 200 km (q - t) overlaid by sea-surface height contours (in m).*

Another five days later, the whole ring as well as its boundary are associated with only weak VBF (Fig. 7.12k). The mixed-layer instability has abated and the resulting submesoscale features are present along the whole boundary of the ring (Fig. 7.12g). This boundary is at this stage associated with strong upscale fluxes into scales larger than 50 km and also into scales larger than 200 km indicating that the submesoscales flux their kinetic energy into the ring. In the centre of the ring, downscale fluxes occur (Fig. 7.12o and 7.12s). Another 20 days later on July 19, and thus a month after the initialization of the frontal instability, the density contrast of the surface ring and its surrounding (Fig. 7.12d) as well as the submesoscale flows around its boundary are much weaker (Fig. 7.12h). The boundary of the ring is still associated with upscale flux into scales larger than 200 km (Fig. 7.12t). This indicates that the absorption of the submesoscale features by the ring is still ongoing.

In this framework, it also fits that the maximum of scale kinetic energy flux shifts to larger scales after the submesoscale season (Fig. 7.6). The kinetic energy provided by the submesoscales reaches the mesoscales with a few months delayed as the absorption needs this time to take effect. Moreover, the largest sources for the surface and winter-time inverse cascade are found at scales around 15 - 20 km (Fig. 7.7f) which are typical scales of features that result from the mixed-layer instability. Our interpretation of these results is that the development of mixed-layer eddies provides the main source for the surface upscale kinetic energy flux in the Agulhas ring path. Supporting this conclusion, we note that this source is missing in the parallel simulation that does not simulate baroclinic mixed-layer instabilities in the ring path (Fig. 7.3 and Fig. 7.7).

A further indication for the mixed-layer instability associated upscale flux is found by comparing the ring path in INALT20r, where no mixed layer instabilities are simulated, to the subgyre region, where some smaller scale instabilities occur in winter in the $1/20°$ simulation (Fig. 7.3). The associated small-scale features contribute to a stronger inverse cascade than in the ring path (not shown). This is consistent with a stronger seasonal cycle of the kinetic energy spectrum and a smaller difference of the spectrum to INALT60 at the mesoscales (Fig. 7.4 and 7.6). Further, this may explain why the spectral slope of the time-mean horizontal-wavenumber spectrum of SSH in INALT20r was found by Schubert et al. (2019) to be close to the observations in the subgyre but too steep in the Agulhas ring path. The most unstable wavelength λ_s for mixed-layer instability can provide a hint as to why the small-scale instabilities

do develop in the subgyre but don't in the ring path of INALT20r. The thermal wind $u_0 = |\nabla_h b|h/f$ with the buoyancy b and the mixed-layer depth h gives in (7.3)

$$\lambda_s = \frac{2\pi|\nabla_h b|h}{f^2}\sqrt{\frac{1+Ri}{5/2}}. \tag{7.4}$$

The winter mean of λ_s computed with $Ri = 1$ at a depth of 30 m in INALT60 is shown in Figure 7.13. λ_s is larger in the AC, ARC and retroflection as well as in the subgyre, smaller in the Agulhas ring path and very small in the open ocean. Thus, in the subgyre, it is more likely that the conditions favour mixed-layer instabilities with such a large λ_s that they are permitted in the $1/20°$ simulation. The evolving features then contribute to a strong inverse cascade and the mesoscales are consistently closer to the observations with respect to the SSH spectral slope.

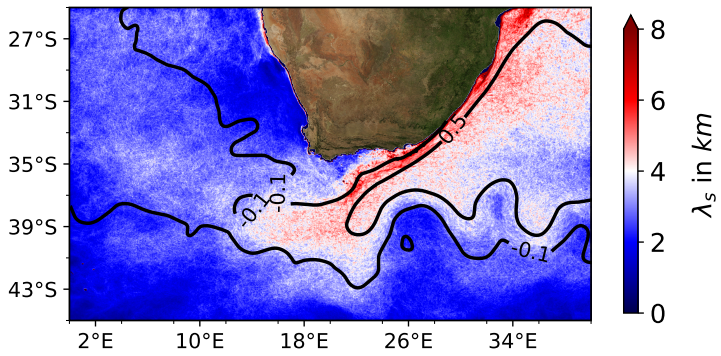

Fig. 7.13: *The most unstable wavelength in the mixed-layer (λ_s computed for 30 m depth) averaged from 2012-2017 over the winter months (JAS) from 5d snapshots of INALT60. Contours show the respective average of the sea-surface height in m.*

7.9 Discussion and Conclusion

In this study, the submesoscale kinetic energy cascade is investigated in the Agulhas region for the first time. This is done on the basis of the submesoscale permitting model INALT60 that simulates the core Agulhas region with a horizontal resolution of $1/60°$ (≈ 1.5 km grid-spacing). Our results indicate that INALT60 resolves almost the full inverse cascade and thus the full energization of the mesoscales by the submesoscale flows. This is consistent with previous results by Schubert et al. (2019) showing that in the Agulhas ring path of INALT60, the time-mean power spectrum of sea-surface height (SSH) agreed very well with the one computed from along-track satellite altimetry, while a $1/20°$ simulation without submesoscale dynamics showed too less power spectral density at all scales. Consistently, in the $1/20°$ simulation, the open ocean inverse cascade is almost absent.

Submesoscale currents flux their kinetic energy to both larger (upscale) as well as to smaller horizontal scales (downscale). In this study, downscale fluxes at the smallest resolved scales ($\approx$ 7 km) are found to be concentrated in frontogenetic regions in the upper 30 m of the ocean. In the Agulhas region, 61 % of the surface downscale flux at a scale of 7 km occur in regions with a frontogenetic tendency of more than 0.1 $((\mathrm{kg/m^3})/\mathrm{km})^2/\mathrm{day}$. As far as we know, this is the first time that the colocation of frontal regions and downscale kinetic energy flux is explicitly shown in the literature. Our results are consistent with D'Asaro et al. (2011) who found enhanced kinetic energy dissipation in a front within the Kuroshio region. They attributed the dissipation to symmetric instability of the front. In our simulation, it is hard to attribute the downscale flux at 7 km to a specific process, as this scale marks the small-scale end of the resolved physics in the model and symmetric instability and other smaller-scale instabilities are only partially or not resolved in the simulation (e.g. Bachman and Taylor, 2014). Further, the scale fluxes are computed based on the model solution that is affected by the (unphysical) model dissipation at these and smaller scales. The impact of the model dissipation on the resulting scale kinetic energy flux might dominate the one of permitted frontal instabilities.

Strong upscale fluxes occur throughout the whole depth of the mixed layer in the winter season. There are several indications that these fluxes are partially attributable to the growth of mixed-layer baroclinic instability driven features and their absorption by mesoscale eddies. First, the winter-time source of the upscale flux (the flux divergence with respect to the scale) is found to be largest at scales around 15 km. These are typical scales of features that develop as a result of mixed-layer

instability (Fox-Kemper et al., 2008). This is consistent with Sasaki et al. (2014) who found at these scales a maximum of the spectrum of the vertical buoyancy flux which is, in the framework of the Lorenz energy cycle, a measure of the energy transfer from eddy potential to eddy kinetic energy and an indicator of baroclinic instability. Second, in a parallel nonsubmesoscale-resolving simulation, these sources for the inverse cascade are almost absent and the mesoscale eddies are too weak. Third, a case study of mixed-layer instability driven features that are absorbed by an Agulhas ring shows an upscale flux of kinetic energy into the scale of the ring along its whole side wall. Fourth, the maximum of scale kinetic energy flux shifts to larger scales after the submesoscale season accompanied by a coincident shift of the maximum in kinetic energy (Fig. 7.6). This is consistent with the notion that the absorption of the smaller scale features needs time to proceed. Fifth, in regions where some submesoscale dynamics are resolved in the $1/20^\circ$ simulation, like the subgyre region, the mesoscale band of the kinetic energy spectrum is closer to the one of INALT60 and the SSH spectral slope is closer to the observations compared to the ring path, where no submesoscale flows are resolved.

In the simulated Agulhas ring path and other open ocean regions, the surface inverse cascade is found to extend down to scales of 13 km, while in the very energetic regions like the retroflection, the Agulhas return current and the subgyre region, the surface inverse cascade changes to forward already at scales of 25 - 50 km. One reason for this is that in the latter regions stronger fronts develop as a consequence of stronger mesoscale eddy interactions. The fronts are in turn associated with stronger downscale fluxes that counteract the upscale flux. At the smallest resolved scales ($\approx$ 7 km), the scale kinetic energy fluxes are dominantly downscale everywhere in the investigated domain. At even smaller scales, the numerical dissipation of the advection scheme further dissipates the kinetic energy. Both, the almost full resolution of the inverse cascade and the imitation of the subgrid-scale forward cascade by the model dissipation contribute to the success of INALT60 in simulating realistic ocean dynamics in the Agulhas ring path across all scales as demonstrated by Schubert et al. (2019). The widely used approach, that the model dissipation (explicit and numerical) takes care of the full subgrid-scale effect in an ocean model, is only valid, if this effect is mainly a downscale kinetic energy flux. In the present study, we show that the scale that has to be resolved to capture the surface inverse cascade, depends on the region. A map of the scale, where the inverse cascade changes to forward from a very high-resolution model (Fig. 7.10) thus provides guidance for the needed horizontal resolution if the model's dissipation is responsible for the full subgrid-scale effects. In this respect, such a map can also guide the distribution of the grid spacing for unstructured meshes.

Our results are consistent with previous modeling studies for other regions. Capet et al. (2008c) found for the California Current system an inverse cascade down to a wavelength (scale) of about 34 km (17 km) and supposed that the forward cascade occurs mainly at fronts - which is shown here explicitly. Qiu et al. (2014) found for the North Pacific Subtropical Countercurrent a change from inverse to forward cascade in winter at wavelengths (scales) of 30 km (15 km). Moreover, they found a similar seasonal cycle of the inverse cascade with stronger upscale fluxes that extend to smaller scales in winter, and a transition of the scale of change to downscale fluxes to larger scales after the submesoscale season during the weakening of the frontal instabilities.

For the computation of the scale kinetic energy flux, we rely here on a coarse-graining approach. In contrast to the classic spectral approach, the coarse-graining approach enables an easy mapping of the cascade and does not require the assumptions of homogeneous and isotropic turbulence that are needed for the spectral approach. We demonstrate that both approaches lead to similar results at smaller scales (< 40 km). At larger scales, the spectral approach is associated with weaker fluxes. We hypothesize that at these larger scales, the assumptions of homogeneous and isotropic turbulence are not valid and thus the coarse-graining results are likely to be more realistic. The coarse graining approach comes in turn along with the limitations that it is costly in terms of computational power as well as data storage capacities. In this study, the scale flux is computed for scales of 300 km and smaller. We assume that for these scales the effect of Earth's curvature on the flux computations can be neglected and thus that the chosen convolution kernel (Eq. 7.1) is a reasonable choice. Future research could compare the fluxes with those computed by a convolution on a sphere (Aluie, 2018). Both approaches on the scale kinetic energy flux are limited in that the fluxes are computed based on the model solutions and thus do not capture the effect of smaller scale flows. Although Capet et al. (2008c) find no change in the scale where the inverse cascade changes to forward when they increased the horizontal resolution from 1.5 km to 750 m, they observe an increase of both up- and downscale fluxes. We thus expect an increase in the amplitude of the fluxes when the model resolution is further increased.

Summarizing, in this study, the submesoscale kinetic energy cascade of the simulated Agulhas region is presented as a function of space and time. The scale kinetic energy flux is largest in winter-time as well as in regions of strong mesoscale activity. The mean winter-time inverse cascade extends to scales of 13 km in the ring path and 25 - 45 km in other parts of the Agulhas region. After the submesoscale season, the

maximum of the upscale flux shifts within a few months to the mesoscales where it is aligned with the seasonal maximum in kinetic energy. Indications are found that the mesoscale absorption of mixed-layer instability eddies is an important process for the oceanic inverse cascade. Consistently, in a parallel nonsubmesoscale-resolving simulation the inverse cascade is almost absent in the ring path and the surface mesoscale kinetic energy is reduced to about 80 %. If our results can be generalized, they indicate that mixed-layer instabilities strengthen mesoscale eddies and thus need to be resolved by ocean models for the representation of the eddies. Alternatively, their strengthening upscale effect needs to be parameterized besides the restratifying effect on the mixed-layer (e.g. Fox-Kemper et al., 2008). The timing of the mesoscale strengthening in early summer fits to that the mesoscale eddy kinetic energy peaks in summer for the largest part of the midlatitude oceans (Rieck et al., 2015). This indicates that submesoscale dynamics are also important for the mesoscale seasonal cycle.

This study focused on the local kinetic energy cascade in the Agulhas ring path and the subgyre region. Besides the local cascade, the strength of the eddies within the Cape Basin is also impacted by the upstream dynamics in the retroflection and along the Agulhas bank. Both regions are associated with strong scale kinetic energy fluxes in the model. The submesoscale open-ocean inverse cascade can not explain that in particular strong Agulhas cyclones are much better represented when submesoscale flows are resolved by the model (Schubert et al., 2019). A follow-on study will investigate the role of submesoscale dynamics in the formation of Agulhas cyclones along the Agulhas bank. A further open question is, which effect the submesoscale dynamics have on Agulhas leakage and its impact on the Atlantic ocean circulation. The leakage itself might be increased due to important submesoscale contributions to the Agulhas cyclone formation. Moreover, submesoscale dynamics play a role for the exchange of Agulhas eddies with their surroundings and thus where and how strong the leakage influences the Atlantic. On the one-hand, submesoscale dynamics drive a strong exchange of water across the boundaries of Agulhas rings (Sinha et al., 2019). On the other-hand, the strengthening of the Agulhas eddies by submesoscale dynamics might shield the eddy cores from mixing with their surroundings. To address this question, longer integration periods are necessary.

7.10 Acknowledgments

This study received funding from the German Federal Ministry of Education and Research (BMBF) of the SPACES projects AGULHAS (Grant 03F0750A) and CASISAC (Grant 03F0796A). J. G. gratefully acknowledges support from the French National Agency for Research (ANR) through the project ISblue "Interdisciplinary graduate school for the blue planet" (ANR-17-EURE-0015) and the project Deeper (ANR-19-CE01-0002-01), and from LEFE/IMAGO through the project AO2017-994457-RADII. The model experiments were executed at the North-German Supercomputing Alliance (HLRN). The authors thank Adekunle Ajayi for sharing his python scripts on the 2D kinetic energy spectrum and the spectral kinetic energy flux that were modified for the here performed computations.

7.11 Author Contributions

René Schubert and Prof. Dr. Arne Biastoch discussed and identified the overall research questions. René Schubert developed the specific strategy, executed the numerical model experiments, decided on the model output analysis techniques, performed all analysis, created all figures, and wrote the text of the study. Prof. Dr. Arne Biastoch, Prof. Dr. Jonathan Gula, Prof. Dr. Richard J. Greatbatch and Prof. Dr. Burkard Baschek contributed ideas to the analysis and reviewed the manuscript. Prof. Dr. Arne Biastoch further contributed ideas to the structure of the manuscript and helped to develop the analysis strategy.

8 Study III: The Role of Submesoscale Dynamics in the Formation of Mesoscale Eddies at the Agulhas Bank

> *We listened carefully to those who had actually made the trip around the cape and especially to those who had sailed both ways around. Their opinions were divided; some reported good passages and others bad, both close to shore and well offshore on the edge of the bank. It was a matter of chance; each skipper had to make his own decision.*
>
> **— S.L. Seaton in Seaton (1980)**

This last main chapter is an organized collection of results in preparation for a further paper that is planned to be submitted to a peer-reviewed international journal after my doctorate. This chapter does not claim to be a finalized scientific study. Copyright in this work may be transferred without further notice.

8.1 Abstract

The formation of mesoscale eddies near the Agulhas Bank is essential for the Agulhas leakage, the warm and salty inflow of Indian Ocean waters into the Atlantic Ocean. The comparison of a submesoscale-permitting ocean general circulation model simulation to a parallel non-submesoscale resolving experiment, as well as to satellite observations indicates that submesoscale dynamics are important for the formation of lee cyclones west of the Agulhas Bank but not for the shedding of Agulhas rings south of the Agulhas Bank. The importance of submesoscale flows for the formation of lee cyclones is attributed to the upstream development of shear-edge eddies forming

at the northern boundary of the Agulhas Current and leaking into the lee cyclones. Energy transfers across temporal scales computed for both model experiments indicate that the region of the shear-edge eddy formation is associated with weak mesoscale barotropic instabilities but strong recurrent submesoscale instabilities. These results combined with those for energy transfers across horizontal scales show that shear-edge eddies are strengthened by the absorption of submesoscale features that develop as a consequence of the submesoscale barotropic instability.

8.2 Introduction

The formation and shedding of mesoscale eddies near the Agulhas Bank is strongly linked to instabilities of the Agulhas Current (AC) (e.g. van Leeuwen et al., 2000; Lutjeharms et al., 2003a,b). North of $34°S$, the northern AC is very stable with respect to mesoscale instabilities due to the steep continental slope in this region (Gründlingh, 1983; Paldor and Lutjeharms, 2009). The major source of variability are large downstream propagating meanders, referred to as Natal Pulses (Lutjeharms and Roberts, 1988; de Ruijter et al., 1999). Natal Pulses develop upstream in the Natal Bight and propagate downstream with a phase speed of 20 km/day (Lutjeharms and Roberts, 1988). On their landward side they are associated with mesoscale cyclones (Gründlingh, 1979). South of the Agulhas Bank, these cyclones are observed to propagate southwestward into the open ocean, to cross the retroflected AC, and to initialize the shedding of Agulhas rings (van Leeuwen et al., 2000; Lutjeharms et al., 2003a). Agulhas rings propagate northwestward and contribute the largest part to the Agulhas leakage, the inflow of warm and salty Indian Ocean waters into the Atlantic, which is of importance for the meridional overturning circulation (De Ruijter et al., 1999; Weijer et al., 2002; Biastoch et al., 2008b, 2015; Lübbecke et al., 2015).

South of $34°S$, shallower continental slopes enable the development of mesoscale instabilities of the AC. Moreover, as the AC separates from the coast, strong horizontal shears between the current and the relatively slowly moving waters on the shelf further contribute to mesoscale as well as submesoscale barotropic instabilities (Lutjeharms et al., 1989; Tedesco et al., 2019). The mesoscale instabilities are associated with downstream-propagating small meanders and shear-edge eddies that grow in size with time (Lutjeharms et al., 1989, 2003a). These boundary phenomena are important for the shelf-interior exchange which is important for the ecosystems on the shelf that is of importance for the South African fishery (Lutjeharms et al., 1989). Shear-edge eddies, sometimes also called "frontal eddies", have a diameter of 50 - 100 km and are associated with warm plumes on their western and northern side (Schumann and van Heerden, 1988; Lutjeharms et al., 1989, 2003b). Both, plumes and shear-edge eddies are observed to extend through the whole water column. In particular the plumes are however surface intensified (Lutjeharms et al., 1989). Two of such plumes are visible in a 1 km horizontal resolution product of the sea-surface temperature (SST) derived with a Moderate Resolution Imaging Spectroradiometer (MODIS, Minnett et al., 2002) in the Agulhas Bank Bight (Fig. 8.1a, ii). The plumes additional indicate the presence of cold-core shear-edge eddies.

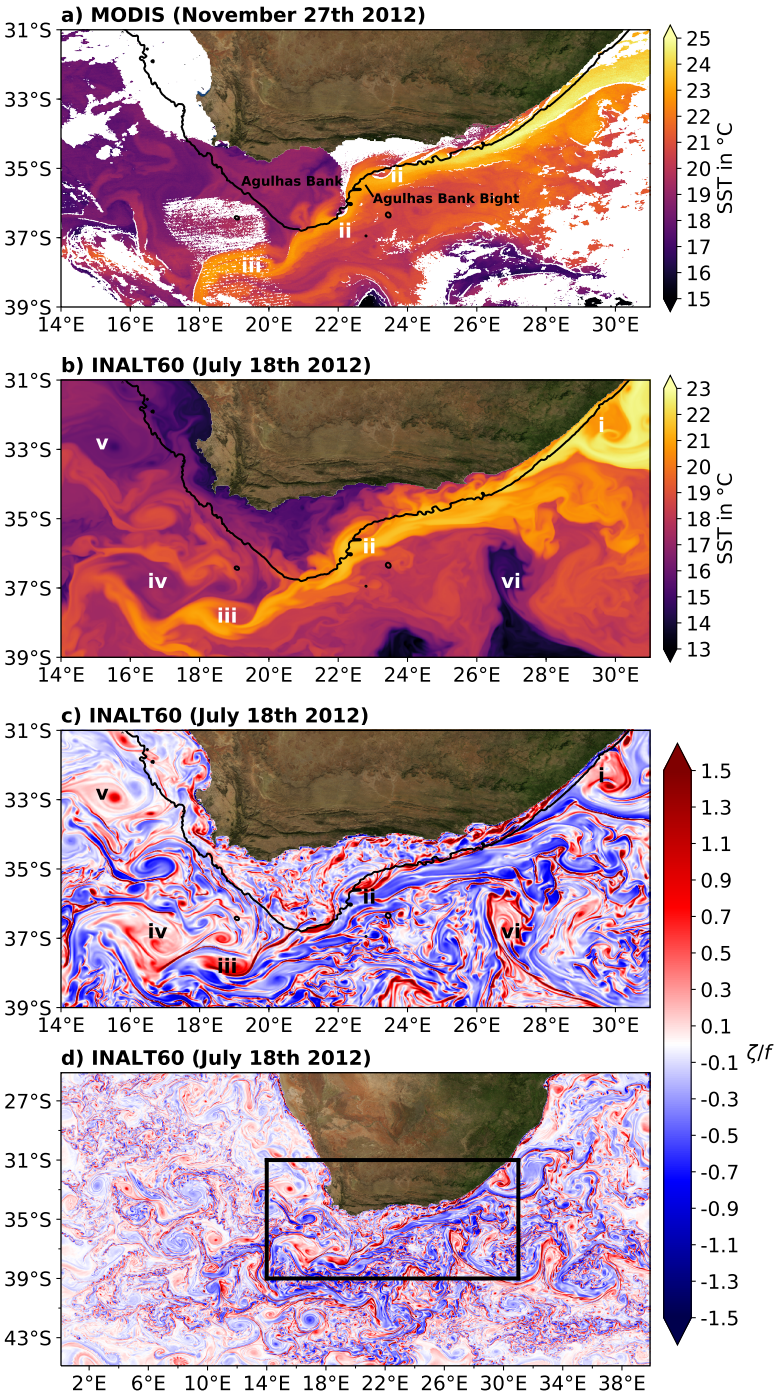

Fig. 8.1: *(a) Observed data from a MODIS SST swath taken on November 27th 2012 (NASA Goddard Space Flight Center, 2015c) compared to (b) a SST snapshot from INALT60 on model day July 18th 2012. Data gaps in (a) are mainly due to clouds. In (c) and (d), the respective snapshot of surface normalized relative vorticity is shown. The black box in (d) marks the region for (a) - (c). The black contour in (a) - (c) shows the 400 m isobath (ETOPO1, www.earthmodels.org/data-and-tools/topography/etopo) highlighting the location of the Agulhas Bank. In (a) - (c) different types of mesoscale cyclonic motions are marked: i) a Natal Pulse inherent cyclone, ii) a shear-edge cyclone in the Agulhas Bank bight, iii) a shear-edge cyclone southwest of the Agulhas Bank, iv) a lee cyclone, v) a cyclone that developed near the upwelling region, and vi) a cyclone shed by an Agulhas Return Current meander.*

In contrast to the shear-edge eddies, the plumes are observed to move onto the shelf and to be occasionally shed as Agulhas filaments northwestward into the South Atlantic providing a further contribution to the Agulhas leakage (Lutjeharms et al., 1989; Lutjeharms and Cooper, 1996). The shear-edge eddies are trapped in the Agulhas Bank Bight between the continental slope and the AC (Lutjeharms et al., 1989, 2003b). From this reservoir of cyclonic motion, vorticity is found to leak downstream towards the tip of the Agulhas Bank that is absorbed by lee cyclones west of the southern Agulhas Bank (Lutjeharms et al., 2003a). Lutjeharms et al. (2003b) formulated the possibility that it is also possible that the strong meandering of the AC lets the trapped shear-edge cyclone escape the Agulhas Bank Bight. The shear-edge eddy southwest of the Agulhas Bank in the observed swath (Fig. 8.1d, iii) is presumably such an escaped cyclone. Lutjeharms et al. (2003b) further hypothesized that this and other large vorticity leakages may even initialize the lee cyclone formation.

The lee cyclones can reach diameters of more than 200 km and detach from the slope (Penven et al., 2001; Lutjeharms et al., 2003a). They move into the Cape Basin where they strongly interact with the Agulhas rings and other eddies (Boebel et al., 2003). This interaction is associated with the formation of submesoscale flows that strengthen the mesoscales (Schubert et al., 2020) and drive a watermass exchange of Agulhas rings with their surroundings with potential impact on the Agulhas leakage (Capuano et al., 2018a; Sinha et al., 2019).

A further submesoscale phenomenon is observed at the northern boundary of the AC. During periods without Natal Pulses, submesoscale vortices with diameters of 10 - 20 km are observed to develop between $35°S$ $(24°E)$ and $33.5°S$ $(28°E)$ (Lutjeharms et al., 2003a; Krug et al., 2017; Tedesco et al., 2019). Similar to the shear-edge eddies, the submesoscale vortices are observed to be associated with warm plumes on their northwestern side. Lutjeharms et al. (2003a) refer to them as "wake eddies" as they observed them to occur upstream of shear-edge cyclones. Tedesco et al. (2019) refer to them as "frontal eddies" as they, as well as Krug et al. (2017), attribute the generation of the submesoscale vortices to submesoscale barotropic shear-instability on the basis of an energy transfer analysis. At $26°E$, the dynamics are found to change as the AC separates from the continental slope (Tedesco et al., 2019). As a consequence, the submesoscale vortices are found to grow to diameters of up to 50 km while traveling downstream (Tedesco et al., 2019).

A major open question is, whether the shear-edge eddies are mainly driven by the mesoscale instabilities of the AC downstream of $26°E$ or whether they are

strengthened by an upscale transfer from the submesoscales. The trapped shear-edge eddies might collect the cyclonic vorticity of downstream-travelling submesoscale features that develop further upstream due to submesoscale barotropic instability. It could even be possible that submesoscale vortices grow to mesoscale shear-edge eddies while traveling downstream. As pointed out above, the shear edge eddies are key for the development of plumes that contribute to Agulhas leakage, as well as for the lee cyclone formation and strength. The lee cyclones strongly interact with the Agulhas rings with potential impact on the Agulhas leakage through the accompanied submesoscale exchange of Agulhas ring waters with their surrounding. Thus, if the submesoscale dynamics at the northern boundary of the AC are important for the shear-edge eddy formation, they are of importance for the Agulhas leakage.

This study addresses the question, which role submesoscale dynamics play for the formation of Agulhas rings, lee cyclones, and shear-edge eddies near the Agulhas Bank. Therefore, two parallel ocean general circulation model experiments are analyzed. The first is the submesoscale-permitting $(1/60)^\circ$ horizontal-resolution simulation "INALT60" and the second the $(1/20)^\circ$ horizontal-resolution simulation "INALT20r" that resolves almost no submesoscale flows. Both experiments are introduced in detail by Schubert et al. (2019) and summarized in section 7.3. A model snapshot of INALT60 on July 18$^{\text{th}}$ 2012 of SST (Fig. 8.1b), as well as of the vertical component of the surface relative vorticity normalized by the planetary vorticity[11] (Fig. 8.1c) shows that the model is able to reproduce the cyclonic features near the Agulhas Bank described above: a Natal-Pulse inherent cyclone (i), shear-edge eddy related plumes in the Agulhas Bank Bight (ii) as well as southwest of the Agulhas Bank (iii) with similar size as the observed ones, as well as a detached lee cyclone (iv).

The study is structured as follows. First, in section 8.3, previous results of Schubert et al. (2019) are discussed in the framework of the dynamical processes outlined above. It is concluded that submesoscale flows have only a minor impact on the Agulhas ring shedding. Further, in section 8.3, it is indicated that the resolution of submesoscale flows improves the representation of lee cyclones in the model. Subsequently, in sections 8.4, 8.5, and 8.6, the kinetic energy transfer through temporal and spatial scales is analyzed to show that submesoscale dynamics are important for the shear-edge eddy formation. A conclusion is provided in section 8.7 and an outlook in section 8.8.

[11] The vertical component of the relative vorticity is given by $\zeta = v_x - u_y$ where u is the zonal velocity component, v is the meridional velocity component, x is the zonal Cartesian axis and y the meridional axis. Partial derivatives of a with respect to b are written throughout this chapter as $\frac{\partial a}{\partial b} = a_b$. The planetary vorticity is given by $f = 2\Omega sin(2\pi \frac{\theta}{360^\circ})$ where $\Omega = \frac{2\pi}{86400}$ 1/s is the angular speed of the Earth and θ the latitude.

8.3 Submesoscales are Not Important for the Agulhas Ring Shedding but for the Development of Lee Cyclones

Schubert et al. (2019) found a general strengthening of eddies in the Agulhas ring path by submesoscale flows. A part of this strengthening was attributed by Schubert et al. (2020) to the submesoscale open-ocean inverse kinetic energy cascade. Consistently, the mean distribution of the maximum sea-surface height (SSH) amplitude (A_{max}) of the eddies in the ring path shifts to larger amplitudes that better compare with the results for the observational L4 Copernicus Marine and Environment Monitoring Service (CMEMS, www.marine.copernicus.eu) satellite altimetry product, if submesoscales are resolved (Fig. 8.2a and 8.2d). The distribution of their scales is similar for both simulations and the observations (Fig. 8.2b and 8.2e). However, if the analysis is restricted to very strong eddies with $A_{max} > 20$ cm, a cyclone-anticyclone asymmetry is found (Fig. 8.2c and 8.2f).

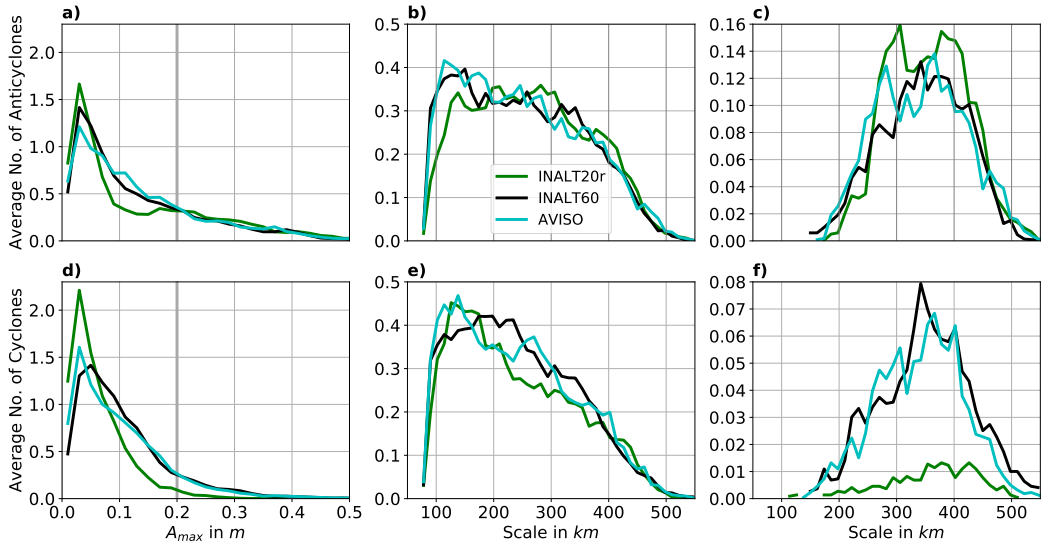

Fig. 8.2: *The results of the SSH-based eddy detection algorithm Schubert et al. (2019) applied to the daily and $0.25°$ horizontal resolution L4 CMEMS altimetric product, as well as to the outputs of INALT60 and INALT20r interpolated onto the observational grid. The figure is a reprint of Figure 11 of Schubert et al. (2019) reduced to the two model experiments that are analyzed for the present study. Shown are histograms of the average number of anticyclones (a) - (c) and cyclones (d) - (f) in the Agulhas ring path ($27°S$ - $41°S$, $1°E$ - $12°E$) as a function of their maximum amplitude A_{max} (a and d) and scale (b and e) for the period 2012 - 2017. The histograms for the eddy scale are shown for all eddies (b and e) and for all eddies with $A_{max} > 20$ cm (c and f).*

The amplitude distribution for strong anticyclones is almost similar for both simulations, as well as very close to altimetric observations. As most of the strong mesoscale anticyclones in the Agulhas ring path are Agulhas rings (e.g. Boebel et al., 2003), this result indicates that the Agulhas ring formation is well represented in both model experiments and further that the submesoscales only have a weak impact on the Agulhas ring shedding.

While the number of strong cyclones is in good agreement with observations in INALT60, the number of strong cyclones cannot be reproduced by INALT20r. Strong mesoscale cyclones in the Agulhas ring path can have different origins and formation mechanisms. The development of lee cyclones west of the Agulhas Bank that detach and propagate into the ring path is one of them. The comparison of the time-mean SSH near the Agulhas Bank (around $37.0°S$, $18.5°E$ see Fig. 8.3 top) shows the presence of a time-mean lee cyclone for the observations, as well as for INALT60 with a similar amplitude. The time-mean lee cyclone is absent in INALT20r. The temporal standard deviation of the SSH, which is a measure of the geostrophic eddy kinetic energy (see section 8.4), exhibits too small values in this region in INALT20r, while INALT60 is close to the observations (Fig. 8.3 bottom). These results indicate that the lee cyclones are better represented in the model, when submesoscales are resolved.

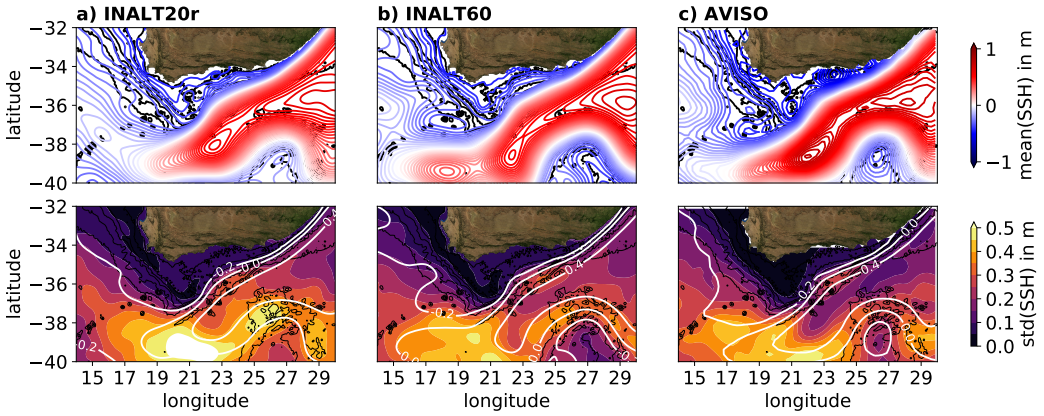

Fig. 8.3: *(a) The representation of the time-mean lee cyclone west of the Agulhas Bank improves with the resolution of submesoscales in the model. The top panels show the 2012 - 2017 time-mean SSH anomaly in m from the non-submesoscale resolving experiment INALT20r, (b) the submesoscale-permitting experiment INALT60 and (c) the observational L4 CMEMS satellite altimetry product. For a better comparison, the domain average has been removed from all mean SSH fields. In the bottom panels, the temporal standard deviation of the SSH in m is shown. White contours show the time-mean SSH in m. Black contours are the 100 m, 250 m, 1000 m, 2000 m, 3000 m, and 4000 m isobaths from the ETOPO1 bathymetry.*

The better representation of the lee cyclones contributes to a better agreement between INALT60 and observations in terms of distribution and numbers of strong cyclones. Other cyclones of different origin and with different formation mechanisms might contribute further to the good representation of strong cyclones in INALT60, for example cyclones that develop at the front of the Benguela upwelling system (Lutjeharms and Stockton, 1987; Boebel et al., 2003; Rubio et al., 2009). Such a cyclone can be seen in the model snapshot (Fig. 8.1b-c, v). The formation of these cyclones potentially also involves submesoscale processes that may be represented in INALT60 but are missing in INALT20r. The cyclone formation near the upwelling regions is not further addressed in this study.

In summary, the results indicate that submesoscale processes are not important for the shedding of Agulhas rings but for the strength of the lee cyclones. The lee cyclones are important for the climate, as they propagate into the Agulhas ring path, where they strongly interact with the Agulhas rings. This interaction drives a submesoscale strengthening of the eddies (Schubert et al., 2020) and a submesoscale exchange of Agulhas ring water with their surroundings (Capuano et al., 2018a; Sinha et al., 2019) and thus is of importance for the Agulhas leakage. The lee eddies are thought to be strengthened or even initialized by shear-edge eddies that develop upstream at the northern boundary of the AC (Lutjeharms et al., 2003b). The fact, that the lee cyclones are better represented, indicates that also the shear-edge eddies are better represented in the model, if submesoscales are resolved. In the next sections, it is investigated, which role the submesoscales play in the formation of shear-edge eddies. Therefore, maps of the kinetic energy transfer through temporal and spatial scales are presented. With those it is indicated which parts of the AC are associated with which instabilities and which parts are associated with upscale fluxes from the smaller scales to the larger.

8.4 Kinetic Energy Transfer Through Temporal Scales

The kinetic energy transfer through a temporal scale T, and thus from the ocean circulation on longer time scales to the one on shorter time scales than T, is derived in this section on the basis of the classic eddy-mean flow energy transfer analysis (e.g. Harrison and Robinson, 1978; Storch et al., 2012). In the classic eddy-mean flow concept, first the primitive equations are Reynolds-decomposed. On the basis of the decomposed equations, the time-mean kinetic and available potential energy are split into a reservoir associated with the kinetic and available potential energy of the time-mean circulation ("Mean Kinetic Energy" (MKE) and "Mean Available Potential Energy"(MPE)) and a reservoir associated with the kinetic and available potential energy of the time-varying circulation ("Eddy Kinetic Energy" (EKE) and "Eddy Available Potential Energy" (EPE)). Subsequently. the energy transfer from the MKE to the EKE is identified in the EKE budget to be

$$MKE \rightarrow EKE = \underbrace{-\rho_0[\overline{u'u'}\overline{u}_x + \overline{u'v'}(\overline{u}_y + \overline{v}_x) + \overline{v'v'}\overline{v}_y]}_{\text{HRS}} \underbrace{-\rho_0[\overline{u'w'}\overline{u}_z + \overline{v'w'}\overline{v}_z]}_{\text{VRS}},$$

where $\rho_0 = 1024$ kg/m^3 is the reference density and w is the vertical velocity component. Overbars denote the mean over the investigated period and dashes deviations from that mean. Positive transfer through the horizontal Reynolds stresses (HRS) is an indicator of barotropic instability and positive transfer through the vertical Reynolds stresses (VRS) of vertical shear-instability (e.g. Storch et al., 2012; Gula et al., 2016). An increase in EKE due to the energy transfer from the EPE into the EKE, which is given by the vertical buoyancy flux $VBF = \overline{w'b'}$ (e.g. Harrison and Robinson, 1978; Storch et al., 2012), is an indicator of baroclinic instability. Here, $b = -\frac{g}{\rho_0}\rho$ is the buoyancy with the potential density ρ and the gravitational acceleration $g = 9.81$ m/s^2.

It is important to note that, while the energy transfer from EPE to EKE equals the one from EKE to EPE, additional terms arise in the EKE to MKE energy transfer that do not exist in the MKE to EKE term (e.g. Storch et al., 2012). These terms transfer energy in space and vanish only when integrated over a closed domain. Maps of HRS and VRS have thus to be interpreted carefully, in particular if they show negative values. Then, they are only interpretable as sinks of EKE that potentially is due to transfers towards the mean flow. Further evidence for the direction of the transfer can be gained when the transfer through temporal scales is compared to the transfer through spatial scales under the assumption that processes with smaller temporal scales are also associated with smaller spatial scales. This is done in section 8.6.

The vertically integrated HRS and VBF averaged over and referenced to the total period (here 2012 - 2017) are commonly used as indicators for the mesoscale barotropic and baroclinic instability of a larger-scale current. They are shown computed for the daily INALT60 output in Figures 8.4a and 8.4b. The VRS is not further addressed here. As expected, HRS and VBF are strongest for the regions of the AC and the ARC. Largest positive values occur for both terms in the AC between $27°E$ and $23°E$ and just south of the Agulhas Bank. The HRS shows much larger values than the VBF. The results indicate that the AC, represented in this case by the time-mean flow, undergoes mixed-baroclinic-barotropic instability in both regions with the barotropic instability being by far the dominant one. For this reason, the remaining study focuses on the kinetic energy transfer. In particular the northern boundary of the AC is associated with strong positive HRS in both regions. The western Agulhas Bank Bight is associated with large negative transfers. Further coherent regions with negative transfers are found southwest of the time-mean lee cyclone, as well as along the western flank of the Agulhas Plateau. Although the results of the energy transfer analysis need to be interpreted with care, when they are negative, they indicate that the mean flow is stabilized in these regions. In the Agulhas Bank Bight, the trapped shear-edge eddies might feed a part of their energy upscale to the AC. West of the retroflection, the lee cyclones (that partly contribute to the mean flow) might be strengthend by the leakage of vorticity from the trapped shear-edge eddies. Finally, the AC might be stabilized by the attachement to the Agulhas Bank.

The energy transfer computations performed for the remaining study are very expensive and thus are only executed for the surface layer. The pattern of the surface mean HRS however, agrees very well with the one of the vertical integral (Fig. 8.4b and 8.4c).

To identify, how the energy transfer changes for different temporal scales T, the period 2012 - 2017 is split into temporal segments of almost equal length T. Subsequently the mean HRS is computed for each segment and averaged over all segments. The computations are executed for annual, semi-annual, monthly and weekly segment lengths representing the kinetic energy transfer through the respective time-scale. Note that, except weekly, the segment lengths are not perfectly equal, due to leap years, the uneven number of days in a non-leap year and the different number of days in a month. For the weekly computations, the remaining 1 or 2 days of the respective year are excluded from the analysis.

In INALT60, the HRS for annual and semi-annual reference periods is generally very similar to the HRS referenced to the total period (Fig. 8.5 right panels). However,

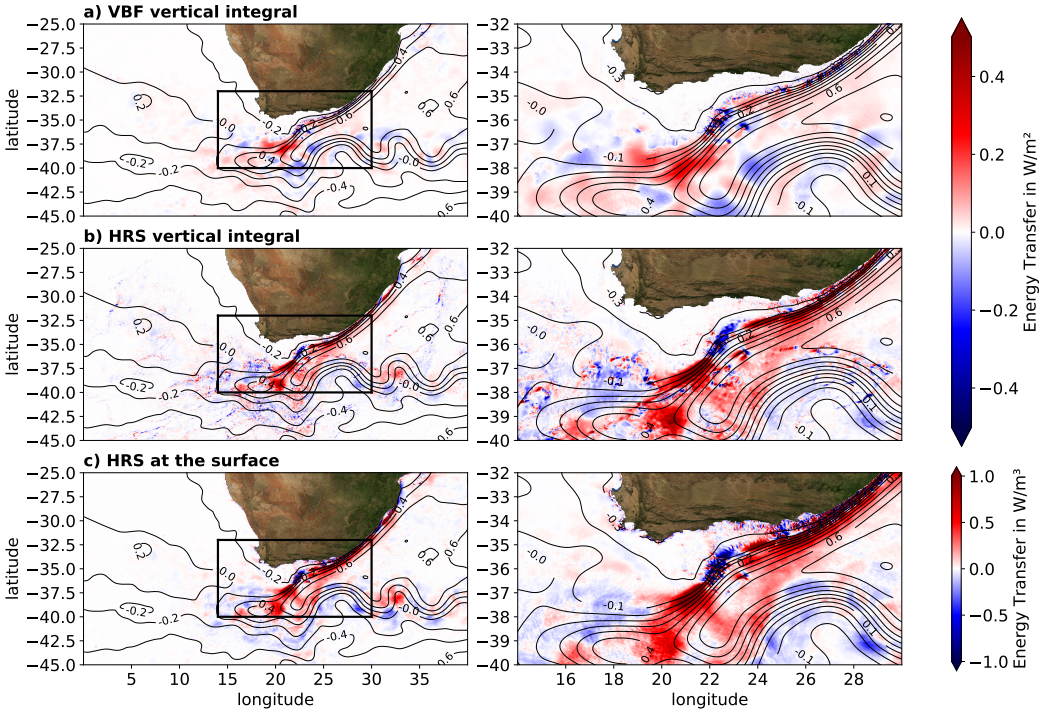

Fig. 8.4: *The vertically integrated energy transfer rates VBF (a) and HRS (b) averaged over and referenced to the period 2012 - 2017 from daily INALT60 data. In (c), the mean HRS in the surface grid cells (upper 1 m) is shown. Thin contours show the time-mean SSH in m. The right panel shows zooms into the marked regions in the left panel.*

the negative transfers south of the time-mean lee cyclone increase with smaller reference period. For a monthly reference period, overall smaller values are found. Even more important, the region of positive HRS between $23°E$ and $27°E$ is confined to the northern boundary of the AC. The pattern for the weekly reference period is again similar to the monthly one but with even smaller values. Besides the noisy HRS over the shelf, it agrees with the vertical integral of HRS presented by Tedesco et al. (2019) for a single one week period from the output of a 750 m horizontal resolution model experiment. Tedesco et al. (2019) show that for the same period, in their simulation, VRS and VBF are much smaller than HRS and thus that the respective submesoscale instabilities at the northern boundary of the AC are attributable to submesoscale barotropic instability. Similar to Tedesco et al. (2019), here we observe that the pattern of strongest HRS at the northern boundary of the AC is similar for all time-scales indicating that the submesoscale instabilites are a locally recurrent process. Similar, the Agulhas Bank Bight is found to be associated with negative HRS for all time-scales.

In INALT20r, the HRS for the different reference periods is similar to INALT60 with respect to both pattern and amplitude (Fig. 8.5). However, INALT20r shows

larger positive HRS at the separation of the AC. Consistently, in the retroflection, the temporal standard deviation of SSH is found to be larger in INALT20r than in INALT60 (Fig. 8.3). Further, almost no negative values are found west of the retroflection in INALT20r, consistent with the too weak lee cyclones in the simulation. Moreover, the positive values of HRS for monthly and weekly periods between $23°E$ and $27°E$ are smaller than in INALT60. The almost absent weekly HRS in INALT20r shows that the process of submesoscale barotropic instability is missing in this simulation.

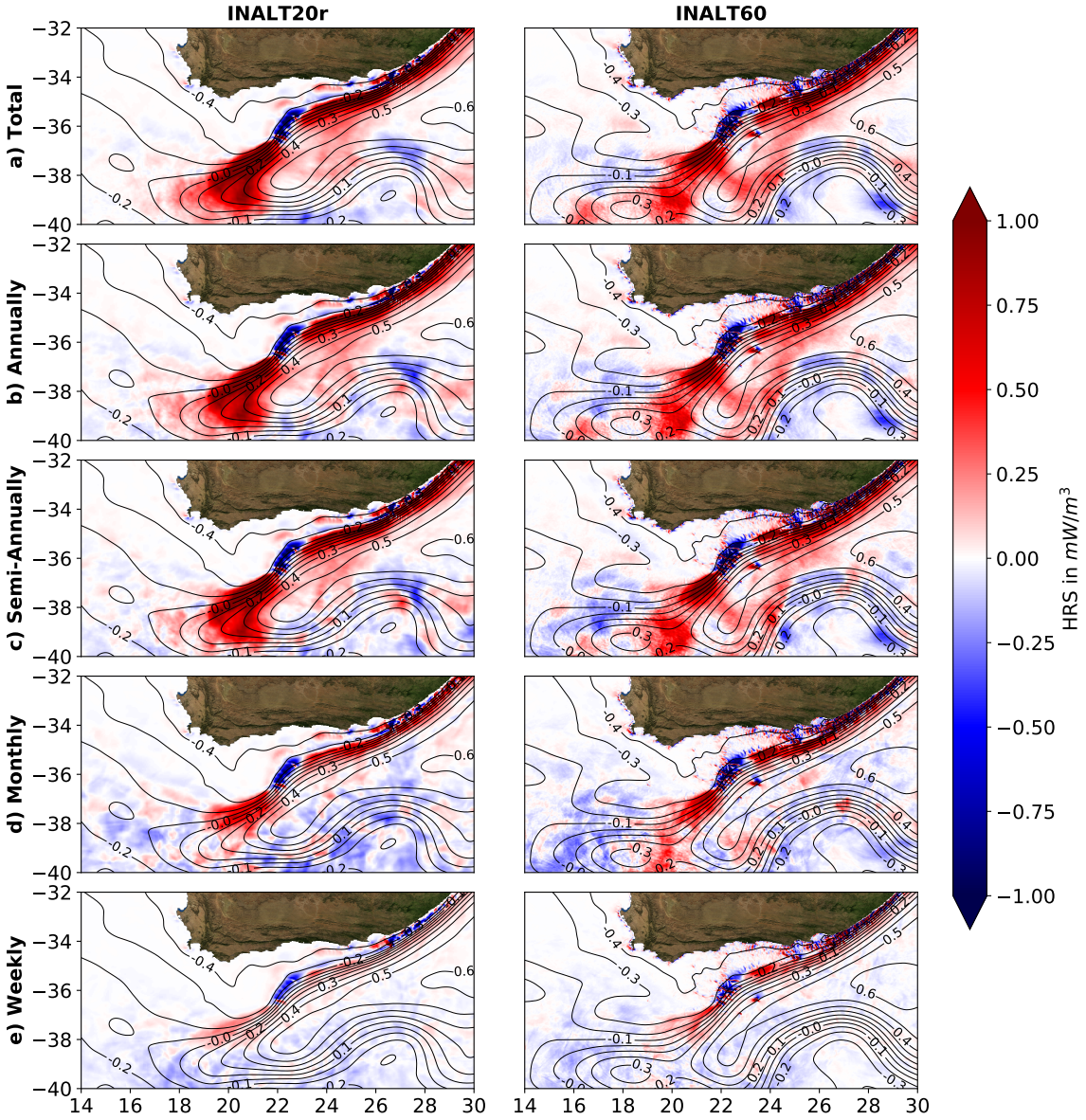

Fig. 8.5: *The surface energy transfer rate HRS (MKE → EKE) computed with different reference periods averaged over the 2012 - 2017 period for INALT20r (left) and INALT60 (right). Thin contours show the time-mean SSH in m.*

8.5 Excluding Periods of Natal Pulses

The evolution of shear-edge eddies (their development upstream of the Agulhas Bank Bight, their entrapment in the bight and leakage into lee eddies) is disturbed by the downstream-propagation of Natal Pulses and associated cyclones. In the present section, the HRS is computed for periods with and without Natal Pulses to investigate, whether the results of the previous section depend on the presence of Natal Pulses and other external disturbances.

Natal Pulses are identified at around $28°E$ along the "Agulhas Current Timeseries (ACT)" section (Beal et al., 2015) similar to the identification method, Krug et al. (2014) used. They identified Natal Pulses along the same section from SSH along-track data as events, where the offshore-distance of the maximum of the southwestward cross-section geostrophic flow is more than one standard deviation larger than on average. As the model output provides the flow for the whole water column, here the vertical integrated transport is used instead of the SSH-based derived geostrophic flow (Fig. 8.6). To account for the variability regarding the short time-scales, which is much stronger in INALT60 compared to INALT20r, a further condition is added on the duration of the event. Here, periods with Natal Pulses at the ACT section are identified as periods, when the offshore-distance of the maximum of the southwestward vertical integrated cross-section transport exceeds the average i) for more than 15 consecutive days and ii) by one standard deviation for at least one day of this period.

The identified periods, shown as darkgrey boxes in Figure 8.6, agree with those identified by eye in animations of the SSH. Events that fulfill only the second condition are not attributable to Natal Pulses. From the SSH animations, it is further identified that Natal Pulses need on average about 100 days from the ACT section to the retroflection. We thus define Natal Pulse periods as 100 day periods starting with the detection of a Natal Pulse at the ACT section (dark- and lightgrey boxes in Fig. 8.6).

Besides the Natal Pulses, also other events can strongly disturb the AC in the region of the shear-edge eddy formation. In INALT60, at the end of the model year 2013, a cyclone detached from the ARC's first meander trough, traveled northwestward and lead to a substantial meandering of the southern AC between December 22nd 2013 and February 11th 2014. This period (see cyan lines in Fig. 8.6b) is not treated separately and is assigned to the "during Natal Pulses" part of the total period.

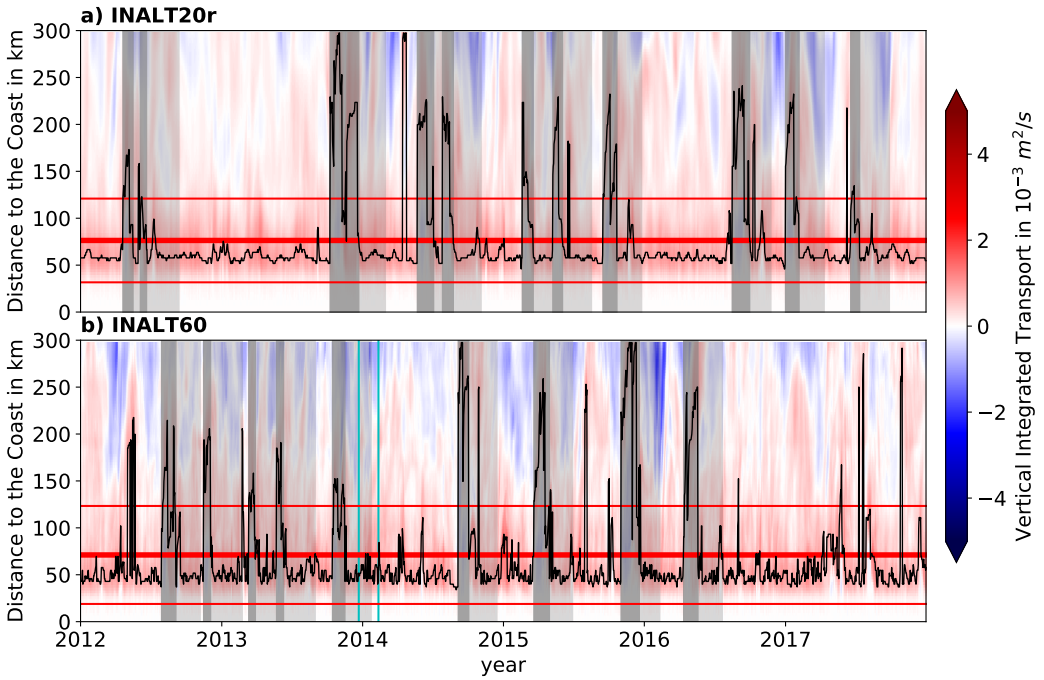

Fig. 8.6: *The vertical integrated southwestward transport at the ACT section (see the thick black line in Fig. 8.7) in INALT20r (a) and INALT60 (b). The black line shows the offshore-distance of the maximum southwestward transport. Red lines mark the average distance plus-minus one standard deviation of the maximum southwestward transport. Darkgrey boxes show the identified periods with Natal Pulses at the ACT. Dark- and lightgrey boxes mark the identified periods with Natal Pulses between the ACT section and the retroflection. The period of a non-Natal-Pulse event that however also strongly disturbed the AC is marked with vertical cyan lines in (b).*

In INALT60, 9 Natal Pulses are identified, two less than in INALT20r. This gives 1.5 and 1.8 Natal Pulses per year, respectively, which is similar to about 1.5 per year identified by Krug et al. (2014). In particular the irregular occurrence, with gaps as long as more than a year in between, agrees with the observations. Due to the irregular occurrence, the question, whether Natal Pulses and their occurrence are systematically different, if submesoscale flows are resolved, cannot be answered on the basis of the short integration period. It is however expected that the submesoscale influence on the Natal Pulses is weak, as the Natal Pulse initialization is controlled by mesoscale instabilities triggered by mesoscale eddies near the Natal Bight (Schouten et al., 2002; Lutjeharms, 2007).

The time-mean SSH pattern is similar for periods with and without Natal Pulses. As expected, in both experiments, the time-mean AC is however associated with a reduced SSH gradient for periods with Natal Pulses compared to those without (Fig. 8.7, contours). The mean HRS is computed for periods with (without) Natal Pulses referenced to the time-mean over all time-steps with (without) Natal Pulses.

The decomposition of HRS from INALT60 into both periods shows that east of $23°E$ most of the transfer, that extends over the whole width of the AC, can be attributed to periods with Natal Pulses. In contrast, the narrow band of large positive HRS at the northern boundary of the AC between $23°E$ and $25°E$ can be mainly attributed to periods without Natal Pulses. The results are consistent with Tedesco et al. (2019), who presented the HRS referenced to a 5-month period without Natal Pulses also showing only a narrow band of strong positive values at the northern boundary of the AC. Figure 8.7 combined with Figure 8.5 indicate that the AC is only weakly unstable with respect to mesoscale barotropic instabilities. In contrast, its northern boundary appears to be strongly unstable to recurrent submesoscale barotropic instabilities.

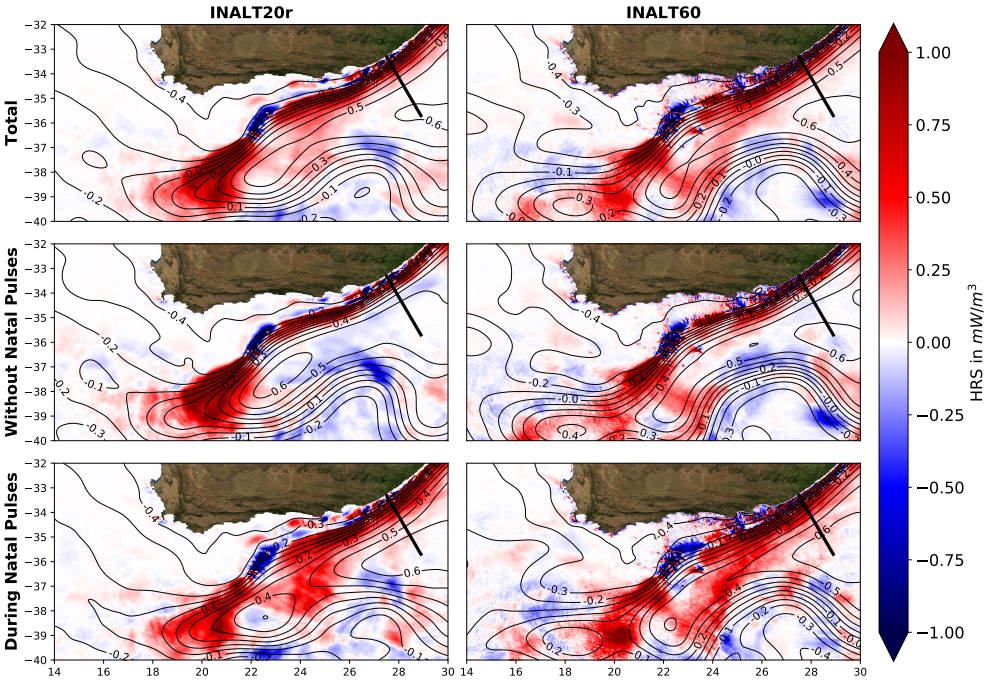

Fig. 8.7: *The surface energy transfer rate HRS (MKE → EKE) computed for the period 2012-2017 (a) referenced to the total period, (b) for periods without Natal Pulses and (c) periods with Natal Pulses for INALT20r (left) and INALT60 (right). Thin contours show the respective time-mean SSH in m. The thick black line shows the position of the ACT section used for Figure 8.6.*

In INALT20r, during periods without Natal Pulses, large positive HRS are also confined to the northern boundary of the AC. However, the band of positive HRS has a much larger width compared to INALT60. This result is interpreted as barotropic instabilities along the northern boundary of the AC which are associated with larger scales than in INALT60. Moreover, the HRS pattern for periods without Natal Pulses is very similar to the pattern of the monthly HRS referenced to the total period

(Fig. 8.5d, left) while the one of INALT60 is closer to the respective weekly HRS (Fig. 8.5e, right). The barotropic instabilities at the northern boundary of the AC in INALT20r might thus consistently also be associated with larger time-scales than those in INALT60.

8.6 Kinetic Energy Transfer Through Spatial Scales

The temporal energy transfer analysis indicated that the AC undergoes both mesoscale and submesoscale barotropic instabilities in the region of the shear-edge eddy development. Downstream, in the Agulhas Bank Bight, negative HRS is found. This indicates a kinetic energy transfer from smaller temporal scales to larger ones. It is thus hypothesized that submesoscale features, resulting from the submesoscale barotropic instability, flux their kinetic energy to the shear-edge eddies and are thus important for their formation and strengthening. However, as discussed above, the mentioned indication needs to be handled with care, as the energy transfer analysis does not strictly separate transfers from the eddy field to the mean flow and transfers of kinetic energy in space.

For more evidence in this respect, the analysis is complemented by the computation of the flux of kinetic energy between horizontal spatial scales. Therefore, a coarse-graining approach is applied that has been developed by Leonard (1975), Germano (1992) and Eyink (2005). In this approach, the primitive equations are low-pass filtered. Here, for the filtering, each horizontal field is convoluted with a two-dimensional top-hat convolution kernel. The top-hat kernel consists of a circle of diameter L associated with the value one surrounded by zeros and is normalized by the area of the circle. The convolution filters out all horizontal scales smaller than L. Similar to the temporal energy transfer approach, the scale kinetic energy flux (the rate of kinetic energy transfer from currents with scales larger than L to currents with scales smaller than L) is identified in the budgets for the kinetic energy of the larger scales (the filtered fields) and the smaller-scales. In contrast to the temporal approach, the resulting scale kinetic energy flux occurs in both budgets without additional terms for one of the two directions. The definition of the scale kinetic energy flux, in distinction to the spatial transfer of kinetic energy, is still associated with a gauge freedom (e.g. Aluie et al., 2018). Here, we use a separation of transfers across scales and in space that is suggested by Aluie et al. (2018) as a suitable one. In contrast to other separations, the resulting scale kinetic energy fluxes are Galilean invariant (independent of the movement of a fictional observer). A summary of the derivation of the scale kinetic energy flux based on Germano (1992) and Aluie et al. (2018), as well as its application to the INALT60 output is presented by Schubert et al. (2020) (sec. 7.5). The horizontal scale kinetic energy flux from the larger to the smaller horizontal scales is derived to be

$$\Pi = -\rho_0[(\overline{u^2} - \overline{u}^2)\overline{u}_x + (\overline{uv} - \overline{u}\,\overline{v})(\overline{u}_y + \overline{v}_x) + (\overline{v^2} - \overline{v}^2)\overline{v}_y],$$

where the overbars denote the filtered fields. Note that the form of Π is equal to the HRS, as for the Reynolds-decomposition $\overline{a'b'} = \overline{ab} - \overline{a}\,\overline{b}$. Further note, that in the present study for a better comparison to the HRS the opposite sign is used as in Schubert et al. (2020).

The surface Π computed from the INALT60 output for L = 7 km, 10 km, 15 km, 20 km, 30 km, 45 km, 60 km and averaged over periods with and without Natal Pulses is shown in Figure 8.8. For horizontal scales of 20 km and smaller, Π is mainly directed towards smaller scales (downscale). In the open ocean, the downscale transfer is mainly confined to frontogentic regions, in particular through scales of 7 km and 10 km (Schubert et al., 2020). Strongest downscale fluxes occur in a narrow band along the northern boundary of the AC upstream of its separation from the continental slope. These fluxes are much larger in periods without Natal Pulses. The narrow band is interrupted in the Agulhas Bank Bight, where upscale fluxes are found for scales larger than 15 km. In the open ocean, the mean fluxes mainly change to upscale at scales larger than 20 km. The pattern along the northern boundary is however found to be consistent throughout the investigated scales.

This pattern along the northern boundary supports the findings in the previous section and is interpreted as follows. Upstream of the Agulhas Bank Bight, submesoscale instabilities dominate the scale kinetic energy flux and are associated with downscale fluxes from the AC to smaller scales. The resulting eddies have diameters of 10 km and grow in size during their downstream propagation (Krug et al., 2017; Tedesco et al., 2019). They feed their kinetic energy upscale into the shear-edge eddies, in particular into the trapped ones in the Agulhas Bank Bight. There, consistently, upscale fluxes are dominant for scales larger than 15 km. Features that leak from the Agulhas Bank Bight are observed to accelerate and to be squeezed south of the tip of the Agulhas Bank (Lutjeharms et al., 2003a). This squeezing contributes to the downscale transfer found for this region. Further, Lutjeharms et al. (2003a) observed that the leaking features are occasionally small compared to the trapped shear-edge eddies. The separation of the small features from the shear-edge eddy might provide a further contribution to the downscale transfer. West of the Agulhas Bank, for scales of 45 km and 60 km a regional maximum in the upscale transfer is found. This is attributed to the absorption of the leaked features by the lee cyclones. For the temporal energy transfer analysis, the negative HRS in this region is strongest for semi-annual periods (Fig. 8.5) indicating that the kinetic energy is transferred mainly to mesoscale features associated with similar time-scales.

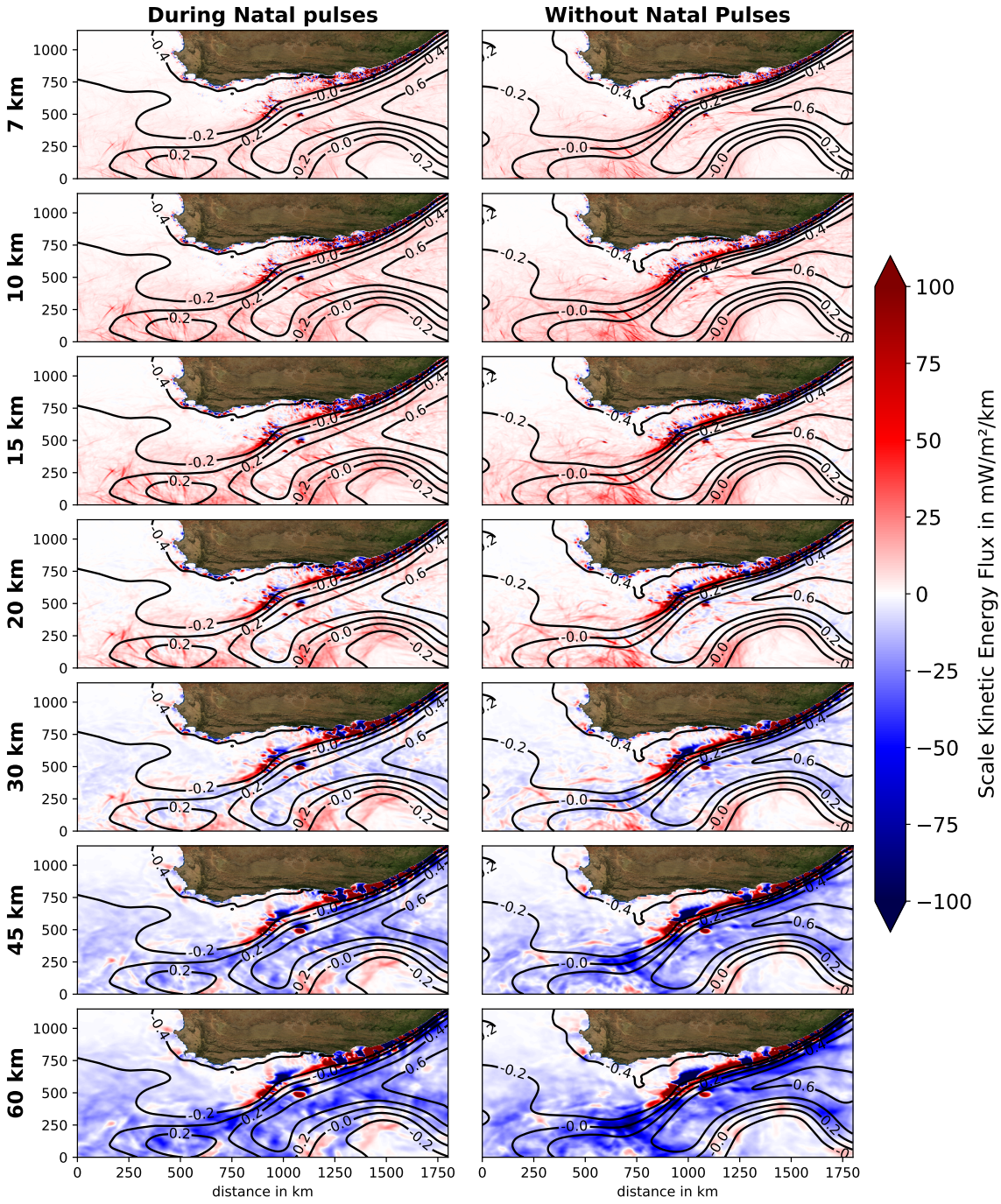

Fig. 8.8: *The surface kinetic energy flux* Π *through different horizontal scales averaged over periods (a) with and (b) without Natal Pulses in INALT60 for the years 2012 - 2017. Negative values show upscale fluxes to larger scales and positive downscale fluxes to smaller scales. The contours show the respective time-mean SSH in m.*

8.7 Conclusion

The present study addresses the role of submesoscale flows in the formation of mesoscale eddies near the Agulhas Bank south of Africa. Therefore, the submesoscale-permitting ocean general circulation model experiment INALT60 and the parallel non-submesoscale-resolving experiment INALT20r are analyzed. Both were introduced and compared with different foci by Schubert et al. (2019) and Schubert et al. (2020). Based on the results of Schubert et al. (2019), first it is argued that the submesoscale dynamics only have a weak impact on the shedding of Agulhas rings. Second, a comparison of the time-mean sea-surface height (SSH) and its temporal standard deviation from the models to a gridded observational product shows that lee cyclones west of the Agulhas Bank are better represented if submesoscales are resolved. The lee cyclones travel into the Agulhas ring path and strongly interact with the Agulhas rings which potentially has an impact onto the Agulhas leakage. Third, the role of submesoscale flows on the formation of shear-edge eddies at the northern boundary of the AC is investigated, as they are important for the lee cyclone formation. A temporal energy transfer analysis, that is a common tool to investigate where a large-scale current undergoes which instabilities frequently, indicates that the Agulhas Current in the region of the shear-edge eddy development is associated with strong recurrent submesoscale instabilities and weak mesoscale barotropic instabilities. A complementing spatial energy transfer analysis indicates that submesoscale features, resulting from the submesoscale barotropic instability, flux their kinetic energy upscale into the shear-edge eddies, in particular in the Agulhas Bank Bight. It is concluded that submesoscale dynamics at the northern boundary are important for the shear-edge eddy and lee cyclone formation but not for the Agulhas ring shedding.

8.8 Outlook

In this section, additional analyses are collected that either could increase the evidence for the conclusions drawn from the presented results or could lead to more specific conclusions. Moreover, scientific open issues consecutive to the present study are formulated.

First, an eddy tracking algorithm applied to the model outputs and the gridded L4 CMEMS SSH product for the eddies in the Cape Basin could confirm that strong anticyclones in the Cape Basin are mainly Agulhas rings. Eddy tracking could further reveal, which part of the improvements in the representation of strong cyclones in INALT60 is attributable to an improved representation of lee cyclones. Moreover, the origins of the eddies in the Cape Basin could be identified and compared to the observations by Boebel et al. (2003) (Fig. 1.4). If the eddies that originate from the upwelling region are also better represented in INALT60, it is worth to investigate the role of submesoscales in their formation on the basis of the model experiments used here.

The development and occurrence of shear-edge eddies needs to be investigated on the basis of observations to judge the quality of the model solution. One could do this on the basis of satellite-based (e.g. Rouault et al., 2010) or better shore-based radar measurements. The latter are existent, but are however not available for the scientific community and the public. The connection of shear-edge eddies and lee cyclones could be analyzed further in the model outputs with a Hovmöller diagramm of SSH along the northern boundary of the AC, similar to Krug et al. (2014). With this method one might also address the development of shear-edge eddies east of the Agulhas Bank bight.

With respect to the conclusion that the shear-edge eddies are strengthened by the absorption of submesoscale features that are a result of the submesoscale barotropic instability at the northern boundary of the AC, the vertical scale of the involved features should be investigated. Tedesco et al. (2019) show that the vertical extent of the strong positive HRS along the northern boundary of the AC is increasing from about 25 m at $28°E$ to about 50 m at $26°E$ implying a downstream growth of the vertical extent of the submesoscale eddies. It remains open, whether this increase continues further downstream.

The results of the temporal energy transfer analysis presented in this study could be further complemented by showing also the decomposition of the VBF and the VRS into periods with and without Natal Pulses. This would reveal whether there is indication for baroclinic and vertical-shear instability of the AC during both periods and how the magnitude of the respective energy transfers relate to the one of the HRS. Further, the development of single shear-edge eddies and of the associated pattern of the spatial scale kinetic energy flux could be investigated to illustrate the absorption of smaller-scale features by the shear-edge eddies. Finally, the temporal as well as spatial energy transfer analyses should also be applied to the model output of the 750 m and 2 km resolution domains of the ROMS model simulation of Tedesco et al. (2019) and directly compared to those of INALT60. The evidence for the drawn conclusions would increase strongly, if the same conclusions are drawn on the basis of two very different ocean models.

In the present study, the simulated submesoscale instabilities at the northern boundary of the AC are not closely investigated. A one-dimensional linear stability analysis for an idealized AC, presented by Tedesco et al. (2019), shows largest perturbation growth rates for wavelengths of 10-15 km consistent with the observed and simulated submesoscale eddies that develop as a result of the submesoscale barotropic instability at the northern boundary of the AC. Thus, the development of the submesoscale eddies is explainable only by the horizontal shear of the flow. A snapshot of surface normalized relative vorticity in INALT60 shows the presence of streaks of cyclonic vorticity downstream of small-scale topographic features at the continental slope (Fig. 8.9a, e.g. around $25°E$ and $26°E$). These features may have a triggering effect on the submesoscale instabilities and potentially impact the shear-edge eddy formation. To identify the influence of such and other small-scale topographic features on the Agulhas dynamics, a parallel INALT60 experiment with smoothed bathymetry is planned. For the smoothing one option would be to convolute the INALT60 bathymetry with a 50 km top-hat convolution kernel (Fig. 8.9b and 8.9c). This choice removes most of the small-scale topographic features, but does not smooth the continental shelf break too strongly. The latter is important, as a strong smoothing of the continental slope is found to be associated with a deceleration of the AC and an increased Agulhas leakage (Speich et al., 2006). Another issue of smoothing the bathymetry is that sea-mounts are broadened by the smoothing (e.g. Fig. 8.9b and 8.9c, $36.5°S$, $23.5°E$). This could lead to a spurious detachment of the large-scale flow to the broadened sea-mount. A solution could be an artificial removement of the sea-mounts before the smoothing.

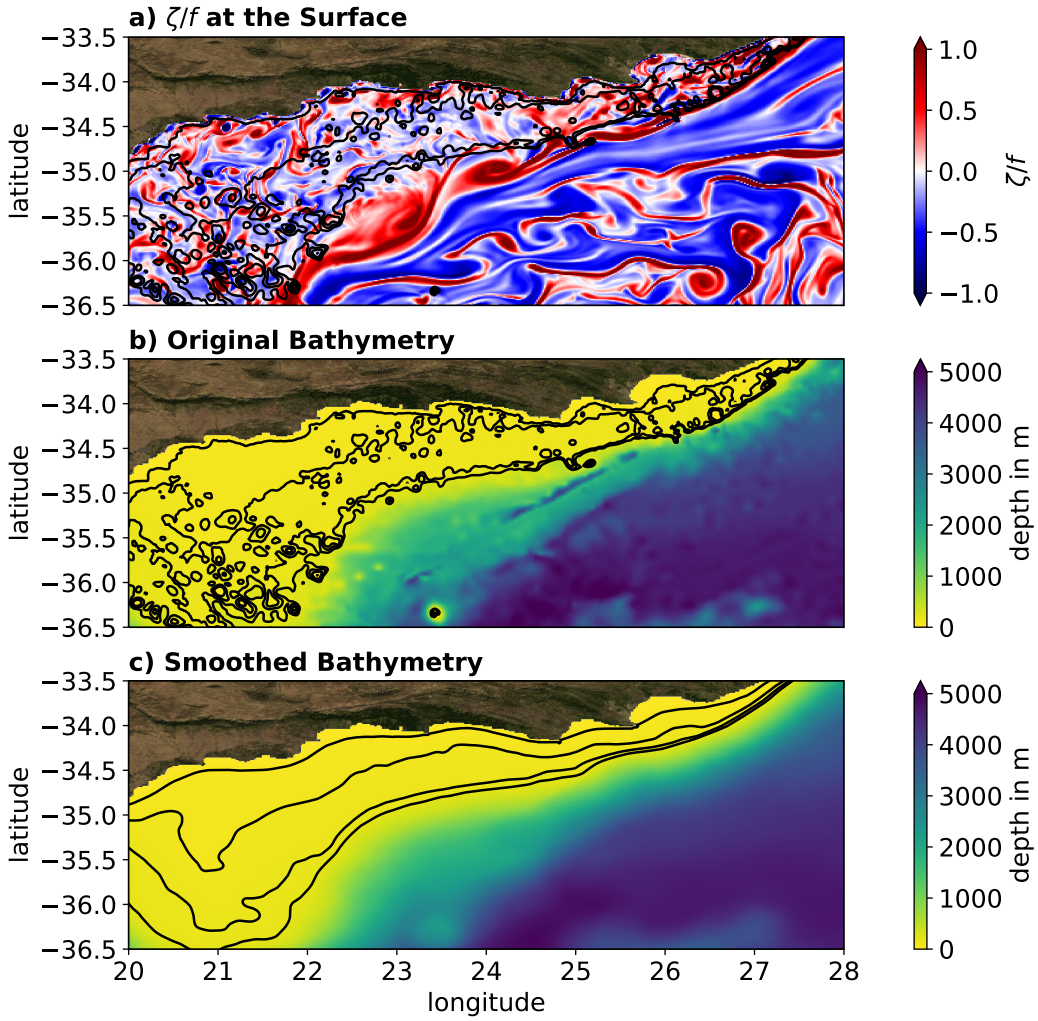

Fig. 8.9: *(a) The surface normalized relative vorticity in INALT60 on model day September 23th 2013 south of Africa, (b) the INALT60 bathymetry and (c) the INALT60 bathymetry smoothed with a 50 km diameter top-hat convolution kernel. Contours show the isobaths from 50 m to 200 m with a contour interval of 50 m.*

Synthesis and Outlook

9

> *After climbing a great hill, one only finds that there are many more hills to climb.*
>
> **— Nelson Mandela**

The small spatial and temporal scales as well as the large variety of submesoscale processes make research on submesoscales themselves and even more on their impact on the larger scales a challenging task with respect to observations, modeling and theory. Progress can be made only iteratively and is achieved in this dissertation by considering all three categories. Existing cutting-edge observations are analyzed in a new way to validate and develop a series of submesoscale-permitting ocean model simulations for the Agulhas region. Subsequently, simulations with different abilities to resolve submesoscale flows are compared and advanced methods on the kinetic energy flux across spatial and temporal scales are applied to the model output. With this strategy, this dissertation found answers to the following questions:

1. How can the simulated Agulhas dynamics be validated against observations for all scales ranging from the large-scales down to the submesoscales?
2. What are the numerical choices to simulate the submesoscale flows as realistic as possible with INALT60?
3. **How and how much do the near-surface submesoscales impact the mesoscale eddies in the Agulhas region?**

Question number 3 is the main question of this dissertation. In the present chapter, the answers that are provided by the chapters 5 to 8 for these questions are synthesized. Further, for each question a bottom line and an outlook is presented. Finally, some results on the effect of submesoscale flows on the Agulhas leakage are shown and discussed in the context of this dissertation.

9.1 How can the simulated Agulhas dynamics be validated against observations for all scales ranging from the large-scales down to the submesoscales?

Ocean models, that aim to simulate the meso- and largescale ocean circulation, are usually validated by comparing the simulated SSH to satellite-based altimetric measurements. Commonly therefore the gridded product provided today by CMEMS (Copernicus Marine Environment Monitoring Service) and previously by AVISO (Archiving, Validation and Interpretation of Satellite Oceanographic data) is used (e.g. Chassignet and Xu, 2017; Schwarzkopf et al., 2019). This gridded product is created by interpolating the measured SSH along the tracks of all available satellite altimetry missions, to a regular daily and $(1/4)^\circ$-horizontal-resolution grid.

Usually, maps of the time-mean SSH are used for the validation of the large-scale circulation and maps of the temporal standard deviation of SSH for the mesoscale circulation. The latter is a measure of the geostrophic eddy kinetic energy. The validation of the simulated large-scale flow is usually complemented by a comparison of vertical sections through the simulated current to those derived from mooring- and ship-based measurements. For the Agulhas Current, one of the few available data-sets to perform such a validation is provided by the Agulhas Current Time-Series Experiment (ACT, Beal et al., 2015) which is also used in this dissertation.

In chapter 6.6, it is demonstrated that the usual validation described above is only of limited usefulness for the Agulhas region. The strong non-linearities of the Agulhas Current system contribute to regional differences in the time-mean flow and the standard deviation of SSH making it impossible to identify systematic differences between the simulated and the observed circulation. This issue is amplified due to the short affordable model integration period for the submesoscale-permitting experiment INALT60. The temporal standard deviation of SSH can further provide only a validation of the integrated eddy activity without any informations on the scale of the eddies. In chapter 6.7, two statistically more robust approaches based on satellite altimetry are presented that provide a validation in dependence of the eddy scale. For the first one, horizontal-wavenumber spectra are directly computed from the along-track data measured by the JASON-2 satellite and the respective tracks from the model outputs. The spectra provide a measure of the geostrophic kinetic energy at specific horizontal scales. Besides the scale dependence, this approach comes along with the advantage that there are only minor interpolations necessary for a clean comparison of measurements and model output. Only the

high-resolution model output data needs to be interpolated onto the satellite tracks. For the second approach, an eddy detection algorithm is applied to the gridded SSH product and to the model data interpolated onto the same grid. This approach complements the first one, as it enables the validation of the eddy number as a function of their scale, strength and sense of rotation. Both approaches combined thus provide a comprehensive, scale-dependent validation and comparison of the simulated mesoscale dynamics.

The simulated submesoscale dynamics are not validatable based on present-day satellite altimetry as the noise in the measurements dominates the signal for scales below 30 km - 40 km in the Agulhas region (Dufau et al., 2016; Schubert et al., 2019). In chapter 6.5, a new validation method for the simulated submesoscale mixed-layer dynamics down to scales of about 7 km is presented: the comparison of the time-mean horizontal-wavenumber spectra of sea-surface temperature (SST) derived from the 1 km-horizontal-resolution Moderate Resolution Imaging Spectroradiometer (MODIS, Minnett et al., 2002) product to those from the model experiments. With this method, the simulated mixed-layer dynamics of the Agulhas region can be validated due to the following arguments. At scales just above 40 km, the slope of the SSH spectrum for both observations and INALT60 is found to follow the prediction by surface quasi-geostrophic theory (Fig. 6.9). For INALT60, this slope continues down to scales of about 10 km. The agreement of the slope with the surface quasi-geostrophic prediction indicates that the submesoscale mixed-layer dynamics are mainly controlled by the surface horizontal buoyancy gradients (e.g. Blumen, 1978; Lapeyre and Klein, 2006). As gradients of the SST strongly contribute to gradients in the buoyancy, the comparison of the SST spectra provides a reasonable validation of the mixed-layer dynamics.

Bottom Line To validate an ocean model from the submesoscales to the large-scales, the common validation against a gridded satellite altimetry product and in situ measurements of large-scale currents, can be combined with i) horizontal wavenumber spectral analysis applied to satellite altimetry along-track data and the respective tracks from the simulated SSH, ii) eddy-detection applied to observed and simulated gridded SSH products, iii) horizontal wavenumber spectral analysis applied to satellite-based 1 km-horizontal-resolution SST swath measurements, as well as the model output.

An alternative direct validation of the submesoscale dynamics, that is not performed for this dissertation, could be achieved with surface velocities from satellite-based radar measurements (Rouault et al., 2010). These measurements are however associated with a horizontal resolution of 4 km to 8 km and thus cover only the large-scale end of the submesoscales. Besides, this data could be particularly useful for the validation of the simulation of smaller mesoscale features near the continental shelf, where the altimetric measurements come to their limits (Volkov et al., 2007). A specific example are shear-edge eddies at the northern boundary of the Agulhas Current (see Rouault et al. (2010)). Moreover, in 2022, the Surface Water and Ocean Topography (SWOT, swot.jpl.nasa.gov) mission is scheduled to start measuring the SSH with a wide-swath radar interferometer. With this technique, the measured SSH will be not only available for a single line along the satellite track, but for a two-dimensional swath. This data will allow to characterize and validate the submesoscale SSH variability in the Agulhas region down to scales of about 10 km (Dufau et al., 2016).

9.2 What are the numerical choices to simulate the submesoscale flows as realistic as possible with INALT60?

For this dissertation, the ocean model configurations INALT20r and INALT60, that were introduced by Schwarzkopf et al. (2019), have been further developed. The focus lied thereby on the optimization of the simulated submesoscales that are resolvable with the given horizontal grid-spacing ($(1/20)°$ and $(1/60)°$).

First, the atmospheric forcing has been changed from COREv2 (Large and Yeager, 2009; Griffies et al., 2009) to JRA55-do (Tsujino et al., 2018). The latter is associated with higher temporal and spatial resolution which was expected to improve the simulation of the circulation on smaller and shorter scales. Second, the vertical resolution is increased for the whole water-column. This was achieved by using 120 instead of 46 z-levels. In the upper 2.000 m, the vertical resolution has been increased in a way that resolves the first three baroclinic modes representing the vertical structure of the horizontal flows (sec. 6.4.2). The respective requirements on the vertical grid-spacing have been identified using the approach of Stewart et al. (2017). Below 2.000 m depth, the vertical grid spacing was reduced from about 250 m to 100 m. This aimed to better resolve the deep flows such as the Agulhas Under Current. Moreover, Capuano et al. (2018b) suggested the use of a high vertical resolution throughout the water-column for a good representation of the Indo-Atlantic exchange. In the upper 20 m, 10 z-levels are used with a minimum vertical extent of 1 m at the surface. This aimed to resolve the mixed-layer dynamics also in summer, when the mixed-layer in the Agulhas region is as thin as 20 m (de Boyer Montégut et al., 2004). Sensitivity experiments with both INALT20r and INALT60, showed however almost no improvements in the simulation of submesoscale dynamics, when only the forcing and the vertical resolution were changed (chapters 5.3 and 6). It was hypothesized that the effect of the standard diffusion and dissipation settings hampers the simulation of the submesoscales in the model.

Indeed, the desired improvements in the simulation of submesoscale flows were achieved for both INALT20r and INALT60 by an additional reduction of the horizontal model diffusion and dissipation. Previously, the standard diffusion and dissipation setup consisted of a total variance dissipation scheme (TVD, Zalesak, 1979) for the discretization of tracer-advection, an energy enstrophy conserving scheme (EEN, Arakawa and Hsu, 1990) for the dicretization of the vorticity term and explicit

diffusion and dissipation in the primitive equations. Tuning the explicit diffusivities and viscositites to minima that still prevent numerical instabilities lead only to weak improvements (chapter 5.3). In contrast, a change to upstream biased schemes (UBS, Farrow and Stevens, 1995; Madec et al., 2016; Webb et al., 1998) without explicit diffusion and dissipation is shown to be associated with a strong improvement of the simulated submesoscales.

The validation of the simulated submesoscale dynamics with horizontal-wavenumber SST spectra showed a good agreement of the further developed INALT60 (using JRA55-do, 120 vertical levels and UBS schemes without explicit diffusion) with the satellite-based high-resolution measurements for the largest part of the Agulhas region. In particular for the Agulhas ring path, which this dissertation focuses on, a very good agreement is found for the further developed INALT60, as well as the further developed INALT20r (Fig. 6.7). Moreover, also the representation of the meso- and largescale circulation is found to be in a better agreement with the observations in INALT20r and in a very good agreement in INALT60 (chapter 6). This confirms the numerical choices that have been made and suggests their application in future high-resolution simulations. Further, this also justifies other settings of the configuration and the model that have not been changed here, for example the use of the hydrostatic approximation or the turbulent kinetic energy closure of Blanke and Delecluse (1993) to parameterize the vertical mixing.

Worth mentioning is also the model output strategy. To resolve the submesoscale temporal variability with the model output in the second nest of INALT60, the variables that were analyzed in this dissertation (velocity components, temperature and salinity, sea-surface height, mixed-layer depth) were written as 4h-means. To save data storage and computational power, this high-frequent output was restricted to the upper 250 m, where this dissertation focuses on. For the whole water-column, all model output variables were written as daily means. Submesoscale dynamics occurring below 250 m (see e.g. Capuano et al., 2018a) are only to a limited extent investigable with this strategy. Additionally to the 4h-means, every fifth day a model snap-shot was written in the output for the upper 250 m. This enabled the investigation of the full spatial variability of the simulated dynamics.

Bottom Line A comprehensive validation of INALT60 against observations shows an extraordinary good representation of the oceanic circulation on all simulated scales from the submesoscale to the large-scale. Key changes to previous configurations that contributed to this success are besides the increase in horizontal resolution i) the use of JRA55-do forcing with higher spatial and temporal resolution compared to COREv2, ii) 120 vertical levels with a grid-spacing of 1 m near the surface increasing to 100 m in the deep ocean that resolves the first 3 baroclinic modes, iii) the use of upstream biased schemes (UBS) for the discretization of the tracer-advection and the vorticity term combined with a switch-off of explicit diffusion and dissipation. Applying these three changes to a previously almost non-submesoscale resolving INALT20r configuration leads to the simulation of large submesoscale flows, as well as to improvements in the simulation of the meso- and large-scale circulation.

One of the major deficiencies of INALT60 is that tides are not simulated explicitly. With a parallel sensitivity experiment including tides, their impacts on the submesoscale dynamics, on the shelf-interior exchange, as well as on the larger scale dynamics could be investigated. Moreover, further sensitivity experiments could help to identify even better diffusion and dissipation settings for the simulation of submesoscales. For example second order centred schemes that are not associated with numerical diffusion and dissipation may be used (Madec et al., 2016). The theoretical approaches on the minimum explicit diffusion and dissipation (summarized in section 3) are then better applicable. Further, the use of scale-aware subgrid models such as the one proposed by Bachman et al. (2017) or Jansen et al. (2019) could be tested to improve the submesoscale dynamics at the small-scale end resolvable with a $(1/20)^\circ$ or a $(1/60)^\circ$ horizontal resolution. Finally, a further reduction of the horizontal grid-spacing below $(1/60)^\circ$ would come along with the potential of resolving a larger portion of the submesoscale spectrum. This presumably would further improve the simulation of the submesoscales at the scales that are investigated in this dissertation.

9.3 How and how much do the near-surface submesoscales impact the mesoscale eddies in the Agulhas region?

To address this question, in this dissertation two different approaches are applied. First, parallel ocean general circulation model experiments, that resolve submesoscale processes to a different degree, are compared to each other and to observations. Second, the transfer of kinetic energy across spatial and temporal scales is investigated on the basis of the model experiments.

Two $(1/20)^\circ$ horizontal resolution simulations, one that almost does not resolve submesoscale dynamics (INALT20r.L120.HighDiff)[12] and one that resolves only the large-scale end of the submesoscales (INALT20r.L120.LowDiff), are compared to a $(1/60)^\circ$ horizontal resolution experiment (INALT60) that resolves a larger portion of the submesoscale spectrum. The more submesoscale flows are resolved by the model, the larger is the spectral density of the time-mean horizontal-wavenumber spectrum of SSH in the Agulhas region and the closer is the spectrum to the one computed from satellite altimetry (sec. 6.7). In the Agulhas ring path, the mesoscale spectral density for INALT60 and the observations is twice as large as for INALT20r.L120.HighDiff. In terms of the surface kinetic energy, INALT60 is associated with 28 % more mesoscale (>100 km) kinetic energy than INALT20r.L120.HighDiff (chapter 7).

To identify, whether the lack of SSH spectral density and kinetic energy is a result of too less or too weak mesoscale eddies, SSH-based eddy-detection following Chelton et al. (2011) was applied for the region of the Cape Basin to the model outputs and the observations. It is shown that the number of eddies and the distribution of their horizontal scale is similar for the model runs and the observations. This, combined with the SSH spectra, points to a strengthening of the mesoscale eddies with the increasing resolution of submesoscale flows.

Indeed, the mean distribution of the maximum SSH amplitude of the eddies in the Cape Basin shows a shift to larger amplitudes (and towards the one of the observations), the more submesoscales are resolved. This is true for both anticyclones and cyclones. However, for strong eddies with maximum SSH amplitudes of more than 20 cm, an anticyclone-cyclone asymmetry is found. Strong anticyclones are

[12] Increasing only the vertical resolution from 46 vertical levels (INALT20r.L46.HighDiff) to 120 vertical levels (INALT20r.L120.HighDiff) was not associated with noteworthy changes in the simulated circulation on all spatial scales (chapter 6). Thus, INALT20r.L46.HighDiff is not further addressed with respect to the submesoscale impact on the mesoscale dynamics.

well represented in all model experiments. Assuming that most of the strong anticyclones in the Cape Basin are Agulhas rings, this indicates that submesoscale flows do have only a weak impact on the Agulhas ring shedding. In contrast, strong cyclones are only found to be well represented in INALT60, while there are much too less strong cyclones in the simulations with less capability in resolving submesoscale flows. One reason for this among others is a better representation of the formation of lee cyclones west of the Agulhas bank. There, a time-mean lee cyclone is found in the SSH field for both the observations and INALT60, while this is absent in INALT20r.L120.HighDiff. The lee cyclones are strengthened by the absorbtion of cyclonic features originating from upstream developing shear-edge eddies (Lutjeharms et al., 2003b) and are observed to detach and to propagate in the ring path (Penven et al., 2001). With the second approach, the computation of the transfer of kinetic energy across spatial and temporal scales, it could be shown that submesoscale features, that emerge from submesoscale barotropic instability at the northern boundary of the Agulhas Current, are important for the strength of the shear-edge eddies and thus for the strength of the lee cyclones (chapter 8). Submesoscale flows thus impact the mesoscale Agulhas dynamics by playing a central role for the formation of mesoscale cyclones.

For the open ocean, the energy transfer analysis across spatial scales revealed an even more important result that might be generally applicable for the global open ocean. In chapter 7, it is shown that the well known mesoscale inverse kinetic energy cascade (from smaller to larger spatial scales) extends in winter down to submesoscales of 13 km in the Agulhas ring path and 25 km in the subgyre region east of the Agulhas Current. For smaller scales, a forward cascade (from larger to smaller spatial scales) is found that is strongest in winter and attributable to frontogenetic regions in the upper 30 m. The submesoscale inverse cascade is also strongest in winter. However, with increasing scale, its maximum shifts to later periods reaching the mesoscales in spring or early summer (depending on the region). The seasonal cycle of the scale kinetic energy transfer is found to be aligned with the one of the kinetic energy. This indicates an important role of the submesoscale inverse cascade for the seasonal cycle of the mesoscales. Largest sources for the inverse cascade are found at scales of about 15 km in winter. These scales are typical for features that emerge from the mixed-layer baroclinic instability (MLI) which is most active in winter (e.g. Fox-Kemper et al., 2008). A case study of a front between Agulhas eddies in the ring path that undergoes MLI shows that the emerging features are absorbed by an Agulhas ring fluxing their kinetic energy into the ring. In summary, the results of chapter 7 suggest that the mesoscale eddies are strengthened in spring or early summer by the absorption of mixed-layer eddies that are mainly formed in

winter as a result of MLI. Consistently, the submesoscale inverse cascade is absent in the non-submesoscale resolving experiment INALT20r.L120.HighDiff contributing to the lack of mesoscale kinetic energy.

With this new insight, one further result of the first approach can be explained. Figure 6.10 shows that the mesoscale spectral slopes of the time-mean SSH spectrum are for INALT20r.L120.HighDiff in particular in the Agulhas ring path too steep, while they are closer to the observations in the subgyre region. An explanation for that could be that the most unstable wavelength in the mixed-layer is smaller in the ring path than in the subgyre (Fig. 7.13). Because of this, the MLI is partially resolved in INALT20r.L120.HighDiff in the subgyre region, while there are absolutely no submesoscale flows simulated in the Agulhas ring path (Fig. 7.3). In the subgyre, consequently, a part of the submesoscale inverse cascade is resolved in INALT20r.L120.HighDiff leading to an improved representation of the mesoscale turbulence (Fig. 6.10 and 7.4). This further highlights the importance of resolving the MLI for the representation of the mesoscale dynamics.

Bottom Line Near-surface submesoscale flows strengthen the mesoscale eddies in the Agulhas region in two different ways. First, in the open ocean, submesoscale mixed-layer eddies emerging from mixed-layer baroclinic instability are found to be absorbed by the mesoscale eddies fluxing thereby their kinetic energy into the mesoscale eddies. Second, submesoscale barotropic instabilities along the northern boundary of the Agulhas current are found to be important for the formation and strengthening of mesoscale cyclones near the Agulhas bank. Both effects combined contribute to an increase of the mesoscale kinetic energy in the Agulhas ring path by 28 %, if submesoscale processes are resolved.

In ocean models that do not resolve the submesoscale MLI, the associated inverse cascade has to be parameterized in addition to the restratification effect of MLIs which is parameterizable with a Fox-Kemper type parameterization (Fox-Kemper et al., 2008). One possibility to implement the submesoscale inverse kinetic energy cascade into coarser-resolution models is the use of recently developed energetically consistent subgrid-scale parameterizations that include a back-scatter term from the subgrid-scale to the resolved scales (e.g. Jansen et al., 2019).

Most of the results with respect to the spatial energy transfer are shown in this dissertation only for the surface layer, as the computational costs are very high. With this, it was not possible to identify, how large the effect of the open-ocean submesoscale inverse kinetic energy cascade is on the mesoscale eddies. For two single model snapshots, one representing the winter and one the summer season,

the analysis has been applied to the upper 250 m. The results show that most of the submesoscale inverse cascade occurs in winter within the mixed-layer (Fig. 7.8). However, there, the upscale flux of kinetic energy depends on the scale and the depth. A future analysis of a mixed-layer integral of the flux could reveal the relative importance for the mesoscale kinetic energy.

At all depths, the mean kinetic energy density in the Agulhas ring path is larger in INALT60 compared to INALT20r.L120.HighDiff (Fig. 9.1). It remains open, whether and how the mesoscale strengthening at the surface by the submesoscale mixed-layer dynamics impacts the deeper layers, whether submesoscale dynamics in the deep ocean (e.g. Capuano et al., 2018a) are also associated with an inverse cascade and which role non-submesoscale processes play for the enhanced kinetic energy in INALT60 throughout the water-column. To investigate that, the output of future model experiments should resolve the submesoscale variability at all depths. For the INALT60 experiment executed here, the high-frequent model output was limited to the upper 250 m to save data storage and computational power.

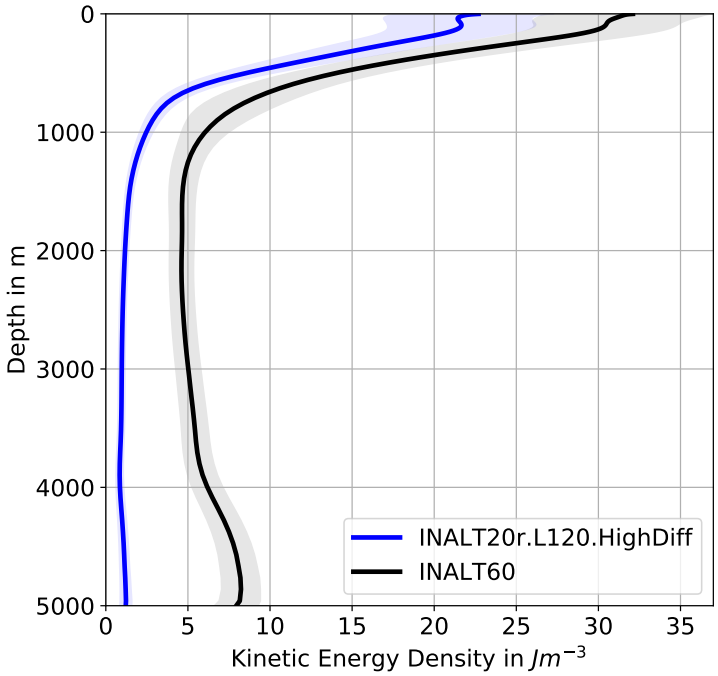

Fig. 9.1: *Mean vertical profile of kinetic energy density in the Agulhas ring path ($1.35°E$ - $14.00°E$, $37.63°S$ - $27.30°S$, similar to the solid box in Figure 7.2a) for the period 2012 - 2017 for INALT60 (black) and INALT20r.L120.HighDiff (blue). Shading shows the range of plus-minus one temporal standard deviation.*

Finally, although the validation in chapter 6 suggests that the mesoscale eddies are represented very well in INALT60, the question remains, how the here presented results would change if the resolution is further increased and the full submesoscale

spectrum is resolved, if tides are explicitely resolved and if the hydrostatic and other approximations are not made for the model equations. This would show, whether also other small-scale processes, that are not resolved (but whichs effect might be directly or indirectly parameterized) in INALT60, matter for the strength of the mesoscale eddies.

9.4 What is the effect of the submesoscales on the Agulhas leakage?

The Agulhas leakage, the inflow of warm and salty Indian Ocean water into the South Atlantic, is of importance for the South Atlantic stratification (De Ruijter et al., 1999) and the Atlantic Meridional Overturning Circulation (Weijer et al., 2002; Biastoch et al., 2008b) and thus for the global climate. The largest contribution to Agulhas leakage can be attributed to Agulhas rings that are irregularly shed from the retroflecting Agulhas Current carrying the Indian Ocean waters with them into the South Atlantic (Lutjeharms, 2007). In ocean models, a common approach to identify the amount of Agulhas leakage is to release every model year virtual Lagrangian particles continuously over one year at a vertical section of the Agulhas Current, to advect them with the model velocities for a reasonably long period, and to identify, how many of those cross the Good Hope line (Ansorge et al., 2005) and travel into the South Atlantic (Biastoch et al., 2009b; Durgadoo et al., 2013; Schwarzkopf et al., 2019). As a transport is attributed to each particle that is kept constant, from the number of particles that cross the Good Hope line, the Agulhas leakage in Sv can be computed. This approach is similar to the estimation of Agulhas leakage based on (much sparser) observational float data presented by Richardson (2007). For the upper 1000 m, Richardson (2007) estimated an Agulhas leakage of about 15 Sv.

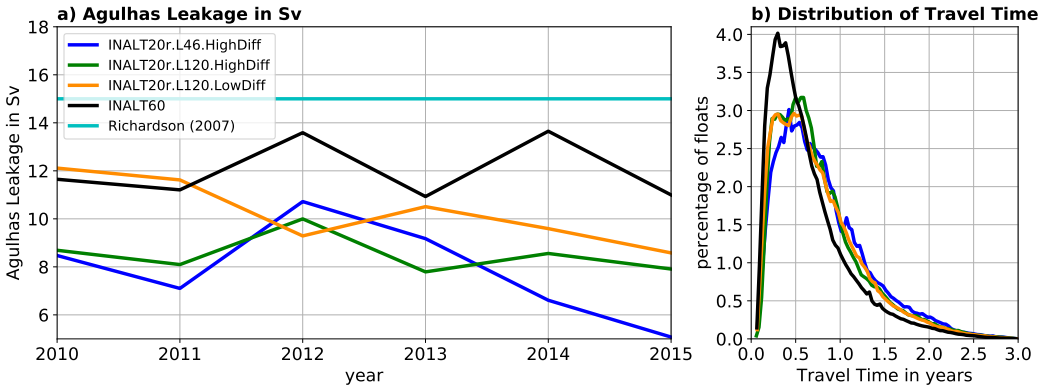

Fig. 9.2: *(a) timeseries of Agulhas leakage computed from the model experiments and compared to 15 Sv identified from measurements for the upper 1000 m by (Richardson, 2007). (b) The distribution of the particle travel time from the ACT to the Good Hope section for the model experiments.*

Applying this approach to the model experiments, perfomed for this dissertation, using daily mean velocities to advect the particles from a vertical section through the AC at $32°S$ over three years, gives the results shown in Figure 9.2a. The more submesoscales are resolved by the model, the larger is the estimated Agulhas

leakage and the closer is the Agulhas leakage to the observed 15 Sv. Moreover, the distribution of the travel time from the release section to the Good Hope line shows that the distribution shifts to shorter travel times, the more submesoscales are resolved (Fig. 9.2b). The affordable integration period of 8 years for INALT60 is too short for robust statistics. Thus, the effect of submesoscales on the Agulhas leakage has not been further investigated in this dissertation. Moreover, in the following, it is argued that the usefulness of the above described approach is reduced when submesoscale flows are resolved by the model making the interpretation of the presented results difficult.

The above described approach bases on the assumption that recently shed Agulhas rings carry the Indian Ocean waters with them through the Good Hope line. Then, the amount of water that originates from the AC and enters the South Atlantic at the Good Hope line is a measure of the inflow of warm and salty Indian Ocean waters. This is only true, if the flow is purely geostrophic. A recent study by Sinha et al. (2019) shows that submesoscale flows with ageostrophic components are able to exchange the Agulhas ring water masses with their surroundings (see Figure 9.3 which is taken from Sinha et al. (2019)). This is consistent with observations from Boebel et al. (2003) and Richardson and Garzoli (2003) who observed floats to leave and enter the Agulhas rings within the eastern part of the Cape Basin (the "Cape Cauldron" (Boebel et al., 2003)). Concluding, the above described approach is useful for ocean models that do not resolve submesoscale flows in the Cape Cauldron, however the effect of the submesoscale exchange of Agulhas ring water with their surrounding is missing in these models.

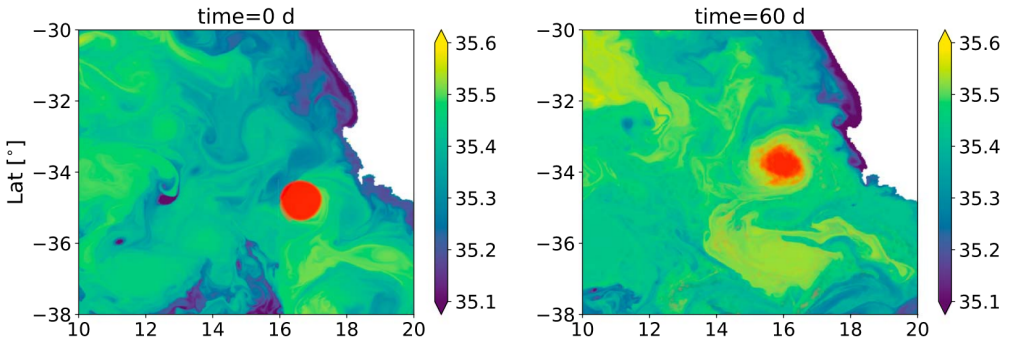

Fig. 9.3: *Submesoscale watermass exchange across the boundary of Agulhas rings: (left) The initial position of 3D particles and (right) their position after 60 days advection by hourly velocities of the submesoscale-permitting simulation llc4320, superimposed on surface salinity concentration (see Sinha et al. (2019) for details). The figure is taken from Sinha et al. (2019).*

The fact that the submesoscales drive an exchange through the boundary of Agulhas ring waters questions the applicability of the above described approach to submesoscale resolving model outputs. Particles that are released in the AC, are shed as part of an Agulhas ring, leave the Agulhas ring in the Cape Cauldron, get colder and fresher in the surrounding water masses and finally nevertheless cross the Good Hope line are contribute to the Agulhas leakage, although they obviously do not contribute to a warm and salty inflow into the South Atlantic. When submesoscale flows are resolved, a new approach to estimate a measure of the inflow of warm and saline water masses into the South Atlantic needs to be developed in the future. An INALT60 study with a longer integration period could provide the basis for that. With such an approach, the effect of the submesoscale exchange on the properties of the water masses that enter the South Atlantic then can be addressed. These properties are what matters for the climate and less whether the water has been in the AC before.

The results of this dissertation further suggest that submesoscale flows at the northern boundary of the AC impact the inflow of warm and salty Indian Ocean water into the Atlantic by playing an important role for the formation and strength of shear edge eddies and lee cyclones (chapter 8). Shear-edge eddies are associated with warm plumes that occasionally drift into the South Atlantic as Agulhas filaments contributing to a direct inflow of Indian Ocean water (Lutjeharms, 2007). Lee cyclones propagate into the Agulhas ring path (Penven et al., 2001), where they strongly interact with the rings (Boebel et al., 2003). The interaction is associated with the formation of submesoscale flows that in turn contribute to the exchange of the Agulhas ring waters with their surrounding (Boebel et al., 2003; Capuano et al., 2018b).

Acknowledgements

First, I want to express my sincere gratitude to *Prof. Dr. Arne Biastoch* for the great supervision of my doctorate. Thank you, Arne, for the possibility to work on the topic, for the freedom to decide how to explore it, for your immense knowledge on the Agulhas current system and its simulation, for sharing your strategic views on scientific decisions, and for your strong continuous support to present my results on conferences, workshops and a summer school. Second, my sincere thank goes to *Dr. Franziska U. Schwarzkopf* (GEOMAR, Kiel) for introducing me to NEMO and for her very enduring help to run the INALT simulations. The success of the numerical model experiments is due to her enormous expertise on solving issues with the model. Third, I thank *Prof. Dr. Richard J. Greatbatch* (GEOMAR, Kiel) and *Prof. Dr. Burkard Baschek* (HZG, Geesthacht) for their constructive feedback during the advisory committee meetings in the framework of the Integrated School of Ocean Sciences (ISOS), their support throughout my doctorate and their contributions to our papers. Thank you, Burkard, for the exciting stay at the Helmholtz Centre Geesthacht. Fourth, I thank *Prof. Dr. Jonathan Gula* (LOPS, Brest) for the constructive discussions, for the great week at LOPS and for his encouragement to work on the paper on the submesoscale kinetic energy flux.

I gratefully acknowledge the support of the ocean dynamics research unit at GEOMAR throughout my doctorate. I thank *Dr. Willi Rath* and *Dr. Markus Scheinert* for the great technical support (Thanks, Willi, in particular for the introduction to Xarray, Dask and GIT!); *Nikole Lorenz* and *Sabine Niewels* for all the help in organizing my doctorate and associated journeys; *Patrick Wagner* and *Dr. Jan-Klaus Rieck* for the many discussions on science, coding and modeling, for proofreading parts of the thesis, as well as for their friendship; *Dr. Klaus Getzlaff*, *Dr. Jan Harlaß* and *Christina Roth* for their help with tricky modelling problems; *Prof. Dr. Claus Böning* and *Prof. Dr. Martin Claus* for the short but fruitful scientific discussions; *Dr. Rafael Abel*, *Dr. Siren Rühs*, and *Dr. Jonathan Durgadoo* for the intellectual exchanges. I thank the whole ocean dynamics group for providing a joyful working environment and having always an open door for questions and discussions.

For the inspiring exchange on my doctoral topic, I thank *Dr. Adekunle Ajayi, Jaard Hauschildt, Prof. Dr. Joakim Kjellson, Dr. Sören Thomsen, Pauline Tedesco, Prof. Dr. Pierrick Penven, Clark Pennelly, Prof. Dr. Julien le Sommer, Prof. Dr. Jean Marc Molines, Dr. Hajo Krasemann, Dr. Johannes Hahn, Prof. Dr. Brian Arbic, Prof. Dr. Hussein Aluie, Prof. Dr. Baylor Fox-Kemper, Prof. Dr. Bernard Barnier, Prof. Dr. Lisa M. Beal, Prof. Dr. Ryan Abernathey, Prof. Dr. Sergey Danilov, Dr. Reiner Onken, Dr. Jeffrey Carpenter, Dr. Meghan F. Cronin* and many many others.

I thank *Ricardo Langner* for providing the open-source latex-template "Clean Thesis" (cleanthesis.der-ric.de) on whichs basis this document has been layouted.

Besides the ocean, its simulation and science in general, my journey-filled doctorate gave me many insights into different societies, their histories, economics, injustices and conflicts. It has been a time of reflection and learning for (and about) me. During the doctorate, I had some of the worst days but many of the best days of my life so far. My heartfelt gratitude goes to all the people that supported me in the former and contributed to the latter: to my family, my friends, my beloved one, and my companions.

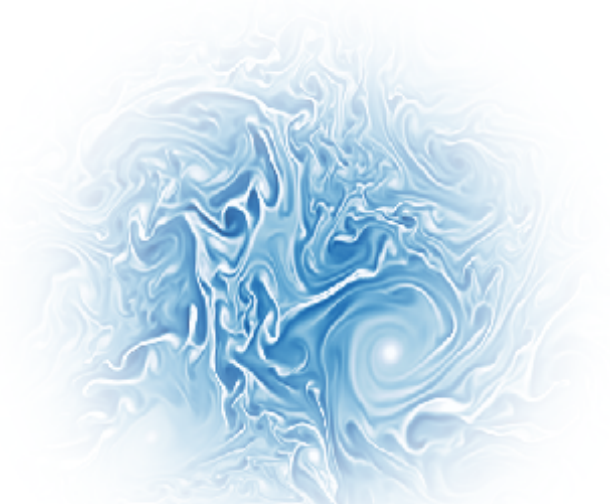

turbulent times

Erklärung

Hiermit erkläre ich, dass ich die vorliegende Dissertation, abgesehen von der Betreuung durch *Prof. Dr. Arne Biastoch*, *Prof. Dr. Richard J. Greatbatch* und *Prof. Dr. Burkard Baschek* nach Inhalt und Form eigenständig und unter Einhaltung der Regeln guter wissenschaftlicher Praxis der Deutschen Forschungsgemeinschaft verfasst habe. Ich habe keine anderen als die angegebenen Hilfsmittel und Quellen verwendet. Diese Dissertation hat weder ganz noch in Teilen an einer anderen Stelle im Rahmen eines Prüfungsverfahrens vorgelegen. Die Dissertation ist eine Mischform zwischen Monographie und kumulativer Dissertation. Kapitel 6 wurde bereits im Journal of Advances in Modeling Earth Systems veröffentlicht. Kapitel 7 wurde im Journal of Physical Oceanography zur Veröffentlichung eingereicht. Beiträge anderer Wissenschaftler*innen zu diesen beiden Kapiteln habe ich kenntlich gemacht. Mir wurde kein akademischer Grad entzogen.

René Schubert
Kiel, den 6.2.2020

Bibliography

Aluie, H. (2018). Convolutions on the sphere: Commuting with differential operators. *arXiv preprint arXiv:1808.03323*.

Aluie, H., Hecht, M., and Vallis, G. K. (2018). Mapping the energy cascade in the North Atlantic Ocean: the coarse-graining approach. *Journal of Physical Oceanography*, 48(2):225–244.

Andrews, D. and Hoskins, B. (1978). Energy spectra predicted by semi-geostrophic theories of frontogenesis. *Journal of the Atmospheric Sciences*, 35(3):509–512.

Ansorge, I., Speich, S., Lutjeharms, J., Goni, G., Rautenbach, C. d. W., Froneman, P., Rouault, M., and Garzoli, S. (2005). Monitoring the oceanic flow between Africa and Antarctica: report of the first GoodHope cruise: research in action. *South African Journal of Science*, 101(1-2):29–35.

Arakawa, A. and Hsu, Y.-J. G. (1990). Energy conserving and potential-enstrophy dissipating schemes for the shallow water equations. *Monthly Weather Review*, 118(10):1960–1969.

Arakawa, A. and Lamb, V. R. (1977). Computational design of the basic dynamical processes of the UCLA general circulation model. *General circulation models of the atmosphere*, 17:173–265.

Arbic, B. K., Polzin, K. L., Scott, R. B., Richman, J. G., and Shriver, J. F. (2013). On eddy viscosity, energy cascades, and the horizontal resolution of gridded satellite altimeter products. *Journal of Physical Oceanography*, 43(2):283–300.

Ardhuin, F., Gille, S. T., Menemenlis, D., Rocha, C. B., Rascle, N., Chapron, B., Gula, J., and Molemaker, J. (2017). Small-scale open ocean currents have large effects on wind wave heights. *Journal of Geophysical Research: Oceans*, 122(6):4500–4517.

Arhan, M., Mercier, H., and Park, Y.-H. (2003). On the deep water circulation of the eastern South Atlantic Ocean. *Deep Sea Research Part I: Oceanographic Research Papers*, 50(7):889–916.

Bachman, S. D., Fox-Kemper, B., and Pearson, B. (2017). A scale-aware subgrid model for quasi-geostrophic turbulence. *Journal of Geophysical Research: Oceans*, 122(2):1529–1554.

Bachman, S. D. and Taylor, J. R. (2014). Modelling of partially-resolved oceanic symmetric instability. *Ocean Modelling*, 82:15–27.

Badin, G., Tandon, A., and Mahadevan, A. (2011). Lateral mixing in the pycnocline by baroclinic mixed layer eddies. *Journal of Physical Oceanography*, 41(11):2080–2101.

Barkan, R., Winters, K. B., and Llewellyn Smith, S. G. (2015). Energy cascades and loss of balance in a reentrant channel forced by wind stress and buoyancy fluxes. *Journal of Physical Oceanography*, 45(1):272–293.

Barlow, R., Lamont, T., Kyewalyanga, M., Sessions, H., and Morris, T. (2010). Phytoplankton production and physiological adaptation on the southeastern shelf of the Agulhas ecosystem. *Continental Shelf Research*, 30(13):1472–1486.

Barnier, B., Brodeau, L., Le Sommer, J., Molines, J.-M., Penduff, T., Theetten, S., Treguier, A.-M., Madec, G., Biastoch, A., Böning, C. W., et al. (2007). Eddy-permitting ocean circulation hindcasts of past decades. *Clivar Exchanges*, 42(12 (3)):8–10.

Barnier, B., Madec, G., Penduff, T., Molines, J.-M., Treguier, A.-M., Le Sommer, J., Beckmann, A., Biastoch, A., Böning, C., Dengg, J., et al. (2006). Impact of partial steps and momentum advection schemes in a global ocean circulation model at eddy-permitting resolution. *Ocean Dynamics*, 56(5-6):543–567.

Beal, L. M. and Bryden, H. L. (1997). Observations of an Agulhas undercurrent. *Deep Sea Research Part I: Oceanographic Research Papers*, 44(9-10):1715–1724.

Beal, L. M., de Ruijter, W. P., Biastoch, A., Zahn, R., Cronin, M., Hermes, J., Lutjeharms, J., Quartly, G., Tozuka, T., Baker-Yeboah, S., et al. (2011). On the role of the Agulhas system in ocean circulation and climate. *Nature*, 472(7344):429.

Beal, L. M., Elipot, S., Houk, A., and Leber, G. M. (2015). Capturing the transport variability of a western boundary jet: Results from the Agulhas Current Time-Series Experiment (ACT). *Journal of Physical Oceanography*, 45(5):1302–1324.

Bell, M. J., Peixoto, P. S., and Thuburn, J. (2017). Numerical instabilities of vector-invariant momentum equations on rectangular C-grids. *Quarterly Journal of the Royal Meteorological Society*, 143(702):563–581.

Biastoch, A., Beal, L., Lutjeharms, J., and Casal, T. (2009a). Variability and coherence of the Agulhas Undercurrent in a high-resolution ocean general circulation model. *Journal of Physical Oceanography*, 39(10):2417–2435.

Biastoch, A. and Böning, C. W. (2013). Anthropogenic impact on Agulhas leakage. *Geophysical Research Letters*, 40(6):1138–1143.

Biastoch, A., Böning, C. W., Getzlaff, J., Molines, J.-M., and Madec, G. (2008a). Causes of interannual–decadal variability in the meridional overturning circulation of the midlatitude North Atlantic Ocean. *Journal of climate*, 21(24):6599–6615.

Biastoch, A., Böning, C. W., and Lutjeharms, J. (2008b). Agulhas leakage dynamics affects decadal variability in Atlantic overturning circulation. *Nature*, 456(7221):489.

Biastoch, A., Böning, C. W., Schwarzkopf, F. U., and Lutjeharms, J. (2009b). Increase in Agulhas leakage due to poleward shift of Southern Hemisphere westerlies. *Nature*, 462(7272):495.

Biastoch, A., Durgadoo, J. V., Morrison, A. K., Van Sebille, E., Weijer, W., and Griffies, S. M. (2015). Atlantic multi-decadal oscillation covaries with Agulhas leakage. *Nature Communications*, 6:10082.

Biastoch, A., Lutjeharms, J., Böning, C. W., and Scheinert, M. (2008c). Mesoscale perturbations control inter-ocean exchange south of Africa. *Geophysical Research Letters*, 35(20).

Biastoch, A., Sein, D., Durgadoo, J. V., Wang, Q., and Danilov, S. (2018). Simulating the Agulhas system in global ocean models–nesting vs. multi-resolution unstructured meshes. *Ocean Modelling*, 121:117–131.

Bishop, C. H. (1993). On the behaviour of baroclinic waves undergoing horizontal deformation. I: The 'RT'phase diagram. *Quarterly Journal of the Royal Meteorological Society*, 119(510):221–240.

Blanke, B. and Delecluse, P. (1993). Variability of the tropical Atlantic Ocean simulated by a general circulation model with two different mixed-layer physics. *Journal of Physical Oceanography*, 23(7):1363–1388.

Blumen, W. (1978). Uniform potential vorticity flow: Part I. Theory of wave interactions and two-dimensional turbulence. *Journal of the Atmospheric Sciences*, 35(5):774–783.

Boccaletti, G., Ferrari, R., and Fox-Kemper, B. (2007). Mixed layer instabilities and restratification. *Journal of Physical Oceanography*, 37(9):2228–2250.

Boebel, O., Lutjeharms, J., Schmid, C., Zenk, W., Rossby, T., and Barron, C. (2003). The Cape Cauldron: a regime of turbulent inter-ocean exchange. *Deep Sea Research Part II: Topical Studies in Oceanography*, 50(1):57–86.

Bolin, B. (1956). An improved barotropic model and some aspects of using the balance equation for three-dimensional flow. *Tellus*, 8(1):61–75.

Boyd, J. P. (1992). The Energy Spectrum of Fronts: Time Evolution of Shocks in Burgers Equation. *Journal of the Atmospheric Sciences*, 49(2):128–139.

Brannigan, L., Marshall, D. P., Naveira-Garabato, A., and Nurser, A. G. (2015). The seasonal cycle of submesoscale flows. *Ocean Modelling*, 92:69–84.

Bryan, K., Manabe, S., and Pacanowski, R. C. (1975). A global ocean-atmosphere climate model. Part II. The oceanic circulation. *Journal of Physical Oceanography*, 5(1):30–46.

Buckingham, C. E., Naveira Garabato, A. C., Thompson, A. F., Brannigan, L., Lazar, A., Marshall, D. P., George Nurser, A., Damerell, G., Heywood, K. J., and Belcher, S. E. (2016). Seasonality of submesoscale flows in the ocean surface boundary layer. *Geophysical Research Letters*, 43(5):2118–2126.

Byrne, D. A., Gordon, A. L., and Haxby, W. F. (1995). Agulhas eddies: A synoptic view using Geosat ERM data. *Journal of Physical Oceanography*, 25(5):902–917.

Callies, J. and Ferrari, R. (2013). Interpreting energy and tracer spectra of upper-ocean turbulence in the submesoscale range (1–200 km). *Journal of Physical Oceanography*, 43(11):2456–2474.

Callies, J., Ferrari, R., Klymak, J. M., and Gula, J. (2015). Seasonality in submesoscale turbulence. *Nature Communications*, 6:6862.

Capet, X., McWilliams, J. C., Molemaker, M. J., and Shchepetkin, A. (2008a). Mesoscale to submesoscale transition in the California Current System. Part I: Flow structure, eddy flux, and observational tests. *Journal of Physical Oceanography*, 38(1):29–43.

Capet, X., McWilliams, J. C., Molemaker, M. J., and Shchepetkin, A. (2008b). Mesoscale to submesoscale transition in the California Current System. Part II: Frontal processes. *Journal of Physical Oceanography*, 38(1):44–64.

Capet, X., McWilliams, J. C., Molemaker, M. J., and Shchepetkin, A. (2008c). Mesoscale to submesoscale transition in the California Current System. Part III: Energy balance and flux. *Journal of Physical Oceanography*, 38(10):2256–2269.

Capuano, T. A., Speich, S., Carton, X., and Blanke, B. (2018a). Mesoscale and submesoscale processes in the Southeast Atlantic and their impact on the regional thermohaline structure. *Journal of Geophysical Research: Oceans*, 123(3):1937–1961.

Capuano, T. A., Speich, S., Carton, X., and Laxenaire, R. (2018b). Indo-Atlantic Exchange, Mesoscale Dynamics, and Antarctic Intermediate Water. *Journal of Geophysical Research: Oceans*.

Casanova-Masjoan, M., Pelegrí, J. L., Sangrà, P., Martínez, A., Grisolía-Santos, D., Pérez-Hernández, M. D., and Hernández-Guerra, A. (2017). Characteristics and evolution of an Agulhas ring. *Journal of Geophysical Research: Oceans*, 122(9):7049–7065.

Charney, J. G. (1971). Geostrophic turbulence. *Journal of the Atmospheric Sciences*, 28(6):1087–1095.

Chassignet, E. P. and Xu, X. (2017). Impact of horizontal resolution (1/12° to 1/50°) on gulf stream separation, penetration, and variability. *Journal of Physical Oceanography*, 47(8):1999–2021.

Chelton, D. B., Deszoeke, R. A., Schlax, M. G., El Naggar, K., and Siwertz, N. (1998). Geographical variability of the first baroclinic Rossby radius of deformation. *Journal of Physical Oceanography*, 28(3):433–460.

Chelton, D. B., Schlax, M. G., and Samelson, R. M. (2011). Global observations of nonlinear mesoscale eddies. *Progress in Oceanography*, 91(2):167–216.

Cronin, M. (1996). Eddy-mean flow interaction in the Gulf Stream at 68 W. Part II: Eddy forcing on the time-mean flow. *Journal of Physical Oceanography*, 26(10):2132–2151.

Cronin, M. F., Tozuka, T., Biastoch, A., Durgadoo, J. V., and Beal, L. M. (2013). Prevalence of strong bottom currents in the greater Agulhas system. *Geophysical Research Letters*, 40(9):1772–1776.

Cushman-Roisin, B. and Beckers, J.-M. (2009). *Introduction to geophysical fluid dynamics: physical and numerical aspects*. Academic press.

D'Asaro, E., Lee, C., Rainville, L., Harcourt, R., and Thomas, L. (2011). Enhanced turbulence and energy dissipation at ocean fronts. *Science*, 332(6027):318–322.

de Boyer Montégut, C., Madec, G., Fischer, A. S., Lazar, A., and Iudicone, D. (2004). Mixed layer depth over the global ocean: An examination of profile data and a profile-based climatology. *Journal of Geophysical Research: Oceans*, 109(C12).

De Ruijter, W., Biastoch, A., Drijfhout, S., Lutjeharms, J., Matano, R., Pichevin, T., Van Leeuwen, P., and Weijer, W. (1999). Indian-Atlantic interocean exchange: Dynamics, estimation and impact. *Journal of Geophysical Research: Oceans*, 104(C9):20885–20910.

de Ruijter, W. P., Van Leeuwen, P. J., and Lutjeharms, J. R. (1999). Generation and evolution of Natal Pulses: solitary meanders in the Agulhas Current. *Journal of Physical Oceanography*, 29(12):3043–3055.

Debreu, L., Vouland, C., and Blayo, E. (2008). AGRIF: Adaptive grid refinement in Fortran. *Computers & Geosciences*, 34(1):8–13.

Donlon, C., Minnett, P., Gentemann, C., Nightingale, T., Barton, I., Ward, B., and Murray, M. (2002). Toward improved validation of satellite sea surface skin temperature measurements for climate research. *Journal of Climate*, 15(4):353–369.

Dritschel, D., Haynes, P., Juckes, M., and Shepherd, T. (1991). The stability of a two-dimensional vorticity filament under uniform strain. *Journal of Fluid Mechanics*, 230:647–665.

Ducousso, N., Le Sommer, J., Molines, J.-M., and Bell, M. (2017). Impact of the Symmetric Instability of the Computational Kind at mesoscale-and submesoscale-permitting resolutions. *Ocean Modelling*, 120:18–26.

Dufau, C., Orsztynowicz, M., Dibarboure, G., Morrow, R., and Le Traon, P.-Y. (2016). Mesoscale resolution capability of altimetry: Present and future. *Journal of Geophysical Research: Oceans*, 121(7):4910–4927.

Durgadoo, J. (2013). *Controls and impact of Agulhas leakage*. PhD thesis, Christian-Albrechts Universität Kiel.

Durgadoo, J. V., Loveday, B. R., Reason, C. J., Penven, P., and Biastoch, A. (2013). Agulhas leakage predominantly responds to the Southern Hemisphere westerlies. *Journal of Physical Oceanography*, 43(10):2113–2131.

Eady, E. T. (1949). Long waves and cyclone waves. *Tellus*, 1(3):33–52.

Emerson, R. W. and Cameron, K. W. (1940). *Nature (1836)*. Scholars' facsimiles & reprints.

Eyink, G. L. (2005). Locality of turbulent cascades. *Physica D: Nonlinear Phenomena*, 207(1-2):91–116.

Farrow, D. E. and Stevens, D. P. (1995). A new tracer advection scheme for Bryan and Cox type ocean general circulation models. *Journal of Physical Oceanography*, 25(7):1731–1741.

Ferrari, R. and Wunsch, C. (2009). Ocean circulation kinetic energy: Reservoirs, sources, and sinks. *Annual Review of Fluid Mechanics*, 41:253–282.

Fichefet, T. and Maqueda, M. M. (1997). Sensitivity of a global sea ice model to the treatment of ice thermodynamics and dynamics. *Journal of Geophysical Research: Oceans*, 102(C6):12609–12646.

Fick, A. (1855). Über Diffusion. *Annalen der Physik*, 170(1):59–86.

Fofonoff, N. P. and Millard Jr, R. (1983). Algorithms for the computation of fundamental properties of seawater.

Fox-Kemper, B., Ferrari, R., and Hallberg, R. (2008). Parameterization of mixed layer eddies. Part I: Theory and diagnosis. *Journal of Physical Oceanography*, 38(6):1145–1165.

Garrett, C. and Munk, W. (1972). Space-time scales of internal waves. *Geophysical & Astrophysical Fluid Dynamics*, 3(1):225–264.

Germano, M. (1992). Turbulence: the filtering approach. *Journal of Fluid Mechanics*, 238:325–336.

Gill, A. E. (1982). *Atmosphere-Ocean Dynamics (International Geophysics Series)*. academic press.

Gille, S. T. (2003). Float observations of the Southern Ocean. part II: Eddy fluxes. *Journal of Physical Oceanography*, 33(6):1182–1196.

Giordani, H. and Caniaux, G. (2001). Sensitivity of cyclogenesis to sea surface temperature in the northwestern Atlantic. *Monthly Weather Review*, 129(6):1273–1295.

Goni, G. J., Garzoli, S. L., Roubicek, A. J., Olson, D. B., and Brown, O. B. (1997). Agulhas ring dynamics from TOPEX/POSEIDON satellite altimeter data. *Journal of Marine Research*, 55(5):861–883.

Gordon, A. L. (1986). Interocean exchange of thermocline water. *Journal of Geophysical Research: Oceans*, 91(C4):5037–5046.

Griffies, S. M. (2004). *Fundamentals of ocean climate models*, volume 518. Citeseer.

Griffies, S. M., Biastoch, A., Böning, C., Bryan, F., Danabasoglu, G., Chassignet, E. P., England, M. H., Gerdes, R., Haak, H., Hallberg, R. W., et al. (2009). Coordinated ocean-ice reference experiments (COREs). *Ocean modelling*, 26(1-2):1–46.

Griffies, S. M., Pacanowski, R. C., and Hallberg, R. W. (2000). Spurious diapycnal mixing associated with advection in az-coordinate ocean model. *Monthly Weather Review*, 128(3):538–564.

Gründlingh, M. L. (1979). Observation of a large meander in the Agulhas Current. *Journal of Geophysical Research: Oceans*, 84(C7):3776–3778.

Gründlingh, M. L. (1983). On the course of the Agulhas Current. *South African Geographical Journal*, 65(1):49–57.

Gula, J., Molemaker, M. J., and McWilliams, J. C. (2014). Submesoscale cold filaments in the Gulf Stream. *Journal of Physical Oceanography*, 44(10):2617–2643.

Gula, J., Molemaker, M. J., and McWilliams, J. C. (2016). Topographic generation of submesoscale centrifugal instability and energy dissipation. *Nature Communications*, 7:12811.

Haine, T. W. and Marshall, J. (1998). Gravitational, symmetric, and baroclinic instability of the ocean mixed layer. *Journal of Physical Oceanography*, 28(4):634–658.

Hamlington, P. E., Van Roekel, L. P., Fox-Kemper, B., Julien, K., and Chini, G. P. (2014). Langmuir–submesoscale interactions: Descriptive analysis of multiscale frontal spindown simulations. *Journal of Physical Oceanography*, 44(9):2249–2272.

Harrison, D. and Robinson, A. (1978). Energy analysis of open regions of turbulent flows—Mean eddy energetics of a numerical ocean circulation experiment. *Dynamics of Atmospheres and Oceans*, 2(2):185–211.

Hecht, M. W., Petersen, M. R., Wingate, B. A., Hunke, E., and Maltrud, M. (2008). Lateral Mixing in the Eddying Regime and a New Broad-Ranging Formulation. *Ocean Modeling in an Eddying Regime*, pages 339–352.

Heisenberg, W. and Bond, B. (1959). *Physics and Philosophy: The Revolution in Modern Science*. Allen & Unwin St. Leonards, Australia.

Held, I. M., Pierrehumbert, R. T., Garner, S. T., and Swanson, K. L. (1995). Surface quasi-geostrophic dynamics. *Journal of Fluid Mechanics*, 282:1–20.

Hernandez, F. and Schaeffer, P. (2001). The CLS01 Mean Sea Surface: A validation with the GSFC00 surface. *CLS Ramonville St Agne, France*.

Hollingsworth, A., Kållberg, P., Renner, V., and Burridge, D. (1983). An internal symmetric computational instability. *Quarterly Journal of the Royal Meteorological Society*, 109(460):417–428.

Holton, L., Deshayes, J., Backeberg, B., Loveday, B., Hermes, J., and Reason, C. (2017). Spatio-temporal characteristics of Agulhas leakage: a model inter-comparison study. *Climate Dynamics*, 48(7-8):2107–2121.

Hosegood, P., Gregg, M. C., and Alford, M. H. (2006). Sub-mesoscale lateral density structure in the oceanic surface mixed layer. *Geophysical Research Letters*, 33(22).

Hoskins, B. (1974). The role of potential vorticity in symmetric stability and instability. *Quarterly Journal of the Royal Meteorological Society*, 100(425):480–482.

Hoskins, B. J. (1975). The geostrophic momentum approximation and the semi-geostrophic equations. *Journal of the Atmospheric Sciences*, 32(2):233–242.

Hoskins, B. J. (1982). The mathematical theory of frontogenesis. *Annual Review of Fluid Mechanics*, 14(1):131–151.

Hsiung, J. (1985). Estimates of global oceanic meridional heat transport. *Journal of Physical Oceanography*, 15(11):1405–1413.

Hurlburt, H. E. and Hogan, P. J. (2000). Impact of 1/8° to 1/64° resolution on Gulf Stream model–data comparisons in basin-scale subtropical Atlantic Ocean models. *Dynamics of Atmospheres and Oceans*, 32(3-4):283–329.

Jansen, M. F., Adcroft, A., Khani, S., and Kong, H. (2019). Toward an energetically consistent, resolution aware parameterization of ocean mesoscale eddies. *Journal of Advances in Modeling Earth Systems*, 11(8):2844–2860.

Jury, M. R., Valentine, H. R., and Lutjeharms, J. R. (1993). Influence of the Agulhas Current on summer rainfall along the southeast coast of South Africa. *Journal of Applied Meteorology*, 32(7):1282–1287.

Kilpatrick, K., Podestá, G., Walsh, S., Williams, E., Halliwell, V., Szczodrak, M., Brown, O., Minnett, P., and Evans, R. (2015). A decade of sea surface temperature from MODIS. *Remote Sensing of Environment*, 165:27–41.

Kjellsson, J. and Zanna, L. (2017). The impact of horizontal resolution on energy transfers in global ocean models. *Fluids*, 2(3):45.

Klein, P., Hua, B. L., Lapeyre, G., Capet, X., Le Gentil, S., and Sasaki, H. (2008). Upper ocean turbulence from high-resolution 3D simulations. *Journal of Physical Oceanography*, 38(8):1748–1763.

Klein, P., Lapeyre, G., Roullet, G., Le Gentil, S., and Sasaki, H. (2011). Ocean turbulence at meso and submesoscales: connection between surface and interior dynamics. *Geophysical & Astrophysical Fluid Dynamics*, 105(4-5):421–437.

Krug, M., Swart, S., and Gula, J. (2017). Submesoscale cyclones in the Agulhas current. *Geophysical Research Letters*, 44(1):346–354.

Krug, M., Tournadre, J., and Dufois, F. (2014). Interactions between the agulhas current and the eastern margin of the agulhas bank. *Continental Shelf Research*, 81:67–79.

Kuhlbrodt, T., Griesel, A., Montoya, M., Levermann, A., Hofmann, M., and Rahmstorf, S. (2007). On the driving processes of the Atlantic meridional overturning circulation. *Reviews of Geophysics*, 45(2).

Lapeyre, G. and Klein, P. (2006). Dynamics of the upper oceanic layers in terms of surface quasigeostrophy theory. *Journal of Physical Oceanography*, 36(2):165–176.

Lapeyre, G., Klein, P., and Hua, B. L. (2006). Oceanic restratification forced by surface frontogenesis. *Journal of Physical Oceanography*, 36(8):1577–1590.

Large, W. G. and Yeager, S. (2009). The global climatology of an interannually varying air–sea flux data set. *Climate Dynamics*, 33(2-3):341–364.

Lavrenov, I. (1998). The wave energy concentration at the Agulhas current off South Africa. *Natural hazards*, 17(2):117–127.

Le Bars, D., Dijkstra, H., and de Ruijter, W. (2013). Impact of the Indonesian Throughflow on Agulhas leakage. *Ocean Science Discussions*, 10:353–391.

Le Traon, P.-Y., Klein, P., Hua, B. L., and Dibarboure, G. (2008). Do altimeter wavenumber spectra agree with the interior or surface quasigeostrophic theory? *Journal of Physical Oceanography*, 38(5):1137–1142.

Legg, S., McWilliams, J., and Gao, J. (1998). Localization of deep ocean convection by a mesoscale eddy. *Journal of Physical Oceanography*, 28(5):944–970.

Legg, S. and McWilliams, J. C. (2001). Convective modifications of a geostrophic eddy field. *Journal of Physical Oceanography*, 31(4):874–891.

Leonard, A. (1975). Energy cascade in large-eddy simulations of turbulent fluid flows. In *Advances in geophysics*, volume 18, pages 237–248. Elsevier.

Lévy, M., Klein, P., and Treguier, A. (2001). Impacts of sub-mesoscale physics on phytoplankton production and subduction. *Journal of Marine Research*, 59(4):535–565.

Lévy, M., Klein, P., Tréguier, A.-M., Iovino, D., Madec, G., Masson, S., and Takahashi, K. (2010). Modifications of gyre circulation by sub-mesoscale physics. *Ocean Modelling*, 34(1-2):1–15.

Lübbecke, J. F., Durgadoo, J. V., and Biastoch, A. (2015). Contribution of increased Agulhas leakage to tropical Atlantic warming. *Journal of Climate*, 28(24):9697–9706.

Lutjeharms, J. (2007). Three decades of research on the greater Agulhas Current. *Ocean Science*, 3(1):129–147.

Lutjeharms, J. and Ansorge, I. (2001). The Agulhas return current. *Journal of Marine Systems*, 30(1-2):115–138.

Lutjeharms, J., Boebel, O., and Rossby, H. (2003a). Agulhas cyclones. *Deep Sea Research Part II: Topical Studies in Oceanography*, 50(1):13–34.

Lutjeharms, J., Catzel, R., and Valentine, H. (1989). Eddies and other boundary phenomena of the Agulhas Current. *Continental Shelf Research*, 9(7):597–616.

Lutjeharms, J. and Cooper, J. (1996). Interbasin leakage through Agulhas Current filaments. *Deep Sea Research Part I: Oceanographic Research Papers*, 43(2):213–238.

Lutjeharms, J., Penven, P., and Roy, C. (2003b). Modelling the shear edge eddies of the southern Agulhas Current. *Continental Shelf Research*, 23(11-13):1099–1115.

Lutjeharms, J. and Roberts, H. (1988). The Natal pulse: An extreme transient on the Agulhas Current. *Journal of Geophysical Research: Oceans*, 93(C1):631–645.

Lutjeharms, J. and Stockton, P. (1987). Kinematics of the upwelling front off southern Africa. *South African Journal of Marine Science*, 5(1):35–49.

Lutjeharms, J. and Van Ballegooyen, R. (1988a). Anomalous upstream retroflection in the Agulhas Current. *Science*, 240(4860):1770.

Lutjeharms, J. and Van Ballegooyen, R. (1988b). The retroflection of the Agulhas Current. *Journal of Physical Oceanography*, 18(11):1570–1583.

Ma, X., Jing, Z., Chang, P., Liu, X., Montuoro, R., Small, R. J., Bryan, F. O., Greatbatch, R. J., Brandt, P., Wu, D., et al. (2016). Western boundary currents regulated by interaction between ocean eddies and the atmosphere. *Nature*, 535(7613):533.

Madec, G. et al. (2014). NEMO ocean engine.

Madec, G. et al. (2016). NEMO ocean engine.

Mahadevan, A. (2016). The impact of submesoscale physics on primary productivity of plankton. *Annual Review of Marine Science*, 8:161–184.

Mahadevan, A., Tandon, A., and Ferrari, R. (2010). Rapid changes in mixed layer stratification driven by submesoscale instabilities and winds. *Journal of Geophysical Research: Oceans*, 115(C3).

Marmorino, G. O., Smith, G. B., North, R. P., and Baschek, B. (2018). Application of airborne infrared remote sensing to the study of ocean submesoscale eddies. *Frontiers in Mechanical Engineering*, 4:10.

McDonagh, E. L., Heywood, K. J., and Meredith, M. P. (1999). On the structure, paths, and fluxes associated with Agulhas rings. *Journal of Geophysical Research: Oceans*, 104(C9):21007–21020.

McWilliams, J. C. (2016). Submesoscale currents in the ocean. *Proceedings of the Royal Society A: Mathematical, Physical and Engineering Sciences*, 472(2189):20160117.

McWilliams, J. C. and Gent, P. R. (1980). Intermediate models of planetary circulations in the atmosphere and ocean. *Journal of the Atmospheric Sciences*, 37(8):1657–1678.

Minnett, P., Evans, R., Kearns, E., and Brown, O. (2002). Sea-surface temperature measured by the Moderate Resolution Imaging Spectroradiometer (MODIS). *IEEE International Geoscience and Remote Sensing Symposium*, 2:1177–1179.

Molemaker, M. J. and McWilliams, J. C. (2010). Local balance and cross-scale flux of available potential energy. *Journal of Fluid Mechanics*, 645:295–314.

Molemaker, M. J., McWilliams, J. C., and Capet, X. (2010). Balanced and unbalanced routes to dissipation in an equilibrated Eady flow. *Journal of Fluid Mechanics*, 654:35–63.

Molemaker, M. J., McWilliams, J. C., and Yavneh, I. (2005). Baroclinic instability and loss of balance. *Journal of Physical Oceanography*, 35(9):1505–1517.

Moore, D. W. and Saffman, P. G. (1975). The instability of a straight vortex filament in a strain field. *Proceedings of the Royal Society of London. A. Mathematical and Physical Sciences*, 346(1646):413–425.

Munk, W. H. (1950). On the wind-driven ocean circulation. *Journal of Meteorology*, 7(2):80–93.

NASA Goddard Space Flight Center, Ocean Ecology Laboratory, . O. B. P. G. (2012). Medium Resolution Imaging Spectrometer (MERIS) Ocean Color Data; 2012 Reprocessing. NASA OB.DAAC, Greenbelt, MD, USA. Dataset accessed [2019-01-29], doi: data/10.5067/ENVISAT/MERIS/L2/OC/2012.

NASA Goddard Space Flight Center, Ocean Ecology Laboratory, . O. B. P. G. (2015a). MODIS Aqua Level 3 SST Thermal IR Annual 9km Daytime v2014.0. Ver. 2014.0. PO.DAAC, CA, USA. Dataset accessed [2019-01-29] at http://dx.doi.org/10.5067/MODSA-AN9D4.

NASA Goddard Space Flight Center, Ocean Ecology Laboratory, . O. B. P. G. (2015b). MODIS Aqua Level 3 SST Thermal IR Annual 9km Nighttime v2014.0. Ver. 2014.0. PO.DAAC, CA, USA. Dataset accessed [2019-01-29] at http://dx.doi.org/10.5067/MODSA-AN9N4.

NASA Goddard Space Flight Center, Ocean Ecology Laboratory, . O. B. P. G. (2015c). MODIS Terra Level 3 SST Thermal IR Annual 9km Daytime v2014.0. Ver. 2014.0. PO.DAAC, CA, USA. Dataset accessed [2019-01-29] at http://dx.doi.org/10.5067/MODST-AN9D4.

NASA Goddard Space Flight Center, Ocean Ecology Laboratory, . O. B. P. G. (2015d). MODIS Terra Level 3 SST Thermal IR Annual 9km Nighttime v2014.0. Ver. 2014.0. PO.DAAC, CA, USA. Dataset accessed [2019-01-29] at http://dx.doi.org/10.5067/MODST-AN9N4.

NASA Goddard Space Flight Center, Ocean Ecology Laboratory, . O. B. P. G. (2016a). GHRSST Level 2P Global Skin Sea Surface Temperature from the Moderate Resolution Imaging Spectroradiometer (MODIS) on the NASA Aqua

satellite. Ver. 2014.0. PO.DAAC, CA, USA. Dataset accessed [2018-08-02] at http://dx.doi.org/10.5067/GHMDA-2PJ02.

NASA Goddard Space Flight Center, Ocean Ecology Laboratory, . O. B. P. G. (2016b). GHRSST Level 2P Global Skin Sea Surface Temperature from the Moderate Resolution Imaging Spectroradiometer (MODIS) on the NASA Terra satellite. Ver. 2014.0. PO.DAAC, CA, USA. Dataset accessed [2018-08-02] at http://dx.doi.org/10.5067/GHMDT-2PJ02.

Nkwinkwa Njouodo, A. S., Koseki, S., Keenlyside, N., and Rouault, M. (2018). Atmospheric signature of the Agulhas Current. *Geophysical Research Letters*, 45(10):5185–5193.

Olson, D. B., Fine, R. A., and Gordon, A. L. (1992). Convective modifications of water masses in the Agulhas. *Deep Sea Research Part A. Oceanographic Research Papers*, 39:S163–S181.

Paldor, N. and Lutjeharms, J. (2009). Why is the stability of the Agulhas Current geographically bi-modal? *Geophysical Research Letters*, 36(14).

Penven, P., Lutjeharms, J., Marchesiello, P., Roy, C., and Weeks, S. (2001). Generation of cyclonic eddies by the Agulhas Current in the lee of the Agulhas Bank. *Geophysical Research Letters*, 28(6):1055–1058.

Putrasahan, D., Kirtman, B. P., and Beal, L. M. (2016). Modulation of SST interannual variability in the Agulhas leakage region associated with ENSO. *Journal of Climate*, 29(19):7089–7102.

Qiu, B., Chen, S., Klein, P., Sasaki, H., and Sasai, Y. (2014). Seasonal mesoscale and submesoscale eddy variability along the North Pacific Subtropical Countercurrent. *Journal of Physical Oceanography*, 44(12):3079–3098.

Qiu, B., Chen, S., Klein, P., Wang, J., Torres, H., Fu, L.-L., and Menemenlis, D. (2018). Seasonality in Transition Scale from Balanced to Unbalanced Motions in the World Ocean. *Journal of Physical Oceanography*, 48(3):591–605.

Rahmstorf, S. (2002). Ocean circulation and climate during the past 120,000 years. *Nature*, 419(6903):207.

Ramachandran, S., Tandon, A., and Mahadevan, A. (2014). Enhancement in vertical fluxes at a front by mesoscale-submesoscale coupling. *Journal of Geophysical Research: Oceans*, 119(12):8495–8511.

Reason, C. (2001). Evidence for the influence of the agulhas current on regional atmospheric circulation patterns. *Journal of Climate*, 14(12):2769–2778.

Rhines, P. B. (1975). Waves and turbulence on a beta-plane. *Journal of Fluid Mechanics*, 69(3):417–443.

Richardson, P. and Garzoli, S. (2003). Characteristics of intermediate water flow in the Benguela current as measured with RAFOS floats. *Deep Sea Research Part II: Topical Studies in Oceanography*, 50(1):87–118.

Richardson, P. L. (2007). Agulhas leakage into the Atlantic estimated with subsurface floats and surface drifters. *Deep Sea Research Part I: Oceanographic Research Papers*, 54(8):1361–1389.

Richman, J. G., Arbic, B. K., Shriver, J. F., Metzger, E. J., and Wallcraft, A. J. (2012). Inferring dynamics from the wavenumber spectra of an eddying global ocean model with embedded tides. *Journal of Geophysical Research: Oceans*, 117(C12).

Rieck, J. K., Böning, C. W., Greatbatch, R. J., and Scheinert, M. (2015). Seasonal variability of eddy kinetic energy in a global high-resolution ocean model. *Geophysical Research Letters*, 42(21):9379–9386.

Ritchie, A. D. (1923). *Scientific Method: An inquiry into the character and validity of natural laws*. Routledge.

Rosso, I., Hogg, A. M., Strutton, P. G., Kiss, A. E., Matear, R., Klocker, A., and van Sebille, E. (2014). Vertical transport in the ocean due to sub-mesoscale structures: Impacts in the Kerguelen region. *Ocean Modelling*, 80:10–23.

Rouault, M. J., Mouche, A., Collard, F., Johannessen, J., and Chapron, B. (2010). Mapping the Agulhas Current from space: An assessment of ASAR surface current velocities. *Journal of Geophysical Research: Oceans*, 115(C10).

Roullet, G. and Klein, P. (2010). Cyclone-anticyclone asymmetry in geophysical turbulence. *Physical Review Letters*, 104(21):218501.

Roullet, G. and Madec, G. (2000). Salt conservation, free surface, and varying levels: a new formulation for ocean general circulation models. *Journal of Geophysical Research: Oceans*, 105(C10):23927–23942.

Rubio, A., Blanke, B., Speich, S., Grima, N., and Roy, C. (2009). Mesoscale eddy activity in the southern Benguela upwelling system from satellite altimetry and model data. *Progress in Oceanography*, 83(1-4):288–295.

Rudnick, D. L. (2001). On the skewness of vorticity in the upper ocean. *Geophysical Research Letters*, 28(10):2045–2048.

Rühs, S., Durgadoo, J. V., Behrens, E., and Biastoch, A. (2013). Advective timescales and pathways of Agulhas leakage. *Geophysical Research Letters*, 40(15):3997–4000.

Rühs, S., Schwarzkopf, F. U., Speich, S., and Biastoch, A. (2018). Cold vs. warm water route–sources for the upper limb of the AMOC revisited in a high-resolution ocean model. *Ocean Science Discussions*.

Sasaki, H. and Klein, P. (2012). SSH wavenumber spectra in the North Pacific from a high-resolution realistic simulation. *Journal of Physical Oceanography*, 42(7):1233–1241.

Sasaki, H., Klein, P., Qiu, B., and Sasai, Y. (2014). Impact of oceanic-scale interactions on the seasonal modulation of ocean dynamics by the atmosphere. *Nature Communications*, 5:5636.

Schluessel, P., Emery, W. J., Grassl, H., and Mammen, T. (1990). On the bulk-skin temperature difference and its impact on satellite remote sensing of sea surface temperature. *Journal of Geophysical Research: Oceans*, 95(C8):13341–13356.

Schouten, M. W., de Ruijter, W. P., and Van Leeuwen, P. J. (2002). Upstream control of Agulhas Ring shedding. *Journal of Geophysical Research: Oceans*, 107(C8):23–1.

Schubert, R., Biastoch, A., Cronin, M. F., and Greatbatch, R. J. (2018). Instability-driven benthic storms below the separated Gulf Stream and the North Atlantic Current in a high-resolution ocean model. *Journal of Physical Oceanography*, 48(10):2283–2303.

Schubert, R., Gula, J., Greatbatch, R. J., Baschek, B., and Biastoch, A. (2020). Strengthening of Agulhas Mesoscales by the Submesoscale Inverse Kinetic Energy Cascade. *Journal of Physical Oceanography (under review)*.

Schubert, R., Schwarzkopf, F. U., Baschek, B., and Biastoch, A. (2019). Submesoscale impacts on mesoscale Agulhas dynamics. *Journal of Advances in Modeling Earth Systems*, 11(8):2745–2767.

Schumann, E. and van Heerden, I. L. (1988). Observations of agulhas current frontal features south of africa, october 1983. *Deep Sea Research Part A. Oceanographic Research Papers*, 35(8):1355–1362.

Schwarzkopf, F. U., Biastoch, A., Böning, C. W., Chanut, J., Durgadoo, J. V., Getzlaff, K., Harlaß, J., Rieck, J. K., Roth, C., Scheinert, M. M., et al. (2019). The inalt family–a set of high-resolution nests for the agulhas current system within global nemo ocean/sea-ice configurations. *Geoscientific Model Development*, 12(7):3329–3355.

Scott, R. B. and Arbic, B. K. (2007). Spectral energy fluxes in geostrophic turbulence: Implications for ocean energetics. *Journal of Physical Oceanography*, 37(3):673–688.

Scott, R. B. and Wang, F. (2005). Direct evidence of an oceanic inverse kinetic energy cascade from satellite altimetry. *Journal of Physical Oceanography*, 35(9):1650–1666.

Seaton, S. L. (1980). Cape of Storms - Around treacherous Cape Agulhas they saled among icebergs. *Cruising World, ISSN 0098-3519*.

Semtner, A. J. and Mintz, Y. (1977). Numerical simulation of the Gulf Stream and mid-ocean eddies. *Journal of Physical Oceanography*, 7(2):208–230.

Sinha, A., Balwada, D., Tarshish, N., and Abernathey, R. (2019). Modulation of Lateral Transport by Submesoscale Flows and Inertia-Gravity Waves. *Journal of Advances in Modeling Earth Systems*, 11(4):1039–1065.

Smagorinsky, J. (1993). Some historical remarks on the use of nonlinear viscosities. *Large Eddy Simulation of Complex Engineering and Geophysical Flows*, 1:69–106.

Soh, H. S. and Kim, S. Y. (2018). Diagnostic characteristics of submesoscale coastal surface currents. *Journal of Geophysical Research: Oceans*, 123(3):1838–1859.

Soufflet, Y., Marchesiello, P., Lemarié, F., Jouanno, J., Capet, X., Debreu, L., and Benshila, R. (2016). On effective resolution in ocean models. *Ocean Modelling*, 98:36–50.

Speich, S., Blanke, B., and Cai, W. (2007). Atlantic meridional overturning circulation and the Southern Hemisphere supergyre. *Geophysical Research Letters*, 34(23).

Speich, S., Lutjeharms, J., Penven, P., and Blanke, B. (2006). Role of bathymetry in Agulhas Current configuration and behaviour. *Geophysical Research Letters*, 33(23).

Stanton, A. and Unkrich, L. (2003). Finding Nemo. *USA, Buena Vista Pictures/Walt Disney Pictures*, 101.

Steele, M., Morley, R., and Ermold, W. (2001). PHC: A global ocean hydrography with a high-quality Arctic Ocean. *Journal of Climate*, 14(9):2079–2087.

Stewart, K., Hogg, A. M., Griffies, S., Heerdegen, A., Ward, M., Spence, P., and England, M. (2017). Vertical resolution of baroclinic modes in global ocean models. *Ocean Modelling*, 113:50–65.

Stöckli, R., Vermote, E., Saleous, N., Simmon, R., and Herring, D. (2005). The Blue Marble Next Generation-A true color earth dataset including seasonal dynamics from MODIS. *Published by the NASA Earth Observatory*.

Stone, P. H. (1966). On non-geostrophic baroclinic stability. *Journal of the Atmospheric Sciences*, 23(4):390–400.

Stone, P. H. (1970). On non-geostrophic baroclinic stability: Part II. *Journal of the Atmospheric Sciences*, 27(5):721–726.

Storch, J.-S. v., Eden, C., Fast, I., Haak, H., Hernández-Deckers, D., Maier-Reimer, E., Marotzke, J., and Stammer, D. (2012). An estimate of the Lorenz energy cycle for the world ocean based on the STORM/NCEP simulation. *Journal of Physical Oceanography*, 42(12):2185–2205.

Swart, N. and Fyfe, J. C. (2012). Observed and simulated changes in the Southern Hemisphere surface westerly wind-stress. *Geophysical Research Letters*, 39(16).

Talley, L. D. (2003). Shallow, intermediate, and deep overturning components of the global heat budget. *Journal of Physical oceanography*, 33(3):530–560.

Tandon, A. and Garrett, C. (1994). Mixed layer restratification due to a horizontal density gradient. *Journal of Physical Oceanography*, 24(6):1419–1424.

Tandon, A. and Garrett, C. (1995). Geostrophic adjustment and restratification of a mixed layer with horizontal gradients above a stratified layer. *Journal of Physical Oceanography*, 25(10):2229–2241.

Taylor, J. R. and Ferrari, R. (2009). On the equilibration of a symmetrically unstable front via a secondary shear instability. *Journal of Fluid Mechanics*, 622:103–113.

Tedesco, P., Gula, J., Ménesguen, C., Penven, P., and Krug, M. (2019). Generation of submesoscale frontal eddies in the Agulhas Current. *Journal of Geophysical Research: Oceans*.

Thomas, L. and Ferrari, R. (2008). Friction, frontogenesis, and the stratification of the surface mixed layer. *Journal of Physical Oceanography*, 38(11):2501–2518.

Thomas, L. and Taylor, J. (2010). Reduction of the usable wind-work on the general circulation by forced symmetric instability. *Geophysical Research Letters*, 37(18).

Thomas, L. N. (2005). Destruction of potential vorticity by winds. *Journal of Physical Oceanography*, 35(12):2457–2466.

Thomas, L. N., Tandon, A., and Mahadevan, A. (2008). Submesoscale processes and dynamics. *Ocean Modeling in an Eddying Regime*, 177:17–38.

Thomas, L. N., Taylor, J. R., Ferrari, R., and Joyce, T. M. (2013). Symmetric instability in the Gulf Stream. *Deep Sea Research Part II: Topical Studies in Oceanography*, 91:96–110.

Tsujino, H., Urakawa, S., Nakano, H., Small, R. J., Kim, W. M., Yeager, S. G., Danabasoglu, G., Suzuki, T., Bamber, J. L., Bentsen, M., et al. (2018). JRA-55 based surface dataset for driving ocean–sea-ice models (JRA55-do). *Ocean Modelling*, 130:79–139.

Tulloch, R., Marshall, J., Hill, C., and Smith, K. S. (2011). Scales, growth rates, and spectral fluxes of baroclinic instability in the ocean. *Journal of Physical Oceanography*, 41(6):1057–1076.

Vallis, G. (2006). Atmospheric and Oceanic Fluid Dynamics: Fundamentals and Large-Scale Circulation (Cambridge).

Van Aken, H., Van Veldhoven, A., Veth, C., de Ruijter, W., Van Leeuwen, P., Drijfhout, S., Whittle, C., and Rouault, M. (2003). Observations of a young Agulhas ring, Astrid, during MARE in March 2000. *Deep Sea Research Part II: Topical Studies in Oceanography*, 50(1):167–195.

van Aken, H. M., Ridderinkhof, H., and de Ruijter, W. P. (2004). North Atlantic deep water in the south-western Indian Ocean. *Deep Sea Research Part I: Oceanographic Research Papers*, 51(6):755–776.

van Leeuwen, P. J., de Ruijter, W. P., and Lutjeharms, J. R. (2000). Natal pulses and the formation of Agulhas rings. *Journal of Geophysical Research: Oceans*, 105(C3):6425–6436.

Volkov, D. L., Larnicol, G., and Dorandeu, J. (2007). Improving the quality of satellite altimetry data over continental shelves. *Journal of Geophysical Research: Oceans*, 112(C6).

Wagner, P., Rühs, S., Schwarzkopf, F. U., Koszalka, I. M., and Biastoch, A. (2019). Can Lagrangian tracking simulate tracer spreading in a high-resolution Ocean General Circulation Model? *Journal of Physical Oceanography*, 49(5):1141–1157.

Walker, N. D. and Mey, R. D. (1988). Ocean/atmosphere heat fluxes within the Agulhas Retroflection region. *Journal of Geophysical Research: Oceans*, 93(C12):15473–15483.

Webb, D. J., De Cuevas, B. A., and Richmond, C. S. (1998). Improved advection schemes for ocean models. *Journal of Atmospheric and Oceanic Technology*, 15(5):1171–1187.

Weijer, W., de Ruijter, W. P., Sterl, A., and Drijfhout, S. S. (2002). Response of the Atlantic overturning circulation to South Atlantic sources of buoyancy. *Global and Planetary Change*, 34(3-4):293–311.

Xu, C., Shang, X.-D., and Huang, R. X. (2014). Horizontal eddy energy flux in the world oceans diagnosed from altimetry data. *Scientific Reports*, 4:5316.

Xu, Y. and Fu, L.-L. (2011). Global variability of the wavenumber spectrum of oceanic mesoscale turbulence. *Journal of Physical Oceanography*, 41(4):802–809.

Xu, Y. and Fu, L.-L. (2012). The effects of altimeter instrument noise on the estimation of the wavenumber spectrum of sea surface height. *Journal of Physical Oceanography*, 42(12):2229–2233.

Yu, L. and Weller, R. A. (2007). Objectively analyzed air–sea heat fluxes for the global ice-free oceans (1981–2005). *Bulletin of the American Meteorological Society*, 88(4):527–540.

Zalesak, S. T. (1979). Fully multidimensional flux-corrected transport algorithms for fluids. *Journal of computational physics*, 31(3):335–362.